UNIVERSITY OF SOUTHAMPTON

NUMERICAL MODELLING AND EXPERIMENTAL STUDY OF ROLLOVER IN CRYOGENIC LIQUIDS AND LIQUID FREON

Ji Quan, SHI

Submitted for the degree of Doctor of Philosophy

INSTITUTE OF CRYOGENICS,
SOUTHAMPTON,
ENGLAND, UK
DECEMBER 1990

TO MY PARENTS

UNIVERSITY OF SOUTHAMPTON

ABSTRACT

FACULTY OF ENGINEERING

INSTITUTE OF CRYOGENICS

Doctor of Philosophy

NUMERICAL MODELLING AND EXPERIMENTAL STUDY OF LNG ROLLOVER IN CRYOGENIC LIQUIDS AND LIQUID FREON

by Ji Quan SHI

A combined numerical and experimental investigation into LNG rollover has been performed, using cryogenic liquids and also liquid freon to simulate a two-layer LNG system.

A numerical model for laminar flows was developed for modelling of rollover in both rectangular and cylindrical vessels. Rectangular vessels were modelled as two-dimensional problems and cylindrical ones as axi-symmetric.

Flow visualization experiments using foreign particles as flow tracers were performed to verify qualitatively the numerical results obtained in a specially designed two-dimensional rectangular tank. A long glass dewar with up to 180cm wall heating length was constructed to study the effect of a turbulent wall boundary layer on the dependence of the surface heat flux on bulk liquid superheat. Schlieren flow visualization was carried out to reveal surface convective patterns.

Results show that in a two-layer system of cryogenic liquids (under atmospheric pressure), the free surface is almost isothermal, whereas the liquid-liquid interface is quasi-adiabatic. Consequently, buoyancy-induced convective flows in the two layers are distinctively different. Due to the cooling action of an isothermal surface, a strong core flow exists in the upper layer; in contrast, high fluid velocity only confines to the boundary layer in the lower layer.

Rollover is characterised by first gradual descent of the interface, then rapid mixing between layers. The migration of the interface is primarily due to entrainment at the interface through the core flow as it impinges on the interface; when the density difference across the interface is small, the core flow can penetrate into the interface. The ratio of base to side heat flux has a strong influence on the rollover pattern. The intensity of the final mixing between layers is closely linked to this ratio. Generally a higher heat flux ratio would lead to a more intensified final mixing.

The 4/3 power law correlation between the surface heat flux and bulk superheat is valid for both laminar and turbulent wall boundary layers.

CONTENTS

NOMENCLATURE

A,	$A = c(g\alpha^2/\nu)^{1/3}$	m/s
A_1,	$A_1 = f_1(g\alpha^2/\nu)^{1/3}$	m/s
πa,	Horizontal wavenumber	1/m
c,	Constant	
C_b,	$C_B = kR_b^{-1/3}(g\beta_T/\alpha\nu)^{1/3}$	
CC	Cartesian coordinates	
CPC	Cylindrical polar coordinates	
d,	Layer depth	m
d_p,	Penetration depth	m
D,	Diffusion conductance $D = \Gamma/\delta$	
f_1, f_2	Functions of density ratio R_ρ	
F,	Mass flow rate $F = u$	
F_T, F_T^d	Temperature flux	m-K/s
F_S,	Salt flux	kg/m^2s
g,	Gravitational acceleration	m/s^2
g',	$g' = g\rho'/\rho$	m/s^2
$\vec{g}$,	$\vec{g} = (0, 0, -g)$	m/s^2
H,	Heat flux	W/m^2
H0,	Enthalpy of liquid at an equilibrium state	J
$\vec{i}$,	Unit vector along x axis	
J,	Total flux of the general variable ϕ	
J_x,	Total flux along x axis	
J_r,	Total flux along r axis	
J_z,	Total flux along z axis	
K,	Kelvin	
k,	Thermal conductivity	W/m-K
$\vec{k}$,	Unit vector along z axis	
L,	Length scale	m

La	Latent heat	kJ/kg
LNG	Liquified natural gas	
$\dot{m}$,	Mass flow rate	kg/s
πn,	Vertical wavenumber	1/m
Nu,	Nusselt number $Nu = Hd/k\Delta T$	
p,	Pressure	Pa
p_0,	Reference pressure	Pa
p',	Pressure deviation form p_0	Pa
P,	Peclet number $P = F/D$	
Pr,	Prandtl number $Pr = \nu/\alpha$	
$\dot{q}$,	Wall heat flux	W/m^2
$\dot{q}_s$,	Surface heat flux	W/m^2
$\dot{Q}$,	Total heat flow rate	W
$\dot{Q}_{sur}$,	Surface heat flow rate	W
r,	Radius	m
r_P,	Radius of a grid point	m
r_e,	Radius of the interface east to the grid point	m
r_e,	Radius of the interface west to the grid point	m
Δr,	Control volume width in CPC	m
Ra,	Rayleigh number $Ra = g\beta_T \Delta T d^3/\nu\alpha$	
Ra^*,	Modified Rayleigh number $Ra^* = g\beta_T \dot{q} d^4/k\nu\alpha$	
Ra_c,	Critical Rayleigh number	
Ra_c^*,	Critical modified Rayleigh number	
Re,	Reynolds number $Re = UL/\nu$	
Rb,	Rayleigh number for sustaining the surface layer $Rb = g\beta_T \Delta T \delta^3/\nu$	
Rs,	Salinity Rayleigh number $Rs = g\beta_S \Delta S d^3/k\nu\alpha$	
R_ρ,	Density ratio $R_\rho = \beta_S \Delta S/\beta_T \Delta T$	

S,	Salinity concentration	kg/m^3
ΔS,	Difference of S	kg/m^3
T,	Temperature	K
T_b,	Bulk liquid temperature	K
T_0,	Liquid surface temperature	K
TO,	Thermal overfill	J
T_{sat},	Saturation temperature of liquid	K
ΔT,	Temperature difference	K
ΔT_b,	Bulk liquid superheat	K
t,	Time	s
U,	Velocity scale	m/s
u,	Horizontal velocity component	m/s
u_e,	Interface velocity	m/s
u_f,	Fluid velocity	m/s
$u_{max,b}$,	Maximum boundary layer velocity	m/s
$u_{max,c}$,	Maximum velocity of a core flow	m/s
u_P,	Velocity of a tracer particle	m/s
$\vec{u}$,	Vector notation of velocity	m/s
w,	Vertical velocity component	m/s
x,	horizontal axis	
Δx,	Control volume width in CC	m
z,	vertical axis	
Δz,	Control volume height	m
α,	Thermal diffusivity	m^2/s
α_S,	Salinity diffusivity	m^2/s
β_T,	Thermal expansion coefficient	1/K
β_S,	Salinity expansion coefficient	m^3/kg
Γ,	Dimensionless diffusion coefficient	
δ, δ_x, δ_r, δ_z	Distance between grid points	m
ϵ,	Relative error	
ζ,	Vorticity	1/s
ζ',	$\zeta' = \zeta/r$	1/m-s

η,	Aspect ratio	
Θ, λ,	Variables between -1 and 1	
μ,	Viscosity	Pa-s
ν,	Kinetic viscosity	m^2/s
ρ,	Liquid density	kg/m^3
ρ_c,	Density of a core flow	kg/m^3
σ,	Exponential power	
ϕ,	General variable (T, S, ζ, ψ)	
χ,	Relaxation factor	
ψ,	Stream function	m^2/s

1.0 INTRODUCTION

1.1 LNG Rollover

For large scale storage of natural gas, its liquid form is preferable for the obvious reason of much smaller volume associated with the liquid state. The major constituent of liquefied natural gas(LNG) is methane, which ranges from 65% to 95% in volume for different sources. Liquefied methane has a boiling point of 112K. Therefore, for economic reason LNG tanks always contain some liquid, termed heel, to maintain a low temperature and avoid cooldown costs.

LNG is a multi-component liquid consisting of mainly methane, heavier hydrocarbons and sometimes nitrogen. Its composition could vary considerably from source to source. For example, pipeline gas in the North-East of the USA may be 95% methane, compared with Libyan LNG which might be 65% methane, 25% ethane and 10% propane and higher hydrocarbons. As well as the source, the preferential evaporation of more volatile components over a period of time could also change the composition and temperature of LNG. This process is called weathering.

Therefore when a cargo of LNG is loaded into a partially filled storage tank, it is often the case that the density of the two liquids are slightly different arising from the differences in temperature and composition. Stratified layers may result if a heavier cargo is bottom-filled and a lighter one top-filled and the two liquids are not adequately mixed.

LNG tanks are well insulated to reduce loss of liquid through vaporization due to heat leak from the surrounding. Heat fluxes are typically of tens of Watts per meter square. This level of heat flux is far too low for nucleate boiling to occur, but high enough to generate a convection loop in the tank, as illustrated in Fig. 1.1a. Liquid in the boundary layer flows upwards over the tank walls, absorbing heat from the surroundings, then across the free surface where the heat is removed by evaporation.

In the case of two stratified layers, the boundary layer in the lower layer is unable to reach the surface, as illustrated in Fig. 1.1b. The superheat in the bottom layer will build up because diffusion across the interface between the two layers is insufficient to match the heat leaking in from the tank walls. This heating continues until the density of the lower layer falls to that of the upper layer, at which point the highly superheated liquid is suddenly allowed to reach the surface. This process, together with the sudden release of the superheat from the lower layer, is rather inaccurately known as "rollover".

In a few instances, the sudden increase in the vaporisation rate has exceeded the vents on the storage tank and caused a serious over-pressurisation of the system to occur. Fortunately, no rupture or leakage has resulted so far.

Rollover can now be effectively prevented by choosing the right filling procedure, i.e., top-filling for a heavier cargo and bottom-filling for a lighter one; or using mechanical mixing devices to mix two liquids. This phenomenon is, however, still not fully understood in terms of the mechanisms and parameters which control the event.

The aim of the study reported in this thesis was to promote further understanding of the above aspects of rollover. The numerical approach was considered to study convective flows within the layers in a multi-layer cryogenic liquid system, and their effect on the mixing of adjacent layers. These numerical investigations were considered important because the convective flows control the behaviour of the interface movement, notably the migration or disappear of the interface. The former allows a gradual release of stored superheat in the lower layer. On the other hand, the quick mixing between the layers as indicated by the latter would result in a sudden release of the stored superheat, accompanied by a sudden, sometimes sharp, increase in the surface evaporation rate.

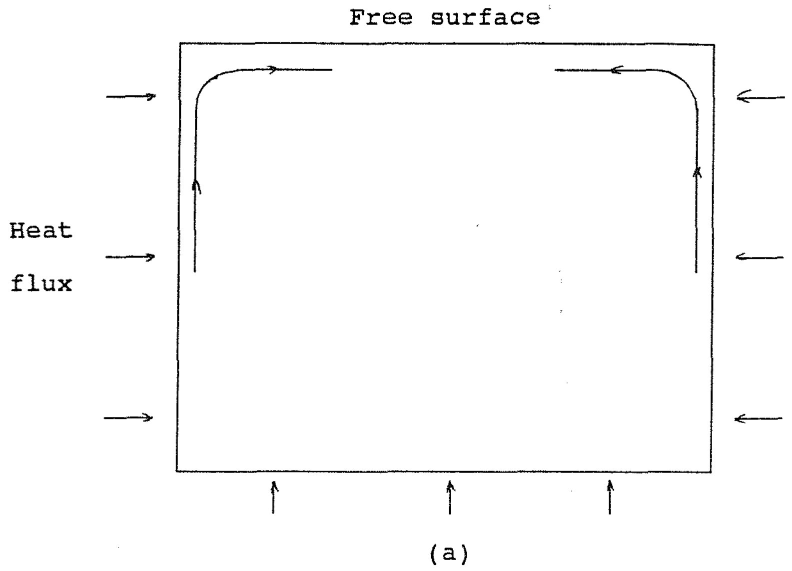

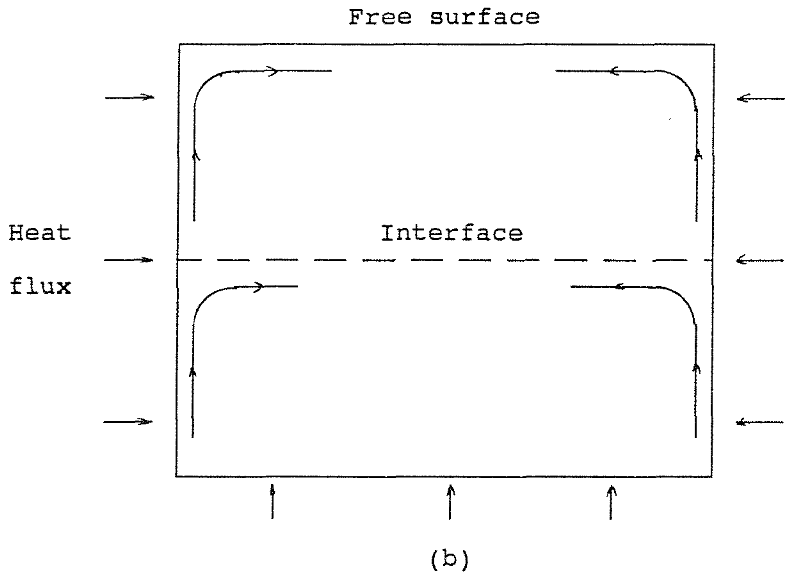

Fig. 1.1 Convective flows in a storage tank;

a) a single layer; b) two stratified layers.

Following a chapter on the theory concerning the dynamics of stratified convecting layers, this thesis describes how the finite control volume technique has been used to study the mixing of initially separate layers in cryogenic liquids. The numerical model has allowed the mixing process to be studied in detail. Flow visualization of rollover was carried out to verify qualitatively the numerical results obtained. The numerical and flow visualization results are discussed, and some firm conclusions are reached about the mechanisms which control the mixing process. In chapter 7 two experimental studies concerning the liquid-vapour interface of stored cryogenic liquids are reported and discussed.

1.2 Previous Investigations

1.2.1 The La Spezia Rollover

Among the few reported LNG rollover incidents[1][2][3], the one occurred at La Spezia, Italy in 1971 has been well documented. In his report[1], Sarsten gives a good account of this particular rollover event. The figures provided in this report have subsequently formed the basis for testing various rollover simulation models put forward in the years following this incident.

The initial composition and properties of the LNG tank heel and ship cargo (before transfer) at La Spezia are given in Table 1.1[1]. Table 1.2 shows some details of the LNG tank involved. The cargo liquid was hotter and heavier than the heel. This is because the ship had been in La Spezia harbour for more than a month and during that time the cargo became heavier and hotter as a result of continuing boil off of light components(mainly methane).

Eighteen hours after filling, tank S-1 experienced a sudden rise in tank pressure, which marked the beginning of rollover. This rollover, accompanied by the evolution of vast amount of LNG vapour, lasted one and quarter hours, with the tank safety valves open in discharge. The tank eventually reached equilibrium at normal tank

Table 1.1 The initial composition and properties of LNG at La Spezia

Composition	Tank heel (mol %)	Esso Brega cargo (mol %)
Methane	63.62	62.26
Ethane	24.16	21.26
Propane	9.36	12.66
Butane	1.45	1.94
Isobutane	0.90	1.20
Pentane	0.05	0.01
Isopentane	0.11	0.06
Nitrogen	0.35	0.02
Temperature (K)	114.36	118.99
Density (kg/m^3)	541.12	544.9
Vapour Pressure (Pa)	3921	16273
Liquid Depth (m)	5.03	17.83

Table 1.2 The LNG tank at La Spezia

Diameter (m)	49.1
Height (m)	26.8
Base Heat Leak (W/m^2)	20.82
Side Heat Leak (W/m^2)	6.94
Tank Pressure (mm H_2O)	250

pressure (250mm water) two hours after the closure of the safety valves. An account of the amount of LNG vapour released throughout this event is given in Table 1.3.

Table 1.3 The record of vapour evolution at La Spezia

Stage	Duration (hr)	Amount of LNG vapour evolved (Ib)	(kg)	Mean rate (kg/hr)
Normal*				450
Filling	13	25,000**	11,300	870
Incubation	18	35,000	15,900	880
Rollover	1.25	330,000	149,700	119,800
After	2	110,000	49,000	25,000

* The boil-off rate calculated using the heat flux data in Table 1.2 by assuming that the tank contains pure methane with a height of 5.05 + 17.83 = 22.86 m.

** This is in addition to the 100,000 Ib of LNG vapour flowing out of the tank due to the displacement of the cargo liquid.

The heavier cargo was bottom filled into tank S-1. The mixing was thus minimum between the cargo and the heel during the filling. The mean boil off rates of LNG during filling and before rollover were about the same, approximately twice the boil off rate at the normal condition. During rollover, this mean rate rose to as high as 250 times of the normal boil off rate.

1.2.2 Mathematical Models

A number of LNG rollover simulation models[3-6] have been proposed since the La Spezia rollover incident. These models more or less share a common framework:

1) LNG in a storage tank is considered as the stable stratification of a number of distinct convecting layers (or cells). The density difference between layers arises from the difference in temperature and composition.

2) Balance of material and thermal energy is performed over each layer, and also in the vapour space in [6]. The thickness of each layer (except the top one) remains constant before mixing, i.e., no entrainment of liquid between adjacent layers.

3) Turbulent transport of heat and mass transfer across the layer interfaces drive adjacent layers towards density equilibration. When two adjacent layers approach density equilibration, they mix (rollover) to form a larger layer with mean characteristics.

4) This layer elimination progress continues until the entire tank liquid becomes a single layer.

5) When the last two layers merge (final tank rollover), the thermal energy accumulated in the lower layer is released at the surface, resulting in a sudden increase in the boil off rate.

There are, however, two significant differences among them, notably, in the ways of handling interfacial heat and mass transfer coefficients and surface evaporation. [3], [4] and [5] use the thermohaline equations of Turner[7] and Huppert[8] to define heat and mass transfer coefficients between adjacent layers. These thermohaline expressions, however, are considered not appropriate by [6] on the ground that they do not allow sufficient mass transfer between layers during the early stage when the density ratio (defined as the ratio of the density changes due to composition and temperature) is too large to account for the vapour generation reported at La Spezia. Instead, inter-layer heat and mass transfer coefficients are determined in the usual way for fully turbulent systems.

Chatterjee et al[4], by assuming the temperature of the top layer is at the same temperature as the film at the top of the tank, calculate the evaporation rate directly from the heat received by the top layer. (The evolved vapour is in thermodynamic equilibrium with liquid in the film). In their second model[3], a standard flash calculation is used for surface evaporation.

The Hashemi-Wesson model[9] is used by Gemerles[5] for handling surface evaporation. In the HW model, the bulk liquid is at a superheated state respect to the tank pressure, and a 4/3 power law is proposed between the surface evaporation rate and bulk fluid superheat (temperature of the bulk liquid in excessive of that at the surface). Heestand et al use a modified version of HW equation, which takes into account the influence of composition as well as the temperature variations in the bulk liquid.

When applied to the La Spezia rollover incident using data given in [1], models[4-6] predict a rollover time in good agreement with the recorded time of 31 hours (from the start of filling), despite the above differences. The predicted peak boil off rate in all three cases are, however, at least of one order smaller than reported in [1].

1.2.3 Experimental Investigations

Morioka and Enya[10] used fresh and salt water to simulate a two-layer stratification in LNG tanks. Experiments were carried out in a two-dimensional laboratory scale rectangular tank equipped with side and base heaters. Flow visualizations using dye show that mixing of layers is characterised by the boundary layer flows rising along the side walls. When the density of two layers approach equalization, the boundary flow in the lower layer penetrates into the upper layer where mixing takes place. As a result, the interface gradually moves down until it disappears at the base. The rollover is thus a gradual process accompanied by the descent of the interface.

Nakano, Sugawara, Yamagata and Nakamura[11] carried out similar experimental studies in liquid freon. Freon 11, whose boiling point at atmospheric pressure is around room temperature, and freon 113 were used to form two stratified layers. The tests were performed in a two-dimensional model tank. In their experiments, two modes of rollover were observed, depending on the position of heating. For base heating only, the interface shows slightly climbing trends but its position hardly changes before mixing. Following the appearing of a large wave motion in the interface, the two layers are quickly mixed as the lower layer liquid rises along the side walls to reach the surface and the upper layer liquid moves down through the centre of the tank. This observation corresponds to the rapid mixing mode assumed by the rollover models[4-6].

In the case of side heating only, the interface descends gradually with the penetration of boundary flow in the lower layer into the upper layer until the interface disappears at the tank base. This gradual mixing mode of rollover is in agreement with the observations made by Morioka et al[10]. Tests with both side and base heating produced mixed results in the rollover modes.

Few rollover experiments have been performed in actual LNG tank. Following the experimental study in a model tank[11], Sugawaru, Kubota and Wuraki[12] conducted an actual LNG tank test to verify the experimental results obtained using the model tank. LNG from two different sources were used to simulate stratification in the tank. In all, five tests were carried out and the following results were obtained:

1) A intermediate layer, resulted from the mixing between layers during filling, exists between two stratified layers in all tests.

2) This intermediate layer gradually becomes thinner with time and a sharp interface is formed. With the thinning of the intermediate layer, interfacial heat and mass

transfer increase.

3) The interface level falls gradually, but rapidly just before intense mixing between layers takes place.

4) The interface movement is dominated by the entrainment mixing at the interface, rather than the penetration of boundary flow along the side walls.

Based on these new findings, a rollover simulation model was proposed by the authors. This model is basically the same as Gemerles's[5], except that the interface level is allowed to move and an intermediate layer is included. The La Spezia rollover incident was examined by this model. Good agreement was obtained in terms of the rollover time, but again the predicted peak boil off rate was at least one order short of the figure reported in [1].

Recently Agbabi[13] carried out an experimental study using cryogenic liquids to simulate a two-layer LNG system. A series of tests with a range of initial density differences and different heating configurations was performed in a vacuum insulated double-walled cylindrical glass dewar. The dewar was equipped with side heating only. Results show that the mixing of layers is primarily due to entrainment at the interface and the intermediate layer can be described by double-diffusive convection theory. No boundary layer penetration has been observed during rollover simulation experiments. This is attributed to the small vertical scale of the test dewar by the author.

1.3 Summary

Rollover simulation models in the analysis of the La Spezia incident, all predict the time to rollover accurately. (This confirms that LNG rollover is indeed a consequence of stable stratification in storage tanks). They, however, fail to explain the very high peak vapour flow rates occurred at La Spezia.

Beduz et al[14] show that in the normal storage of cryogenic liquids, surface evaporation is controlled by the bulk superheat via a thin surface layer which contains a very large temperature gradient. This temperature gradient provides a large thermal impedance for heat transfer at the surface. Maher and Gelder[15] discussed the possible consequence of the destruction of this thin surface layer in a rollover event. Calculations show that if an 2.7m thick layer with a superheat of 3°C were flashed at rollover, a total of 360,000kg vapour would be generated. Assuming the rollover lasting over a period of two minutes, the mean rate could reach 10 million kg/hr. The actual vapour flow rate, however, would be substantially less than the above theoretical value due to the reestablishing of the surface layer. Though grossly simplified, this rollover model does provide a possible explanation to the very high peak vapour flow rates observed in the La Spezia rollover.

Most rollover simulation models assume that the interface between layers is fixed before mixing taking place. In contrast to this assumption, rollover simulation experiments show that the interface level does change with time. Two mechanisms have been identified, namely the entrainment mixing at the interface and the boundary layer penetration.

2.0 THEORETIC CONSIDERATIONS

It has been shown that LNG rollover arises from stratification of liquid in storage tanks. A tank containing a layer of homogenous LNG under normal storage conditions is believed to have no risk of rollover, unless its content is rich in nitrogen, then a spontaneous stratification of liquid may be possible due to the preferential evaporation of nitrogen[3]. Convective flows generated by heat leak would keep the bulk liquid mixed and free from stratification.

Thermal Overfill

Beduz et al[14] introduce the concept of thermal overfill to explain the boil-off variations in isobaric storage of cryogenic liquids. Thermal overfill, TO, is defined as the sum of the excess enthalpy of the stored liquid over H0, the value of enthalpy when the liquid is at equilibrium state with the tank pressure. Mathematically,

$$\frac{\partial(TO)}{\partial t} = \dot{Q} - \dot{m}La \tag{2.1}$$

where

$\dot{m}$ ———— vapour flow rate,
$\dot{Q}$ ———— rate of total heat input,
La ———— latent heat of the liquid.

If the heat removal rate at the surface is less than that of the total heat input, i.e., $\dot{m}La < \dot{Q}$, then the right hand side of equation (2.1) is positive and thermal energy is accumulated in the liquid. This is likely to happen when a LNG tank is stratified. When $\partial(TO)/\partial t$ is positive over a period of time, then a hazardous storage situation, such as rollover, is built up.

In this chapter some relevant theories are considered which concern convection in stratified liquids, namely, double-diffusive convection and mixing across a density interface. But first, some basic fluid dynamics and parameters of importance in this study are introduced.

2.1 Basic Fluid Dynamics

2.1.1 Equations of Motion, and Assumptions

The liquid is assumed incompressible and non-diffusive. This means

$$\frac{D\rho}{Dt} = 0 \tag{2.2}$$

where D/Dt denotes differentiation following the motion. The continuity equation in vector notation is

$$\nabla \cdot \vec{u} = 0 \tag{2.3}$$

where $\vec{u}$ = (u, v, w) is the velocity. The momentum(Navier-Stokes) equations with the force of gravity included can be written as

$$\rho\frac{D\vec{u}}{Dt} = \rho[\frac{\partial \vec{u}}{\partial t} + (\vec{u}\cdot\nabla\vec{u})] = -\nabla p + \rho\vec{g} + \mu\nabla^2\vec{u} \tag{2.4}$$

where $\vec{g}$ = (0, 0, -g), the x and y axes being the horizontal plane and z vertically upwards. If the viscosity μ can be neglected (inviscid flow), equation (2.4) reduces to the Eular equations of motion.

There are three assumptions which are widely used to simplify the Eular equation.

Hydrostatic assumption

Assuming p_0 and ρ_0 are the values of p and ρ in a reference state of hydrostatic equilibrium at which $\nabla p_0 = \rho_0 \overline{g}$, the Eular equations can be written in terms of the deviations p' and ρ' from this state as

$$\rho \frac{D\overline{u}}{Dt} = -\nabla p' + \rho' \overline{g} \tag{2.5}$$

where $p' = p - p_0$ and $\rho' = \rho - \rho_0$. This implies that only differences of density ρ' from some standard value are relevant in determining the effect of gravity. In a two-layer system, for example, the layer with the standard density ρ_0 may be regarded as weightless, and that with density $\rho = \rho_0 + \rho'$ as if it were acted only by a reduced gravitational acceleration $g' = g\rho'/\rho$.

Linearization

Linearization processes omit the non-linear terms such as $u\partial u/\partial x$ in comparison with $\partial u/\partial t$ in equation (2.5). Linearization of equation (2.5) leads to

$$\rho \frac{\partial \overline{u}}{\partial t} = -\nabla p' + \rho' \overline{g} \tag{2.6}$$

This procedure is justified when the motion and velocities are of small amplitude.

Boussinesq approximation

In this approximation the density deviation ρ' is assumed to be small compared to ρ_0, i.e., $\rho'/\rho_0 << 1$. Rewriting equation (2.5) in the form

$$(1+\frac{\rho'}{\rho_0})\frac{D\vec{u}}{Dt} = -\frac{\nabla p'}{\rho_0} + \frac{\rho'}{\rho_0}\vec{g} \qquad (2.7)$$

it follows that ρ'/ρ_0 may be neglected in the inertia term, but is retained in the buoyancy term. That is equivalent to saying that the density variation can be neglected except when giving rise to buoyancy. When viscosity and diffusivity are also included, variations of fluid properties are also neglected in this approximation.

The Boussinesq approximation may be made in combination with the linear approximation. The linearized Boussinesq momentum equations for an inviscid flow are

$$\frac{\partial\vec{u}}{\partial t} = -\frac{\nabla p'}{\rho_0} + \frac{\rho'}{\rho_0}\vec{g} \qquad (2.8)$$

2.1.2 Flow Parameters

For a layer of liquid heated from below, the Prandtl and Rayleigh number are the two relevant flow parameters. The Prandtl number(Pr) is the ratio between the kinetic viscosity and the thermal diffusivity, Pr $= \nu/\alpha$. The Rayleigh number(Ra) is defined as

$$Ra = \frac{g\beta_T\Delta T d^3}{\nu\alpha} \qquad (2.9)$$

where

ΔT	————	temperature difference across the layer,
d	————	depth of the layer,
β_T	————	the thermal expansion coefficient, defined as

$$\beta_T = -\frac{1}{\rho}\frac{\partial \rho}{\partial T} \tag{2.10}$$

It therefore expresses the balance between the driving buoyancy forces and the two diffusive processes which retard the motion. When Ra exceeds a certain value for given boundary conditions, cellular convective motions will set in. This limit is called the critical Ra number(Ra_c). For example, the Ra_c for a layer of liquid with two free conducting horizontal boundaries is $27\pi^4/4 \approx 657$.

In heterogeneous flows the overall Richardson number(Ri_o) gives a measure of the relative importance of buoyancy over inertial force. It is defined as

$$Ri_o = \frac{g'L}{U^2} \tag{2.11}$$

where U and L are the typical scales of velocity and length.

2.2 Double Diffusive Convection

2.2.1 Mechanism of Instability

Double-diffusive convection refers to convection in fluids in which there are gradients of two (or more) properties with different molecular diffusivity and opposing effects on vertical density distribution. Its study arise from the observation of ocean motions by oceanographers, and because heat and salt contents are then the relevant properties, the process has been called 'thermohaline' or 'thermosolutal' convection.

The form of motion depends on whether the driving energy comes from the substance of higher or lower diffusivity. Two possible kinds of motions are proposed[16][17]: 1) a 'salt fountain' when warm salty water overlies colder fresher water of higher density; 2) oscillatory motions when these two are reversed, i.e., warm salty water beneath colder fresher water. In the first case, consider a long narrow heat-conducting pipe inserted vertically into such a region of ocean, as shown in Fig. 2.1a. If an initially upward flow of fresh water in the pipe is generated, say by pumping, it would quickly reach the same temperature as the surroundings at the same level through heat conduction. While it remains fresher and thus lighter than its surrounding liquid, it would continue to flow up along the pipe. The driving energy here is the difference in potential energy between salt water and fresh water at the same level.

In the second case, a parcel of liquid is considered which is isolated from its surroundings by a thin conducting shell, as shown in Fig. 2.1b. Supposing it is displaced upward from its equilibrium position, it will lose heat to the surroundings but remains saltier, therefore will be pulled back under gravity towards its original position. The subsequent overshooting of the parcel from its neutral equilibrium position will lead to a continuing oscillatory motion, with the buoyancy force reversing each half cycle.

It turns out that both motions can be set up in the ocean, as pointed out by Stern[17]. This is because the transfer of salt is slower relative to heat due to its smaller molecular diffusivity. Both long convecting cells and oscillatory motions have been observed in the ocean. They are called 'finger' and 'diffusive' regimes respectively.

2.2.2 Linear Stability Analysis

Linear stability theory concerns the stability of a flow to infinitesimal disturbances. It starts with a solution of the equations of motion representing the flow. This solution is superimposed with a small perturbation, and then substituted back into the original equations. The resulting equations determine growth or decay of the perturbation as time passes. All terms involving the square of the amplitude of the perturbation are neglected. It is this simplification that limits the linear theory to infinitesimal

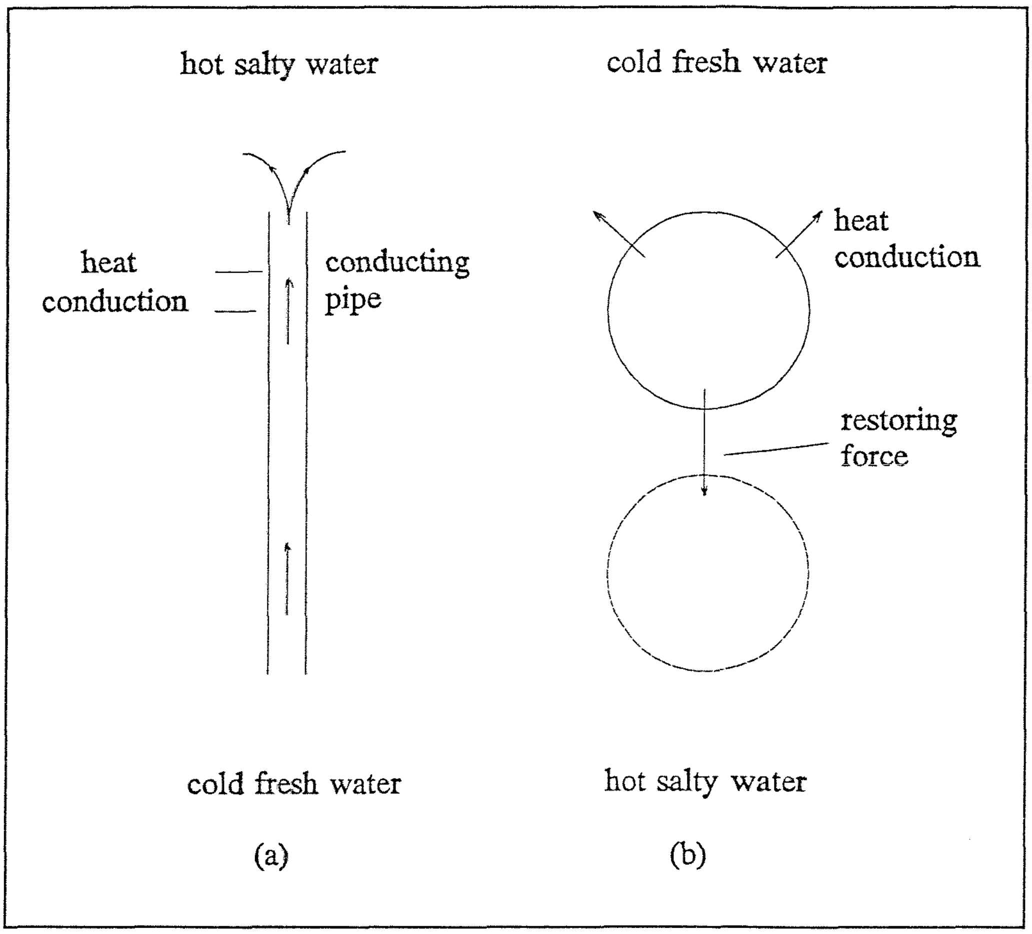

Fig. 2.1 Two possible kinds of motion in a double-diffusive system.

(a) 'salt fountain', (b) oscillating element.

disturbances. If the perturbation grows, the starting flow is not stable and will break down. This is the sufficient condition for instability. If the perturbation decays, the starting flow will prevail. This is the necessary condition for stability.

The stability problem of a system containing linear opposing gradients of two properties to infinitesimal disturbances has been studied by Stern[17], Veronis[18], Bains & Gill[19] and Neild[20]. In the analysis to be described below(see Turner[21]), the motion is restricted to two-dimension(xz plane, z vertically upwards); free horizontal boundaries above and below are assumed which are held at fixed concentrations (temperature and salinity).

The density distribution can be written in the linear approximation as

$$\rho = \rho_m(1 - \beta_T T + \beta_S S) \tag{2.12}$$

where ρ_m is the mean density at height z (which is assumed to vary linearly between z=0 and z=d). T and S are the temperature and salinity respectively; β_T and β_S are the thermal and salinity expansion coefficient. β_S is defined as

$$\beta_S = \frac{1}{\rho}\frac{\partial \rho}{\partial S} \tag{2.13}$$

The governing equations are the linearized Boussinesq equations

$$\frac{\partial u}{\partial t} = -\frac{1}{\rho_0}\frac{\partial p'}{\partial x} + \nu\nabla^2 u$$

(2.14)

$$\frac{\partial w}{\partial t} = -\frac{1}{\rho_0}\frac{\partial p'}{\partial z} + g\beta_T T - g\beta_S S + \nu\nabla^2 w$$

and the two linearized diffusion equations

$$\frac{\partial T}{\partial t} + w\frac{dT_m}{dz} = \alpha\nabla^2 T \tag{2.15}$$

$$\frac{\partial S}{\partial t} + w\frac{dS_m}{dz} = \alpha_S\nabla^2 S \tag{2.16}$$

where α_S is the salinity diffusivity, dT_m/dz and dS_m/dz are the mean gradients of T and S. Eliminating the pressure terms in equations (2.14), and introducing stream function ψ

$$u = \frac{\partial\psi}{\partial z}, \qquad w = -\frac{\partial\psi}{\partial x} \tag{2.17}$$

above equations may be rewritten as

$$(\frac{\partial}{\partial t} - \nu\nabla^2)\nabla^2\psi = \beta_S\frac{\partial S}{\partial x} - \beta_T\frac{\partial T}{\partial x} \tag{2.18}$$

$$(\frac{\partial}{\partial t} - \alpha\nabla^2)T = \frac{\partial\psi}{\partial x}\frac{dT_m}{dz} \tag{2.19}$$

$$(\frac{\partial}{\partial t} - \alpha_S\nabla^2)S = \frac{\partial\psi}{\partial x}\frac{dS_m}{dz} \tag{2.20}$$

Scaling with α and d, together with $-dT_m/dz \cdot d = \Delta T$ for T and $-dS_m/dz \cdot d = \Delta S$ for S, one obtains the dimensionless form of equations (2.18), (2.19) and (2.20)

$$(\frac{1}{Pr}\frac{\partial}{\partial t} - \nabla^2)\nabla^2\psi = -Ra\frac{\partial T}{\partial x} + Rs\frac{\partial S}{\partial x} \tag{2.18a}$$

$$(\frac{\partial}{\partial t} - \nabla^2)T = -\frac{\partial\psi}{\partial x} \tag{2.19a}$$

$$(\frac{\partial}{\partial t} - \tau\nabla^2)S = -\frac{\partial\psi}{\partial x} \tag{2.20a}$$

Where

τ	————	diffusivity ratio, $\tau = \alpha_S/\alpha$.
Rs	————	the salinity Rayleigh number, defined as

$$Rs = \frac{g\beta_S \Delta S d^3}{\nu\alpha} \tag{2.21}$$

Note all the variables in equations (2.18a) to (2.20a) are now dimensionless. The boundary conditions at z = 0, 1 are

$$\psi = 0, \quad \frac{\partial^2\psi}{\partial z^2} = 0, \quad T = S = 0 \tag{2.22}$$

The following set of functions are found to satisfy equations (2.18a) to (2.20a)

$$\psi \sim e^{\sigma t}\sin(\pi a x)\cos(\pi n z)$$

$$(2.23)$$

$$T,\ S \sim e^{\sigma t}\cos(\pi a x)\sin(\pi n z)$$

where πa and πn are the horizontal and vertical wavenumbers. $\sigma = \sigma_r + i\sigma_i$ is generally a complex number. The real part σ_r represents the growth rate. If $\sigma_r > 0$ the perturbation will grow, and decay if $\sigma_r < 0$. Therefore $\sigma_r = 0$ represents the marginal stability. The imaginary part σ_i allows for an oscillatory behaviour.

Substitution of equations (2.23) into equations (2.18a) to (2.20a) leads to

$$\sigma^3 + (Pr+\tau+1)k^2\sigma^2 + [(Pr+\tau Pr+1)k^4 - (Ra-Rs)Pr\pi^2a^2/k^2]\sigma$$

$$+ [Prk^6 + (Rs-Ra)Pr\pi^2a^2] = 0 \tag{2.24}$$

where $k^2 = \pi^2(a^2+n^2)$. σ can be determined when the other parameters in equation (2.24) are specified. For fixed Pr and diffusivity ratio τ, the stability boundaries(minimum Ra with $\sigma_r=0$) corresponding to two straight lines in the Ra, Rs plane whose equations are

$$XZ:\quad Ra = \frac{Rs}{\tau} + \frac{27\pi^4}{4}$$

$$(2.25)$$

$$XW:\quad Ra = Rs\frac{Pr+\tau}{Pr+1} + (1+\tau)(1+\frac{\tau}{Pr})\frac{27\pi^4}{4}$$

These are drawn, diagrammatical but not to scale, in Fig. 2.2.

In the quadrant where Ra is negative and Rs positive, both gradients are stabling and no growth is possible. In the opposite quadrant where Ra is positive and Rs negative, all points are unstable above XZ. Therefore $Ra_e = Ra - Rs/\tau = 27\pi^4/4$ represents an effective Rayleigh number having the same role as the critical Rayleigh number Ra_c in ordinary convection.

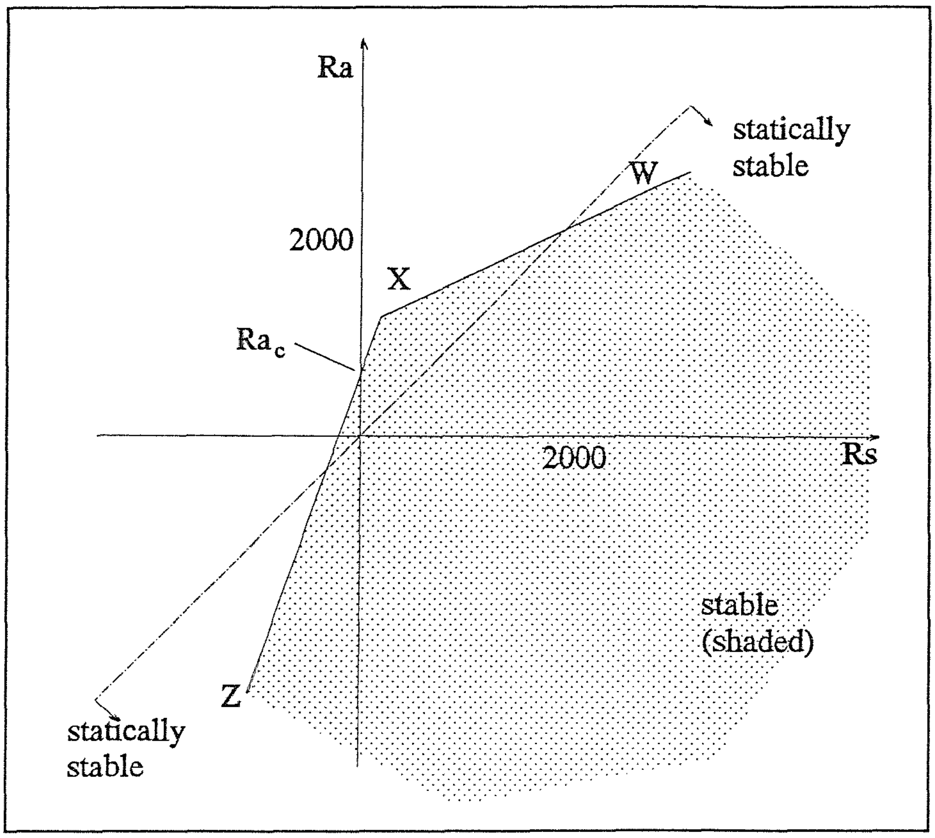

Fig. 2.2 Stability diagram for a double-diffusive system.

In the finger regime(lower left quadrant), instability sets in above XZ with direct motions($\sigma_i=0$). In the diffusive regime(upper right quadrant) just above XW, the motions are oscillatory. Note instability can occur in these two regimes even when the net density field is statically stable (the half plane to the right of the straight line Ra = Rs).

2.2.3 The Fluxes Across a Diffusive Interface

Turner[22] was the first to investigate the fluxes across a sharp density interface in a double-diffusive system. A quasi-steady two-layer system was considered, with salty water beneath fresh water and heated from below. The results obtained were analyzed against the calculated temperature fluxes for natural convection held between two horizontal solid planes at fixed temperatures.

For a layer of liquid heated from below, it has been demonstrated that

$$Nu = cRa^{1/3} \qquad (2.26)$$

where

Nu ———— the Nusselt number, defined as

$$Nu = \frac{Hd}{k\Delta T} = \frac{F_T d}{\alpha \Delta T} \qquad (2.27)$$

ΔT ———— temperature difference across the layer,
H ———— actual heat flux,
k ———— thermal conductivity of the liquid,
F_T ———— temperature flux, $F_T = H/\rho c_p$,
d ———— depth of the layer,
c ———— a constant, depending on the boundary conditions

Using the definition of the Nu and Ra, equation (2.26) can be rewritten as

$$\beta_T F_T = A(\beta_T \Delta T)^{1/3} \tag{2.28}$$

where A = $c(g\alpha^2/\nu)^{1/3}$ having the dimensions of velocity. Note F_T in above equation is independent of d.

In a two-layer system, the flux of the driving component $F_T{}^d$ across a convecting layer of depth d to the interface may be described as

$$Nu = f(Ra,\ Rs,\ Pr,\ \tau) \tag{2.29}$$

where Nu = $F_T{}^d d/\alpha\Delta T$, $F_T{}^d$ is the flux of T in a double diffusive system. In any experiments, Rs/Ra = $\beta_S\Delta S/\beta_T\Delta T$ is known, and Pr and τ are fixed, where ΔT and ΔS are the difference of T and S across the lower layer. A plausible form of equation (2.29) which removes the dependence of $F_T{}^d$ on d is

$$Nu = f_1\left(\frac{\beta_S \Delta S}{\beta_T \Delta T}\right) Ra^{1/3} \tag{2.30}$$

This is equivalent to

$$\beta_T F_T^d = A_1 (\beta_T \Delta T)^{1/3} \tag{2.31}$$

where $A_1 = f_1(R_\rho)(g\alpha^2/\nu)^{1/3}$ having the dimensions of velocity.

It is to be understood that f_1 and A_1 can depend on molecular properties but once the two components are specified, they should be functions only of the density ratio

$R_\rho = \beta_S\Delta S/\beta_T\Delta T$. The deviation of A_1 from A gives a measure of the effects of increasing ΔS on F_T, the flux of T when only ΔT is present.

Equation (2.31) divided by equation (2.28) and assuming that the ΔT is same in the two equations,

$$\frac{F_T^{\,d}}{F_T} = \frac{A_1}{A} = \frac{f_1(R_\rho)}{c} \tag{2.32}$$

Therefore $F_T^{\,d}/F_T$ can be expressed as a function of R_ρ only. The temperature fluxes measured by Turner[22] for the heat-salt double-diffusive system expressed in this way are shown in Fig. 2.3a. For $R_\rho < 2$, the measured flux is greater than the calculated value for solid planes. As R_ρ -> 1, $F_T^{\,d}$ increases sharply as the layers approach density equalization. When $R_\rho > 2$, the measured flux falls progressively as R_ρ increases. Agbabi[13] measured the temperature flux across the interface between two stratified layers of cryogenic liquids. The results show that the temperature flux(divided by the value of two solid plains) follows a similar variation with the density ratio R_ρ as in the salt-heat double-diffusive system.

An empirical function has been suggested by Huppert[8] which fits Turner's measurements to the experimental accuracy

$$\frac{A_1}{A} = 3.8\left(\frac{\beta_S\Delta S}{\beta_T\Delta T}\right)^{-2} \tag{2.33}$$

The salt flux F_S may be derived in a similar way. Using the dimensional argument leading to equation (2.30), one can obtain

$$\frac{F_S d}{\alpha_S\Delta S} = f_2(R_\rho)Ra^{1/3} \tag{2.34}$$

Equation (2.34) divided by equation (2.30) and rearranging,

$$\frac{\beta_S F_S}{\beta_T F_T} = (\frac{f_1}{f_2}) R_\rho \tau = f(R_\rho) \qquad (2.35)$$

where d is omitted from F_T^d.

For given molecular properties, equation (2.35) shows the ratio of the fluxes(expressed as the contribution to the density flux) is another systematic function of R_ρ. Turner's salt flux measurements expressed in this way are shown in Fig. 2.3b. As R_ρ -> 1, $\beta_S F_S / \beta_T F_T$ -> 1 also, suggesting the heat and salt are transported by the same turbulent motions at a breaking interface. As R_ρ increases to 2, the flux ratio falls rapidly, since the molecular processes become increasingly important.

2.3 Mixing Across a Density Interface

Huppert[8] studied the stability in the context of double-diffusive convection of an finite layer with intermediate properties between two semi-infinite convecting layers, say, with fixed difference ΔT and ΔS. Two different regions have been identified according to the property of $f(R_\rho)$. When $f(R_\rho)$ is constant(e.g. $R_\rho > 2$ in Turner's heat-salt experiments), for every $T = \Delta T(1+\theta)/2$ of the middle layer, there is a corresponding $S = \Delta S(1+\lambda)/2$ to render it in a state of stable equilibrium (θ and λ are between -1 and 1). If $f(R_\rho)$ is not constant, the central layer will eventually emerge with one of the two layers.

The mixing of stratified liquids by external driven turbulence has been studied by a number of researchers[23][24][25]. Rouse and Dodu[23] considered mixing across a density interface using a vertically oscillating grid. A well-mixed layer is formed, bounded by a sharp interface which moves away from the turbulence-generating

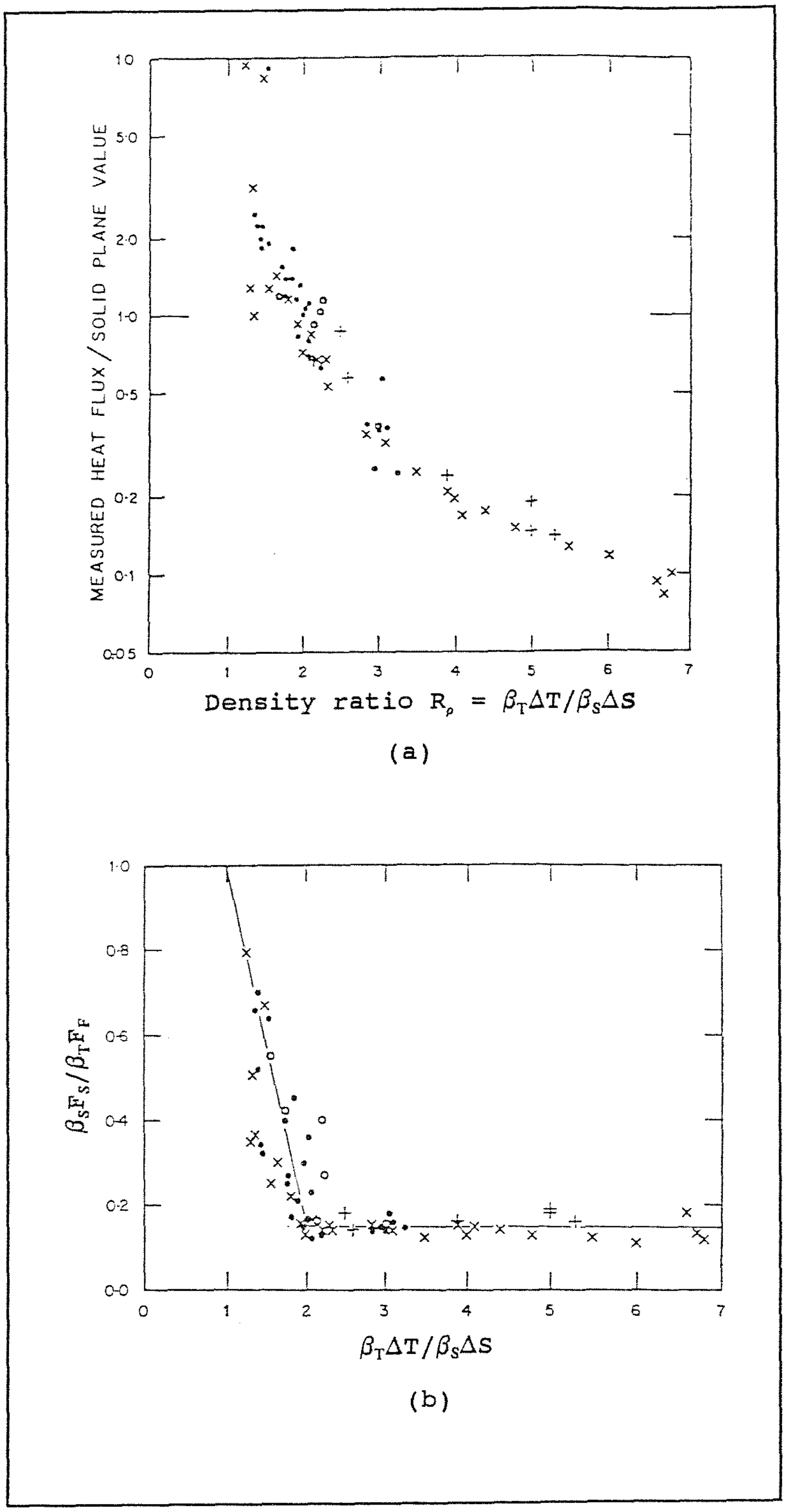

Fig. 2.3 The measured heat and mass flux across an interface between a layer of hot salty water below a layer of cold fresh water, against the density ratio: a) the measured temperature flux compared to the calculated solid plain value; 2) the ratio of the potential energy changes due to the transfer of salt and heat across the interface. From Turner[22].

source as fluid is entrained across it from the quiescent fluid into the stirred layer. The mixing process is described by Turner[25] as the intermittent breaking of forced internal waves, which tends to thicken the interface, followed by the sweeping away of the liquid by the stirring in the layers, which sharpens the interface. Turner[25] stirred both layers and found that when the stirring is applied at the same rate, the interface remains sharp and central. If, on the other hand, the stirring is unsymmetrical, the interface moves away from the region of more vigorous stirring until the entrainment rates on the two sides balance.

Supposing initially the mixing represents the balance between the buoyancy and the inertia force along, from a dimensional reasoning the entrainment velocity u_e can be expressed as a function of an overall Richardson number

$$\frac{u_e}{U} = f(Ri_o) \qquad (2.36)$$

where $Ri_o = g\Delta\rho L/\rho U^2$, $\Delta\rho$ is the density difference across the interface, U and L are the velocity and length scales characteristic of the fluid motion near the interface. The following power law relationship

$$\frac{u_e}{U} \sim Ri_o^{-3/2} \qquad (2.37)$$

has been found by Turner[25] and Bains[26] in two different experiments.

Bains[26] studied mixing at a density interface (fresh/salty water) caused by a plume or jet impinging on it. The plume(or jet) entrains heavier liquid through its end as it impinges on the interface. Observations show that the mechanism of entrainment is primarily by large eddies scooping heavier liquid between them as each intersects a roughly spherical eddy. Measurements of entrained volume flux show it to be in proportional to the -2/3 power of an overall Richardson number[1]. In this case the overall Richardson number is determined by the local properties of the plume(jet)(the central line velocity and the nominal radius) and the density difference across the interface.

---

[1] Bains[26] actually used the Froude number(Fr) as the dimensionless parameter, $Fr = Ri_o^{-1/2}$.

3.0 THE NUMERICAL MODEL

3.1 Why a Numerical Approach

The existing mathematic rollover simulation models, based on the balance of heat and mass in each layer, do not take into account the effect of convective flows on the mixing of adjacent layers. Yet many experimental results have shown that the interface level falls due to entrainment at the interface or boundary layer penetration, suggesting that convective flows are important in the course of mixing.

Numerical modelling in this study was primarily aimed at looking in some detail into the convective flows in stably stratified layers in cryogenic liquids and how these flows affect and control the mixing process. The work intended to bring out some basic aspects of the mechanisms which control mixing, rather than simulating full-scale LNG rollover event. With this in mind, a laminar model was considered, though thermally-induced convective flows in commercial storage LNG tanks are fully turbulent.

The model includes two versions, namely, cartesian coordinates(CC) version and cylindrical polar coordinates(CPC) version, corresponding to rectangular and cylindrical storage vessels. Rectangular vessels are modelled as two-dimensional problems and cylindrical ones as axi-symmetric.

The CC version of the model will be presented first. For simplicity, first a model for two-dimensional homogeneous flows, called the one-component model, is considered. The accomplished one-component model is then expanded to one capable of dealing with heterogeneous flows containing two (more) miscible components. The resulting model is called the two(multi)-component model. The CPC version of the model basically shares the same framework with the CC version; it will be described only in terms of the differences between the two versions.

ONE-COMPONENT MODEL IN CC

3.2 Problem and Basic Assumptions

Consider a layer of cryogenic fluid contained in a rectangular vessel, which is subject to a uniform heat flux along two opposite walls. Thermal-induced convective flows at cross-sections perpendicular to the heated walls are of interest. The ends effect may be neglected, and therefore these flows may be regarded as two-dimensional (say in xz plane with z axis upwards) if the dimension of the vessel along the y-axis is much greater than the other two. The solution domain is shown in Fig. 3.1.

Before proceeding to construct a numerical model for solving the proposed problem, two basic assumptions are made about the flow medium.

1) The fluid is Newtonian;

2) The fluid is incompressible;

The Boussinesq approximation is also assumed. Temperature difference within stored cryogenic liquids is usually less than 10 degrees of Kelvin, this would cause less than 5% change in fluid density. Therefore the use of the Boussinesq approximation is justified. In a two-component system considered later, this approximation also requires density variation due to fluid composition differences to be small.

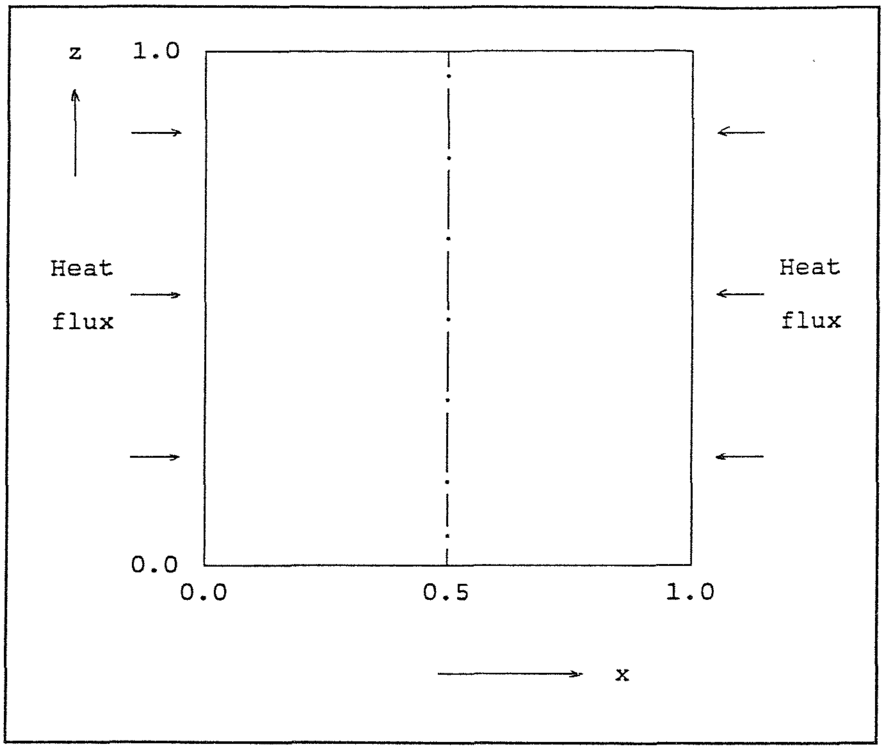

Fig. 3.1 The solution domain in cartesian coordinates.
x=0.0 and 1.0, non-slip walls; x=0.5, the central line;
z=0.0, non-slip adiabatic base; z=1.0, isothermal free surface.

3.3 Mathematical Formulation

3.3.1 Governing Differential Equations

The governing differential equations (in cartesian coordinates) are the Navier-Stokes equations

$$\frac{\partial u}{\partial t} + u\frac{\partial u}{\partial x} + w\frac{\partial u}{\partial z} = -\frac{1}{\rho_0}\frac{\partial p}{\partial x} + \nu\left(\frac{\partial^2 u}{\partial x^2} + \frac{\partial^2 u}{\partial z^2}\right)$$

$$\frac{\partial w}{\partial t} + u\frac{\partial w}{\partial x} + w\frac{\partial w}{\partial z} = -\frac{1}{\rho_0}\frac{\partial p}{\partial z} + \nu\left(\frac{\partial^2 w}{\partial x^2} + \frac{\partial^2 w}{\partial z^2}\right) + g\beta_T T \tag{3.1}$$

the energy equation(in conservative form)

$$\frac{\partial T}{\partial t} + \frac{\partial (uT)}{\partial x} + \frac{\partial (wT)}{\partial z} = \alpha(\frac{\partial^2 T}{\partial x^2} + \frac{\partial^2 T}{\partial z^2}) \tag{3.2}$$

and the continuity equation

$$\frac{\partial u}{\partial x} + \frac{\partial w}{\partial z} = 0 \tag{3.3}$$

Note the density has been linearized, $\rho = \rho_0(1 - \beta_T T)$. There are four dependent variables, namely, the velocity components u and w, pressure p and temperature T. Pressure p may be eliminated by cross-differentiating the two equations in (3.1). The outcome forms the vorticity transportation equation,

$$\frac{\partial \zeta}{\partial t} + \frac{\partial (u\zeta)}{\partial x} + \frac{\partial (w\zeta)}{\partial z} = \nu(\frac{\partial^2 \zeta}{\partial x^2} + \frac{\partial^2 \zeta}{\partial z^2}) - g\beta_T \frac{\partial T}{\partial x} \tag{3.4}$$

where ζ is vorticity, defined as

$$\zeta = \frac{\partial u}{\partial z} - \frac{\partial w}{\partial x} \tag{3.5}$$

The velocity components u and w may be expressed as the first derivative of the stream function ψ,

$$u = \frac{\partial \psi}{\partial z}, \quad w = -\frac{\partial \psi}{\partial x} \tag{2.17}$$

Substituting above expressions into equation (3.5), one obtains the Poisson equation

$$\frac{\partial^2 \psi}{\partial x^2} + \frac{\partial^2 \psi}{\partial z^2} = \zeta \qquad (3.6)$$

Now a new set of differential equations is formed, i.e, the vorticity transportation equation (3.4), the energy equation (3.2), the Poisson equation (3.6) and the continuity equation (3.3). Though there are now five unknown variables, namely u, w, ζ, ψ and T, the number of main dependent variables are actually reduced to three, i.e., ζ, ψ and T. This is because u and w can be readily derived from the stream function ψ through equation (2.17). The other advantage associated with the stream function-vorticity approach is that the use of staggering grid, which is normally required otherwise, can be avoided.

3.3.2 Normalization of the Governing Equations

A usual practice is to convert the governing equations into dimensionless form. The advantage is that numerical results can be more readily interpreted in terms of the major dimensionless parameter(s), which are formed out of the normalisation process. Scaling with α and height of the solution domain d, together with $\dot{q}d/k$ for temperature, the dimensionless form(with a overbar) of all the variables can be obtained,

$$\bar{x} = \frac{x}{d}, \quad \bar{z} = \frac{z}{d}, \quad \bar{t} = \frac{t}{d^2/\alpha}, \quad \bar{T} = \frac{T}{\dot{q}k/d};$$

$$\bar{u} = \frac{u}{\alpha/d}, \quad \bar{w} = \frac{w}{\alpha/d}, \quad \bar{\psi} = \frac{\psi}{\alpha}, \quad \bar{\zeta} = \frac{\zeta}{\alpha/d^2} \qquad (3.7)$$

where $\dot{q}$ is the wall heat flux and k the thermal conductivity. Substituting the dimensionless variables into equations (3.2) and (3.4), then rearranging,

$$\frac{\partial \bar{T}}{\partial \bar{t}} + \frac{\partial(\bar{u}\bar{T})}{\partial \bar{x}} + \frac{\partial(\bar{w}\bar{T})}{\partial \bar{z}} = \frac{\partial^2 \bar{T}}{\partial \bar{x}^2} + \frac{\partial^2 \bar{T}}{\partial \bar{z}^2} \tag{3.2a}$$

$$\frac{\partial \bar{\zeta}}{\partial \bar{t}} + \frac{\partial(\bar{u}\,\bar{\zeta})}{\partial \bar{x}} + \frac{\partial(\bar{w}\,\bar{\zeta})}{\partial \bar{z}} = Pr\left(\frac{\partial^2 \bar{\zeta}}{\partial \bar{x}^2} + \frac{\partial^2 \bar{\zeta}}{\partial \bar{z}^2}\right) - PrRa^{*}\frac{\partial \bar{T}}{\partial \bar{x}} \tag{3.4a}$$

where Ra* is the modified Rayleigh number, defined as

$$Ra^{*} = \frac{g\beta_T \dot{q} d^4}{k\alpha\nu} \tag{3.8}$$

Omitting the overbars, equations (3.2a) and (3.4a) reduce to

$$\frac{\partial T}{\partial t} + \frac{\partial(uT)}{\partial x} + \frac{\partial(wT)}{\partial z} = \frac{\partial^2 T}{\partial x^2} + \frac{\partial^2 T}{\partial z^2} \tag{3.2b}$$

$$\frac{\partial \zeta}{\partial t} + \frac{\partial(u\zeta)}{\partial x} + \frac{\partial(w\zeta)}{\partial z} = Pr\left(\frac{\partial^2 \zeta}{\partial x^2} + \frac{\partial^2 \zeta}{\partial z^2}\right) - PrRa^{*}\frac{\partial T}{\partial x} \tag{3.4b}$$

The form of the continuity and Poisson equation remain unchanged after normalisation.

3.3.3 Boundary Conditions

Two assumptions are made regarding the liquid surface. Firstly the surface is considered as non-evaporating; secondly it is stress free, i.e. a free surface. Though these assumptions are not strictly valid, they greatly simplify the computation. The first one indicates that there is no loss of liquid at the surface. This means that d is unchanged during the course of computation, and consequently a fixed grid of control volumes can be used. The second assumption indicates that there is no external force acting upon the surface.

In the storage of cryogenic liquids, since heat leak is inevitable, there will be continuous evaporation of liquid at the surface under its vapour pressure. But if storage containers are well insulated, the daily loss of liquid is trivial (order of 0.5%) compared with the whole content. The second assumption is based upon the fact that, for cryogens, their vapours have much less viscosity than liquids.

The first assumption implies that w velocity vanishes at the surface. The second one suggests that the gradient of u velocity is zero there. From the definition of vorticity and stream function, it follows that vorticity and stream function are zero and constant at the surface respectively.

Under atmospheric pressure the surface of cryogenic liquids is isothermal. All walls are considered non-slip. This means u, w and ψ there are zero and constant respectively. Here zero is chosen for the stream function at all four boundaries. As specified in the problem, the side walls are subject to a uniform heat flux. The base is considered as adiabatic. These are also shown in Fig. 3.1.

3.4 Numerical Procedure

3.4.1 Control Volume Discretization Method

So far a set of governing differential equations, together with the appropriate boundary conditions, has been established for the proposed problem. A discretization method is now required to transfer each equation into a set of algebraic equations, which can be solved using established numerical methods. It was decided, among various discretization schemes, to use Patanker's[27] control volume method for the parabolic equations, namely, the vorticity and the energy equation. The epilitic Poisson equation may be considered as a special form of the parabolic equation, the discretization of which is much more straight forward.

In the control volume method, the solution domain under study is divided into a number of sub-domains, called control volumes. Each control volume is considered as a uniform unit and is represented by properties at an internal point, called node. The node is usually chosen at the centre of each control volume. Over each control volume the integration of the differential equation to be discretized is performed to form a set of finite volume equations. A distinctive advantage associated with this method is that all variables are conserved over each control volume, and consequently, over the entire solution domain.

3.4.2 Profile Assumptions

Some assumptions must be made about the profile of concerned variables between the node points. The two most common are piecewise-linear and stepwise as shown in Fig. 3.2 (one-dimensional along x axis).

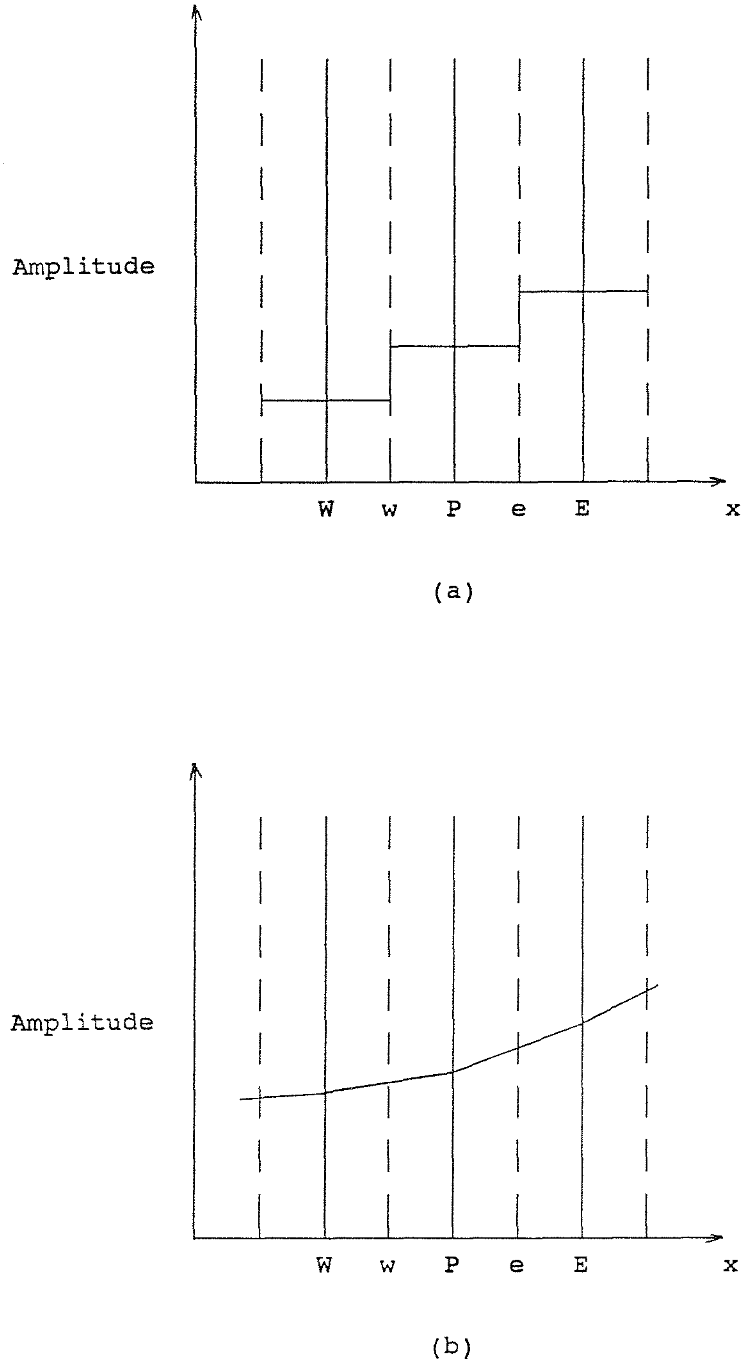

Fig. 3.2 The two most common profiles:

(a) stepwise; (b) piecewise-linear.

3.4.3 Discretization of the parabolic vorticity and energy equation

General Differential Equation

Equations (3.2b) and (3.4b) may be fitted into a general form

$$\frac{\partial \phi}{\partial t} + \frac{\partial (u\phi)}{\partial x} + \frac{\partial (w\phi)}{\partial z} = \Gamma(\frac{\partial^2 \phi}{\partial x^2} + \frac{\partial^2 \phi}{\partial z^2}) + So \tag{3.9}$$

with $\Gamma = 1$, $So = 0$ for the energy equation and $\Gamma = Pr$, $So = -PrRa^{*}\partial T/\partial x$ for the vorticity equation, where ϕ is a general variable.

Equation (3.9) may be rewritten in a more compact form

$$\frac{\partial \phi}{\partial t} + div(\vec{u}\phi) = div[\Gamma grad(\phi)] + So \tag{3.10}$$

where

$$div = \frac{\partial}{\partial x} + \frac{\partial}{\partial z}, \quad grad = \frac{\partial}{\partial x}\vec{i} + \frac{\partial}{\partial z}\vec{k}$$

$\vec{i}$ and $\vec{k}$ are the unit vectors along the x and z axes. The four terms in equation (3.10) are called the unsteady term, the advection term, the diffusion term and the source term respectively.

Discretization of the General Differential Equation

Discretization will be performed on the general differential equation (3.9). By introducing a total flux J for the general variable ϕ,

$$J_x = u\phi - \Gamma\frac{\partial\phi}{\partial x}, \quad J_z = w\phi - \Gamma\frac{\partial\phi}{\partial z} \tag{3.11}$$

equation (3.9) may be rewritten as

$$\frac{\partial\phi}{\partial t} + \frac{\partial J_x}{\partial x} + \frac{\partial J_z}{\partial z} = So \tag{3.12}$$

The integration of the above equation over a time period Δt and the central control volume in Fig. 3.3 yields

$$[\phi_P(t+\Delta t) - \phi_P(t)]\Delta x\Delta z + \int_t^{t+\Delta t}(J_e - J_w)dt + \int_t^{t+\Delta t}(J_n - J_s)dt$$

$$= So_P\Delta x\Delta z\Delta t \tag{3.13}$$

where J_e, J_w, J_n and J_s are the integrated total flux of ϕ at the four control volume interfaces. In the integration, stepwise profile assumptions have been used for the unsteady and source terms. By applying stepwise profiles also in the time dimension, equation (3.13) may be rewritten as

$$\frac{(\phi_P^1 - \phi_P^0)\Delta x\Delta z}{\Delta t} + (J_e - J_w)^m + (J_n - J_s)^m = So_P\Delta x\Delta z \tag{3.14}$$

where the supscripts 0 and 1 refer to the beginning and end of the time interval Δt respectively. The supscript m can take either 0 or 1, depending on whether the explicit(m=0) or implicit scheme (m=1) is chosen. With the explicit scheme, one assumes that the values of the integrated total fluxes are known, calculated at the

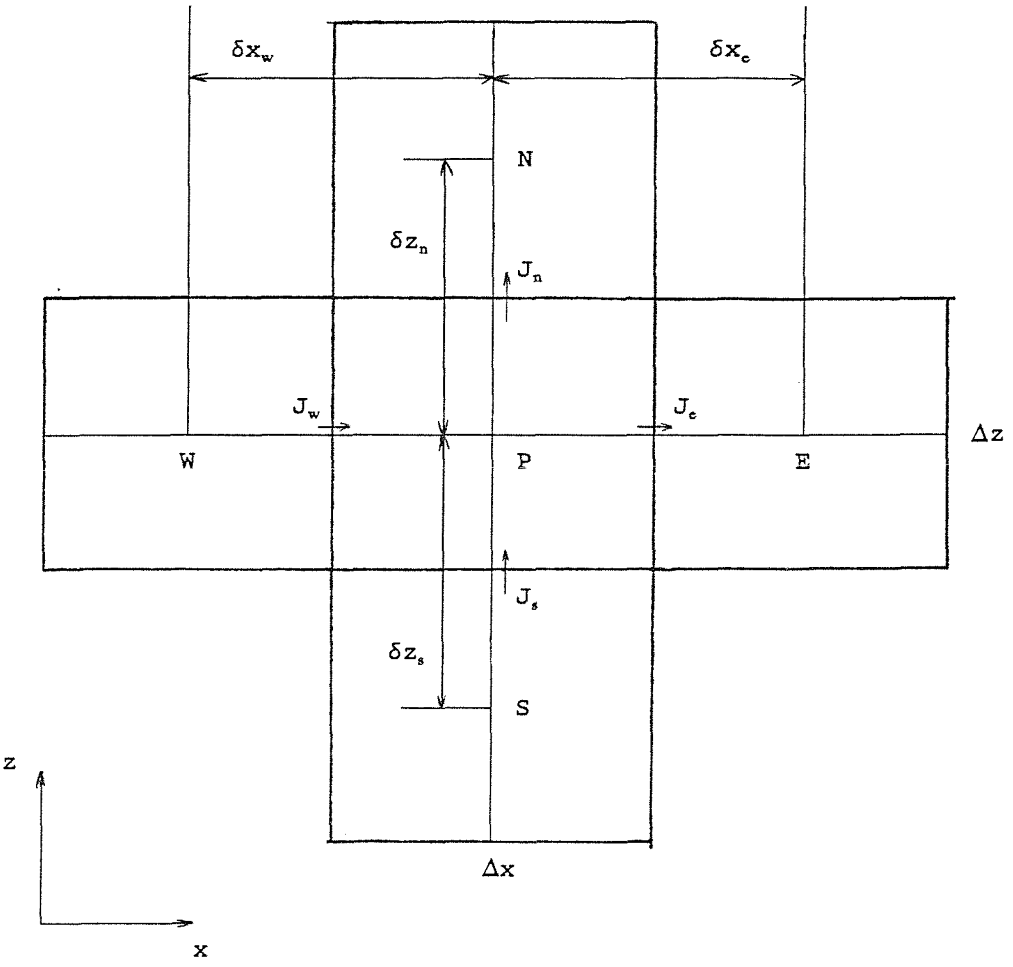

Fig. 3.3 A typical cluster of control volumes in cartesian coordinates.

beginning of the time step. On the other hand, with the implicit scheme, one assumes that the values of the integrated total fluxes are unknown, taken as the values at the end of the time step. Note m may take different values along the two dimensions(x and z) (see ADI scheme below).

A similar integration of the continuity equation (3.3) yields

$$(F_e - F_w)^m + (F_n - F_s)^m = 0 \tag{3.15}$$

where F_e, F_w, F_n and F_s are the mass flow rate at the four control volume interfaces; the supscript m is same as in equation (3.14). Taking the product of equation (3.15) and $\phi_P{}^m$, subtracting equation (3.14) and rearranging

$$\frac{(\phi_P^1 - \phi_P^0)\Delta x \Delta z}{\Delta t} + (J_e - F_e\phi_P)^m - (J_w - F_w\phi_P)^m + (J_n - F_n\phi_P)^m$$

$$- (J_s - F_s\phi_P)^m = So_P\Delta x\Delta z \tag{3.16}$$

It can be shown (see Appendix I) that those terms in the bracket may be expressed as

$$J_e - F_e\phi_P = A_E(\phi_P - \phi_E), \qquad J_w - F_w\phi_P = -A_W(\phi_P - \phi_W)$$

$$(3.17)$$

$$J_n - F_n\phi_P = A_N(\phi_P - \phi_N), \qquad J_s - F_s\phi_P = -A_S(\phi_P - \phi_S)$$

The definition and the physical meaning of coefficients A_E to A_S are given in Appendix I. Substituting above expressions into equation (3.16), the general discretization equation is derived

$$A_P^0\phi_P^1 = A_E(\phi_E-\phi_P)^m + A_W(\phi_W-\phi_P)^m + A_N(\phi_N-\phi_P)^m + A_S(\phi_S-\phi_P)^m + b \tag{3.18}$$

where

$$A_P^0 = \frac{\Delta x \Delta z}{\Delta t}, \qquad b = A_P^0\phi_P^0 + So_P\Delta x\Delta z$$

3.4.4 Discretization of the Epilitic Poisson Equation

The integration of equation (3.6) over the central control volume in Fig. 3.3 yields

$$[(\frac{\partial\psi}{\partial x})_e - (\frac{\partial\psi}{\partial x})_w]\Delta z + [(\frac{\partial\phi}{\partial z})_n - (\frac{\partial\psi}{\partial z})_s]\Delta x = \zeta_P\Delta x\Delta z \tag{3.19}$$

where stepwise profile assumptions have been used. The first derivatives of stream function may be approximated using piecewise-linear profile assumptions to yield

$$\frac{(\psi_E-\psi_P)\Delta z}{\delta x_e} + \frac{(\psi_W-\psi_P)\Delta z}{\delta x_w} + \frac{(\psi_N-\psi_P)\Delta x}{\delta z_n} + \frac{(\psi_S-\psi_P)\Delta x}{\delta z_s} = \zeta_P\Delta x\Delta z \tag{3.20}$$

where δx and δz are the node distances. Rearrange,

$$A_P\psi_P = A_E\psi_E + A_W\psi_W + A_N\psi_N + A_S\psi_S + b \tag{3.21}$$

where

$$A_E = \frac{\Delta z}{\delta x_e}, \quad A_W = \frac{\Delta z}{\delta x_w}, \quad A_N = \frac{\Delta x}{\delta z_n}, \quad A_S = \frac{\Delta x}{\delta z_s}$$

$$A_P = A_E + A_W + A_N + A_S$$

$$b = -\zeta_P \Delta x \Delta z$$

3.5 Solution

3.5.1 Outline of the Solution Procedure

The solution procedure is a time-marching one: following a set of estimated initial values for each variable, the final solution is achieved by using the time-marching technique. In each time step, the energy equation is solved first to provide an updated temperature field for the evaluation of the source term in the vorticity equation. The solution of the vorticity equation is then fed into the Poisson equation to yield the stream function, from which velocity components and wall vorticity can be derived. The whole process then repeats itself until a preset time step or steady state is reached.

3.5.2 Solution of the general discretization equation - ADI method

The general discretization equation is

$$A_P^0 \phi_P^1 = A_E(\phi_E - \phi_P)^m + A_W(\phi_W - \phi_P)^m + A_N(\phi_N - \phi_P)^m + A_S(\phi_S - \phi_P)^m + b \tag{3.18}$$

where

$$A_P^0 = \frac{\Delta x \Delta z}{\Delta t}, \qquad b = A_P^0 \phi_P^0 + So_P \Delta x \Delta z$$

m can take 0 or 1 corresponding to explicit or implicit scheme respectively. Though neither of these two schemes is actually used, their merits will be briefly discussed first. The favoured scheme, the alternating-direction implicit(ADI), will be introduced thereafter.

The explicit scheme

The explicit formulation of equation (3.18) is

$$A_P^0 \phi_P^1 = A_E \phi_E^0 + A_W \phi_W^0 + A_N \phi_N^0 + A_S \phi_S^0 + b \tag{3.22}$$

where A_P^0 is the same as in equation (3.18) and

$$b = (A_P^0 - A_E - A_W - A_N - A_S) \phi_P^0 + So_P \Delta xz$$

The general variable ϕ is expressed explicitly in terms of the known quantities which exist at the beginning of the time step. This has the considerable advantage of computational simplicity. The general variable of each node may be solved separately, say, using Gaussian elimination algorithm. There is, however, a serious limitation associated with this scheme: the time step allowed is usually small. Take the case of one-dimensional transient heat conduction as an example, the maximum time step allowed is $\delta x^2/2\alpha$, where δx is the node distance and α is thermal diffusivity. If a time step larger than this value is chosen, the solution will become unstable.

The implicit scheme

The above limitation on the time step is avoided in the implicit scheme because it is unconditionally stable. The implicit formulation of equation (3.18) is

$$A_P^1 \phi_P^1 = A_E \phi_E^1 + A_W \phi_W^1 + A_N \phi_N^1 + A_S \phi_S^1 + b \tag{3.23}$$

where A_P^0 is the same as in equation (3.18) and

$$A_P^1 = A_P^0 + A_E + A_W + A_N + A_S$$

$$b = A_P^0 \phi_P^0 + So_P \Delta x \Delta z$$

There are five unknown variables in the equation. Therefore it is no longer possible to calculate ϕ of each node separately, but rather it is necessary to solve a set of simultaneous equations.

A matrix is called a tri-diagonal one if all the elements not on the leading and two adjacent diagonals are zero. For a set of algebraic equations whose coefficient matrix is tri-diagonal, there are very efficient algorithms available to solve them, for example, the tri-diagonal algorithm(TDA). In order to be able to use the TDA, several alternative schemes have been developed, among them is the well-known alternating-direction implicit (ADI) scheme.

The ADI scheme

This is basically a semi-implicit scheme, in which the implicit scheme is used in one direction and the explicit scheme in the other. Each time step is divided into two halves, between them the implicit direction alternates. The ADI formulation of equation (3.18) is

$$A_P^{1/2}\phi_P^{1/2} = A_E\phi_E^{1/2} + A_W\phi_W^{1/2} + b^{1/2} \tag{3.24a}$$

for the first half of the time step, and

$$A_P^1\phi_P^1 = A_N\phi_N^1 + A_S\phi_S^1 + b^1 \tag{3.24b}$$

for the second half of the time step, where

$$A_P^{1/2} = A_P^0 + A_E + A_W$$

$$b^{1/2} = A_N\phi_N^0 + A_S\phi_S^0 + (A_P^0 - A_N - A_S)\phi_P^0 + So_P\Delta x\Delta z$$

$$A_P^1 = A_P^0 + A_N + A_S$$

$$b^1 = A_E\phi_E^{1/2} + A_W\phi_W^{1/2} + (A_P^0 - A_E - A_W)\phi_P^{1/2} + So_P\Delta x\Delta z$$

$$A_P^0 = 2\Delta x\Delta z/\Delta t$$

By moving the unknown terms on the right hand side of the above two equations, i.e, $\phi_E^{1/2}$, $\phi_W^{1/2}$, ϕ_N^1 and ϕ_S^1, to the left hand side, the resulting two sets of equations can be solved using TDA.

3.5.3 Solution of the Discretized Poisson Equation - SOR method

The poisson equation is solved using the successive over-relaxation (SOR) method. Equation (3.21) now becomes

$$A_P\psi_P = \psi_P' + \frac{\chi(A_E\psi_E + A_W\psi_W + A_N\psi_N + A_S\psi_S + b - A_P\psi_P')}{A_P} \qquad (3.25)$$

where ψ_P' is the stream function which exists at the previous iteration; χ is a relaxation factor. For over-relaxation, $\chi \geq 1$. In general, convergence will be largely speeded up by updating the stream function whenever possible, i.e., always using the latest data available during computation. With the vector processing facility available in this university, this is, however, not necessarily the quickest way to achieve convergence as far as CPU time is concerned. To be able to use the vector facility, recursion in programming has to be avoided. This requires that, if computation is advanced from left to right and upwards, only nodes to the South of the nodes under computation are updated whenever possible.

3.5.4 Evaluation of Velocity Components From the Stream Function

Normal velocities at control volume interfaces are required in the solution, as shown in Fig. 3.4. From the definition of stream function, this demands the stream function at the corners of each control volume. The easiest way to achieve this is through linear interpolation of stream functions at four surrounding nodes. For example, the stream function at corner A can be found as

$$\psi_A = \frac{\Delta x \Delta z \psi_{WN} + \Delta x_W \Delta z \psi_N + \Delta x_W \Delta z_N \psi_P + \Delta x \Delta z_N \psi_W}{(\Delta x + \Delta x_W)(\Delta z + \Delta z_N)}$$

Stream functions at corner B and C can be calculated in a similar way. Now velocity component u at D and w at E can be obtained by assuming a piecewise-linear profile between two neighbouring corners,

$$u_D = \frac{\psi_A - \psi_C}{\Delta z}, \qquad w_E = \frac{\psi_B - \psi_A}{\Delta x} \tag{3.27}$$

It is important to derive velocity components directly from stream function so that the continuity equation (3.3) is always satisfied.

3.5.5 The Wall Vorticity

The wall vorticity may be derived from the Taylor expansion for the stream function at a nodal point next to the wall. Taking the situation shown in Fig. 3.5, for example, one could write

$$\psi_1 = \psi_0 + (\frac{\partial \psi}{\partial z})_{z=0} h + \frac{1}{2}(\frac{\partial^2 \psi}{\partial z^2})_{z=0} h^2 + 0(h^3) \tag{3.28}$$

From the above equation the wall vorticity can be derived. At z=0, $\psi = 0$ (by assumption), $\partial\psi/\partial z = u = 0$ and $w = 0$. Therefore the first two terms on the right hand side of equation (3.28) are zero, and from equation (3.6)

$$(\frac{\partial^2 \psi}{\partial z^2})_{z=0} = (\zeta - \frac{\partial^2 \psi}{\partial x^2})_{z=0} = \zeta_0 + (\frac{\partial w}{\partial x})_{z=0} = \zeta_0$$

Equation (3.28) thus becomes

$$\psi_1 = \frac{1}{2}\zeta_0 h^2 + 0(h^3)$$

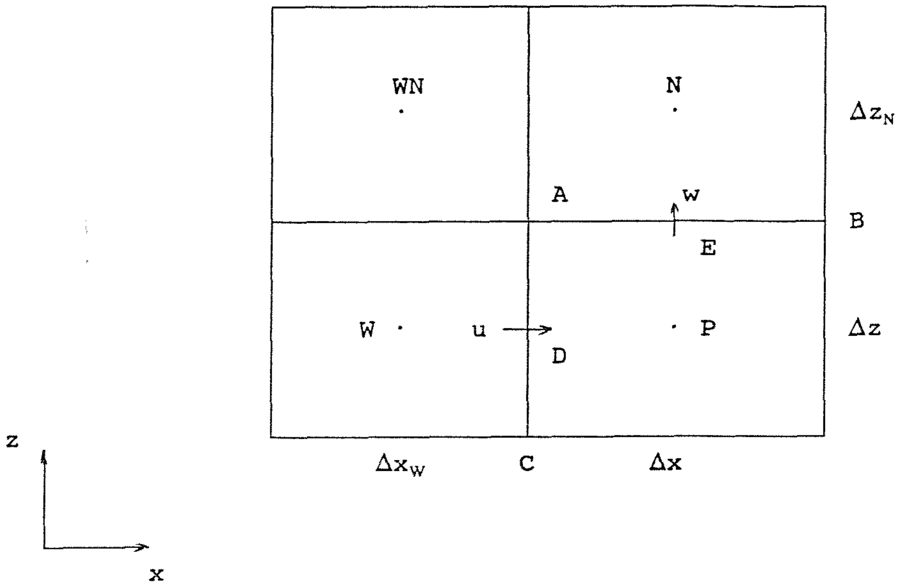

Fig. 3.4 Derivation of velocity components from stream function.

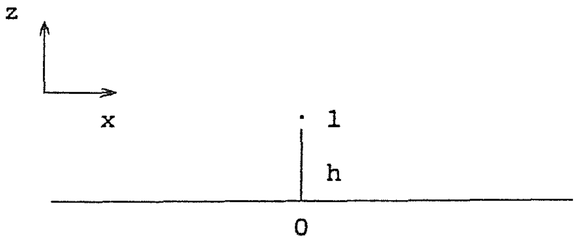

Fig. 3.5 Derivation of the wall vorticity.

Rearranging

$$\zeta_0 = \frac{2\psi_1}{h^2} \tag{3.29}$$

Vorticity along the vertical wall may be derived in a similar manner.

3.6 Control Volume Mesh

All the boundaries are located along control volume faces. Non-uniform control volumes are used in both x and z directions to achieve high resolution in the boundary layer and core region. Temperature measurements carried out by Beduz[14] on a pool of evaporating liquid nitrogen show that there exists a very thin surface layer with a steep temperature gradient. To accommodate for this thin surface layer, very fine control volumes are required in that region.

TWO-COMPONENT MODEL IN CC

So far the one-component model has been developed. This model will now be expanded to deal with heterogeneous flows containing two (or more) miscible components. Here, for simplicity, only two-component flows will be considered, but multi-component systems can be dealt with just the same. The major constituent is called the solvent, the other the solute. As has been said, the use of the boussinesq approximation requires the density variation due to composition as well as temperature difference to be small.

3.7 Modifications for the Two-Component Model

With the addition of the solute, two modifications are required in the mathematical formulation of the problem. Firstly a differential equation and appropriate boundary conditions for the solute must be included. Secondly the vorticity equation (3.4) should take into account the buoyancy force resulting from the horizontal gradient of the solute. These appear to be the necessary and only modifications which must be made.

Differential Equation for the Solute

The differential equation governing the behaviour of the solute is

$$\frac{\partial S}{\partial t} + \frac{\partial (uS)}{\partial x} + \frac{\partial (wS)}{\partial z} = \alpha_S\left(\frac{\partial^2 S}{\partial x^2} + \frac{\partial^2 S}{\partial z^2}\right) \tag{3.30}$$

where S is the concentration of the solute and α_S the diffusivity of the solute in the solvent. Using the scales in equation (3.7) and assuming ΔS to be the scale of the solute concentration, equation (3.30) may be readily normalized,

$$\frac{\partial S}{\partial t} + \frac{\partial (uS)}{\partial x} + \frac{\partial (wS)}{\partial z} = \tau\left(\frac{\partial^2 S}{\partial x^2} + \frac{\partial^2 S}{\partial z^2}\right) \tag{3.30a}$$

where $\tau = \alpha/\alpha_S$ is the ratio of the two diffusivities. This is identical with the result of assuming $\Gamma = \tau$ and So $= 0$ in the general differential equation (3.9).

Boundary Conditions for the Solute

There will be no loss of the solute at the surface since the assumption of a non-evaporating surface still holds here. If considering LNG as a binary system consisting of methane and another higher hydrocarbon, this assumption would imply that the composition of liquid remains unchanged after 'flashing' at the surface. This is, of course, not true due to the preferential evaporation of the methane component. This assumption therefore tends to lessen the actual density of fluid in the surface layer. It is also assumed that there is no exchange of the solute between the liquid and the walls. Therefore

$$\frac{\partial S}{\partial n} = 0 \tag{3.31}$$

holds at all four boundaries, where $\vec{n}$ is the direction normal to the boundary. Since the two liquids are miscible, no extra boundary conditions are required within the liquid body.

<u>Vorticity Transportation Equation</u>

Due to the presence of the solute, equation (3.4) needs to be rewritten as

$$\frac{\partial \zeta}{\partial t} + \frac{\partial (u\zeta)}{\partial x} + \frac{\partial (w\zeta)}{\partial z} = \nu\left(\frac{\partial^2 \zeta}{\partial x^2} + \frac{\partial^2 \zeta}{\partial z^2}\right) - g\beta_T\frac{\partial T}{\partial x} + g\beta_S\frac{\partial S}{\partial x} \tag{3.32}$$

Normalisation of the above equation yields

$$\frac{\partial \zeta}{\partial t} + \frac{\partial (u\zeta)}{\partial x} + \frac{\partial (w\zeta)}{\partial z} = Pr\left(\frac{\partial^2 \zeta}{\partial x^2} + \frac{\partial^2 \zeta}{\partial z^2}\right) - PrRa^*\frac{\partial T}{\partial x} + PrRs\frac{\partial S}{\partial x} \tag{3.32a}$$

where Rs is the solute Rayleigh number as defined before,

$$Rs = \frac{g\beta_s \Delta S d^3}{\alpha \nu} \tag{2.21}$$

This is identical with the outcome of assuming $\Gamma = \mathrm{Pr}$ and $\mathrm{So} = -\mathrm{PrRa}^{*}\partial T/\partial x + \mathrm{PrRs}\partial S/\partial x$ in the general differential equation (3.9).

Solution Procedure

Since the solute appears in the source term of the modified vorticity equation (3.32a), the finite volume equation for the solute is solved before the vorticity equation.

TWO-COMPONENT MODEL IN CPC

Of the three major parts of the model, namely the mathematical formulation, discretization of the differential equations and solution of the finite volume equations, the last two are almost the same between the two versions. The differences mainly lie in the mathematical formulation. This part of the chapter is devoted to address these differences.

3.8 Solution Domain and Boundary Conditions

It was decided to model cylindrical vessels as a axi-symmetric problem. Figure 3.6 shows the solution domain in cylindrical polar coordinates. Apart from the left boundary (the axi-symmetric axis), the conditions at the other three boundaries are exactly the same as those in the cartesian coordinates described above. The boundary conditions at r=0 can be determined from the symmetry property

$$u = 0, \quad \frac{\partial w}{\partial r} = 0, \quad \frac{\partial T}{\partial r} = 0, \quad \frac{\partial S}{\partial r} = 0;$$

$$\psi = 0, \quad \zeta = \frac{\partial u}{\partial z} - \frac{\partial w}{\partial r} = 0. \tag{3.33}$$

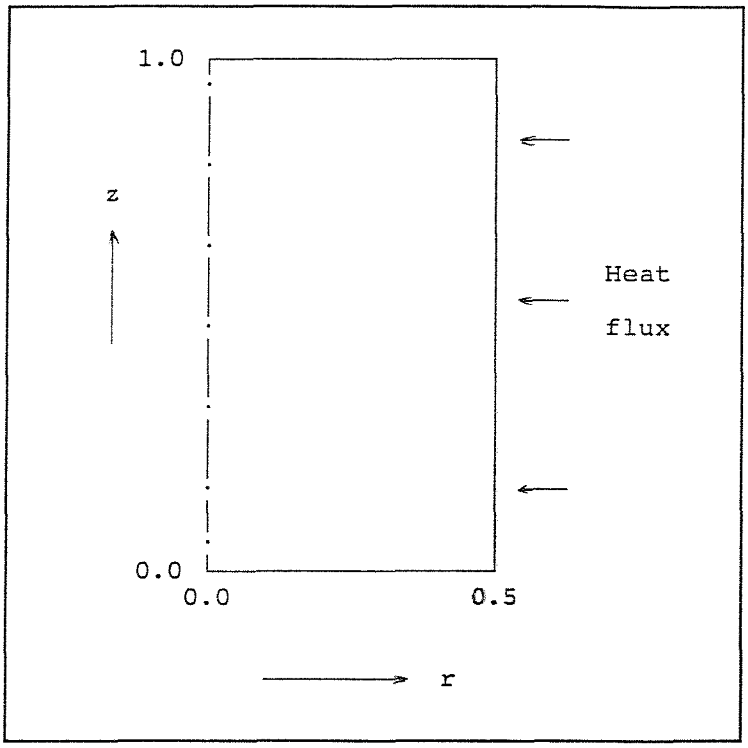

Fig. 3.6 The solution domain in cylindrical polar coordinates. r=0.0, the axi-symmetric axis; r=0.5, non-slip wall; z=0.0, non-slip adiabatic base; z=1.0, isothermal free surface.

3.9 Mathematical Formulation

3.9.1 Governing Differential Equations

The governing differential equations (in cylindrical polar coordinates) are the Navier-Stokes equations

$$\frac{\partial u}{\partial t} + u\frac{\partial u}{\partial r} + w\frac{\partial u}{\partial z} = -\frac{1}{\rho_0}\frac{\partial p}{\partial r} + \nu(\frac{\partial^2 u}{\partial r^2} + \frac{1}{r}\frac{\partial u}{\partial r} + \frac{u}{r^2} + \frac{\partial^2 u}{\partial z^2})$$

(3.34)

$$\frac{\partial w}{\partial t} + u\frac{\partial w}{\partial r} + w\frac{\partial w}{\partial z} = -\frac{1}{\rho_0}\frac{\partial p}{\partial z} + \nu(\frac{\partial^2 w}{\partial r^2} + \frac{1}{r}\frac{\partial w}{\partial r} + \frac{\partial^2 w}{\partial z^2})$$

$$+ g\beta_T T - g\beta_S S$$

the energy equation(in conservative form)

$$\frac{\partial T}{\partial t} + \frac{\partial (uT)}{\partial r} + \frac{uT}{r} + \frac{\partial (wT)}{\partial z} = \alpha(\frac{\partial^2 T}{\partial r^2} + \frac{1}{r}\frac{\partial T}{\partial r} + \frac{\partial^2 T}{\partial z^2}) \qquad (3.35)$$

the solute equation(in conservative form)

$$\frac{\partial S}{\partial t} + \frac{\partial (uS)}{\partial r} + \frac{uS}{r} + \frac{\partial (wS)}{\partial z} = \alpha_S(\frac{\partial^2 S}{\partial r^2} + \frac{1}{r}\frac{\partial S}{\partial r} + \frac{\partial^2 S}{\partial z^2}) \qquad (3.36)$$

and the continuity equation

$$\frac{\partial u}{\partial r} + \frac{u}{r} + \frac{\partial w}{\partial z} = 0 \tag{3.37}$$

where the density has been linearized, $\rho = \rho_0(1 - \beta_T T + \beta_S S)$.

Eliminating the pressure terms in equations (3.34), and introducing vorticity as $\zeta = \partial u/\partial z - \partial w/\partial r$, one obtains the vorticity transportation equation

$$\frac{\partial \zeta}{\partial t} + u\frac{\partial \zeta}{\partial r} + w\frac{\partial \zeta}{\partial z} = \nu(\frac{\partial^2 \zeta}{\partial r^2} + \frac{1}{r}\frac{\partial \zeta}{\partial r} - \frac{\zeta}{r^2} + \frac{\partial^2 \zeta}{\partial z^2}) + g\beta_S\frac{\partial S}{\partial r} - g\beta_T\frac{\partial T}{\partial r} \tag{3.38}$$

The stream function in CPC is defined as

$$u = \frac{1}{r}\frac{\partial \psi}{\partial z}, \qquad w = -\frac{1}{r}\frac{\partial \psi}{\partial r} \tag{3.39}$$

Substituting u and w into the definition of vorticity, one obtains the Poisson equation

$$\frac{\partial}{\partial r}(\frac{1}{r}\frac{\partial \psi}{\partial r}) + \frac{\partial}{\partial z}(\frac{1}{r}\frac{\partial \psi}{\partial z}) = \zeta \tag{3.40}$$

If $\zeta' = \zeta/r$, instead of simply ζ, is used as the dependent variable[28], equation (3.38) may be rewritten as

$$\frac{\partial\zeta}{\partial t} + \frac{\partial(u\zeta)}{\partial r} + \frac{u\zeta}{r} + \frac{\partial(w\zeta)}{\partial z} = \nu(\frac{\partial^2\zeta}{\partial r^2} + \frac{1}{r}\frac{\partial\zeta}{\partial r} + \frac{\partial^2\zeta}{\partial z^2})$$

$$+ 2\nu\frac{\partial\zeta}{\partial r} + g\beta_S\frac{\partial S}{\partial r} - g\beta_T\frac{\partial T}{\partial r} \tag{3.41}$$

3.9.2 Normalization

Using the scales in equation (3.7) (note the scale for stream function is now dα), and ΔS for the solute, the dimensionless forms of equations (3.41), (3.35) and (3.36) can be obtained

$$\frac{\partial\zeta}{\partial t} + \frac{\partial(u\zeta)}{\partial r} + \frac{u\zeta}{r} + \frac{\partial(w\zeta)}{\partial z} = Pr(\frac{\partial^2\zeta}{\partial r^2} + \frac{1}{r}\frac{\partial\zeta}{\partial r} + \frac{\partial^2\zeta}{\partial z^2})$$

$$+ 2Pr\frac{\partial\zeta}{\partial r} + PrRs\frac{\partial S}{\partial r} - PrRa^*\frac{\partial T}{\partial r} \tag{3.41a}$$

$$\frac{\partial T}{\partial t} + \frac{\partial(uT)}{\partial r} + \frac{uT}{r} + \frac{\partial(wT)}{\partial z} = \frac{\partial^2 T}{\partial r^2} + \frac{1}{r}\frac{\partial T}{\partial r} + \frac{\partial^2 T}{\partial z^2} \tag{3.35a}$$

$$\frac{\partial S}{\partial t} + \frac{\partial(uS)}{\partial r} + \frac{uS}{r} + \frac{\partial(wS)}{\partial z} = \tau(\frac{\partial^2 S}{\partial r^2} + \frac{1}{r}\frac{\partial S}{\partial r} + \frac{\partial^2 S}{\partial z^2}) \tag{3.36a}$$

The form of the Poisson equation and continuity equation are unchanged after normalization.

3.9.3 The General Differential Equation

It can be seen that equations (3.41a), (3.35a) and (3.36a) share a common form, which, for a general variable ϕ, is

$$\frac{\partial \phi}{\partial t} + \frac{\partial (u\phi)}{\partial r} + \frac{u\phi}{r} + \frac{\partial (w\phi)}{\partial z} = \Gamma\left(\frac{\partial^2 \phi}{\partial r^2} + \frac{1}{r}\frac{\partial \phi}{\partial r} + \frac{\partial^2 \phi}{\partial z^2}\right) + So \qquad (3.42)$$

with $\Gamma = 1$, So $= 0$ for the energy equation; $\Gamma = \tau$, So $= 0$ for the solute equation and $\Gamma = \nu$, So $= (2\mathrm{Pr}/r)\partial\zeta'/\partial r + \mathrm{PrRa}^*\partial S/\partial r - \mathrm{PrRa}^*\partial T/\partial r$ for the vorticity equation. Note the term $(2\mathrm{Pr}/r)\zeta'/\partial r$ in equation (3.41a) has been included into the source term So. When the vorticity equation is integrated over control volumes to yield finite volume equations, this term as a whole is taken as a constant for each control volume.

With the following mathematical manipulations,

$$\frac{\partial (u\phi)}{\partial r} + \frac{ur}{r} = \frac{1}{r}\frac{\partial (ru\phi)}{\partial r}, \qquad \frac{\partial (w\phi)}{\partial z} = \frac{1}{r}\frac{\partial (rw\phi)}{\partial r}$$

$$\frac{\partial^2 \phi}{\partial r^2} + \frac{1}{r}\frac{\partial \phi}{\partial r} = \frac{1}{r}\frac{\partial}{\partial r}\left(r\frac{\partial \phi}{\partial r}\right), \qquad \frac{\partial^2 \phi}{\partial z^2} = \frac{1}{r}\frac{\partial}{\partial z}\left(r\frac{\partial \phi}{\partial z}\right) \qquad (3.43)$$

equation (3.42) may be rewritten as

$$\frac{\partial \phi}{\partial t} + \frac{1}{r}\left[\frac{\partial (ru\phi)}{\partial r} + \frac{\partial (rw\phi)}{\partial z}\right] = \frac{\Gamma}{r}\left[\frac{\partial}{\partial r}\left(r\frac{\partial \phi}{\partial r}\right) + \frac{\partial}{\partial z}\left(r\frac{\partial \phi}{\partial z}\right)\right] + So \qquad (3.44)$$

By introducing a total heat flux for the general variable ϕ,

$$J_r = u\phi - \Gamma\frac{\partial\phi}{\partial r}, \quad J_z = w\phi - \Gamma\frac{\partial\phi}{\partial z} \tag{3.45}$$

equation (3.44) may be rearranged into

$$\frac{\partial\phi}{\partial t} + \frac{1}{r}\left[\frac{\partial(rJ_r)}{\partial r} + \frac{\partial(rJ_z)}{\partial z}\right] = So \tag{3.46}$$

3.10 Discretization

The general differential equation

The general differential equation (3.46) may be discretized following the similar procedure leading to equation (3.18). In cylindrical polar coordinates, the integral element is rdrdz. Therefore the (1/r) term in equation (3.46) will be immediately cancelled out during the integration. In the unsteady and source terms r is approximated by r_P, the radius of a node point.

The poisson equation

The integration of equation (3.40) over the central control volume in Fig. 3.7 yields

$$r_P\Delta z\left[\left(\frac{1}{r}\frac{\partial\psi}{\partial r}\right)_e - \left(\frac{1}{r}\frac{\partial\psi}{\partial r}\right)_w\right] + \Delta r\left[\left(\frac{\partial\psi}{\partial z}\right)_n - \left(\frac{\partial\psi}{\partial z}\right)_s\right] = \zeta_P r_P \Delta r \Delta z \tag{3.47}$$

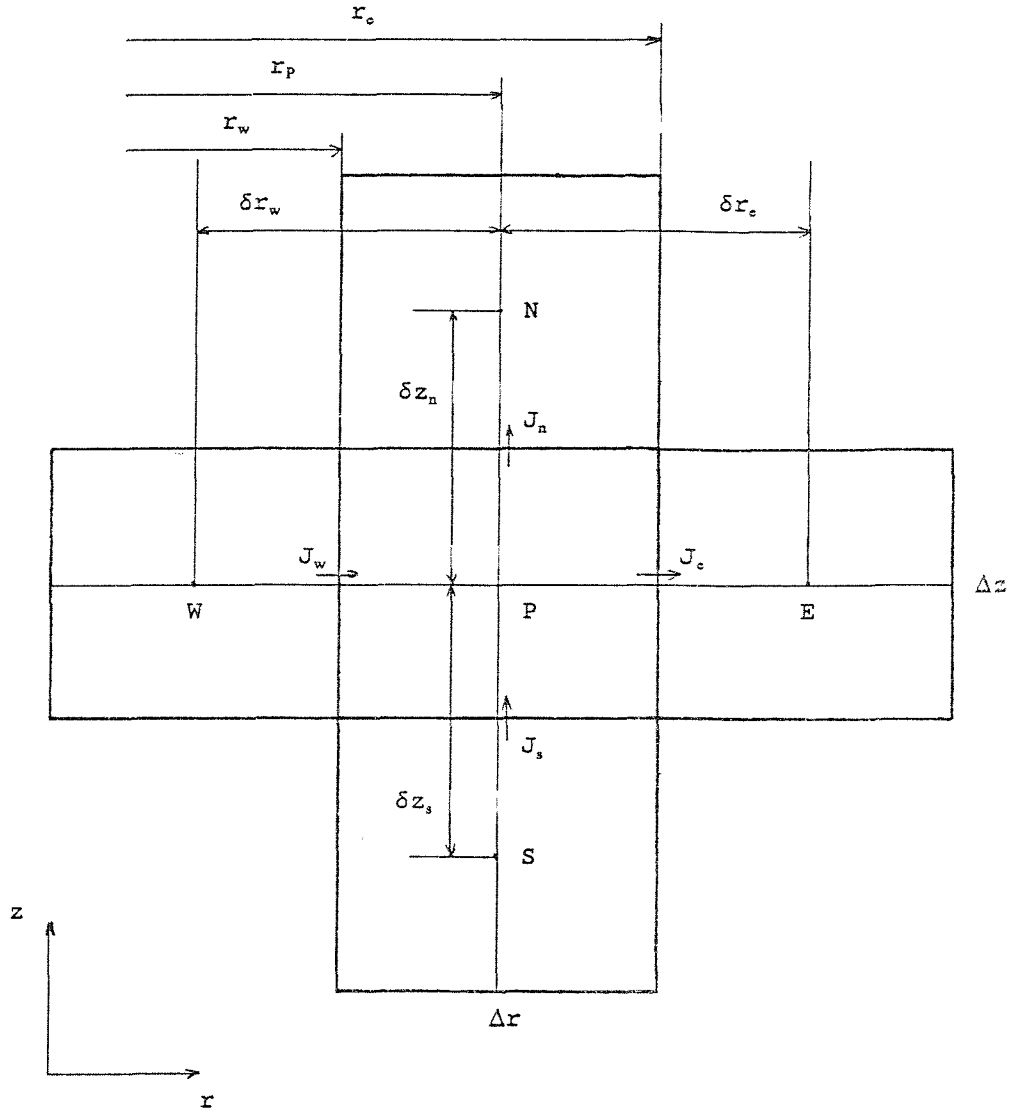

Fig. 3.7 A typical cluster of control volumes in cylindrical polar coordinates.

where stepwise profile assumptions have been used. Applying piecewise-linear profiles to the first derivatives of the stream function, and rearranging

$$A_P\psi_P = A_E\psi_E + A_W\psi_W + A_N\psi_N + A_S\psi_S + b \tag{3.48}$$

where

$$A_E = \frac{r_P\Delta z}{r_e\delta r_e}, \quad A_W = \frac{r_P\Delta z}{r_w\delta r_w}, \quad A_N = \frac{\Delta r}{\delta z_n}, \quad A_S = \frac{\Delta r}{\delta z_s}$$

$$A_P = A_E + A_W + A_N + A_S$$

$$b = -\zeta_P' r_P^2 \Delta r \Delta z$$

For control volumes just next to the central line, clearly $r_w = 0$, and thus $A_W \to \infty$. Consequently, $A_P \to \infty$. This singularity problem was solved by locating control volumes across the central line. These thus appear as "half" volumes in the solution domain. The stream function for these volumes are defined(0), so no calculation is required, thus avoiding the singularity problem.

3.11 Solution

Once the general differential equation (3.46) and the poisson equation (3.40) are discretized, the resulting control volume equations can be solved using the same algorithms as before(see 3.5). The methods are also similar through which the velocity components and the wall vorticity are derived from the stream function. The only complication is that ζ' at $r=0$ needs to be determined.

Evaluation of ζ' at the symmetric axis

At the symmetric axis, r=0, ζ=0, but the value $\zeta' = \zeta/r$ is so far undecided. Clearly some assumptions must be made about the profile of ζ near r=0. Since ζ is connected to ψ through velocity, one practice is to assume ψ as a polynomial of radius r in the vicinity of r=0[28]. From equation (3.40), at least a fourth order polynomial is required. Considering at r=0,

$$\psi = 0, \quad \frac{\partial \psi}{\partial r} = 0, \quad \frac{\partial w}{\partial r} = \frac{\partial}{\partial r}\left(-\frac{1}{r}\frac{\partial \psi}{\partial r}\right) = 0.$$

it follows that a plausible form of the polynomial is

$$\psi = ar^4 + br^2 \tag{3.49}$$

where a and b are the coefficients which can be determined in terms of the stream function of the two nodes immediately away from the symmetric axis. Now ζ' at r=0 can be obtained

$$\zeta'_{r=0} = 8a \tag{3.50}$$

4.0 VALIDITY OF THE MODEL

In the last chapter a numerical model has been developed for thermally-induced laminar flows in both rectangular and cylindrical vessels. Naturally the model should only be used to predict laminar flows. Therefore in order to apply the model effectively, it is important to define the conditions under which laminar flows prevail. This is the task of this chapter. Only convective flows in rectangular vessels are considered because the computational stability method used here is not applicable to flows in cylindrical vessels. Homogeneous flows (one-component model) will be dealt with first. More complicated heterogeneous flows(two-component model) are discussed later. In the end, some conclusions on the validity of the model(cartesian coordinates version) are drawn.

4.1 Critical Ra^* number of Homogeneous Flows

Thermal-induced convective flows in rectangular vessels are considered as two-dimensional in the model. No assumption of symmetry is made as might seem reasonable because the geometry and the boundary conditions are symmetric about the central plain of the vessel. Numerical results show that flows are indeed symmetric about the central line of the solution domain(Fig. 3.1) when the (modified) Rayleigh number is small. This is shown schematically in Fig. 4.1. The liquid in the boundary layer moves upwards over the side wall, absorbing heat from the surroundings, then across the free surface where part or all of the absorbed heat is removed by conduction; the two opposing surface flows meet at the centre of the surface, and generate a strong downward flow. This resulting flow is called the core flow (of the convective loop). When the Ra^* exceeds a certain value for a given liquid(Pr) and aspect ratio of the solution domain (η = height/width), instability is observed to occur in the core flow. The occurrence of instability implies that the flows under computation are no longer stable in the present form. Consequently, this symmetry is destroyed. This instability of the core flow will be analyzed in the next section.

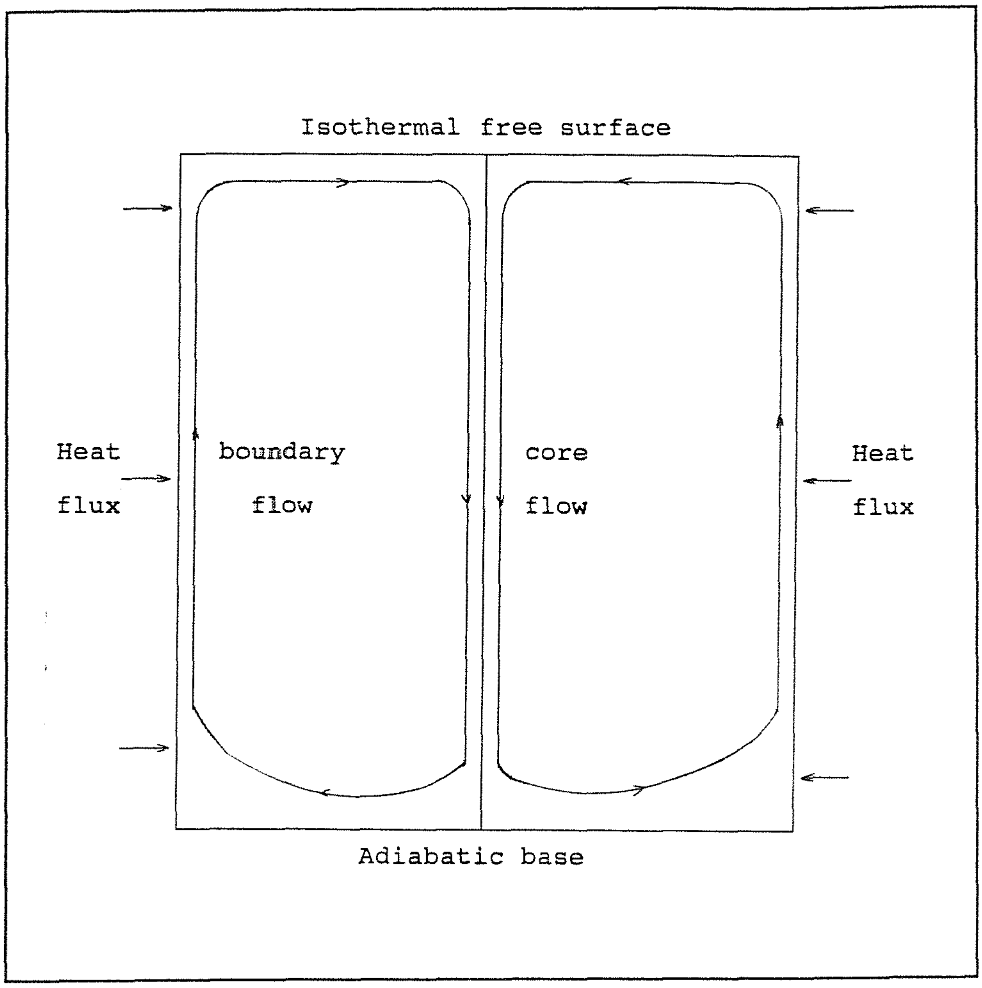

Fig. 4.1 Schematic convective loop of symmetric laminar flows.

The lowest Ra^* at which instability starts to break out is termed the critical Rayleigh number (Ra^*_c). The Ra^*_c for a given flow, i.e, fixed Pr and η, may be found by using a computational trial-and-error procedure: if the flow under computation is symmetric about the central line up to the steady state, the present Ra^* is smaller than the Ra^*_c; on the other hand, if instability breaks out during a numerical run, then the present Ra^* is greater than or equals to the Ra^*_c. Starting from an arbitrary chosen Ra^*, one can eventually locate a narrow range of Ra^* which includes the actual Ra^*_c through a series of trial-and-error numerical runs. For liquid nitrogen ($Pr=2.32$) in a square domain($\eta=1$), the Ra^*_c is found to be between 10^8 and $5x10^8$.

Unless otherwise stated, numerical results used in this chapter are from the runs with $Pr=2.32$ and $\eta=1$.

4.2 Instability of the Core Flow

4.2.1 Free Shear Flow

Figure 4.2 shows a mid-plane vertical velocity profile just before the break out of instability($Ra^*=5x10^8$). It can be seen that velocity gradients are mainly confined to the boundary layer and core region. The velocity distribution in the core region shows some similarity with that of a two-dimensional laminar free jet, an example of which is shown in Fig. 4.3. The implication of this similarity will be seen later. With the local concentration of shear as such in these two regions, it is expected that instabilities would most likely start to break out here.

The Reynolds number of the core flow may be defined as $Re = w_{max}L/\nu$ (w_{max} and L see Fig. 4.2). It can be seen that the Re of the core flow is about the same order as that of the boundary flow (Re based on the maximum velocity and thickness of the boundary layer). In general, shear flows away from any solid boundaries (called free shear flows) are much less stable than those near a wall. (The order of critical Re for free jets is typically 10, compared with typically 1000 for velocity boundary layers[29].) The stabilising effect of a solid boundary is apparently an important factor. In view of this fact, it might be anticipated that the core flow here would be much less stable than the boundary flows.

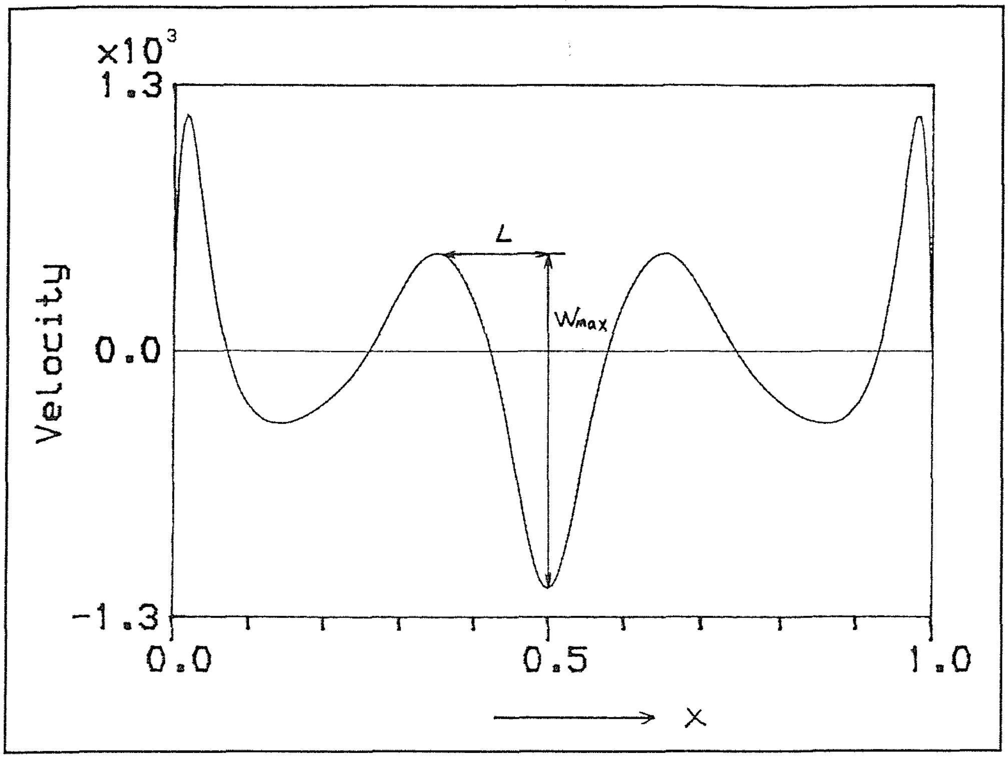

Fig. 4.2 Vertical velocity profile at z=0.5 ($Ra^*=5x10^8$).

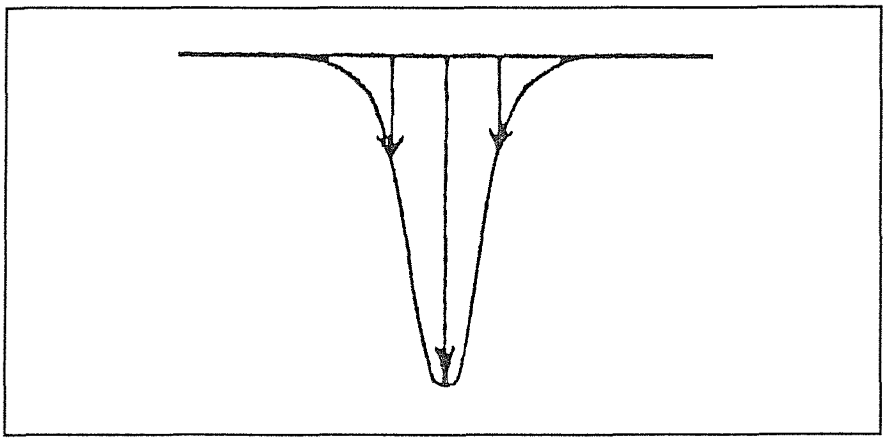

Fig. 4.3 Velocity profile of a two-dimensional free jet.

4.2.2 Source of Disturbances

Instability is a result of spontaneous amplification of disturbances present in a flow. The disturbances leading to the instability of the computed core flow originate from the computer round-off errors.

For symmetric flows in the present solution domain (Fig. 3.1) in theory variables such as vorticity and stream function at the central line (symmetric axis) should be identically zero. In computer computations, however, this feature could not be strictly preserved due to machine round-off errors and the subsequent elevation of these 'errors' by the computational method used. After one time step, stream function and vorticity at the central line are typically of orders of 10^{-20} and 10^{-72} respectively in all the numerical runs which have been carried out. The huge contrast in the magnitude between the stream function and vorticity is due to the fact that different algorithms are used in their solutions: non-iterative for the vorticity; yet iterative for the stream function. In the solution of the vorticity equation, vorticity at the central line almost directly results from the computer round-off errors, therefore is extremely small. The stream function, on the other hand, is obtained through numerous iterations in the solution of the Poisson equation. As a result, these initial round-off errors expand exponentially before eventually levelling off at the order of 10^{-20}, as shown in Table 4.1.

The stream function and the vorticity at the central line grow rapidly in the subsequent time steps, reaching the orders of 10^{-12} and 10^{-9} respectively after about 1000 time steps. This time a different mechanism is in action, which stems from the fact that the vorticity and Poisson equation are coupled. Note the base vorticity is calculated from $\varsigma = 2\psi/h^2$ (equation (3.29)), where ψ is the stream function of the node next to the wall and δz the distance between the nodes. Since h is much less than unity, the base vorticity has a magnitude of at least the same order as the stream function. This means that after one time step the base vorticity is about 50 orders higher than the vorticity of other nodes at the central line. In the following time steps the base vorticity serves as a huge source for the vorticity at the central line. Since vorticity forms the source term in the Poisson equation, increases in the vorticity at the central line would result in increases in the stream function there. Meanwhile, if the stream function of the node next to the base is increased, the base vorticity would increase proportionally through equation (3.29). A self-perpetual process is thus formed in which increases in either the stream function or vorticity would result in increases in the other, and vice versa. This process terminates when the vorticity values at the central line become of about same order.

Table 4.1 Increase in the order of magnitude of the stream function at the central line in the first time step with the number of iterations.

No. of iterations	Order of magnitude
1	10^{-76}
2	10^{-74}
10	10^{-56}
20	10^{-32}
50	10^{-23}
100	10^{-21}
1000	10^{-20}

These elevated round-off errors in the early stage of the flow development act as perturbations to the computation followed. If they start to grow later at some stage, instability is indicated. Otherwise the flow is considered as stable.

4.2.3 Amplification of the Perturbations

For $Ra^* \leq 10^8$, the order of magnitude of the stream function and vorticity at the central line remain almost unchanged, at 10^{-12} and 10^{-9} respectively. When the Ra^* is increased to $5x10^8$, these perturbations are observed to grow (instability) at one stage and consequently the symmetry is destroyed. The occurrence of instability is found progressive earlier in time with further increase in the Ra^*.

Since the magnitudes of these perturbations are extremely small, the instabilities encountered correspond to infinitesimal perturbations. According to linear hydrodynamic stability theory, the initial growth of infinitesimal disturbances is exponential. Table 4.2 shows the expansion of the stream function disturbances at the central line in the run with $Ra^*=5x10^8$. It can been seen that initially the growth rate follows roughly an exponential law. This is followed by a period in which the growth rate decreases, eventually approaching to zero. When the infinitesimal disturbances have been amplified, the non-linear terms in the vorticity equation become important and would come into play. In this case, the non-linear effects resulted in the levelling off of the stream function.

4.2.4 The Form of Initial Instability

Figure 4.4 shows a sequence of profiles of the stream function at the central line following the start of instability ($Ra^* = 5x10^8$). Two observations could be made here. Firstly, the form of the disturbances is seen gradually evolving into a roughly sinusoidal one. This form of initial instability has been observed in free jets. Secondly the wave motion is mainly confined to the bottom half of the cavity, indicating the core flow is most unstable there. This may be explained by considering the thermal force involved in the core flow. Figure 4.5 shows the horizontal temperature profile at three different levels in the run $Ra^*=5x10^8$. There is a substantial temperature gradient in the core flow just below the surface. This temperature gradient will generate a buoyancy force which is along the direction of the core flow. Such a force would enhance the stability of the core flow. As the core flow travels down, this temperature gradient, thus the buoyancy, is gradually diminished. There are two factors for this: 1) the bulk liquid becomes cooler away from the surface; 2) the core flow, absorbing heat from the surrounding, is increasing in temperature as it descends. These can be seen clearly in Fig. 4.5. This feature is common to convective flows with an isothermal surface. Sometimes the buoyancy force is against the core flow. When the Ra^* is greater than 10^8, reversal of the core flow is observed at progressively larger depth as time progresses. An example is shown in Fig. 4.6. When the buoyancy force acts against the core flow, its stability will be reduced.

Table 4.2 Amplification of the stream function perturbations ($Ra^* = 5x10^8$).

Time ($x10^{-2}$)	ψ	$\Delta t=t_2-t_1$ ($x10^{-2}$)	ψ_2/ψ_1
0.62	$2.0x10^{-11}$		
		0.62	7000
1.24	$1.4x10^{-7}$		
		0.57	3800
1.81	$5.3x10^{-4}$		
		0.81	264
2.62	$1.4x10^{-1}$		
		0.40	1.8
3.02	$2.5x10^{-1}$		

where $t_1(\psi_1)$ and $t_2(\psi_2)$ are the two adjacent times(stream function values).

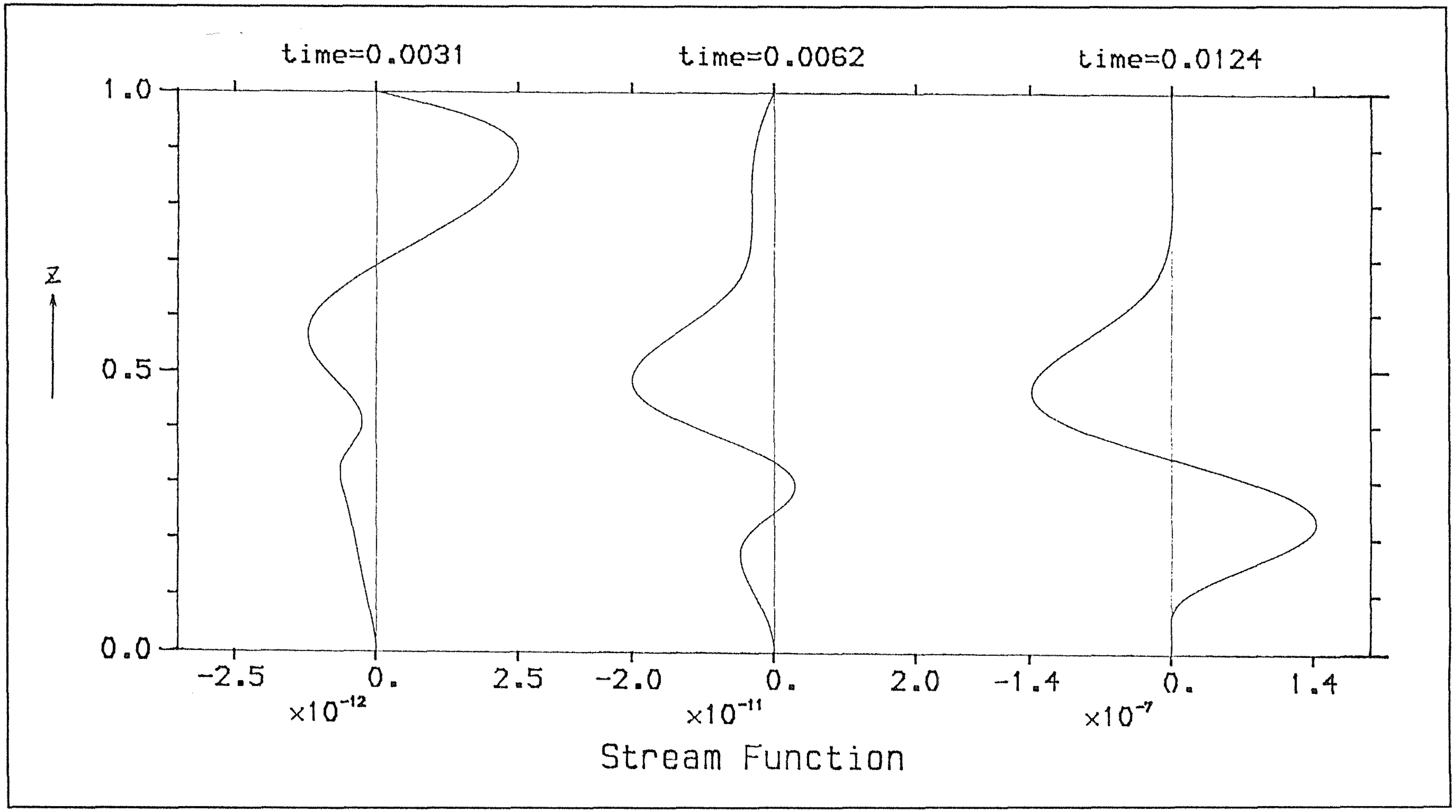

Fig. 4.4 Evolution of the form of the stream function perturbations at $Ra^*=5x10^8$ (to be continued).

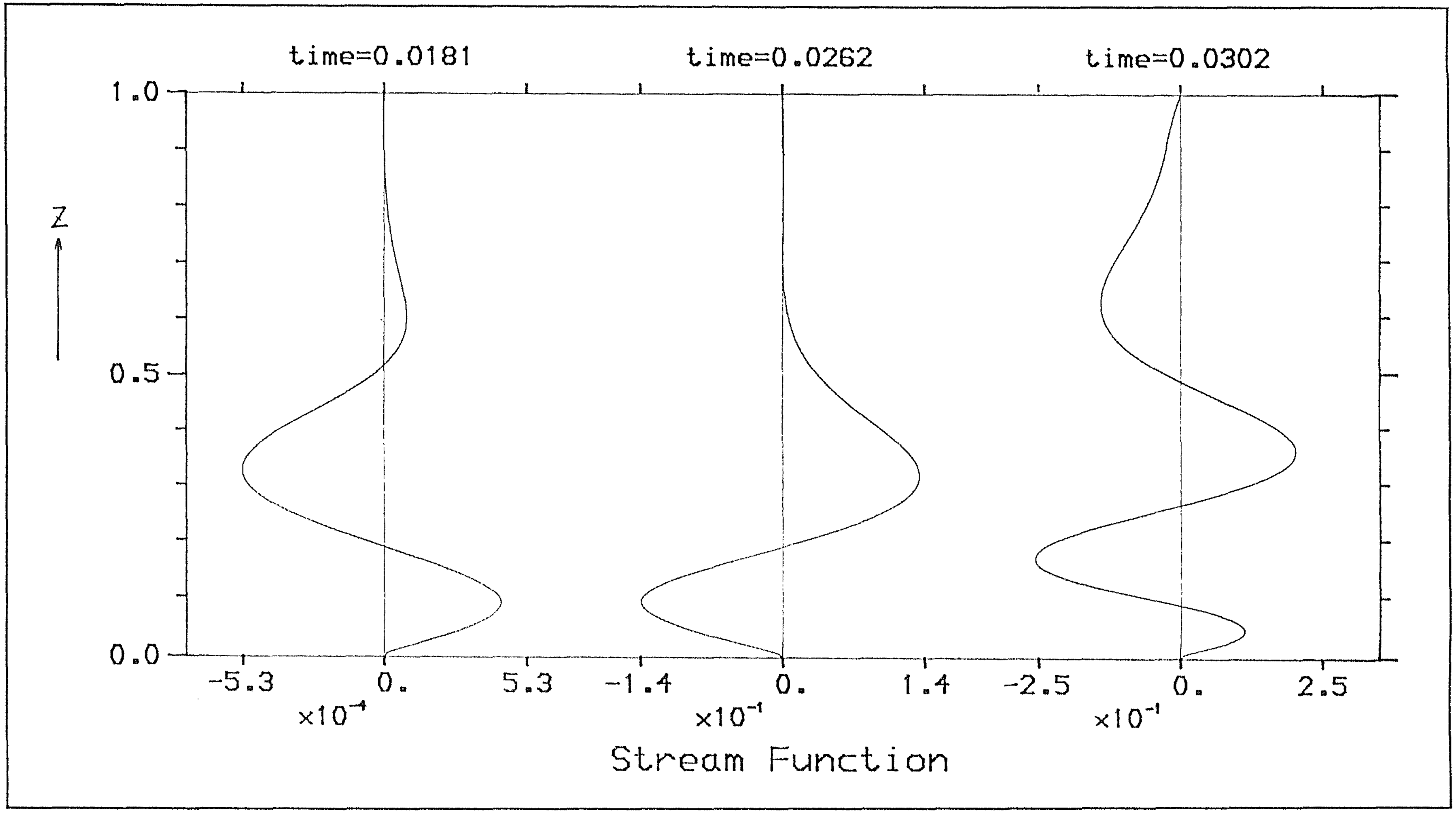

Fig. 4.4 (continuing)

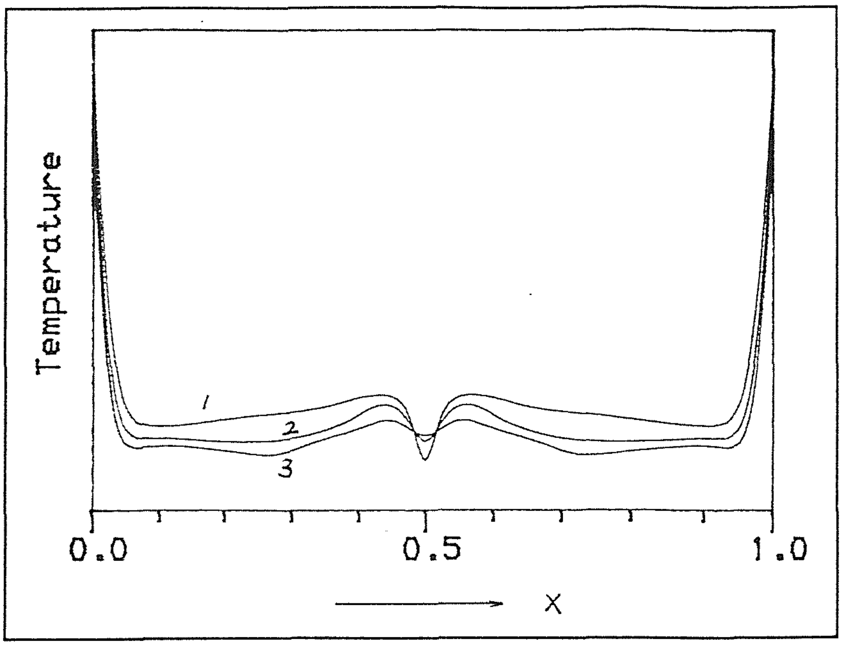

Fig. 4.5 Variation of the temperature distribution across the core flow with liquid depth z. 1: z=0.9; 2: z=0.7; 3: z=0.5.

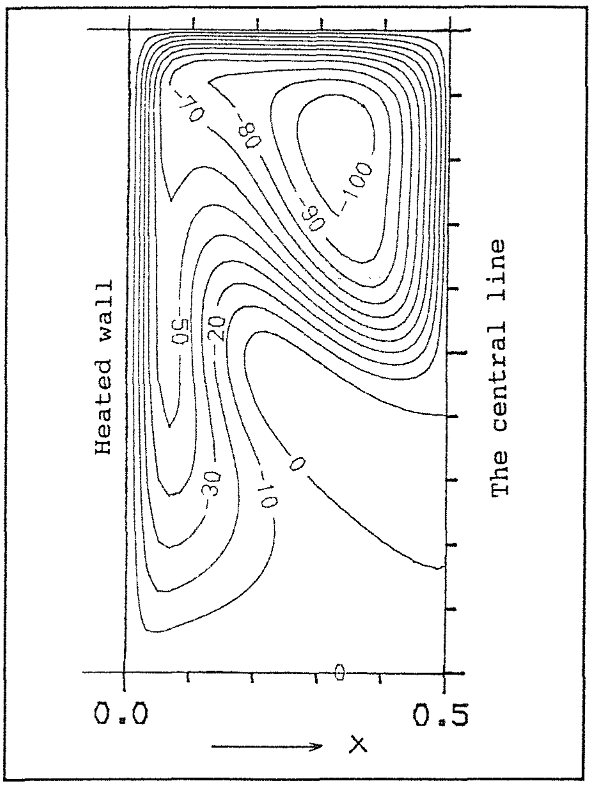

Fig. 4.6 Reversal of the core flow ($Ra^*=5x10^8$).

4.3 Critical Ra* Number of Heterogeneous Flows

To complete the specification of a two-component system, the initial distribution of the solute and the diffusivity ratio τ are required, in addition to those parameters for a layer of homogeneous liquid, i.e., Ra*, Pr and η. Here a system of two stratified layers of equal thickness with a step density interface is considered. The stratification results from the presence of a heavier solute in the lower layer. Numerical runs have been carried out on such a two-layer system of liquid nitrogen(LIN), with liquid oxygen(LOX) as solute. The results (with $\eta=1$) show that instability (in roughly sinusoidal form) starts to occur in the core flow of the upper layer at a smaller Ra* number than before. The critical Ra* was found to be between 10^7 and 10^8. This is because the presence of a heavier solute in the lower layer could significantly increase the velocity of the core flow of the upper layer (for more details see next chapter).

4.4 Grid-Dependence Check

Grid-dependence check of the instability described above was conducted in terms of the form of the instability and the lowest Ra* at which instability occurs (Ra$^*_c$). Using a finer mesh of 99x100 (compared with 49x43 before), the results for homogeneous flows, i.e., the Ra$^*_c$ is between 10^8 and $5\text{x}10^8$ and the roughly sinusoidal wave form of the instability, are confirmed.

4.5 On Validity of the Model(CC Version)

So far it has been established using computational methods that the critical Ra* number is between 10^8 and $5\text{x}10^8$ for LIN in a square cavity, and even lower for a two-layer LIN/LOX system. The physical significance of these figures may be appreciated by putting them into the context of a laboratory scale dewar.

Using the properties of LIN at the normal boiling point (77.4K),

$$\begin{aligned} \beta_T &= 5.77\text{x}10^{-3} && 1/\text{K}, \\ k &= 1.40\text{x}10^{-1} && \text{J/m-K}, \\ \nu &= 1.96\text{x}10^{-7} && \text{m}^2/\text{s}, \\ \alpha &= 8.44\text{x}10^{-8} && \text{m}^2/\text{s}, \end{aligned}$$

the modified Rayleigh number($Ra^* = g\beta_T d^4\dot{q}/k\alpha\nu$) is

$$Ra^* = 2.45\text{x}10^{13}\dot{q}d^4 \qquad (4.1)$$

To yield $Ra^* < 5\text{x}10^8$, that is

$$2.45\text{x}10^{13}\dot{q}d^4 < 5\text{x}10^8$$

the following condition must be satisfied

$$\dot{q}d^4 < 2\text{x}10^{-5} \qquad (4.2)$$

This means that even for a d as small as 0.1m, $\dot{q}$ can not be larger than 0.2W/m^2. This heat flux is at least a factor of 50 smaller than the normal heat leak into large cryogenic storage tanks.

Therefore the Ra^* allowed for the present model(CC version) is at least a factor of 50 smaller than those normally encountered in the laboratory scale rollover simulation experiments using cryogenic liquids. When dewar of vertical length scale greater than 0.1m are used, this figure could rise to thousands (the order of magnitude of Ra^* is typically 10^{12} in Agbabi's[13] experiments). This outcome also suggests that buoyancy-induced convective flows in cryogenic liquids in most laboratory scale dewar are likely to be far from laminar.

5.0 NUMERICAL RESULTS

5.1 Validation of the Computer Code

Before the model was put into use, its computer code was tested against the bench mark solution of Davis [30] up to Rayleigh numbers of 10^6. The problem considered is that of natural convection of air induced by differential wall heating (constant wall temperatures) in a square cavity. By modifying the boundary conditions, i.e., a constant wall heat flux to constant wall temperatures and an isothermal free surface to an adiabatic wall, the present one-component model can be readily adapted to solve this problem. The predictions by this model together with the bench mark solution for a number of representative variables are given in Table 5.1. For Rayleigh numbers up to 10^5, a 40x40 uniform grid of control volume was found adequate; at $Ra=10^6$, a finer grid of 80x80 was used. As can be seen in Table 5.1, the predictions by this (modified) model are within 5% (except the $\overline{Nu}$ at $Ra=10^5$) of the bench mark solution.

The numerical simulations of rollover were performed on a two-layer system in cryogenic liquids. The stratification was caused by the presence of a heavier solute in the lower layer. Numerical results obtained in cartesian coordinates will be presented first; a numerical run is examined in detail. The results of the two runs carried out in cylindrical polar coordinates will be discussed briefly in the end.

Table 5.1 Numerical predictions of the present model compared with the bench mark solution

	ψ_{mid}	ψ_{max}	u_{max}	w_{max}	$\overline{Nu}$
Ra = 10^3 (40x40)					
B.M.	1.174	____	3.649	3.697	1.118
P.M.	1.220	____	3.745	3.789	1.129
$\epsilon(\%)$	3.9		2.6	2.5	1.0
Ra = 10^4 (40x40)					
B.M.	5.071	____	16.178	19.617	2.243
P.M.	5.211	____	16.417	20.092	2.320
$\epsilon(\%)$	2.8		1.5	2.4	3.6
Ra = 10^5 (40x40)					
B.M.	9.911	9.612	34.73	68.59	4.519
P.M.	9.427	9.612	35.86	70.81	4.716
$\epsilon(\%)$	3.5	3.9	3.3	3.2	5.4
Ra = 10^6 (80x80)					
B.M.	16.32	16.75	64.63	219.36	8.800
P.M.	16.67	17.25	66.90	225.53	9.126
$\epsilon(\%)$	2.1	3.5	3.5	2.6	3.7

where

B.M. ———— bench mark solution,

P.M. ———— predictions of present model,

ϵ ———— relative difference between above two,

ψ_{mid} ———— stream function at the middle of the cavity,

ψ_{max} ———— maximum value of stream function,

u_{max} ———— maximum horizontal velocity at the vertical middle plane,

w_{max} ———— maximum vertical velocity at the horizontal middle plane,

$\overline{Nu}$ ———— average Nusslt number within the cavity.

NUMERICAL RESULTS IN CARTESIAN COORDINATES

In order to give some confidence to the predictability of the two-component model, the performance of the one-component model is first assessed.

5.2 One-Component Model

5.2.1 Convective Flows With an Isothermal Surface

Convective flows of a layer of liquid nitrogen in a square domain(Fig. 3.1) were studied. The initial values of all the variables were assumed zero. The steady state results of three runs with $Ra^{*}=10^{6}$, 10^{7} and 10^{8} are discussed and some comparison is made with previous experimental and theoretical results. (In the steady state, all the input heat is removed at the surface). Due to the symmetry of the flows, only the left half solution domain is displayed.

Stream Function and Temperature Contours

Figure 5.1 shows the stream function contour of these three runs. In each contour map, the left border is the heated wall(x=0), and the right one the central line (x=0.5). It therefore can be deduced that the flow direction is clockwise. The contour heights in each contour map are of equal interval. Therefore the fluid velocity may be inferred from the spacing of the contour lines. It can be seen that at $Ra^*=10^6$ the stream lines are relatively evenly spaced over the domain. As the Ra^* is increased, the stream lines become denser in the border regions at the expense of the bulk area. This change in the distribution the stream lines indicates that fluid motions are more confined to the border regions. This is expected since the driving buoyancy force becomes more dominant over the viscous force as the Ra^* is increased. At $Ra^*=10^8$, a secondary loop is observed within the primary one. Figure 5.2 shows the vertical velocity profile of the three runs at the middle plane (z=0.5). It can be seen that the maximum velocity of the boundary layer and core region increase steadily as the Ra^* is increased. From $Ra^*=10^6$ to 10^7, the velocities have risen by about a factor of 3 and doubled from $Ra^*=10^7$ to 10^8. A common feature may be noticed that the maximum velocity of the core flow is about 40% higher than that of the boundary layer.

The corresponding temperature contours of above steady state flows are given in Fig. 5.3. A thin layer with a large temperature gradient is observed just beneath the surface in all three contours. As the Ra^* is increased, it becomes progressively thinner with a larger temperature gradient; meanwhile the bulk liquid becomes more homogeneous. These features can also be seen in the temperature profiles at x=0.25 shown in Fig. 5.4.

The existence of this thin surface layer (with upward temperature gradient) is determined by the presence of an isothermal surface. In steady state, all the heat absorbed by the liquid is removed at the surface. The presence of a large temperature gradient is therefore necessary to transfer heat to the surface. As the input heat is increased, a larger temperature gradient is required at the surface, and the surface layer will generally become thinner. This surface layer will be studied in more detail below.

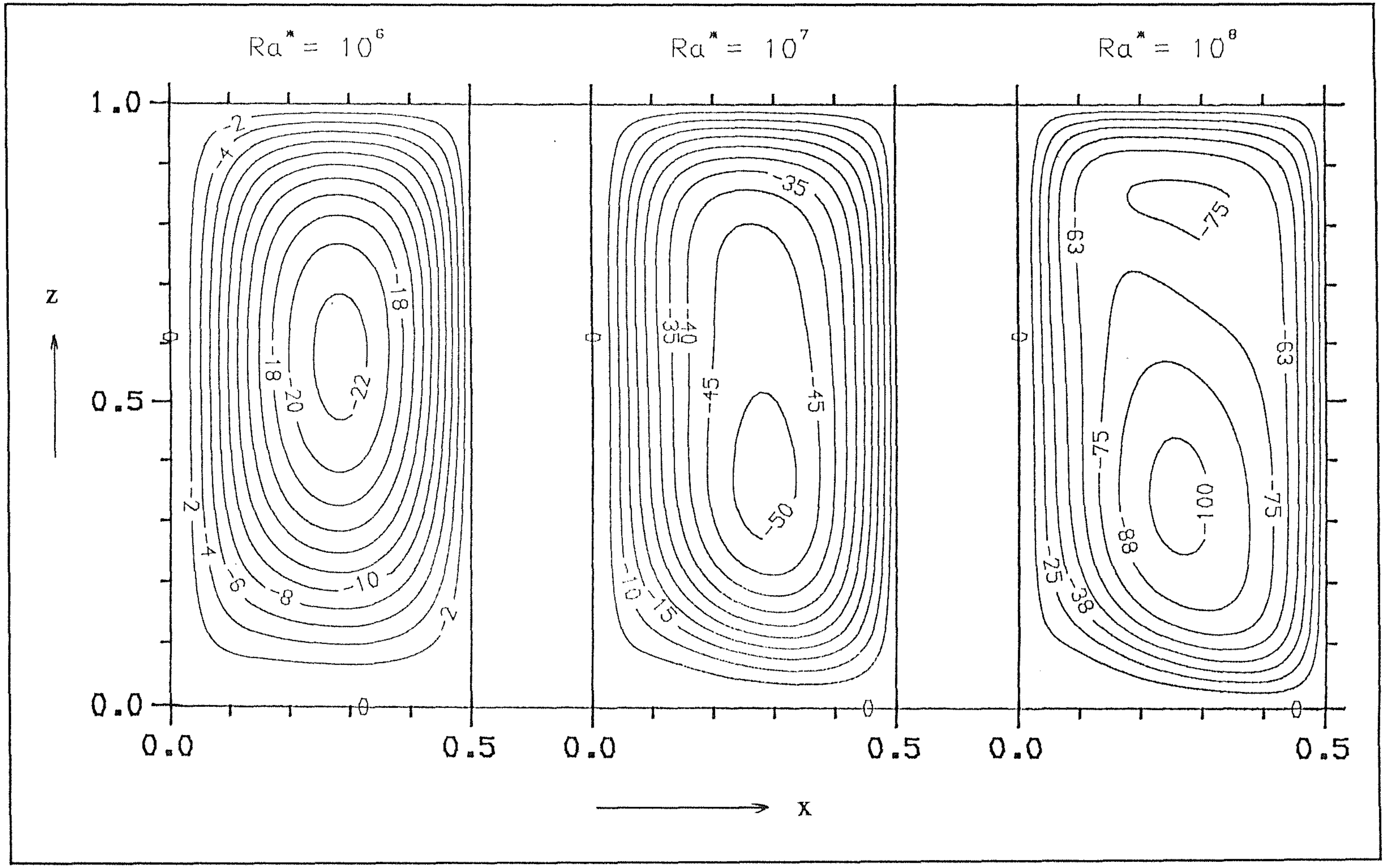

Fig. 5.1 Stream function contour maps. x=0.0, the heated wall; x=0.5, the central line; z=0.0, base; z=1.0, the isothermal free surface.

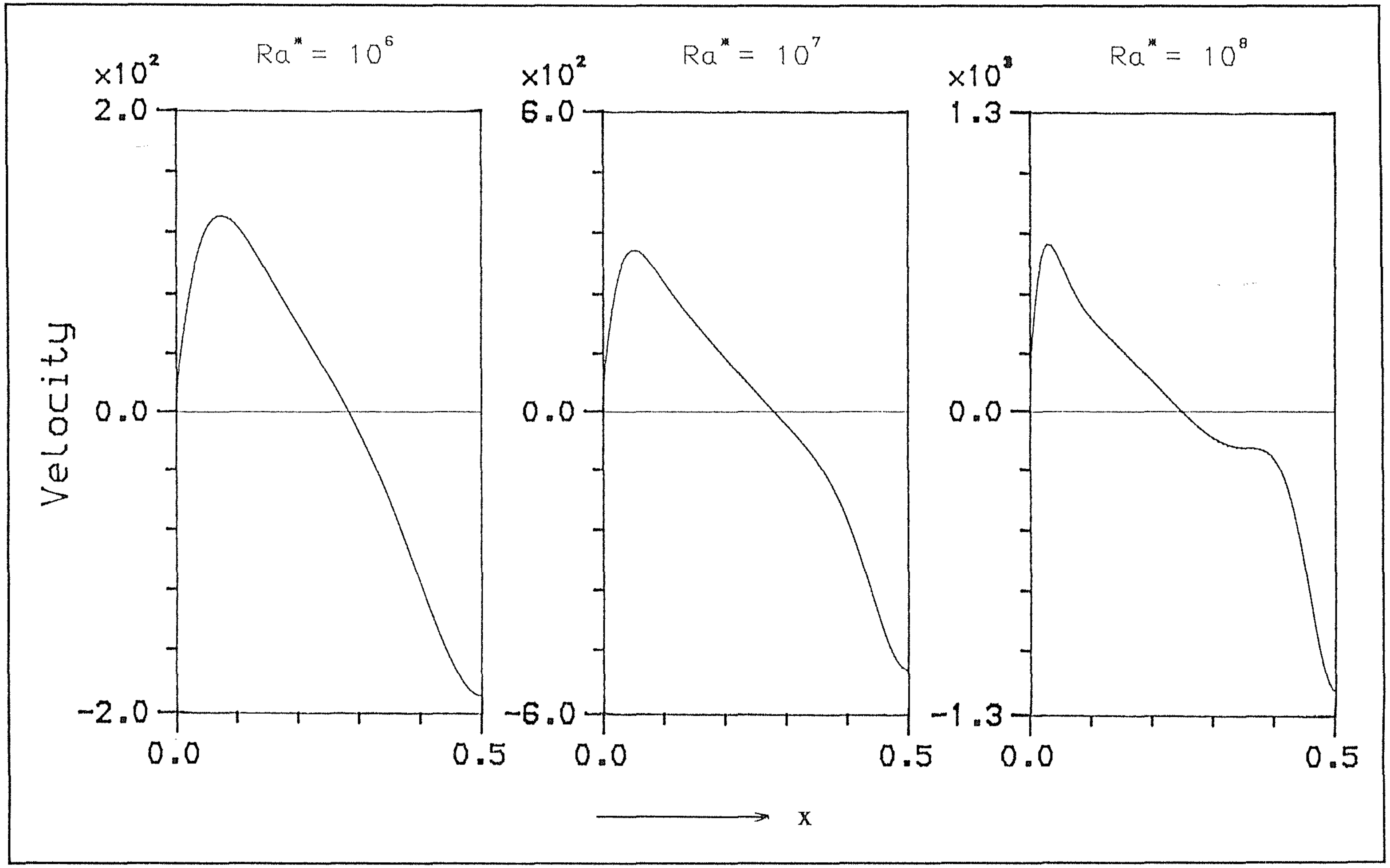

Fig. 5.2 Vertical velocity profiles at $z=0.5$. $x=0.0$, the heated wall; $x=0.5$, the central line.

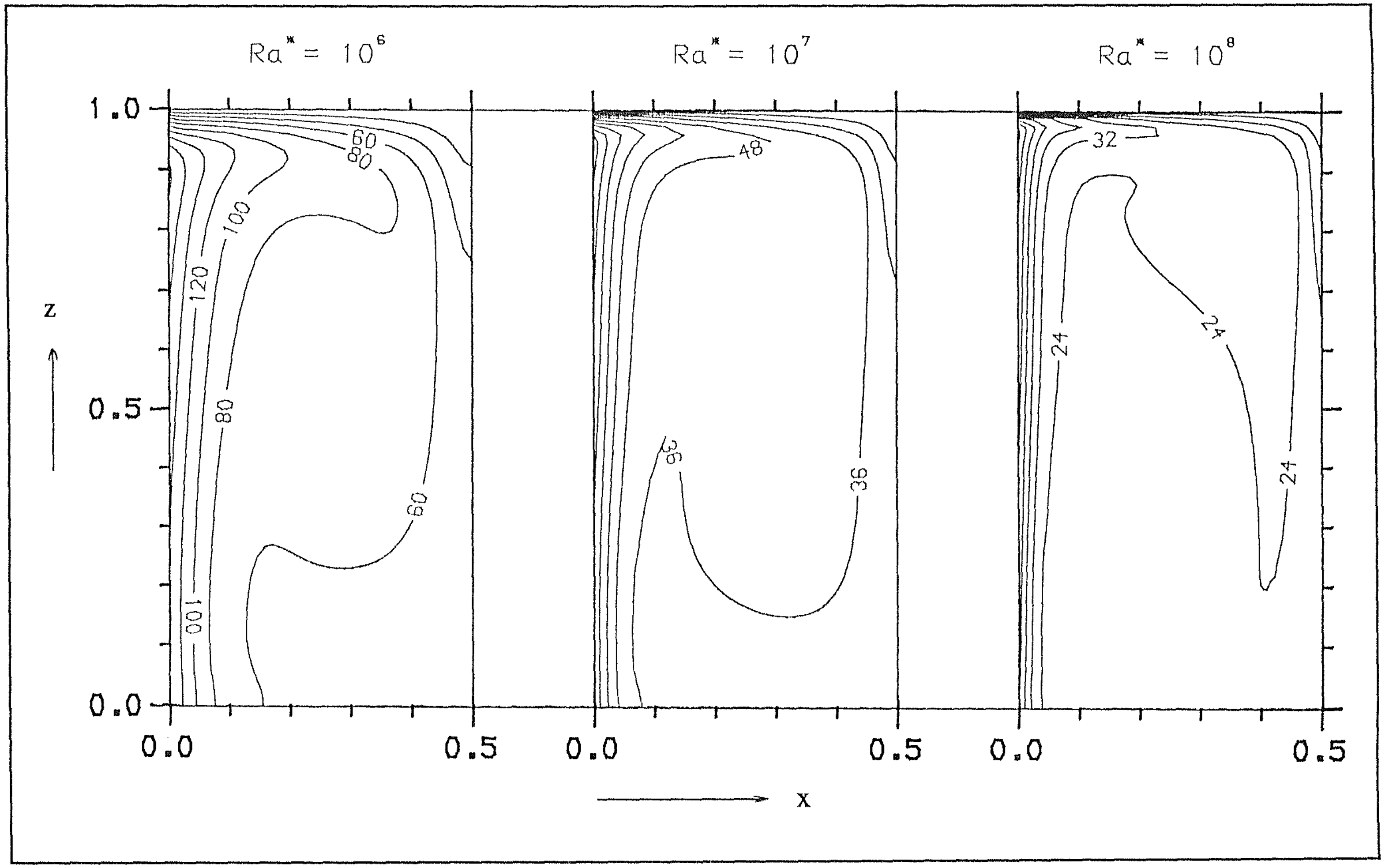

Fig. 5.3 Temperature contour maps. x=0.0, the heated wall; x=0.5, the central line; z=0.0, base; z=1.0, the isothermal free surface.

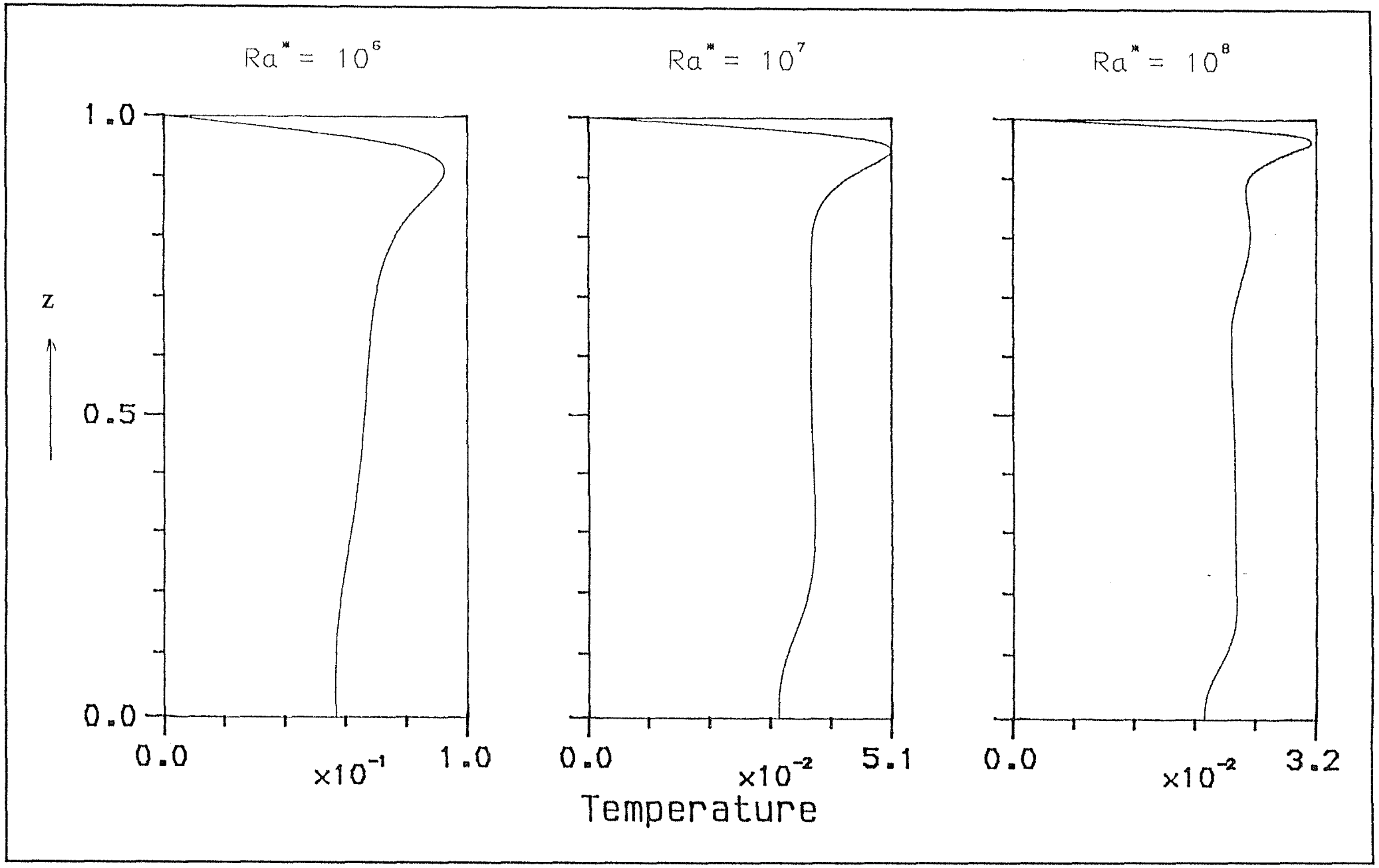

Fig. 5.4 Temperature profiles at x=0.25 taken from Fig. 5.3.

The Surface Layer

Figure 5.5a shows the vertical temperature profile at four locations evenly placed across the (half) domain. It can be seen that the temperature gradient of the surface layer becomes less pronounced towards the central line. This is expected: since a hot surface flow will continuously lose heat as it moves across the surface, the greatest temperature gradient thus will occur where the hot boundary layer flow meets the surface.

A close look of this surface layer reveals that immediately beneath the surface there is a very thin sub-layer of less than 1% of the height of the cavity with almost linear temperature gradients, as shown in Fig. 5.5b.

The existence of such a sub-layer at the surface is in agreement with the temperature measurements carried out by Beduz et al[14] for a deep pool of liquid nitrogen in steady state conditions. (The exact Ra^* is not given, but it is believed to be of the order of 10^{11}). A thin layer 0.3mm thick with a liner temperature gradient of order of 5000K/m has been found just beneath the surface. A temperature gradient of this order is required for heat transfer to the surface, where evaporation takes place.

Surface Heat Flux vs Bulk Superheat

The bulk superheat is defined as $\Delta T_b = T_b - T_0$, where T_b is the bulk liquid temperature and T_0 the surface temperature. Since $T_0 = 0$ (assumed), $\Delta T_b = T_b$. We define the bulk liquid temperature T_b as the average over the region from $x=0.1$ to 0.4 and from $z=0.1$ to 0.9 (so that the border regions are excluded). The ΔT_b values for the above three flows are given in Table 5.2. In steady state with $\eta=1$, the surface heat flux $\dot{q}_s$ is twice of the wall heat flux $\dot{q}$.

According to Heshemi & Wesson[9], the variation of the surface heat flux with bulk superheat should follow the 4/3 power law. Plotted in an arbitrary (log-log) scale, the numerical predictions are shown in Fig. 5.6. The fitted straight line (for Ra^* in the range between 10^6 and 10^8) may be expressed as

$$\dot{q}_s = 744 \text{ x } \Delta T^{4/3} \qquad W/m^2.$$

This is in good agreement with the expression calculated from HW model(using properties of liquid nitrogen at the normal boiling point),

$$\dot{q}_s = 724 \text{ x } \Delta T^{4/3} \qquad W/m^2.$$

However, some elements of coincidence can not be ruled out due the somewhat arbitrary way used for calculating the bulk liquid temperature.

Table 5.2 Bulk superheats in steady state

Ra^*		10^6	10^7	10^8
$\dot{q}$ (x C_1)	W/m^2	1	10	100
ΔT_b (x C_2)	K	6.9	38	240

where $C_1 = k(\alpha\nu/g\beta_T)d^{-4}x10^6$, $C_2 = (\alpha\nu/g\beta_T)d^{-3}x10^4$ and d is the liquid depth.

5.2.2 Convective Flows With an Adiabatic Surface

The convective flows discussed above are bounded by an isothermal surface. In this section convective flows with an adiabatic free surface is considered. It will be seen that the interface separating two stratified layers closely resembles an adiabatic one. The study of flows with an adiabatic surface therefore will be helpful in understanding the flow development in the lower layer of a two-layer system. A numerical run has been performed on the same flow configuration as before with $Ra^*=10^7$, except now the surface is adiabatic. The evolution of the flow in this run are shown in Figures 5.7, 5.8 and 5.9.

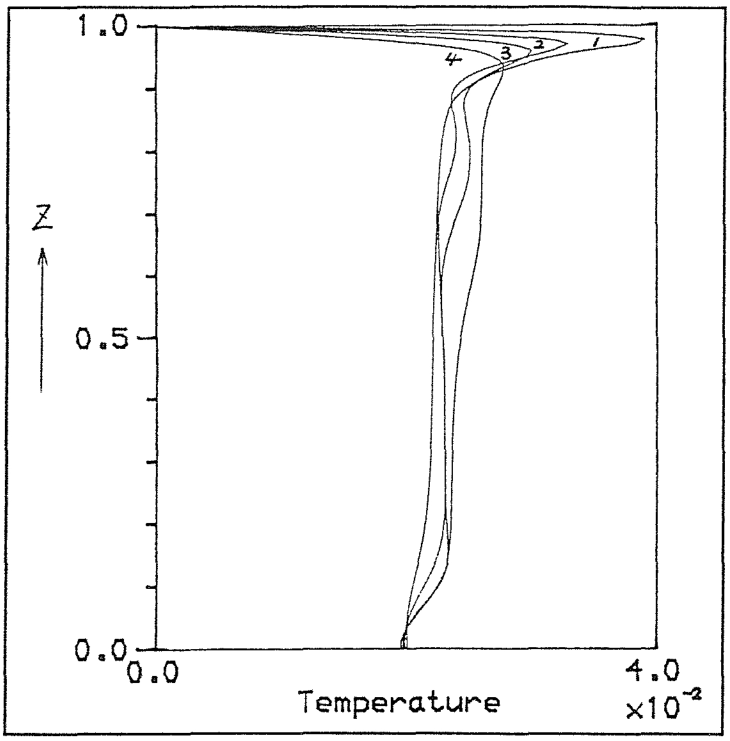

Fig. 5.5a Temperature profile at four locations ($Ra^*=10^8$);
1: x=0.1; 2: x=0.2; 3: x=0.3; 4: x=0.4.

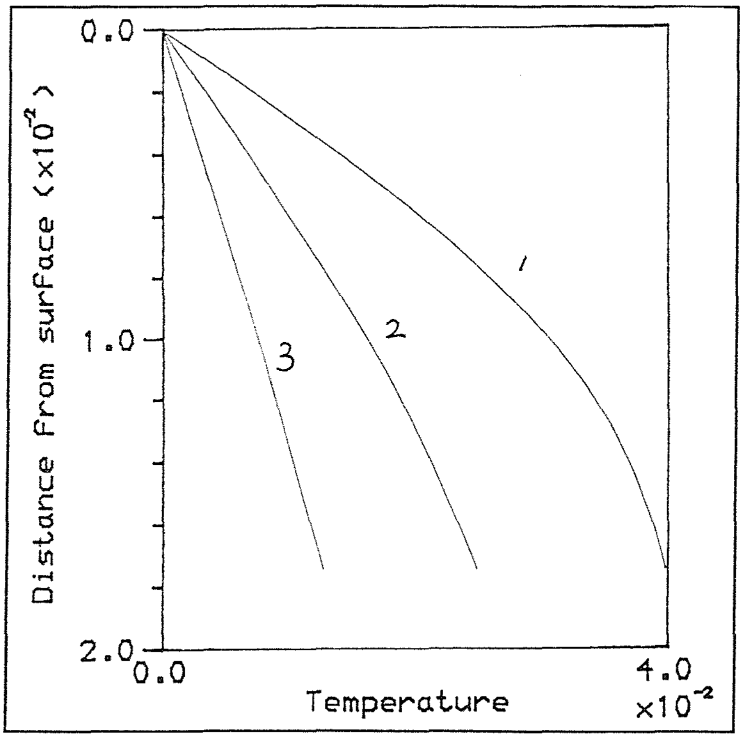

Fig. 5.5b Linear temperature profile of the surface layer ($Ra^*=10^8$);
1: x=0.092; 2: x=0.24; 3: x=0.407.

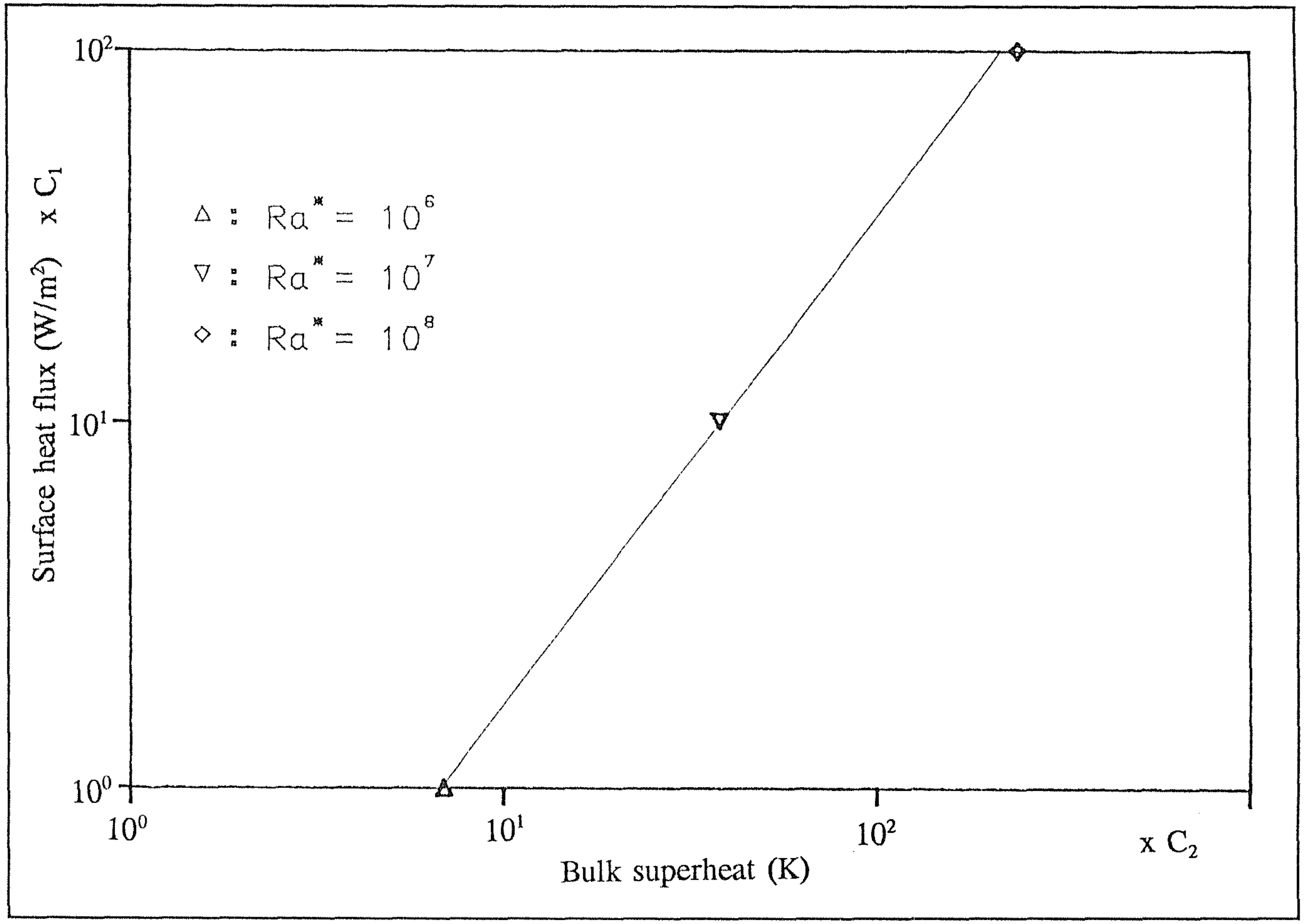

Fig. 5.6 The model predictions plotted in an arbitrary (log-log) scale to fit the 4/3 power dependence of the surface heat flux on the bulk superheat in liquid nitrogen.

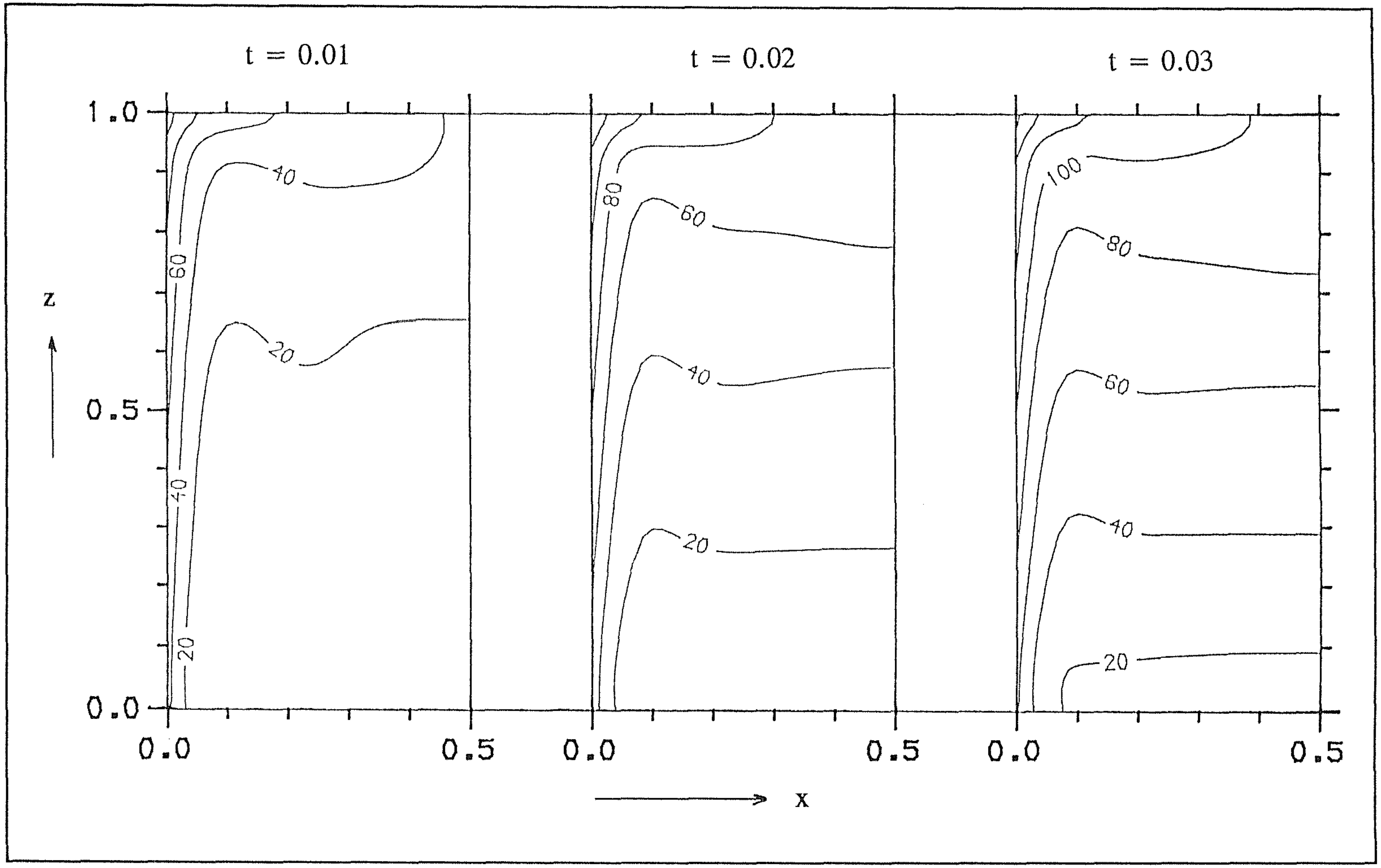

Fig. 5.7 Temperature contour maps ($Ra^*=10^7$). x=0.0, the heated wall; x=0.5, the central line; z=0.0, base; z=1.0, the adiabatic free surface.

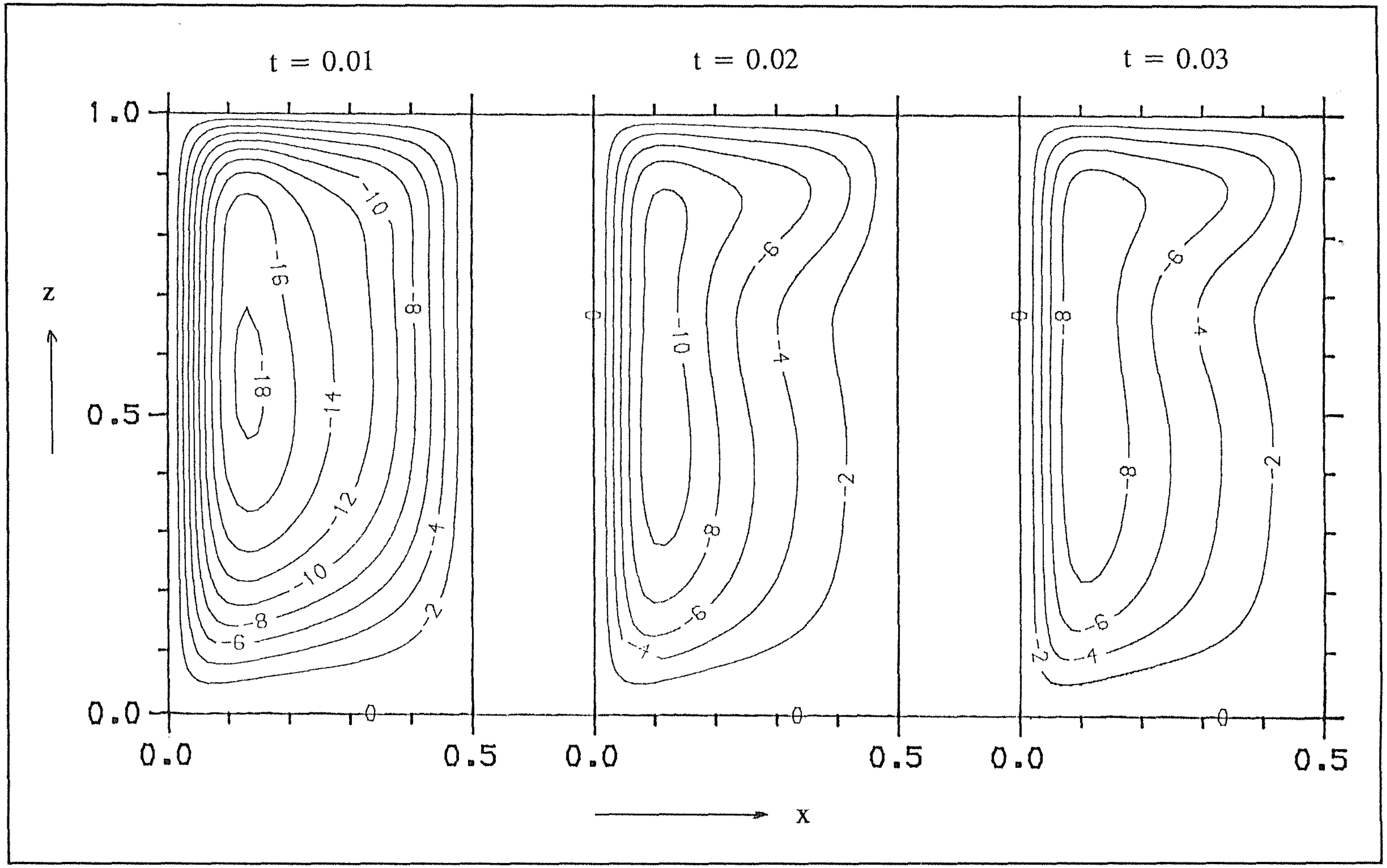

Fig. 5.8 Stream function contour maps ($Ra^*=10^7$). x=0.0, the heated wall; x=0.5, the central line; z=0.0, base; z=1.0, the adiabatic free surface.

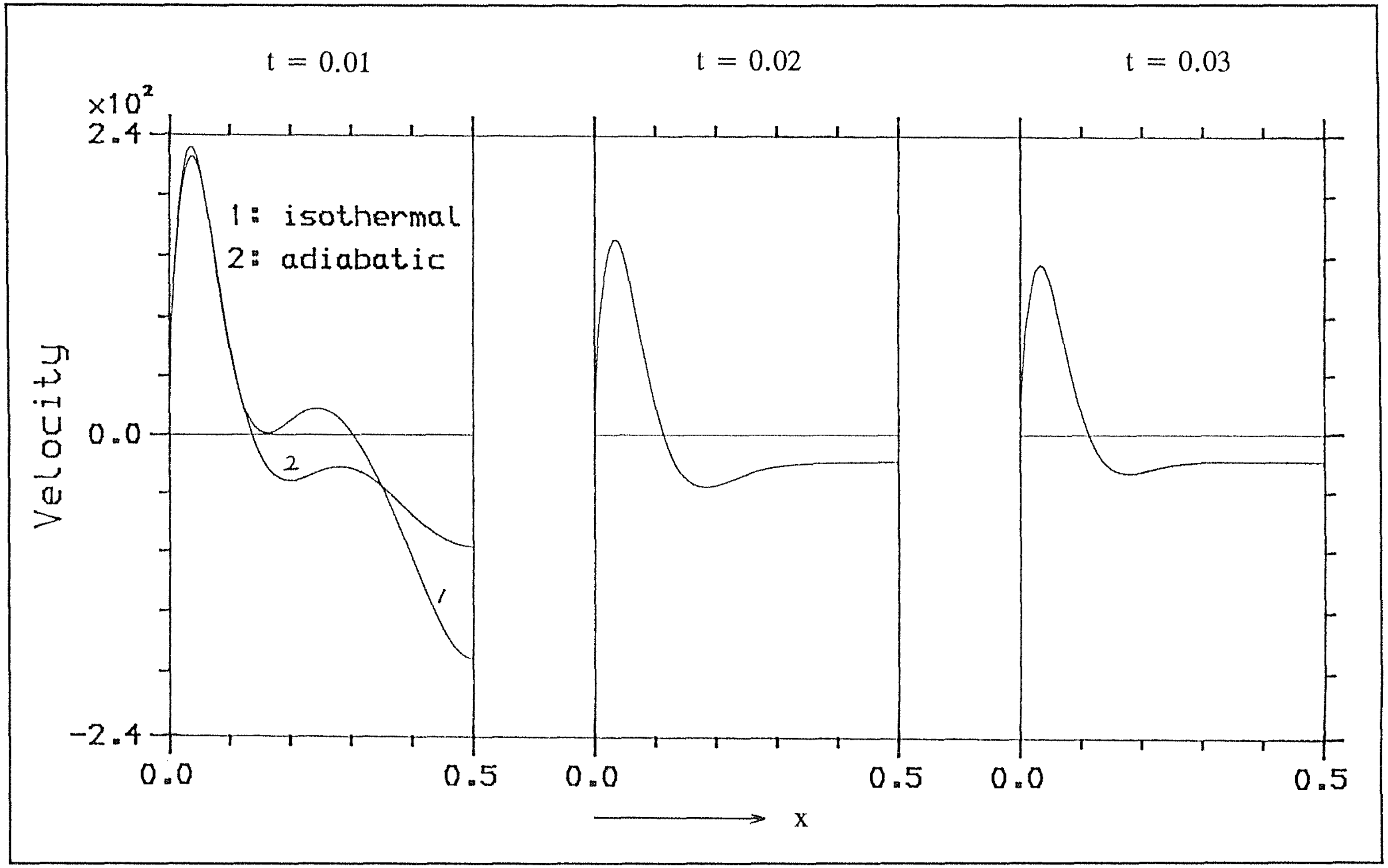

Fig. 5.9 Vertical velocity profiles at z=0.5 ($Ra^*=10^7$). x=0.0, the heated wall; x=0.5, the central line.

Figure 5.7 illustrates the temperature contour at three times. An adiabatic surface means that, in contrast to an isothermal one, there is no heat transfer at the surface. The whole body of the liquid therefore will become increasingly warmer as time goes on, and the highest temperatures(apart from in the heated wall regions) will be at the surface. These are clearly shown in the temperature contours in Fig. 5.7. Perhaps the most striking feature is that the temperature gradient in the bulk liquid is nearly linear, similar to the case of heat conduction.

Figure 5.8 shows the corresponding stream function contours. It can be seen that in all three contours the stream lines are much closer in the wall region than in the bulk and core region. This means the (vertical) fluid velocity of the boundary layer is much higher. At $t=0.02$, a substantial reduction in the strength of the convective loop is observed. These features may be seen more clearly in the vertical velocity profiles given in Fig. 5.9. The substantial reduction in the velocity from $t=0.01$ to $t=0.02$ may be explained by referring back to the temperature contours in Fig. 5.7. In this figure we can see that the temperature gradient of the liquid has increased substantially in the same period. Since the temperature is higher closer to the surface, the stratification is stable, and therefore there is a retarding force on the convective flow. When the temperature gradient of the liquid is increased, so is this retarding force. Consequently the velocity of the convective flow would be reduced.

Back to Fig. 5.9, velocity profile No. 1 $t=0.01$ is obtained with an isothermal surface, otherwise it is exactly the same as the adiabatic profile No. 2. Although the velocity distribution in the boundary layer are almost the same, the core flow of the adiabatic velocity profile is much less pronounced than that of the isothermal one. Further more, at $t=0.02$, the core flow, characterised by a jet-shaped velocity profile, has completely disappeared from the velocity profile (at $z=0.5$). It has been shown in chapter 4 that the cooling effect of an isothermal surface can induce a positive temperature gradient within the core flow (see Fig. 4.5). In contrast, the temperature of an adiabatic surface is higher than the liquid below. Consequently the temperature gradient of the core flow will be exactly the opposite to the one in Fig. 4.5, i.e., temperature decreases away from the central line. Clearly such a temperature gradient would generate a buoyant force which acts against and thus would slow down the core flow.

It can be seen from the stream function contours in Fig. 5.8 that the flow pattern appears almost unchanged after t=0.02. For laminar flows with an isothermal surface, a steady state will eventually be reached, in which all the heat absorbed by the liquid is removed at the surface. Since there is no heat loss at an adiabatic surface, the temperature of the liquid will increase steadily as time passes by. After some time, the flow is in a quasi-steady state. In this state the temperature gradient will increase gradually while the velocity will decrease slowly; but the patterns of the velocity and temperature distribution will remain almost unchanged.

5.3 Two-Component Model

5.3.1 Fluid Media & Initial Conditions

Numerical simulations were performed on a LIN/LOX two-layer system. LIN/LOX were used by Agbabi's[13] in his rollover simulation experiments. By applying the argument of fugacity and using the results of Krichevsky et al[31], it has been shown that LIN and LOX solution can be regarded as ideal. At very low concentrations, which is the case here, the diffusivity of LOX in LIN α_S may be calculated using Wilke & Chang's equation, which yields $\alpha_S = 2.74\text{x}10^{-9}\ m^2/s$. Two other equations are also available[32][33], giving α_S $2.16\text{x}10^{-9}$ and $2.79\text{x}10^{-9}$ respectively. Here the value $2.74\text{x}10^{-9}$ has been chosen for α_S. Consequently the diffusivity ratio $\tau = \alpha/\alpha_S = 0.0325$.

All variables were set to zero except the concentration of LOX. The concentration profile was stepwise across the interface; the concentration was zero in the upper layer, with a step jump to a finite value in the lower layer. The depth of the two layers were equal.

5.3.2 The Quasi-Adiabatic Nature of the Interface

In the two-layer system defined above, the upper layer is bounded(at the top) by an isothermal free surface and the lower layer by the interface. At the isothermal surface, there exists a thin surface layer with a larger temperature gradient. The interface temperature, in contrast to the surface, is free to vary when the temperature of the adjacent liquid changes. Therefore the build up of any sizable temperature gradient is prevented. In addition the heat conductivity of LIN is poor, and so the interface is very close to adiabatic with a relatively small heat flow across it.

5.3.3 Results and Discussion

The results to be presented are from a numerical run with $Ra^*=10^7$, $Rs=3x10^6$ and $\eta=1$. (The density difference between the layers was less than 0.001%). In this run the symmetry of the flow was assumed about the central line of the solution domain (refer to Fig. 3.1); computation was carried out over the left half of solution domain.

In order to understand how two initially stratified layers are mixed up in a simulation run, a regular output of a set of data including all the parameters is necessary from the start of the run to the final state when the two layers are mixed and form one single layer. Each data set represents the state of the flow at the moment that data set is drawn. Therefore, from such a series of data sets, the evolution of the flow under study may be followed. The state of a flow represented by a set of data may be best illustrated by a set of contour maps of the representative parameters. A series of these sets of contour maps can be used to display the flow at different stages.

i) Contour Maps & Profiles

To illustrate the evolution of the flow under study, a time sequence of sets of contour maps is displayed in Fig. 5.10a-l. In every set there are four contours, each for a different parameter. They are, from left to right, temperature, LOX concentration, density and stream function. For each individual contour, the left boundary is the heated wall($x=0$) and the right one the central line($x=0.5$). The density is a function of the temperature and the concentration of solute(LOX). Assuming that the initial density of the top layer is zero (the reference point), then

$$\frac{\rho'}{\rho_0} \sim SRs - TRa^{*} \tag{5.1}$$

where S and T are the dimensionless concentration and temperature. The contour heights of the density contour are calculated as $S - T(Ra^{*}/Rs)$. It is thus perfectly normal if a negative contour height appears in the density contour map. It only states that the density is less than the reference value(zero). Contour heights in all the contours have been multiplied by an appropriate factor, 1000 for the temperature, concentration and density contours and 10 for the stream function contour, in order to be consistent in contour labelling. Figure 5.11 shows a time sequence of vertical profiles at $x=0.25$ of the temperature, concentration and density. Figure 5.12 illustrates the vertical velocity profiles in the two layers(when there are still two distinctive layers). The two profiles are chosen such that in the upper layer the central line velocity of the core flow reaches a maximum; and in the lower layer the velocity of the wall boundary layer reaches a maximum.

Set 1 (Fig. 5.10a) time = 0.005

The stream function contour

At $t=0.005$ the stream function contour shows clearly primary temperature driven convective loops(clockwise) in the upper and lower layers. The flow in the boundary layer of the lower layer is unable to overcome the density difference at the interface; it spreads inwardly after impinging on the interface. At the interface, there is a small loop(anti-clockwise) obviously driven by the viscose drag arising from the two opposing flows bounding the interface.

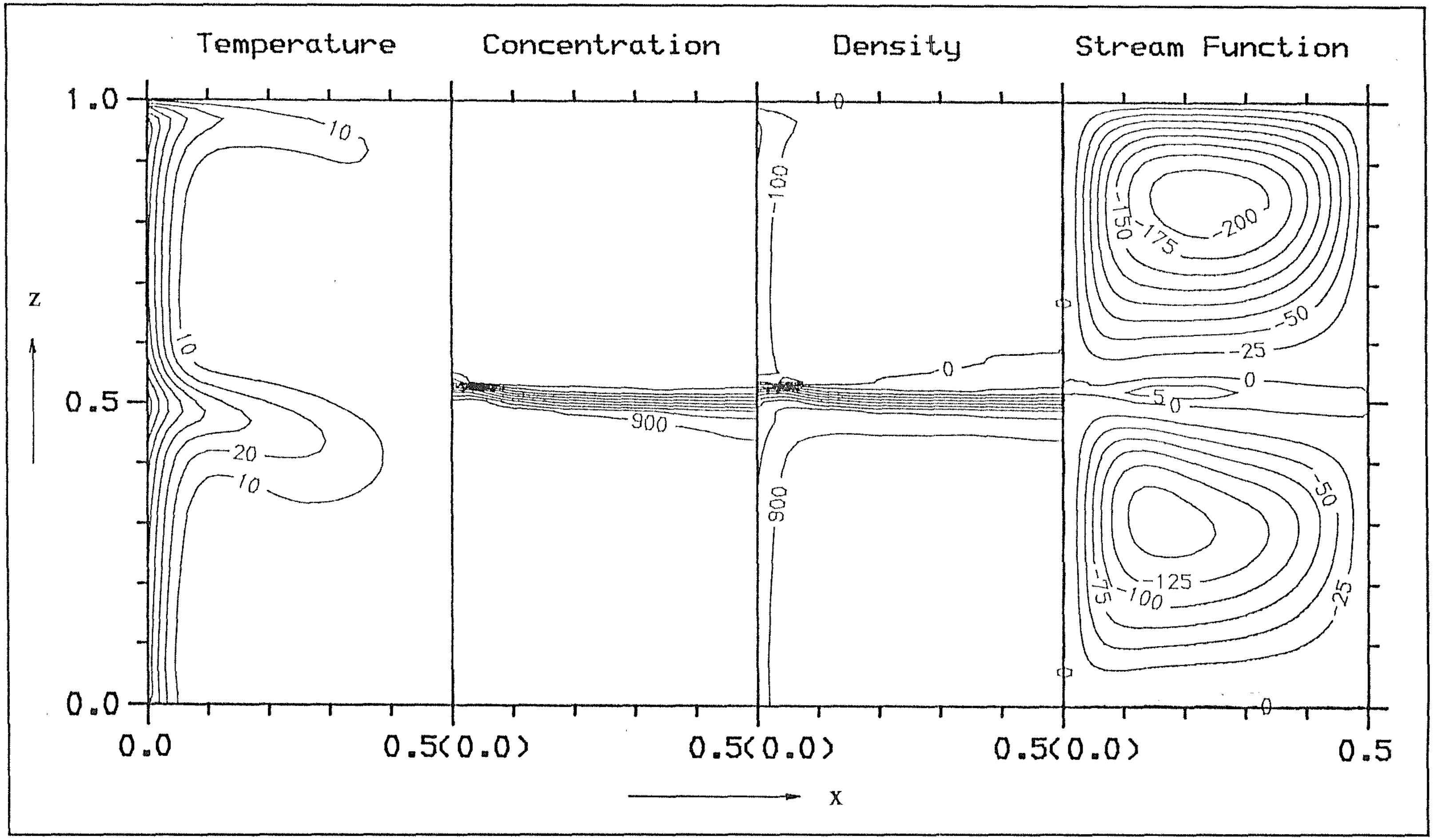

(a) set 1, time=0.005

Fig. 5.10(a-l) A time sequence of (12) contour sets of T, S, density and ψ showing the mixing process of two layers which are subject to uniform side heating only. x=0.0, the heated wall; x=0.5, the central line; z=0.0, base; z=1.0, the isothermal free surface.

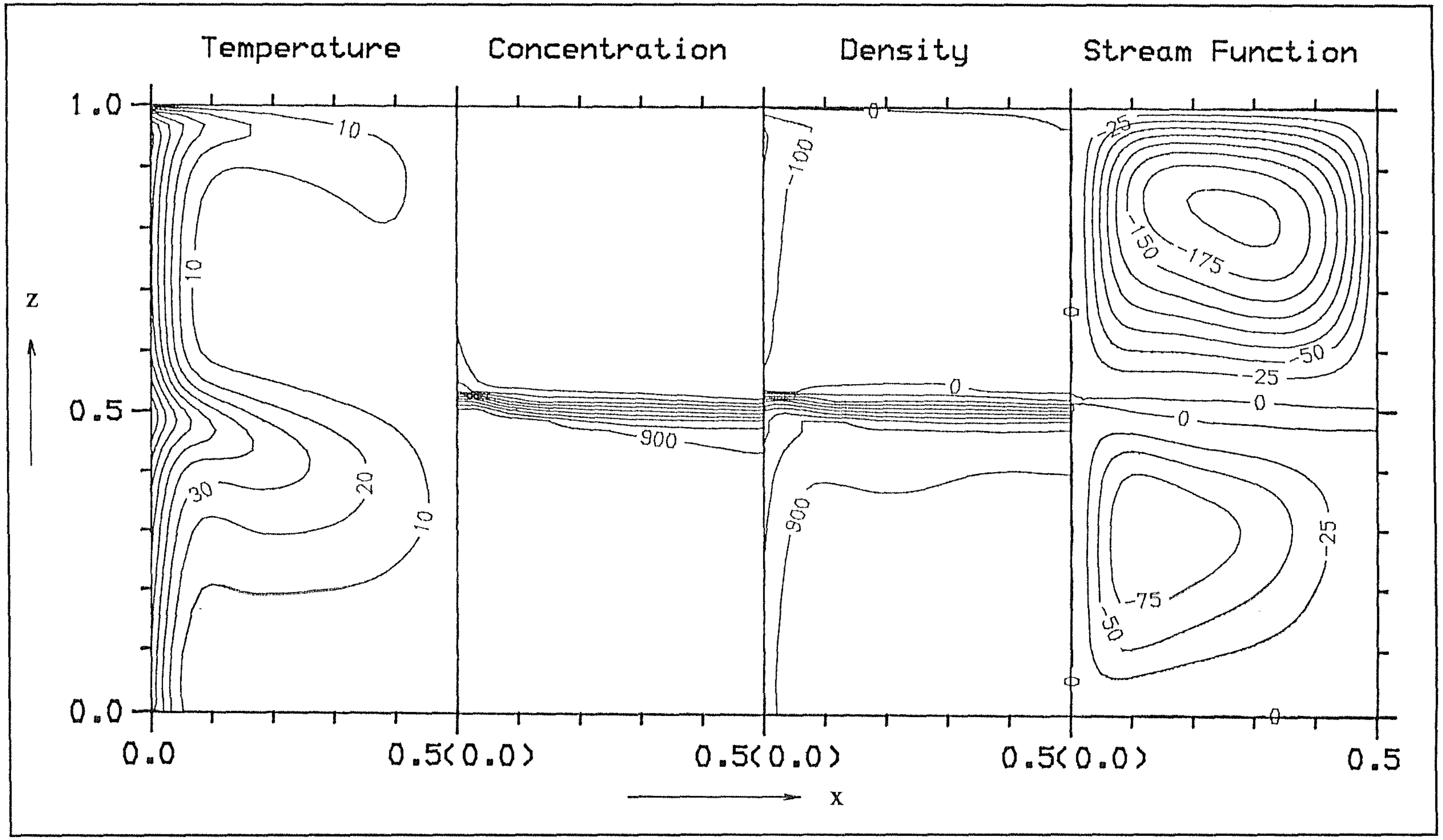

(b) set 2, time=0.01

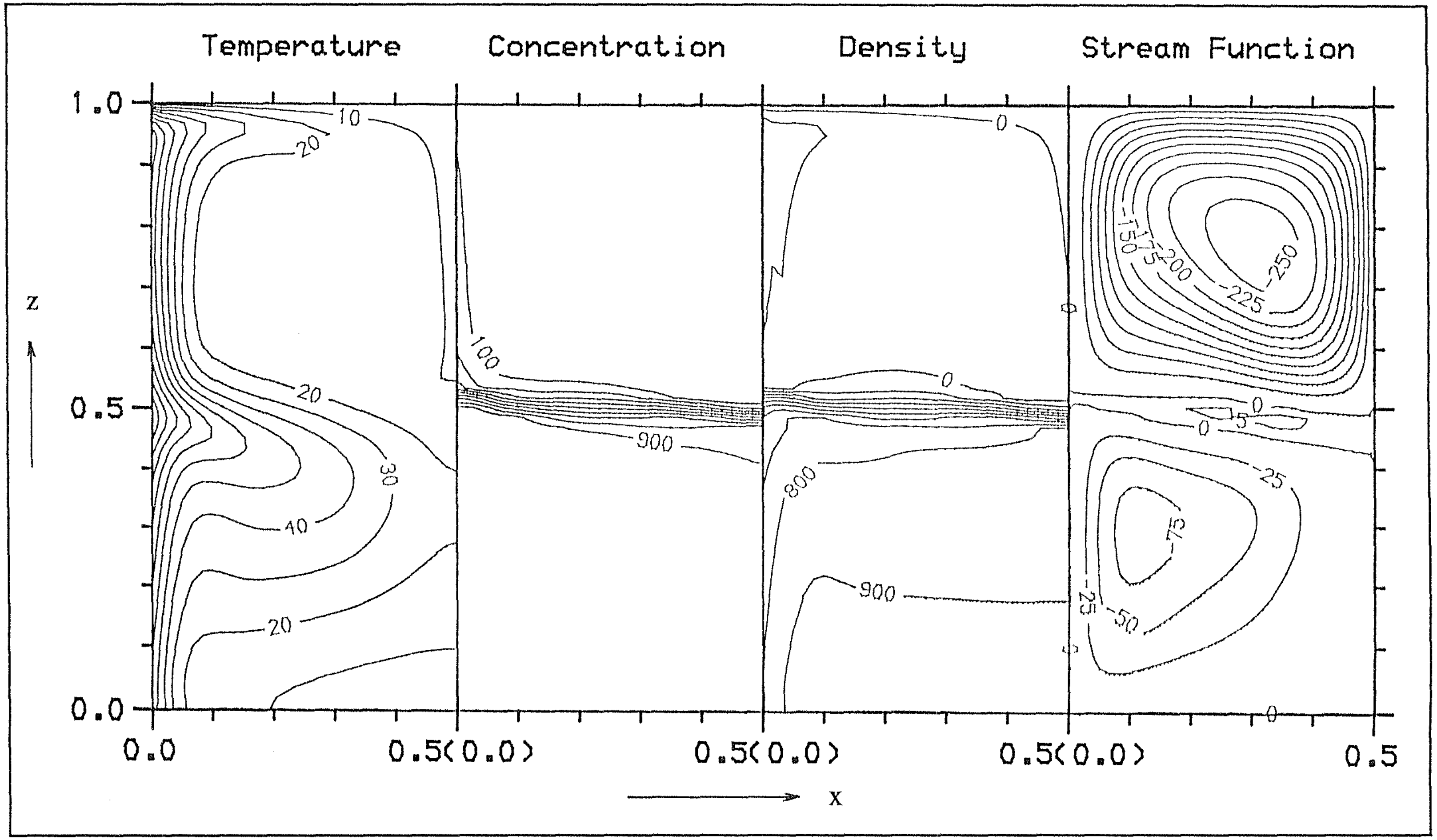

(c) set 3, time=0.02

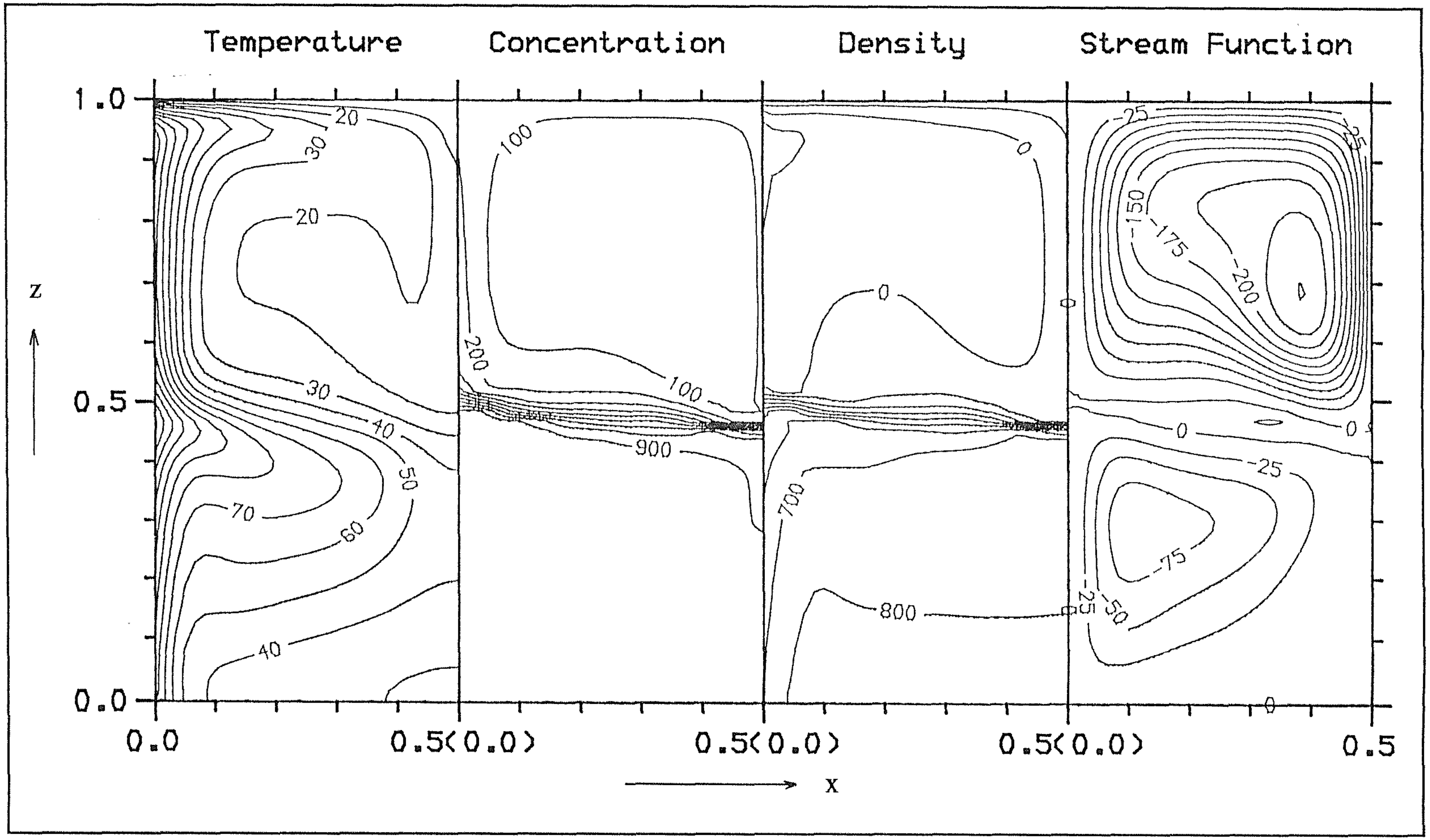

(d) set 4, time=0.04

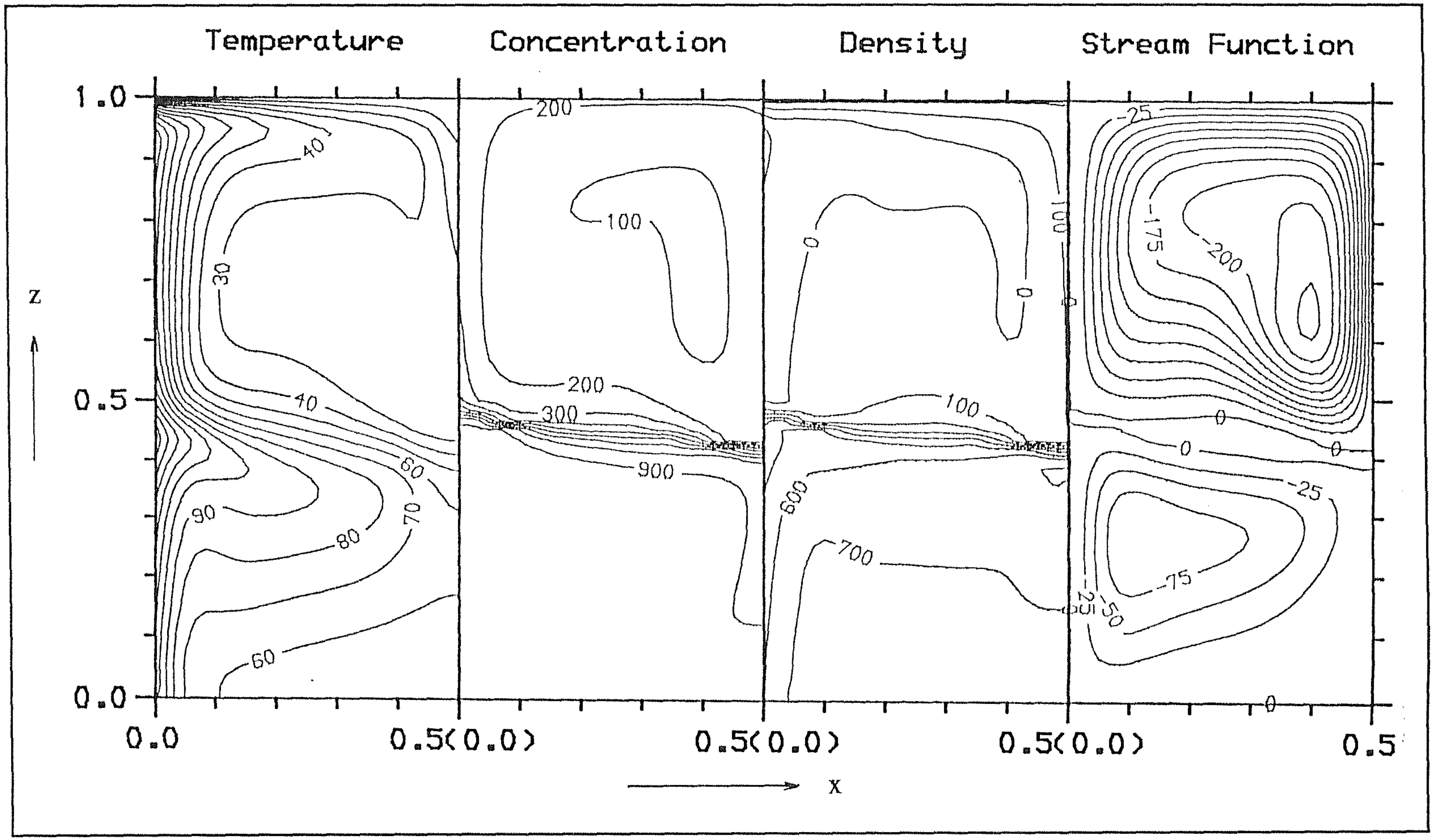

(e) set 5, time=0.06

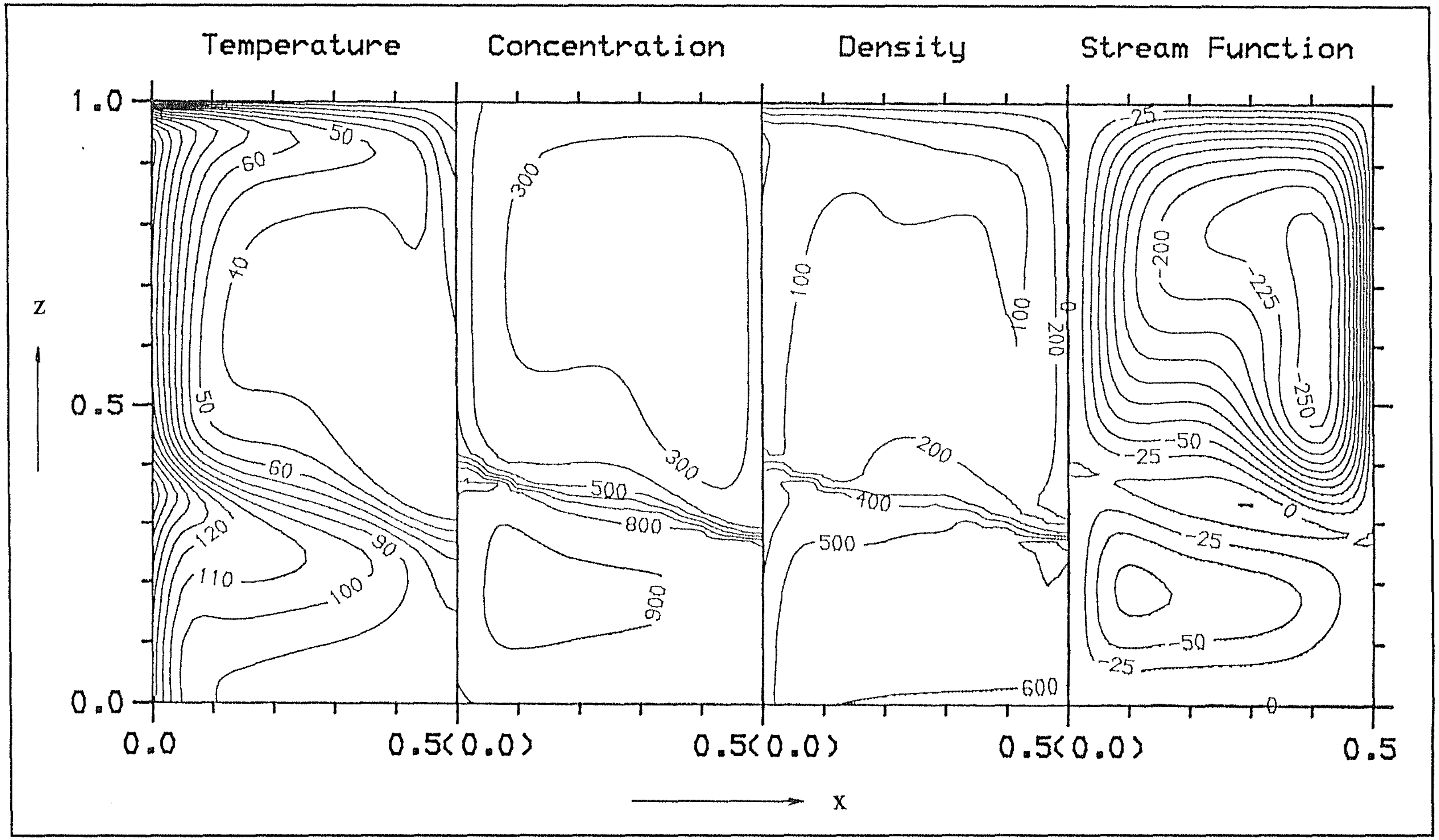

(f) set 6, time=0.10

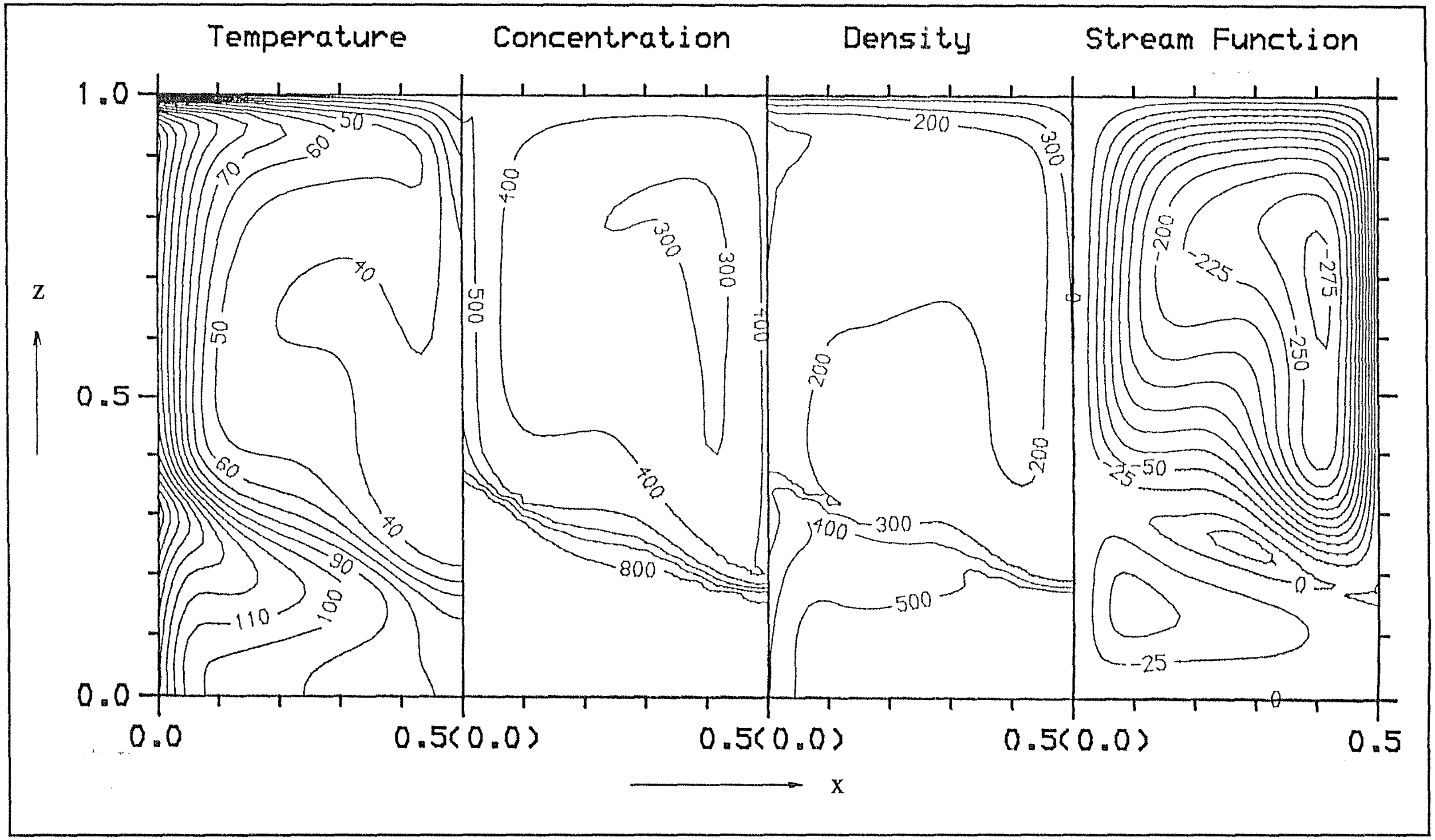

(g) set 7, time=0.12

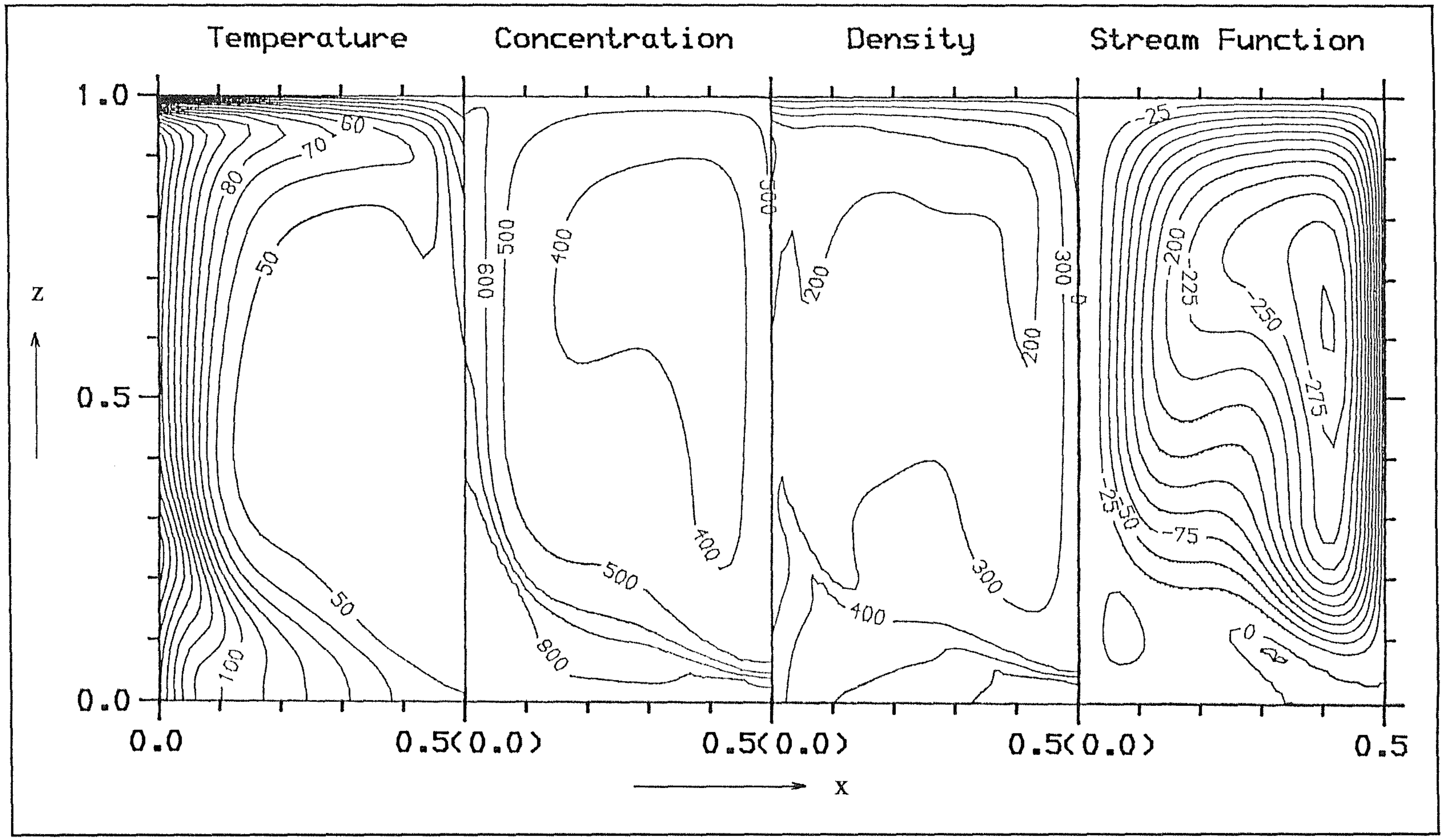

(h) set 8, time=0.14

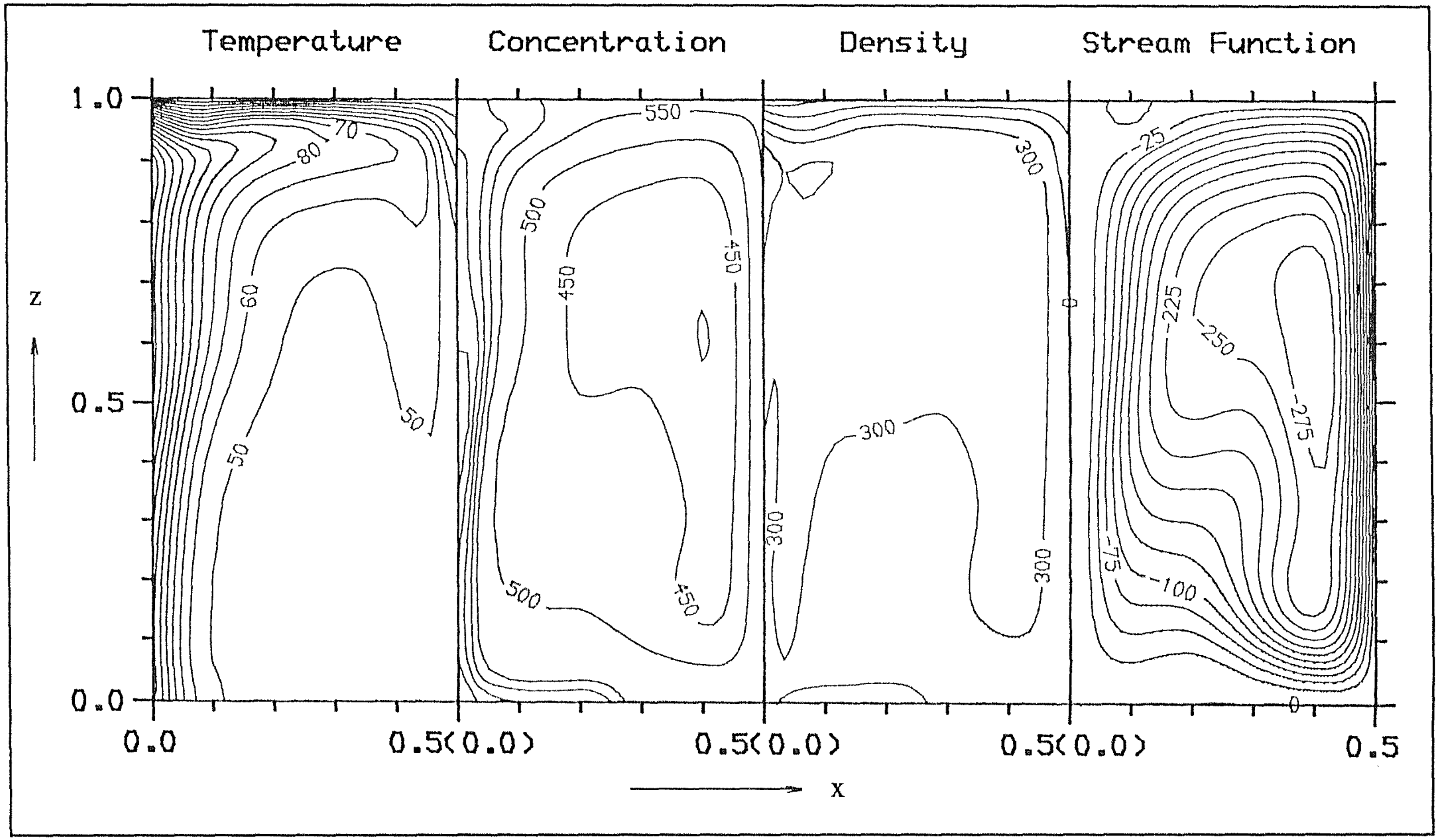

(i) set 9, time=0.16

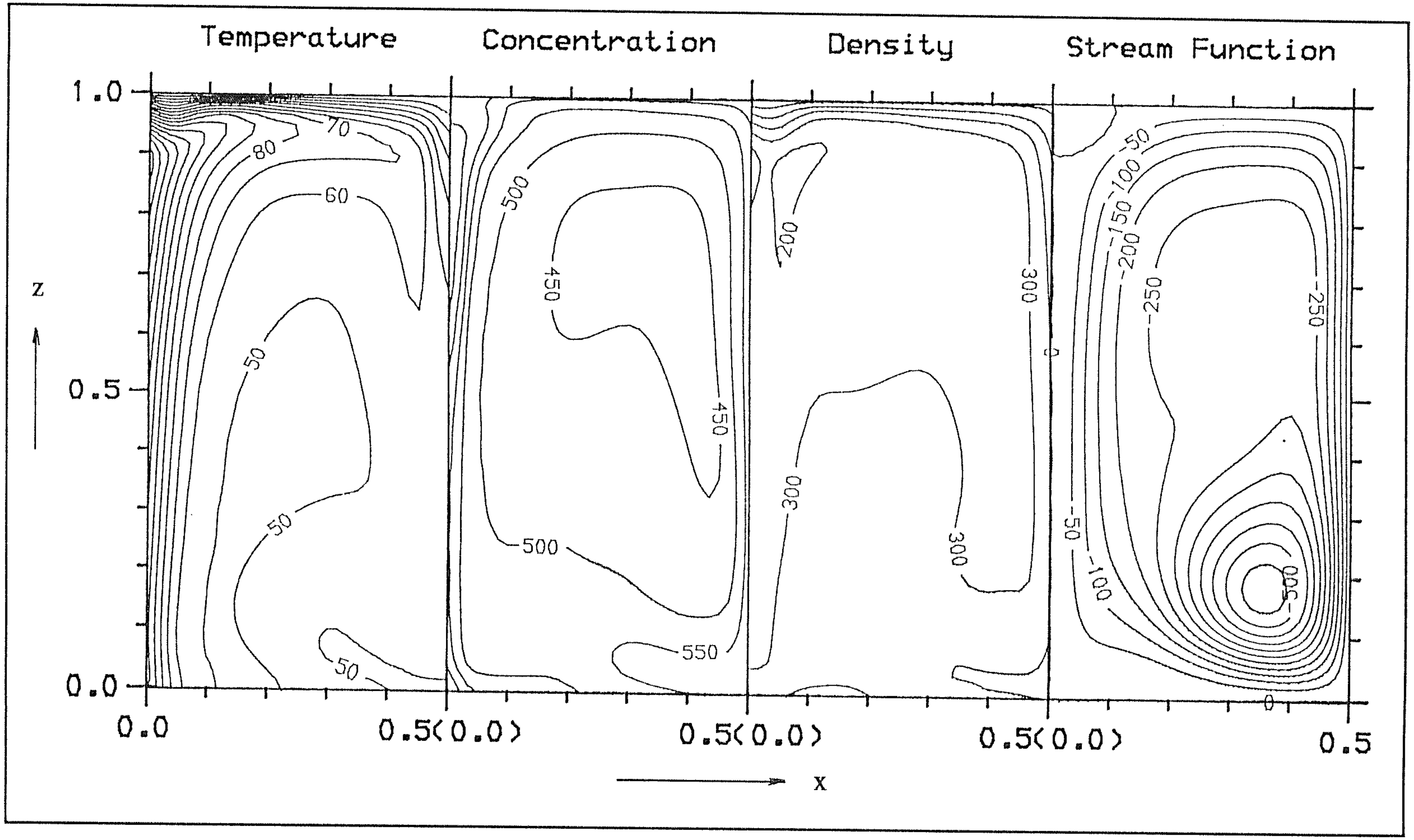

(j) set 10, time=0.165

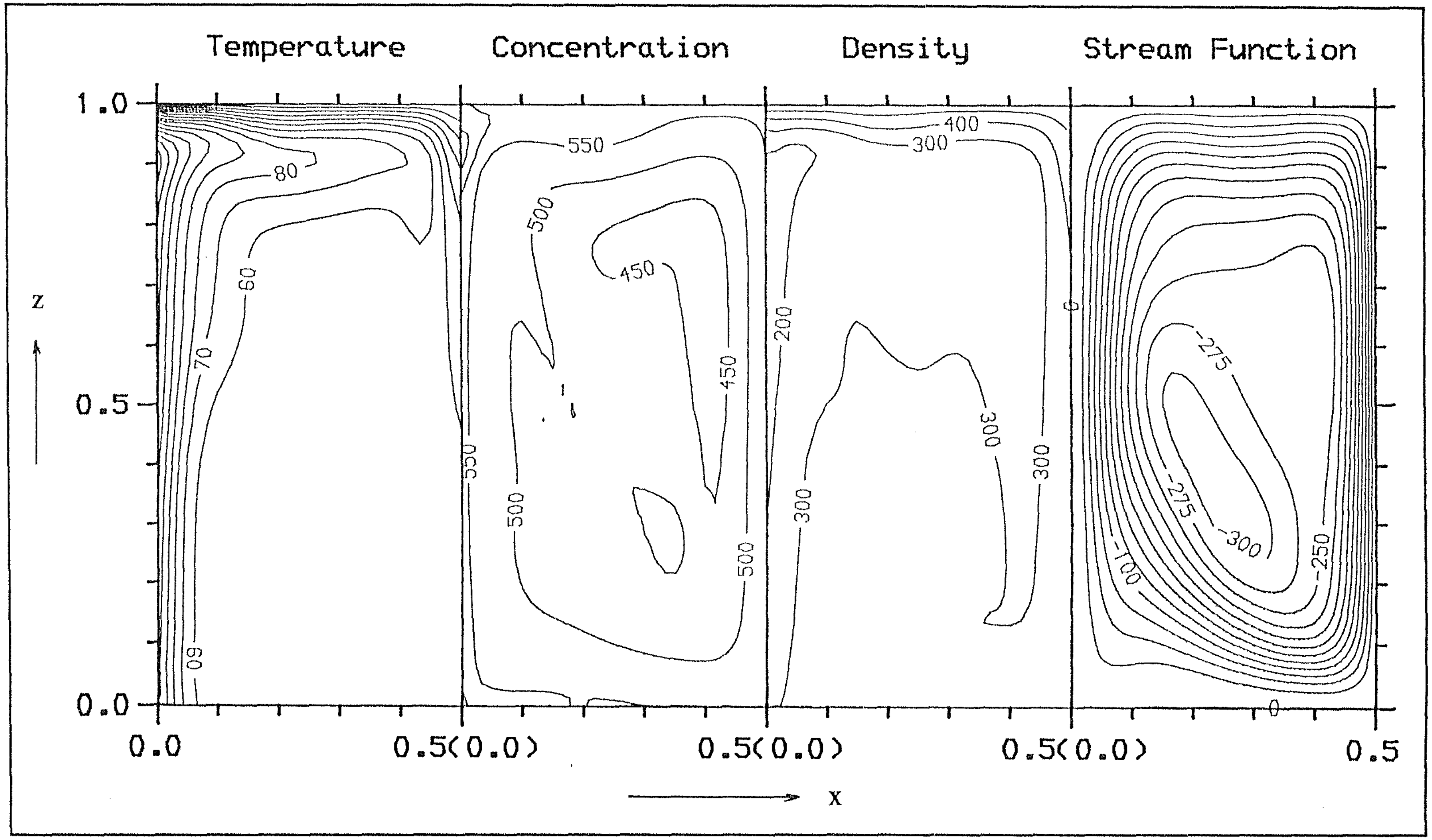

(k) set 11, time=0.17

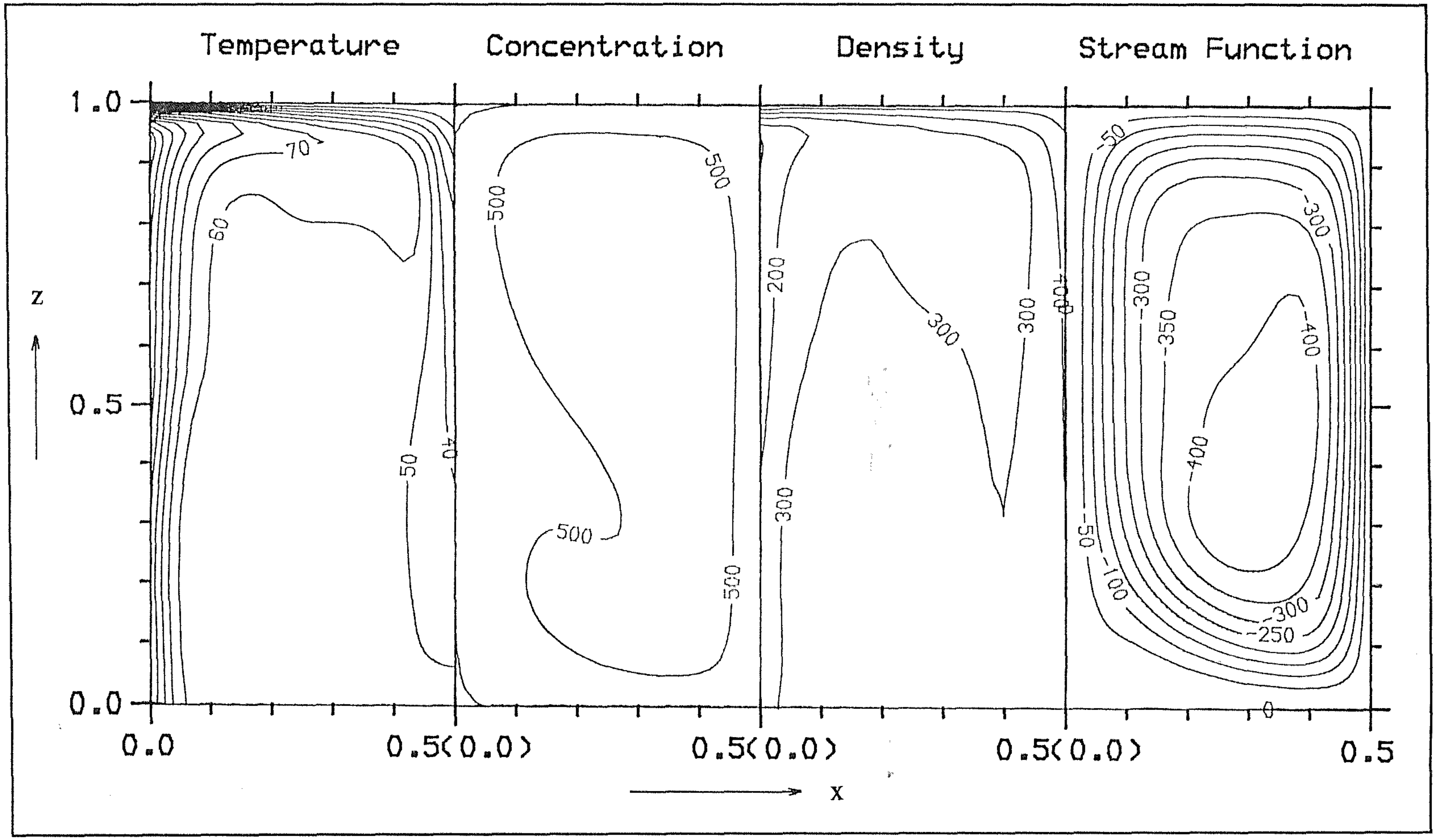

(l) set 12, time=0.175

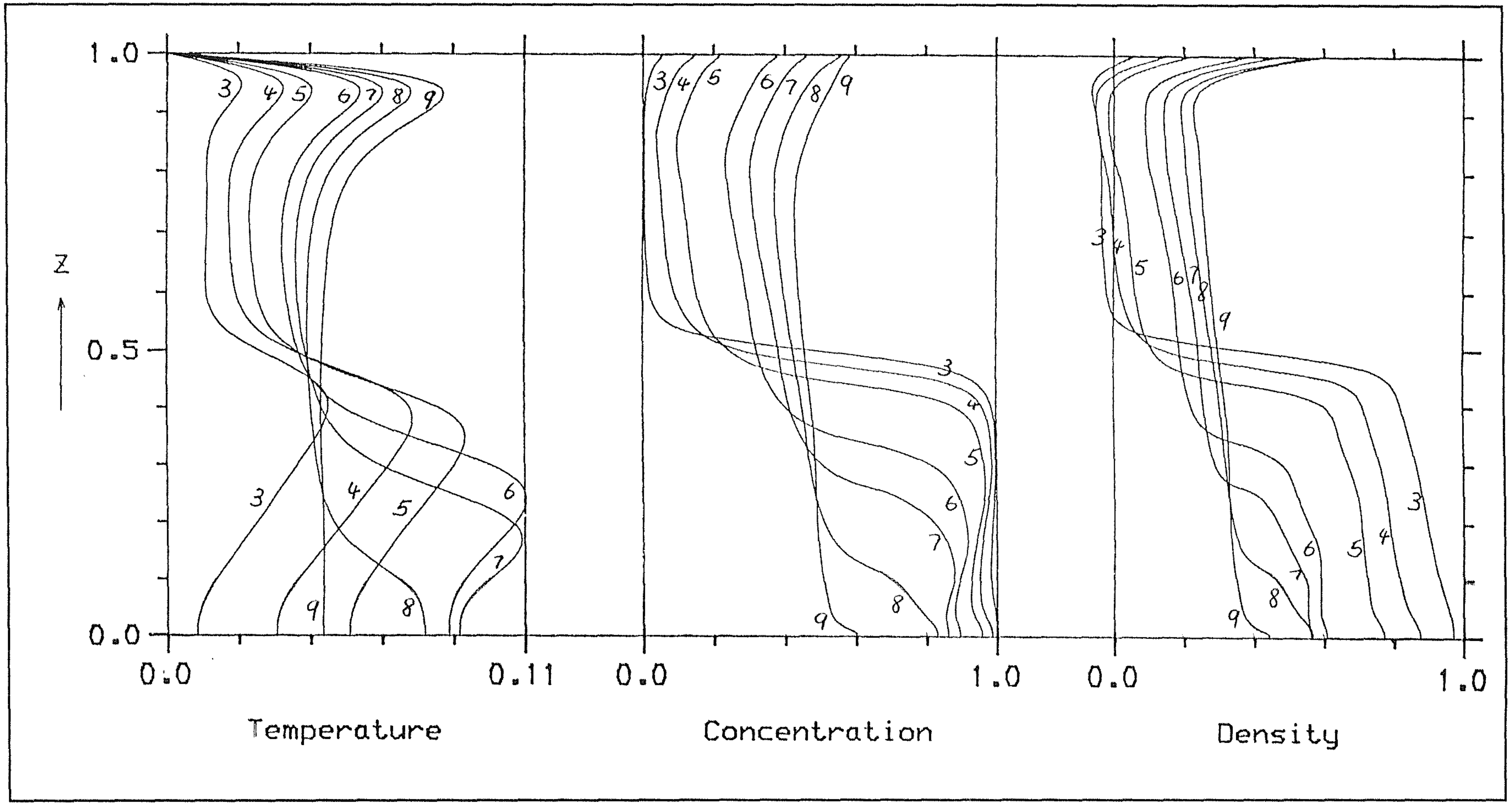

Fig. 5.11 Profiles of the temperature, concentration, stream function and density contour maps at x=0.25; the labels refer to the order of the contour sets. z=0.0, base; z=1.0, the isothermal free surface.

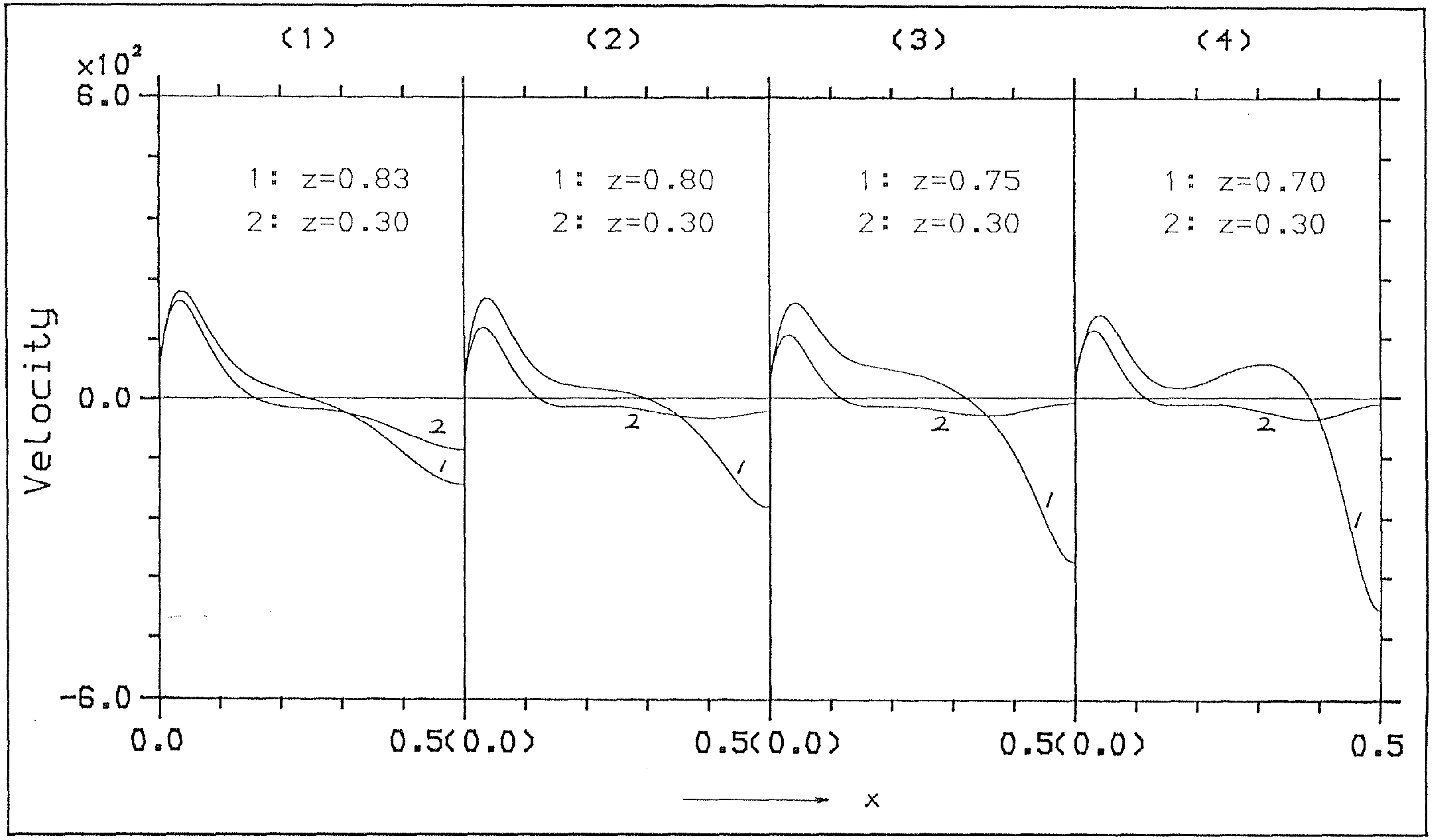

sets 1-4

Fig. 5.12 The maximum velocity profile (see text) in the upper(No.1) and lower(No.2) layer; the number on the top of each box refers to the order of the contour sets (1-8). x=0.0, the heated wall; x=0.5, the central line.

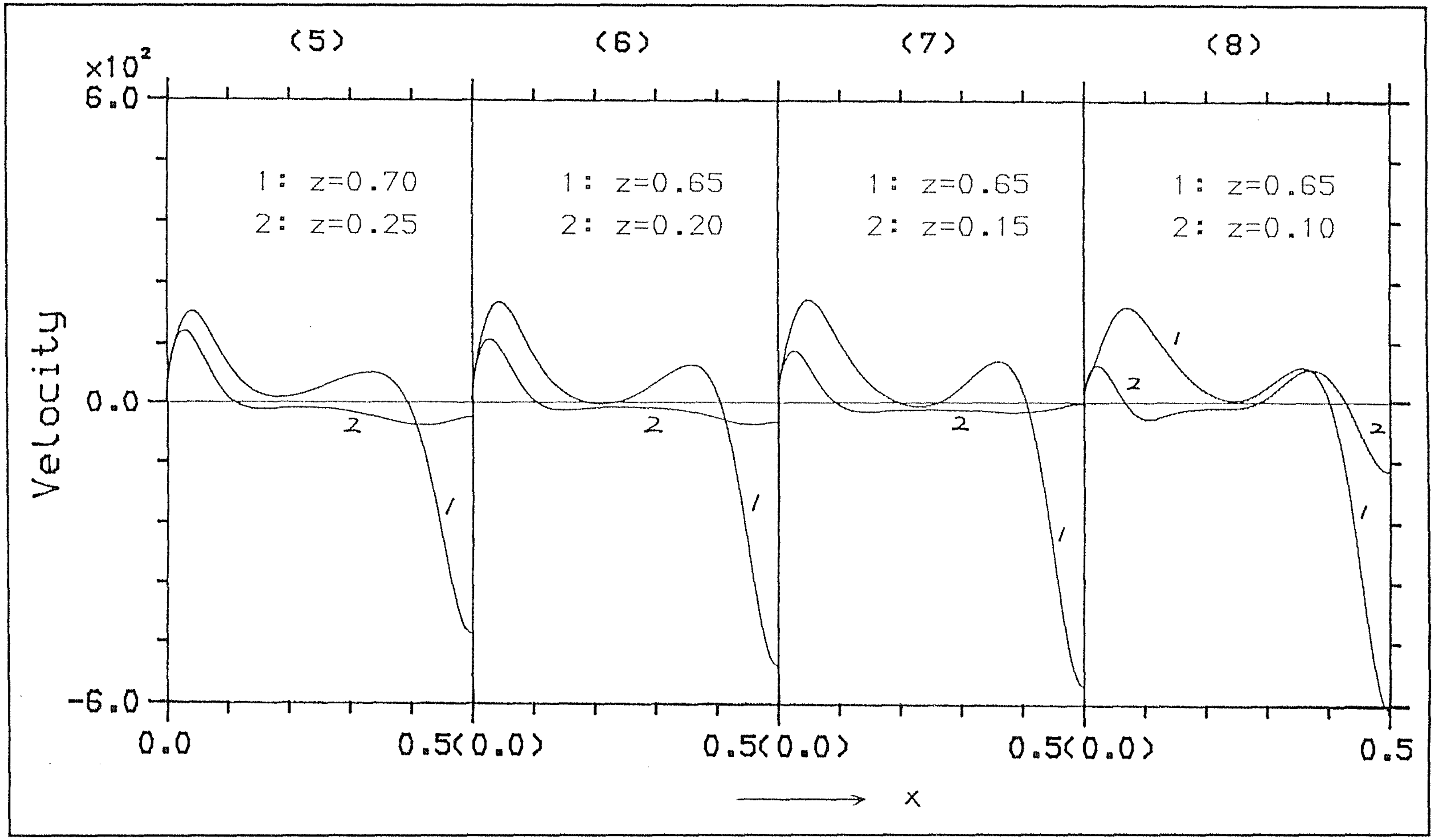
(5)
(6)
(7)
(8)
x10²
6.0
0.0
-6.0
Velocity
1: z=0.70
2: z=0.25
1: z=0.65
2: z=0.20
1: z=0.65
2: z=0.15
1: z=0.65
2: z=0.10
1
2
0.0
0.5(0.0)
0.5(0.0)
0.5(0.0)
0.5
x

sets 5-8

The contour pattern of the lower layer exhibits similar features to the ones in Fig. 5.8, notably, the stream lines are closer in the wall boundary layer than outside the boundary layer, including the core region. The velocity profiles in Fig. 5.12(1) show that the core flow of the lower layer is substantially weaker than that of the upper layer. These observations, together with the evidence provided in the temperature contour (see below), confirm the argument put forward in section 5.3.2 that the interface is quasi-adiabatic.

The temperature contour

It is evident that more heat is retained in the lower layer than in the upper layer. This means more heat is removed at the surface than is transferred from the lower layer to the upper layer. Note the build up of the (nearly horizontal) temperature gradient beneath the interface in the lower layer. This behaviour was also predicted in the case of a single layer with an adiabatic surface(Fig. 5.7 at $t=0.01$).

The concentration and density contours

In the concentration contour the initial stepwise profile of the LOX concentration spreads out on both sides by diffusion.

The density distribution is determined by the concentration as well as the temperature distribution. At the interface, the contribution from the concentration apparently outweighs that from the temperature. Away from the interface, however, the temperature appears as a major contributor to the density. The latter is because at this stage the concentration distribution in the layers is still almost homogeneous. It will be seen that the temperature remains the dominant factor in deciding the density distribution in the lower layer. Consequently the density gradient in the lower layer plays a similar role in the flow development as the temperature gradient does in an homogeneous flow(see section 5.2.2).

Set 2 (Fig. 5.10b) time = 0.01

The stream function contour

In the lower layer a dramatic reduction in the number of the stream lines (from 6 to 3) is observed. This means an equally significant decrease in the velocity field, as is clearly shown in the velocity profile in Fig. 5.12(2). This flow development in the lower layer is very similar to that observed previously in a single layer(Figures 5.7 and 5.9). As has been said, the temperature is a major contributor to the density distribution in the lower layer. The increase in the temperature gradient(see the temperature contour) would result in an increase in the density gradient(see the density contour).

The change in the convective loop of the top layer is much less drastic than in the lower layer. The stream line loop has expanded towards the central line and the interface. This change in the flow pattern results from the increase in the velocity of the core flow, as is clearly shown in Fig. 5.12(2). The maximum velocity of the boundary layer, however, remains almost unchanged. This implies that the rise in the velocity of the core flow is primarily due to the increase in the temperature gradient within the core flow(see Fig. 4.5), and a corresponding increase in the buoyancy force acting on the core flow. This conclusion is also supported by the observation that the position of the maximum velocity of the core flow has dropped from $z=0.83$ at $t=0.005$(set 1) to 0.8 at $t=0.01$(set 2).

The temperature contour

The temperature gradient has increased substantially in the lower layer. This is the primary reason for the slow down of the convective flow there.

The concentration & density contours

The interface has widen slightly in both contours due to diffusion. There is evidence that LOX at the edge of the interface is being swept away by the convective current in the upper layer, and that some of the solute is transported by the boundary flow all the way up to the surface. The former can be appreciated by the upward curving of the contour lines at the interface in the concentration contour, and the latter by the presence of a small patch of liquid with positive density just beneath the surface near the central line in the density contour. The density of the liquid in the wall region of the upper layer, however, is still negative because of the higher liquid temperature there.

Set 3 (Fig. 5.10c) time = 0.02

The stream function contour

The convective loop in the lower layer is further weakened due to the increase in the density gradient (see also Fig. 5.9(3)).

In contrast, the convective loop in the upper layer becomes increasingly stronger(two more stream lines than before). The velocity of the core flow has increased considerably, as shown in Fig. 5.9(3) (notice the further descent in the position of the maximum velocity in the core flow). A new acceleration force is now in action, namely the buoyant force resulting from the concentration gradient across the core flow (see the concentration & density contour below). The core flow starts to impinge on the interface. The effect of this impingement is already noticeable, the interface being pushed down at the central end. Notice that the shift towards the central line of the small velocity loop at the interface; this implies the position of the maximum shear across the interface is also shifting in the same direction.

The temperature contour

The whole lower layer is thermally stratified. In contrast, the bulk liquid of the upper layer is almost uniform in its temperature distribution. This contrast can be seen more clearly in the vertical temperature profile No. 3 shown in Fig. 5.11.

The concentration & density contours

Due to the impingement by the core flow the interface (at the central line end) has been pushed down by about 2% of the height of the domain in both contours.

In the concentration contour, more solute is swept away at the interface by the increasingly stronger convective current in the upper layer. The convective flow could also carry the solute further, reaching about half way down the central line as shown in the density contour. Consequently, a concentration gradient is formed at the central region. This means that, in addition to the existing temperature gradient, the core flow now also contains a concentration gradient. This concentration gradient is such that the concentration of LOX decreases away from the central line (this may not be obvious in this set, but it can be seen clearly in the next set). Therefore it will induce a gravitational force which is with the core flow. Because of the presence of this concentration gradient, the velocity of the core flow would be considerably greater than that of a homogenous flow. This is why the critical Ra^* is smaller in a two-layer system(see section 4.3).

It is evident from the slightly reversed concentration profile(No. 3) in the lower layer in Fig. 5.11 that LIN is also swept away at the interface and transported down near the base region by the convective loop.

Set 4 (Fig. 5.10d) time = 0.04

The stream function contour

In the upper layer an important flow development is observed: with further increase in velocity, the core flow starts to penetrate into the interface before spreading out. Based on a simple energy conservation consideration (neglecting frictional force and entrainment), the penetration depth by a well-shaped core flow may be determined. Assuming a core flow of characteristic velocity U and density ρ_c impinging on an interface with a linear density gradient of $d\rho/dz$, the penetration depth d_p may be expressed as,

$$\frac{1}{2}\rho_c U^2 = g\frac{d\rho}{dz}d_p^2$$

or

$$d_p^2 = \frac{\rho_c U^2}{2g(d\rho/dz)} \qquad (5.2)$$

Clearly, the greater the U and ρ_c and the smaller the density gradient $d\rho/dz$, the larger the penetration depth d_p will be.

The concentration & density contours

When the core flow penetrates into the interface, it entrains heavier liquid from the interface into the upper layer. This is clearly shown in the concentration contour. The contour pattern in the top layer closely follows that of the stream function, suggesting that the mixing is mainly carried out through advection.

Through this penetration and entrainment by the core flow, the upper layer increases in the volume at the expense of the lower layer.

Sets 5-8 (Fig. 5.10e-i) times 0.06, 0.10, 0.12, 0.14

The development of the flow during this period is dominated by the steady downward penetration and the entrainment by the core flow. As more liquid is entrained and subsequently mixed into the upper layer, the frontier of the top layer advances steadily downwards at the expense of the lower layer(see also Fig. 5.11).

This penetration of the core flow is self-perpetual. From equation (5.2) the penetration depth d_p is influenced by U, ρ_c and $\partial\rho/\partial z$. As the core flow penetrates into the interface, it entrains heavier liquid into the upper layer. Consequently the density of the upper layer (including the core flow) will increase; the density gradient at the interface will in general decrease. The velocity of the core flow will increase(see Fig. 5.12(5-8)) due to the increase in the temperature and concentration gradient of the core flow (see the temperature and concentration contours). From equation (5.2), it is clear that the core flow could penetrate deeper.

It can be seen from Fig. 5.11 that the temperature has risen steadily in both layers. Since the increasing rate is higher in the lower layer, the temperature difference between the layers widens at the same time. The temperature of the lower layer and the temperature difference between the layers reach a peak at about t=0.1(set 6). From then on the temperature difference decreases to zero as the lower layer is diminishing.

Sets 9-12 (Fig. 5.10i-l) times 0.16, 0.165, 0.17, 0.175

During this period, the last remnant of the highly concentrated and hot liquid is gradually mixed into the main stream. Finally a single layer is formed. The temperature and stream function contours in set 12 are very similar to those of a single layer with the same Ra^* (see Figures 5.1 and 5.3), as would be expected. The detail of this flow development will be discussed in section 5.3.3(iii).

ii) The Interface Movement

The movement of the interface is shown in Fig. 5.13. Here the interface level is chosen as the height of the interface at the central-line end. The interface hardly moves in the time period up to t=0.02(set 3). Gradually it descends at an increasing rate, corresponding to the period marked by the penetration and entrainment by the core flow. The interface completely vanishes at about t=0.15 after heating.

iii) Surface Heat Flow Rate

The surface heat flow rate Q_{sur}, i.e., the rate at which heat is removed at the surface, is also shown in Fig. 5.13 with Q_{sur} expressed as a percentage of the heat input. The Q_{sur} curve of this run is compared with that of a single layer under the same heating condition(the unmarked curve). In the present run, the Q_{sur} increases steadily before reaching a peak at about t=0.14. By comparing the Q_{sur} curve in the same period for a single layer, the accumulation of heat in the lower layer is evident. The Q_{sur} then undergoes a short period of strong up-down oscillations. After reaching the highest peak at t=0.165, the Q_{sur} gradually approaches the equilibrium value. These later developments in the Q_{sur} may be understood by referring back to the relevant contour maps, that is, sets 9-12(Fig. 5.10h-l). The oscillations in the Q_{sur} can be related to the build-up and destruction of a large non-streamlined concentration gradient at the surface (see sets 9 & 11).

With the disappearing of the bottom layer, the remaining highly concentrated hot liquid is gradually swept to the sidewall by the now single-loop convective flow. This substantially increases the concentration gradient in the boundary layer, as can be seen in the sets 8 and 9. Since the gravitational force generated by the concentration gradient opposes the thermal driving force, an increase in the gradient will slow down the boundary flow. The build up of the non-streamlined concentration gradient at the surface is an indication of this slow down in the velocity: the velocity boundary layer has not enough momentum to carry the highly concentrated liquid along the stream lines. This slow down of velocity is believed to cause the decrease in the Q_{sur} from

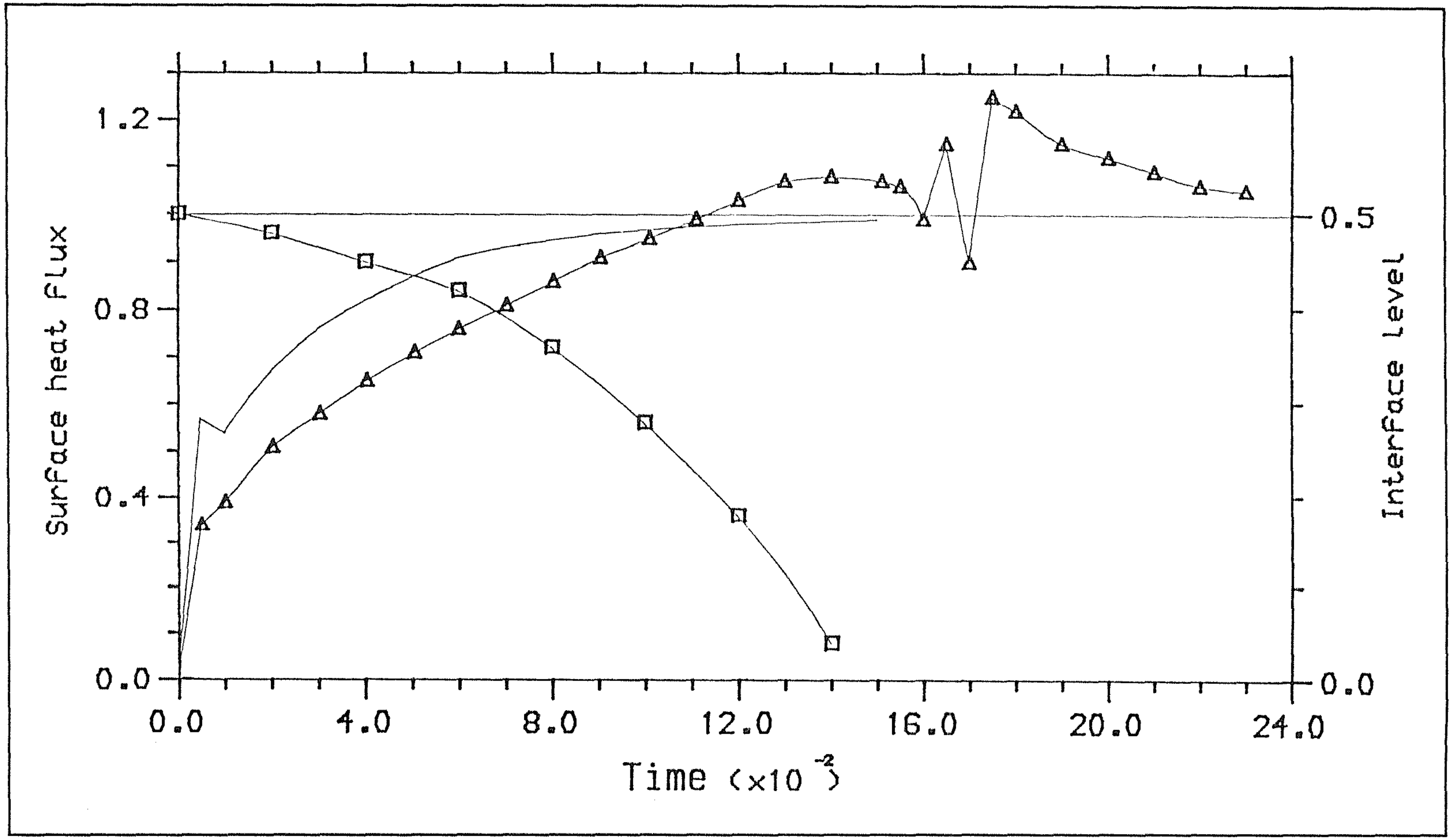

Fig. 5.13 Time variation of the surface heat flux and the interface level.
Δ: surface heat flux; : interface level; -:, surface heat flux for single layer.

t=0.14(set 8), since the hot liquid in the boundary layer now takes a longer time to reach the surface. When the gravitational force generated by the concentration gradient outweighs the thermal buoyancy force, a flow reversal could result, as observed in sets 9 and 10. When eventually a lump of the hot and highly concentrated liquid is carried across the surface, the Q_{sur} undergoes a sharp rise from t=0.16(set 9). Meanwhile the core flow is experiencing a large acceleration (see the stream function contour in set 10). This intermittent removal of the hot and concentrated liquid in the boundary layer continues until the remaining hot liquid is mixed into the main stream of the flow.

At t=0.17(set 12), a single layer with almost uniform concentration distribution is formed. From then on, the flow behaves almost as a true single layer, with the Q_{sur} gradually approaching to the equilibrium value.

5.4 Grid Dependence Check

i) The one-component model

A non-uniform control volume grid of 49x43 was first used. The steady state results obtained were then linearly interpolated for the two finer grids, namely, 75x73 and 99x100. The results obtained using the 75x73 grid are presented here. The maximum velocity of the boundary layer and the core flow at the middle plane(z=0.5) were compared. The outcome of this comparison is shown in Table 5.3. It can be seen that the grid 75x73 is sufficient at $Ra^*=10^6$; the errors rise up to 3% at $Ra^*=10^8$.

Table 5.3 Grid dependence check

grid	49x43	75x73	99x100
		$Ra^* = 10^6$	
$w_{max,b}$	133.1	131.0	131.4
$\epsilon(\%)$	1.3	0.3	
$w_{max,c}$	-193.0	-189.9	-189.8
$\epsilon(\%)$	1.7	0.05	
		$Ra^* = 10^7$	
$w_{max,b}$	341.9	329.2	325
$\epsilon(\%)$	4.9	1.3	
$w_{max,c}$	-535.5	-520.5	-512.9
$\epsilon(\%)$	4.4	1.5	
		$Ra^* = 10^8$	
$w_{max,b}$	830.0	792.5	769.7
$\epsilon(\%)$	7.8	3.0	
$w_{max,c}$	-1310.6	-1293.1	-1261.2
$\epsilon(\%)$	3.9	2.5	

where

$w_{max,b}$ ———— the maximum velocity of the boundary layer at the middle plane (z=0.5),

$w_{max,c}$ ———— the maximum velocity of the core flow at the middle plane (z=0.5).

ii) The two-component model

In the stability tests in the last chapter, a relative coarse non-uniform control volume grid of 49x43 was used. For the two combinations of Ra^* and Rs, namely, $Ra^*=10^7$ with $Rs=10^6$ and $Ra^*=10^7$ with $Rs=3x10^6$, flows were found stable and symmetric throughout the computation. The run with the combination of $Ra^*=10^7$ and $Rs=3x10^6$ was then repeated using a finer grid of 75x73. The results of this run are presented here. To cut down the running time, the computation was performed on only half of the flow domain by assuming the flow was truly symmetric about the central line of the domain. This conduct was justified by the small magnitudes of the stream function and vorticity at the central line($< 10^{-8}$). The main flow features in the two runs were found to be very similar.

NUMERICAL RESULTS IN CYLINDRICAL POLAR COORDINATES

Two cases have been examined, both in a dewar of 140mm radius and 240mm height. The initial concentration conditions were identical in both cases; from the bottom to a height 136mm (57% of the total height), LIN/LOX mixture with a density 1% greater than pure LIN, and from a height 160mm to the top (33% of the total height), pure LIN. Between these two layers is an immediate layer (10% of the total height) with uniform concentration (density) gradient. In the first case the side wall heat flux was 25 W/m^2 into the top and intermediate layers (initial positions) and 31.5 W/m^2 into the bottom layer with an adiabatic base. The second case was identical except that the heat flux into the bottom layer was 115 W/m^2 from the base only, with the heat flux into the top and intermediate layers at 25 W/m^2. In each case the initial total heat flow into each layer is identical, but they represent the two extremes of bottom layer heating. The results of the two runs show that the mixing between layers is primarily due to the gradual downward penetration and entrainment by the core flow (or central jet) of the top layer. This prediction is in agreement with the mixing process described above in cartesian coordinates. The mixing of layers in the second case, however, takes a longer time than in the first one, as clearly shown in the surface heat flow rate in Fig. 5.14. This is because although the heat flow into the bottom layer is identical in the two cases, convection generated by the base heating is much stronger than by the side wall heating. The convection loops generated by the base heating are quite transient; sometimes a single loop, sometimes a cellular pattern. The effect of this convection is to maintain a uniform density distribution in the bottom layer and thus to prevent the intermediate layer spreading downwards. The intermediate layer is therefore kept thin and a relatively large density gradient is maintained. From equation (5.2) the penetration depth of the core flow will be reduced. Consequently the advancing of the intermediate layer is slowed down.

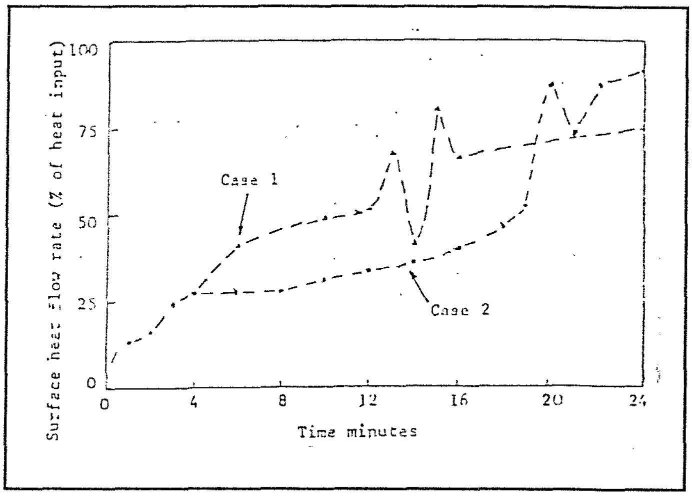

Fig. 5.14 Surface heat flow rate.

The above rollover simulations were carried out before the stability study described in chapter 4. The Ra^* in the first case was at least of order of 10^{12}. We now know that such high Ra^* is almost certain beyond the range of the model. The results therefore need to be treated very carefully.

6.0 FLOW VISUALIZATION OF ROLLOVER

Numerical results by the two-component model in the last chapter show that the mixing process of two initially stratified layers is characterised by two continuing processes: the process of steady downward penetration by the core flow of the convective loop in the upper layer and the process of entrainment whereby higher density liquid is entrained and mixed into the upper layer. These two processes go hand in hand, and eventually the lower layer is completely mixed into the upper layer and the whole liquid becomes one single layer. The purpose of this flow visualization experiment was to qualitatively verify this prediction by the model.

6.1 Choice of Method

Among various techniques available for flow visualization [34], the one employing small particles as flow tracer was chosen because it is most suitable for observing recirculating flow. The principle of this method is very straightforward: if the density of a particle matches that of the flowing liquid to be seeded, the gravitational force is balanced by the buoyancy; in addition, if the particle is also assumed to be massless, it is expected to follow the flow of the liquid. Therefore, by adding sufficient number of particles, the invisible flow may be made visible by tracing the movements of these particles. This is, of course, the ideal situation. In reality, this exact match in density can rarely be realised; and particles always have mass, no matter how tiny they are. But if the approximation of these two conditions is close enough(or in the second condition, the inertia of the particle may be neglected compared with the momentum of flow), flow visualization of acceptable accuracy can still be achieved.

While this method is simple, easy to operate and straightforward, it has limitations. An obvious one is that the fluid velocity of the flow under study(u_f) can not be too small. Since the density of the tracer particles seldom matches to that of the fluid, a buoyant force will always be present. For effective flow visualization, $u_f >> u_p$ must be satisfied, where u_p is the velocity of the particles associated with the buoyancy acting upon them. Generally a minimum fluid velocity of order of 1mm per second is required to meet this consideration.

6.2 Testing Fluid

Ideally LIN and LOX should be used since they are the liquids in which numerical simulations were performed. The low boiling point of LIN(77K), however, requires extremely good insulation of the test tank in order to minimise heat leaks from the surroundings. This condition itself may not be difficult to be met in laboratory, say, by using double-walled vacuum insulation, and better still, a LIN bath in addition to the vacuum insulation. The present experiment, however, also demands good viewing as well as controllable uniform wall heating. To meet all the requirements at the same time has proved to be not a easy task.

Early flow visualisation experiments were performed in cylindrical double-walled glass dewar. Two dewars had been used. The first one, which was also used by Agbabi[13] in his rollover simulation experiments, has a layer of semi-transparent(for viewing) metal oxide coating on the outside wall of the inner dewar, through which, controllable heat input to the inner dewar may be provided. Apart from the vacuum insulation between the two dewar, a surrounding LIN bath was also used. It was later found that this coating had not been painted smoothly enough to provide a uniform heat flux. A second dewar was then used to overcome this shortcoming. A double-walled vacuum insulated testing dewar was placed inside another dewar, with a continuous flow of cold nitrogen gas in the annular space as shielding. In this case, radiation from the cold gas temperature into the testing liquid provided a natural means of heating. As a result, the homogeneity of heating was improved. But the previous ease of control of heating power was lost.

The use of a less volatile testing media easier to handle at room temperature was thus desirable. On this ground, freon 11 and 113, which have been successfully used by Nakand et al[11], were chosen. The relevant properties of freon 11 together with those of liquid nitrogen, are listed in Table 6.1.

Table 6.1 Properties of freon 11 compared with those of liquid nitrogen

	freon 11[*]	LIN
T_{sat} (K)	296.8 (23.8°C)	77.4
k (Wm/K)	0.381[**]	0.140
ν (m^2/s)	2.77×10^{-7}	1.96×10^{-7}
α (m^2/s)	2.99×10^{-7}	8.44×10^{-8}
β_T (1/K)	3.7×10^{-3}[***]	5.77×10^{-3}
Pr	0.93	2.32

[*] at 30°C

[**] the value at 20°C

[***] mean value from the saturation temperature to the critical temperature

The saturation temperature of freon 11 under one atmosphere is 23.8°C, which is a couple degrees higher than the usual room temperature in the laboratory. This means that freon 11 is usually sub-saturated in the laboratory. This has serious implications. The surface temperature of a layer of sub-saturated liquid in a container varies with its partial vapour pressure just above the surface according to the equilibrium curve of that liquid. In an open tank the partial pressure of vapour is generally less than the equilibrium pressure of the liquid at room temperature. (This is why a sub-saturated liquid open to the surrounding is evaporating all the time at room temperature). Consequently the surface temperature will be slightly lower than the room temperature. If the liquid is left undisturbed for a long period, a dynamic equilibrium may be reached whereby the vapour generation rate at the surface is balanced by the dissipation of vapour to the surrounding. When this happens, the partial vapour pressure and thus the surface temperature will remain stable. In other words, an effectively isothermal surface is maintained.

Now consider what will happen if a uniform sidewall heat flux is applied to the liquid. This will generally result in an increase in the evaporation rate at the surface; and the larger the heat flux, the higher will be the evaporation rate. There are two possible outcomes: 1) the previous dynamic equilibrium could still be preserved if this increase in the evaporation rate does not exceed the vapour dissipation capacity of the surrounding. Consequently a nearly isothermal surface is still maintained. 2) the dissipation capacity of the surrounding is exceeded by the increase in the vapour generation. The partial pressure of the vapour therefore will rise, until a new balance between the two processes, i.e., the generation and dissipation of vapour, is reached. Meanwhile the surface temperature will increase accordingly to the equilibrium value with the new vapour pressure. During this transient period, the surface resembles an adiabatic one.

In order to comply with the isothermal surface condition assumed in the model, it is important to keep the variations in the surface temperature as small as possible. From the above analysis, this requires an low heat flux and a high dissipation rate of vapour at the surface.

6.3 Tracer Particles and Seeding Method

The quality of flow visualization using suspended particles depends on two factors: how well the tracer particles follow the flow they are in and their ability to reflect a beam of light. The former decides to what extent the motions of the particles represent that of the flowing liquid. Clearly, the better the two densities match up, the closer will the particles follow the flow. The latter is quite obvious, a minimum light reflectability of the particle is required for clear viewing.

In a two-layer stratification, in order to observe flow patterns in the two layers, both of them need to be seeded, but not necessarily at the same time. In fact, since the interface has been predicted to drop steadily, the seeding of only the upper layer is favourable. By doing so, the flow pattern in the upper layer, especially the predicted existence of a core flow and its downward penetration into the layer below, as well as the movement of the interface can be observed. Flow visualization of the lower layer may be made by seeding that layer only in a separate run.

The search for the right particle(s) proved to be time consuming. After many attempts, polyester was found to be very satisfactory for the upper layer seeding. Polyester is a white powder which matches perfectly in density with freon 11 and reflects light well. Red coloured fluorescein sodium has also been used, primarily in the lower layer seeding.

The visualisation of the lower layer was found much less effective than that of the upper layer for the heat flux used in the experiments. This is primarily due to the fact that liquid velocities in the lower layer are much lower than that in the upper layer.

6.4 Flow Visualisation System

The set up of the experimental system for flow visualisation is shown in Fig. 6.1. A high intensity parallel beam from *a* is redirected down through mirror *b* and illuminates a cross section of the tank *c*. Observation or recording of flow in the illuminated cross-section may be made at *d*.

The key equipment is the test tank, a 12cmx12cmx20cm (wide x deep x long) rectangular container, designed and constructed for this experiment. The sidewalls and the base are made of 1.5mm thick copper plates. Independently-controlled electrical heaters are mounted on the side walls and the base. The base plate is separated from the two side ones by insulation material to reduce heat transfer between them. The front window is made of 9mm thick perspex to provide good insulation, as well as viewing. Apart from the front window, all the inner walls are painted black to enhance the contrast of picture. The whole tank, with the exception of the front and top, is insulated with thick polystyrene to reduce heat exchange with the surrounding.

The tank is not sealed at the top. (During the experiments the tank was covered with a perspex plate.) This was found to be essential in the present experiment. An unsealed tank enables the rapid dissipation of vapour generated at the surface to the surrounding; therefore an quasi-isothermal surface may be maintained(see section 6.2). On the other hand, if the tank is sealed at the top(except for at least one opening for venting), evaporated vapour will accumulate in the vapour space. Consequently the partial vapour pressure and thus the surface temperature will increase towards their new equilibrium values. In this transient period, the surface would behave like an adiabatic one.

Numerical simulations in the last chapter have shown that convective flows with an isothermal surface are very different from those with an adiabatic one, in terms of flow pattern and velocity distribution. A clear contrast has indeed been observed

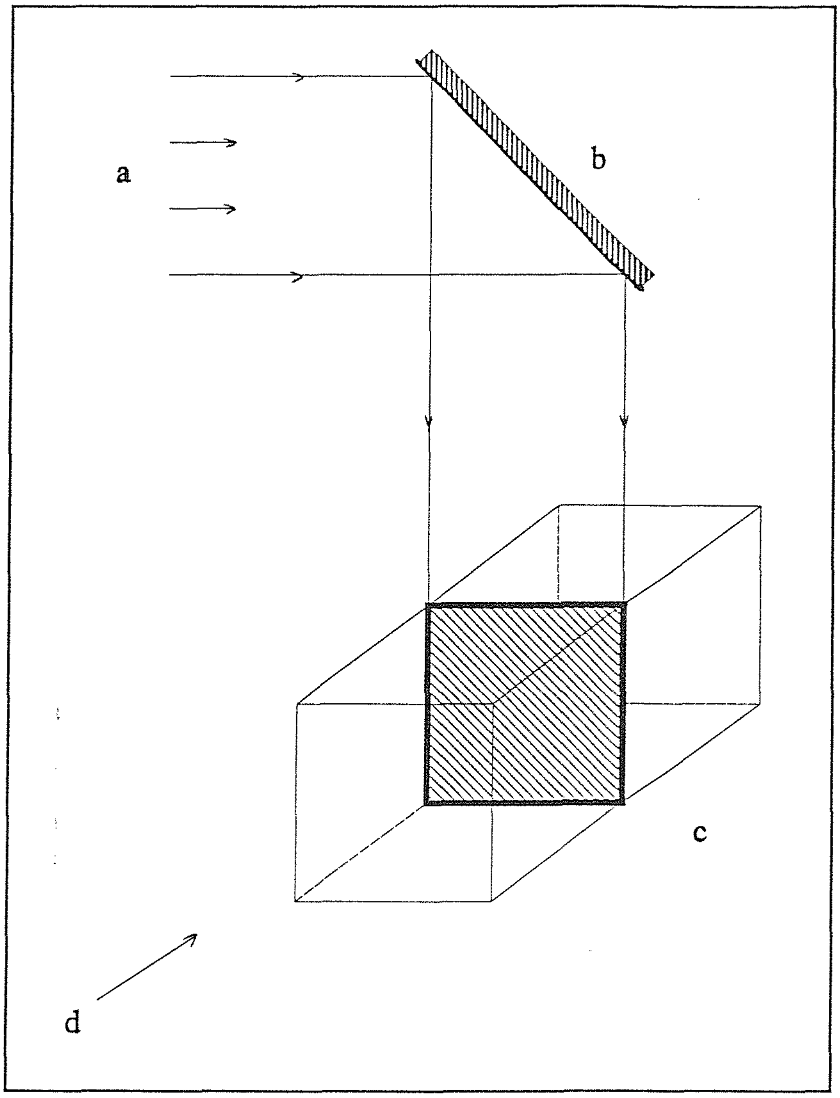

Fig. 6.1 Flow visualization system. a: beam of parallel light, b: reflecting mirror, c: test tank, d: viewing point.

between convective flows in an unsealed (open or covered) tank and a sealed one. In an unsealed tank, a recirculating loop is clearly observed, with hot liquid rising along the heated walls and a core flow descending down in the central area; whereas the flow velocity in an sealed tank is much weaker and no strong downward flow is observed. These observations are in broad agreement with the numerical predictions.

An unsealed tank means, unfortunately, that the boil-off rate can not be recorded directly during experiments.

6.5 Experimental Procedure

After the system is properly set up, the tank is first filled with pure freon 11 to about 5cm high and left for some time to reach equilibrium. The mixture of freon 11 and small amount of freon 113 is then slowly bottom filled through a thin capillary. In this way, a system of two stratified layers is formed. Next the seeding particles are spread into the tank, which is then covered with a perspex plate to reduce any disturbances from the surrounding during experiments. The tank is then left for about half an hour so that the perturbations induced during the filling can be dissipated. Now appropriate heaters are switched on to start heating. Meanwhile a video camera is set to start recording.

6.6 Results

Two experimental runs(both with upper layer seeding) are reported here, one with side-heating only, the other with both side and base heating. In both runs, the pre-filling density difference between the layers was 1% and the wall heat flux was about 40W/m^2(assuming all the heat generated by the electrical heaters enters the tank).

This heat flux would yeild a Ra* of order of 10^9, 100 times as high as encountered in the numerical simulation. However, heat flux of such magnitude has been found necessary.

Preliminary flow visualisation experiments on one single layer show that there are convective motions of considerable velocity in an unsealed tank many hours after the completion of filling(no heating applied). The liquid rises along the walls as if a heat flux were applied; a strong downward flow moves from side to side frequently. In contrast, no visible motions could be observed when the tank is sealed at the top. Considering this observation and the fact that the surface temperature is lower than the bulk liquid temperature for an evaporating liquid, one is lead to the conclusion that these motions result from the instability of the surface layer. When a reasonable heat flux(40 W/m^2) is applied through the side walls, these motions would slow down initially due to the rising of the heated liquid to the surface, before being replaced by flows with a more regular flow patter.

This regular flow pattern basically agrees with the predictions by the model: a convective loop could be clearly identified with rising boundary flows along the walls and a strong downward core flow where the two transverse surface flows meet. However, the core flow, which is apparently not laminar, does not always stay at the centre. Instead, it moves about off the centre from time to time(but much less frequently than the wall heater was switched on). This behaviour of the core flow at high Ra* is expected; the model predicts that if the Ra* exceeds a critical value, the core flow will become unstable.

Two time sequences of flow visualization photographs displaying the evolution of flow in the two runs are given in Fig. 6.2 and Fig. 6.3. A exposure time of 4 seconds was used for these photographs. Care was taken to match the dimensions of the prints to those of the tank cross-section. These photographs thus recorded the true trajectories of the seeding particles, illustrated in the photographs as short bright lines. It should be noted that the length of one trajectory does not necessary represent the whole distance travelled by a particle in the period of 4 seconds. Because the flow was not strictly two-dimensional, a particle could well enter and leave the illuminated section during the exposure time. Therefore the velocities of the seeding particles directly derived from the lengths of their trajectories are very likely to be smaller than their true values. The interface movement in these two runs is given in Fig. 6.4.

6.6.1 Side heating only(Fig. 6.2)

Three distinct stages are observed leading to the complete mixing of the contents of the tank after about 200 minutes.

Stage 1 0 - 47 minutes, (photographs a - e)

The merging of the intermediate layer into the top layer

Photograph a, t = 15 minutes

Fifteen minutes after the heat is supplied (the starting point of recording), two broad layers, with the upper one seeded, are observed. In the seeded upper layer two sub-layers may be identified by a sudden change in the brightness of the picture. The three layers are called, from the bottom up, the bottom layer, the intermediate layer and the top layer. The formation of the intermediate layer is apparently caused by the mixing of two liquids of different densities during filling. In some runs where the lower layer is seeded, this sub-stratification is also observed in the lower layer.

As a result of the sub-stratification in the upper layer, the convective flow is confined to the top layer, and there is hardly any motion in the intermediate layer. The flow pattern, especially the strong core flow, can be clearly identified. It should be noted that the core flow does not always stay at the centre, as mentioned before in the case of a single layer.

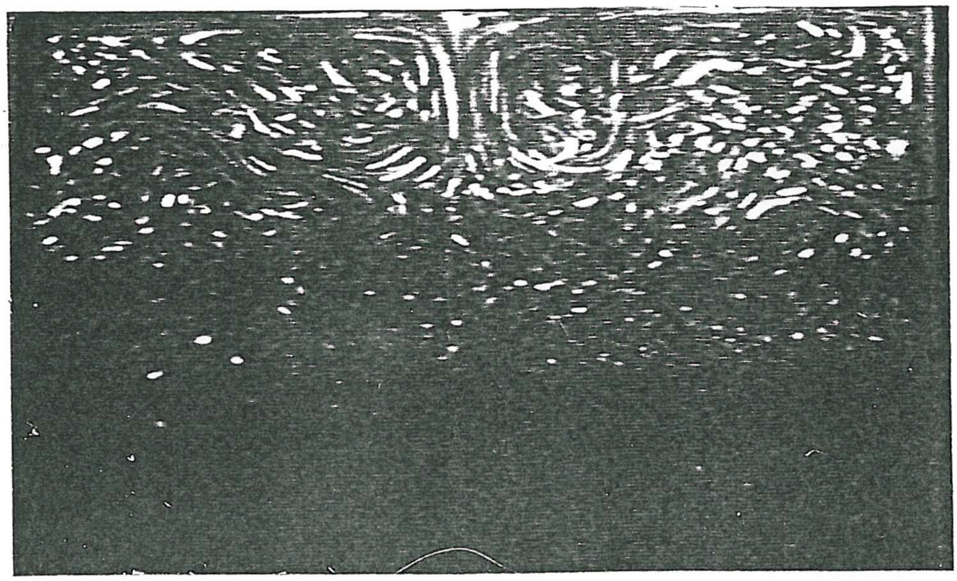

(a) t = 15 minutes

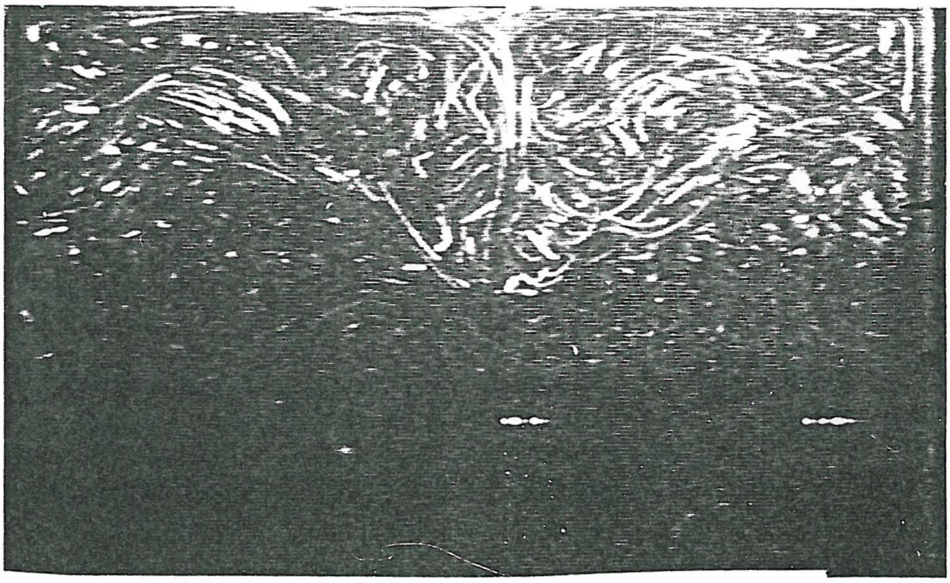

(b) t = 20 minutes

Fig. 6.2 Flow visualization photographs (a-l) showing the mixing of initially stratified layers which are subject to uniform side heating only.

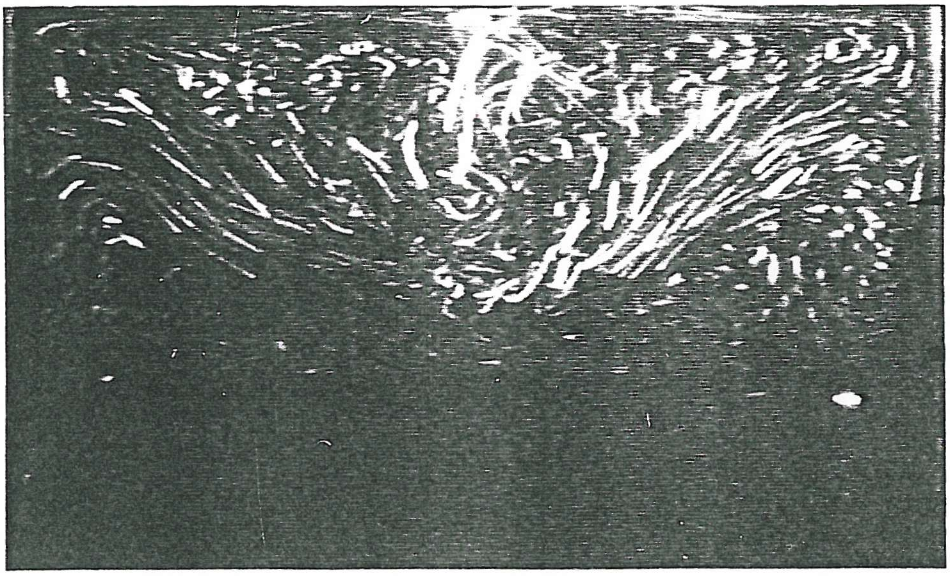

(c) t = 25 minutes

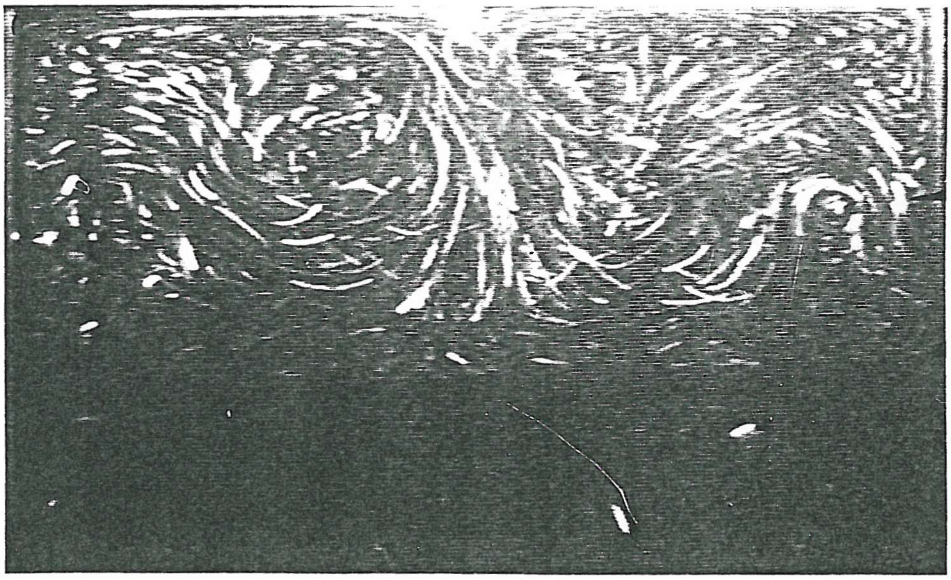

(d) t = 30 minutes

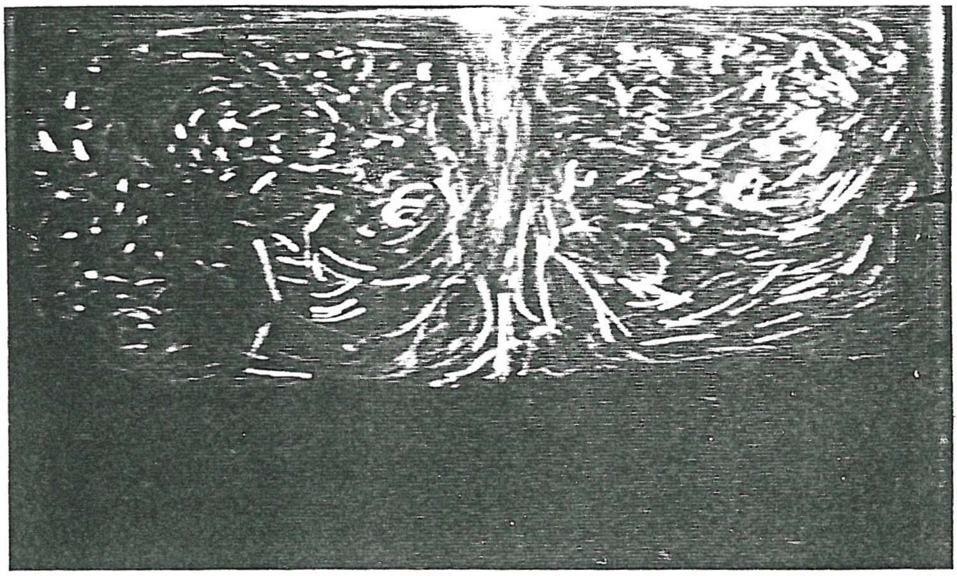

(e) t = 45 minutes

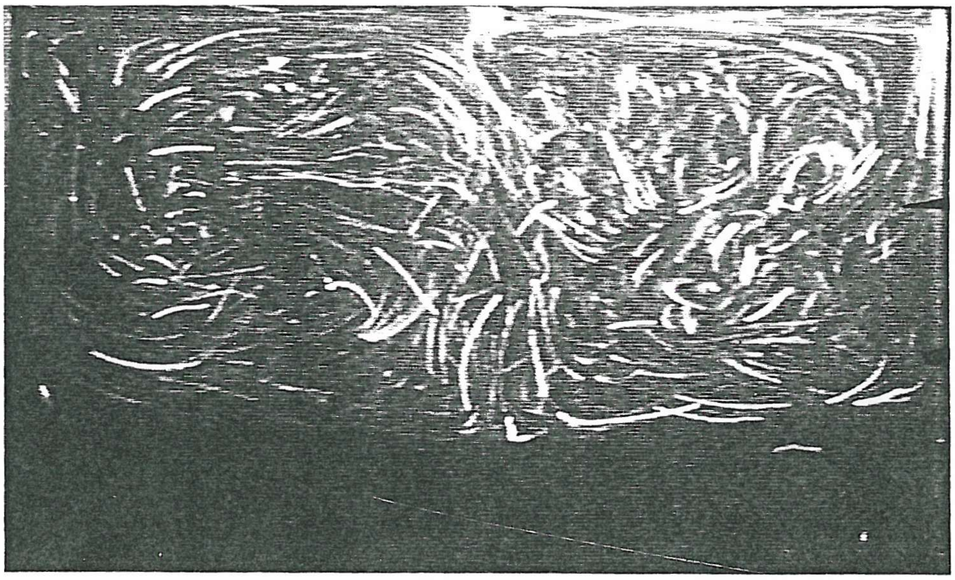

(f) t = 125 minutes

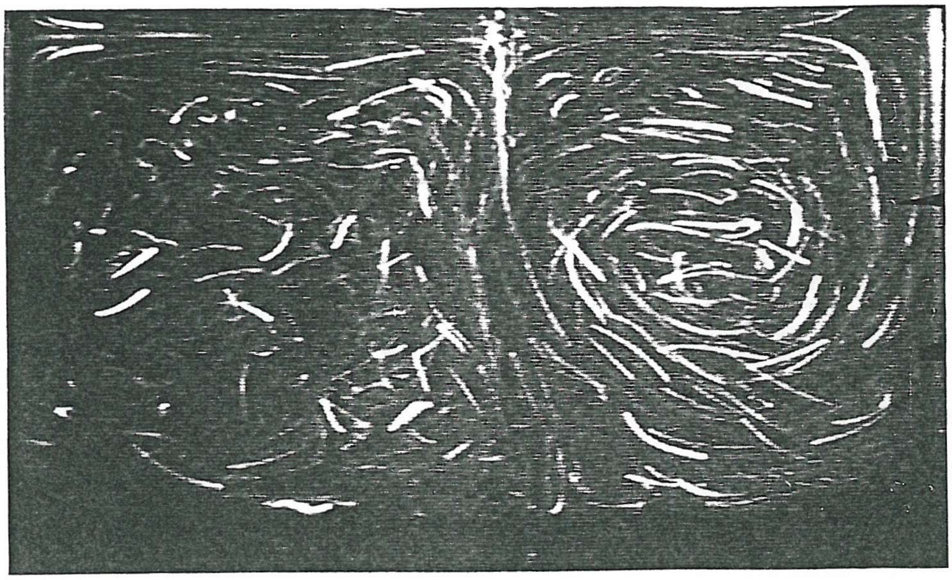

(g) t = 185 minutes

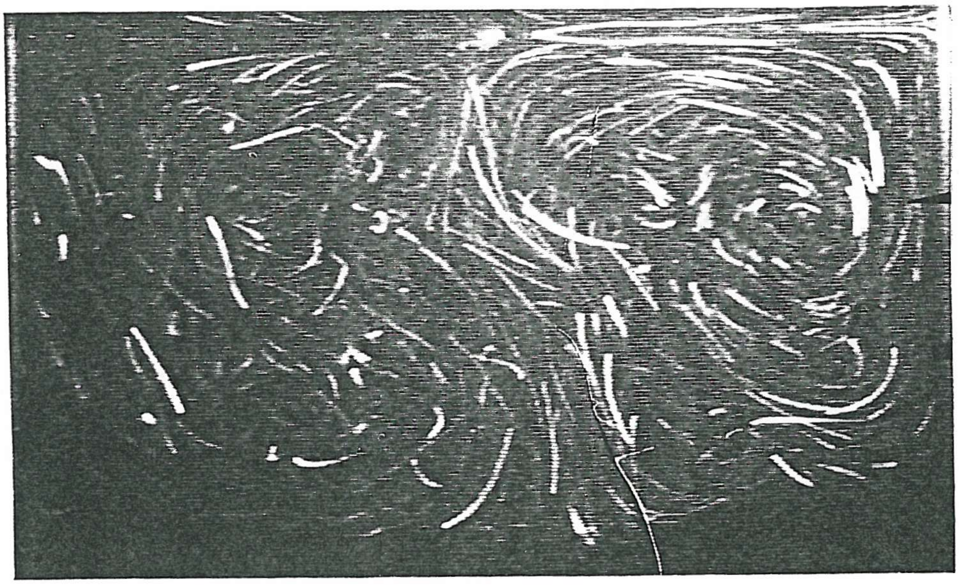

(h) t = 188 minutes

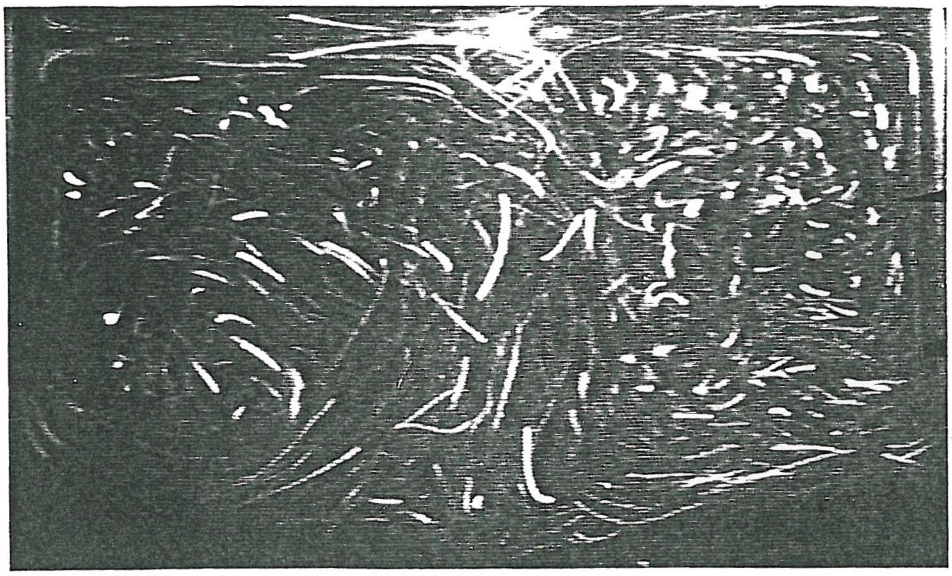

(i) t = 191 minutes

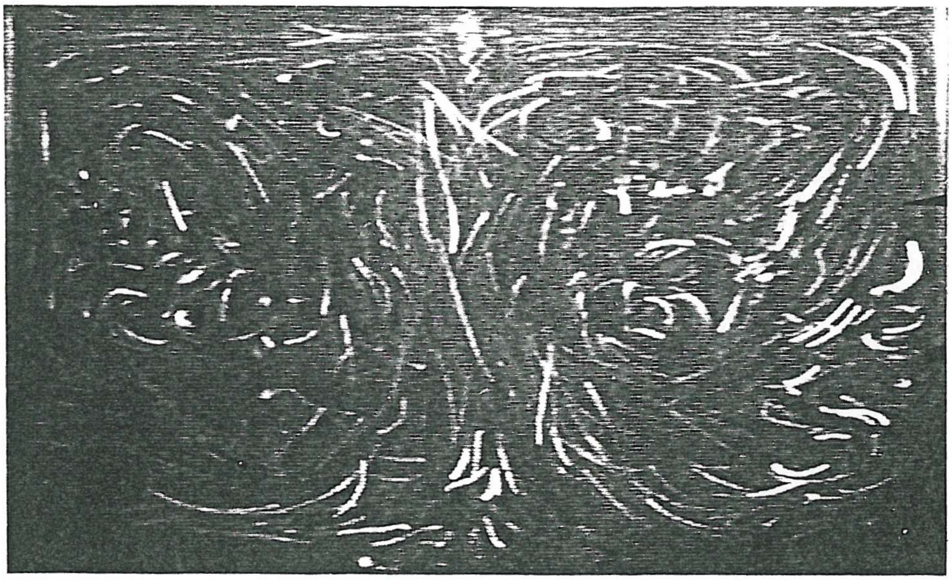

(j) t = 194 minutes

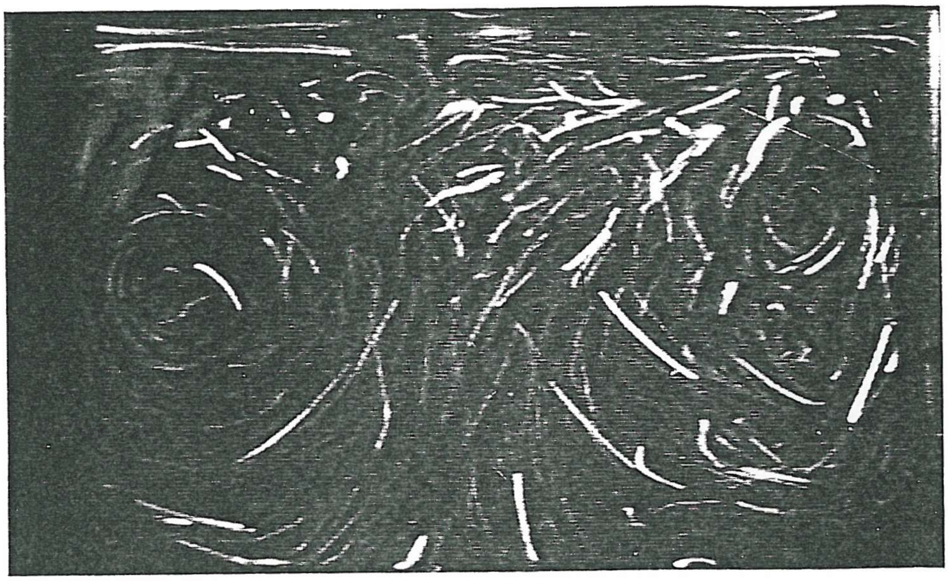

(k) t = 197 minutes

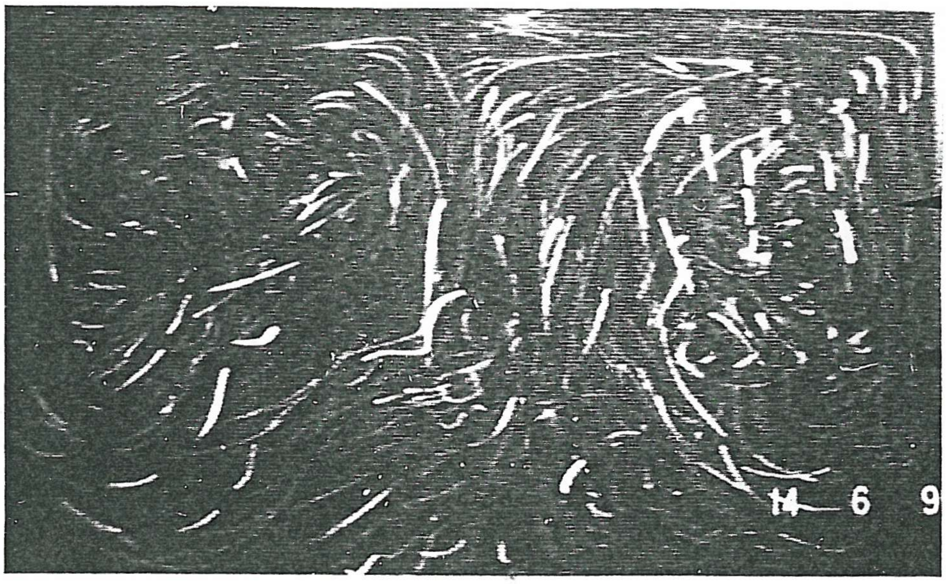

(l) t = 200 minutes

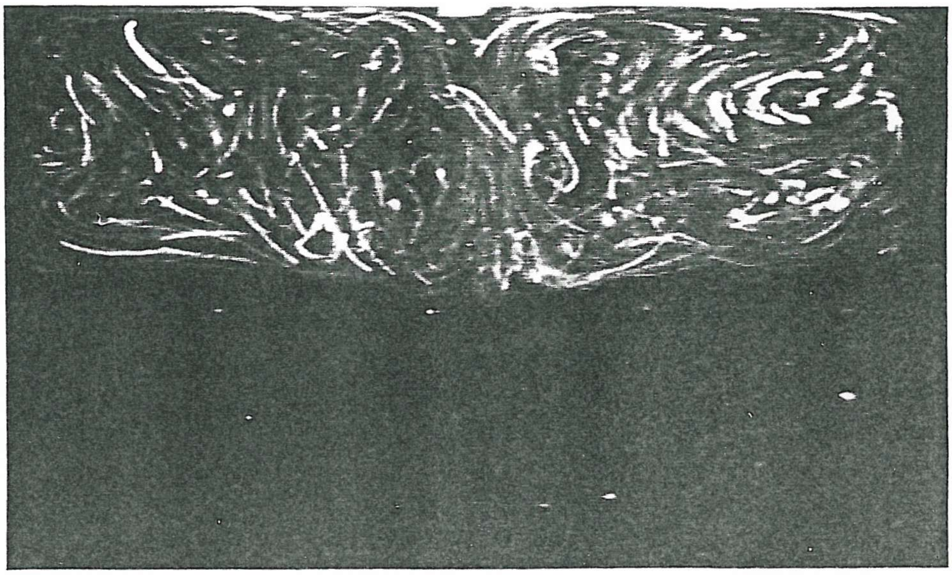

(a) t = 5 minutes

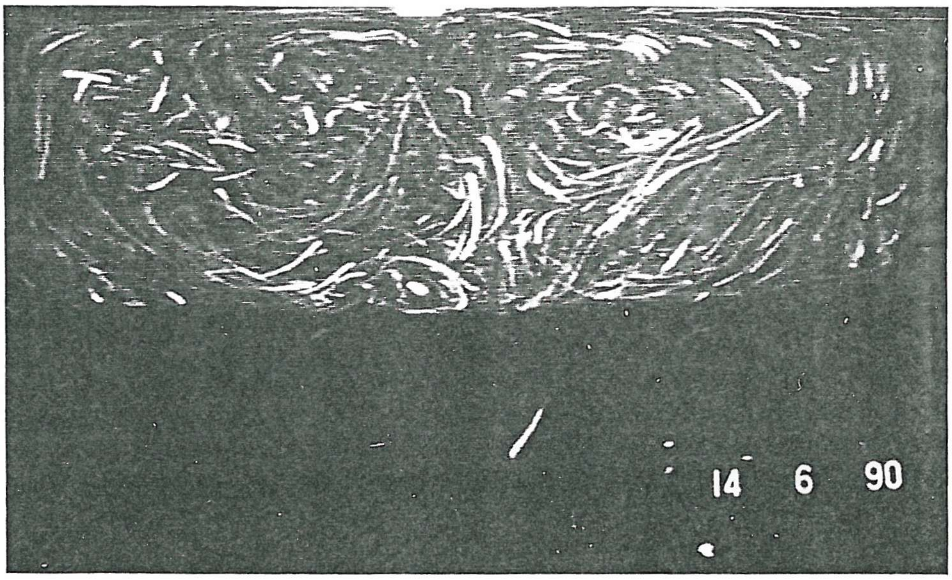

(b) t = 80 minutes

Fig. 6.3 Flow visualization photographs (a-j) showing the mixing of initially stratified layers which are subject to uniform side and base heating.

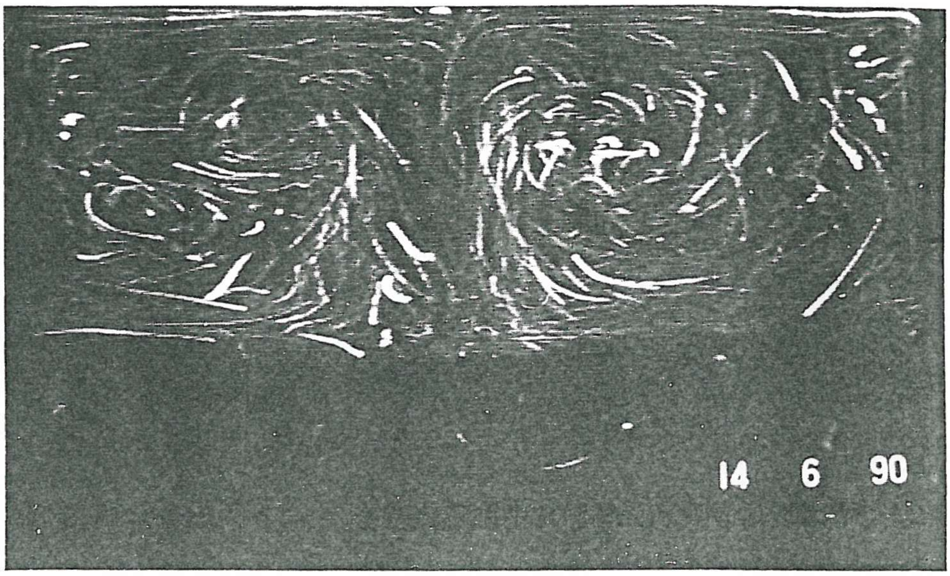

(c) t = 140 minutes

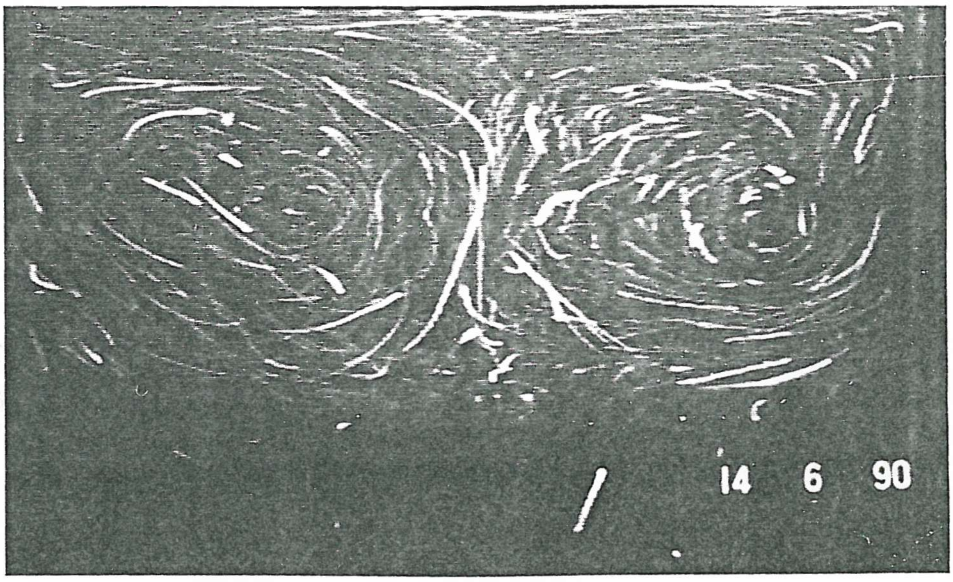

(d) t = 170 minutes

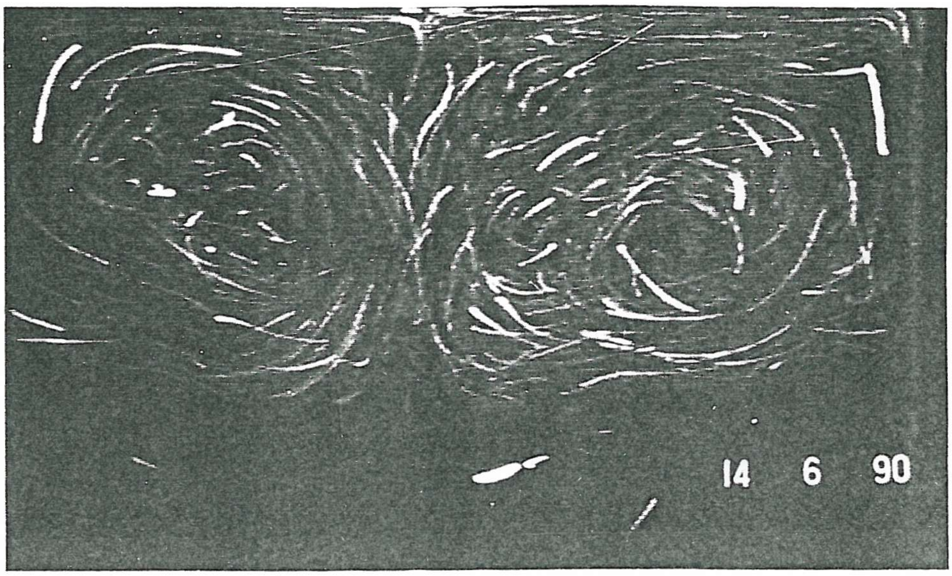

(e) t = 172 minutes

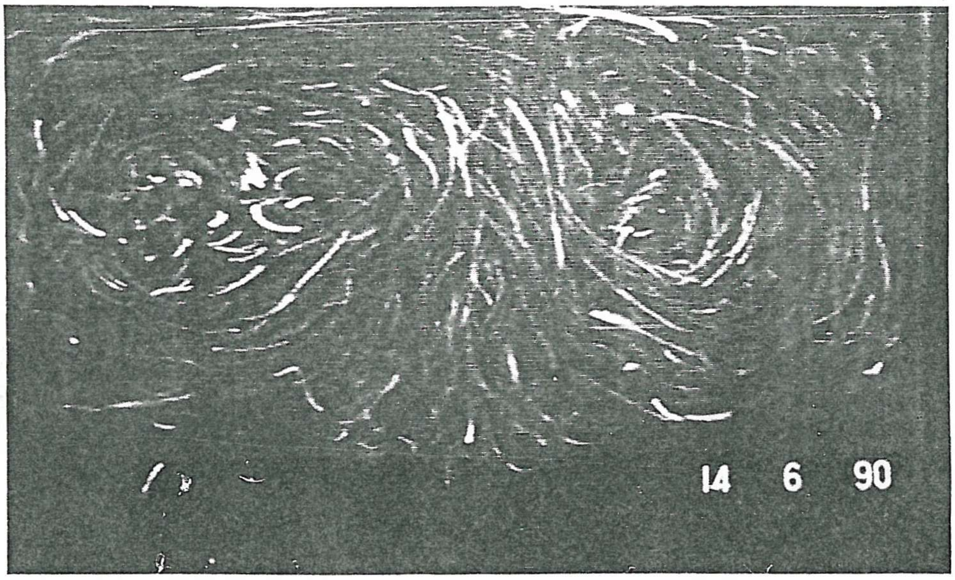

(f) t = 175 minutes

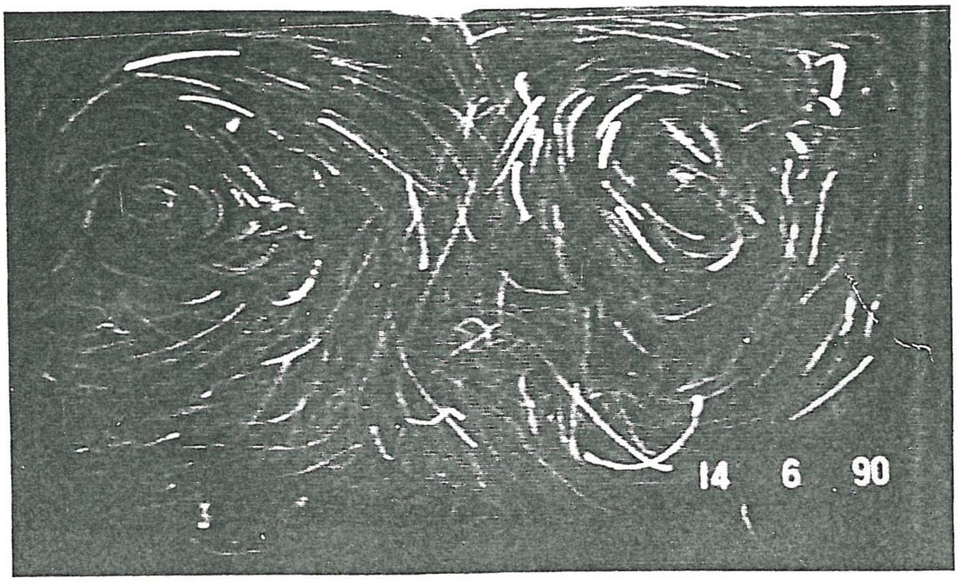

(g) t = 177 minutes

(h) t = 180 minutes

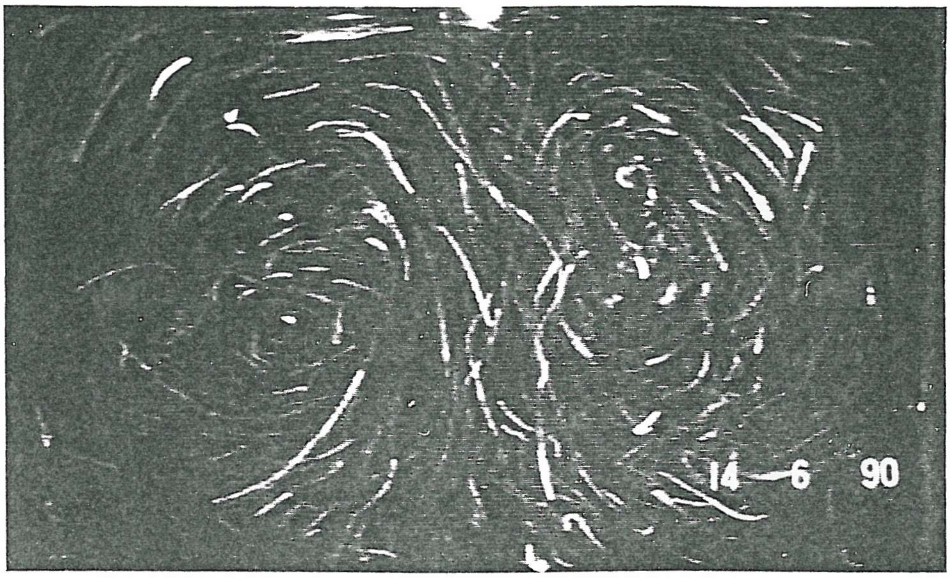

(i) t = 182 minutes

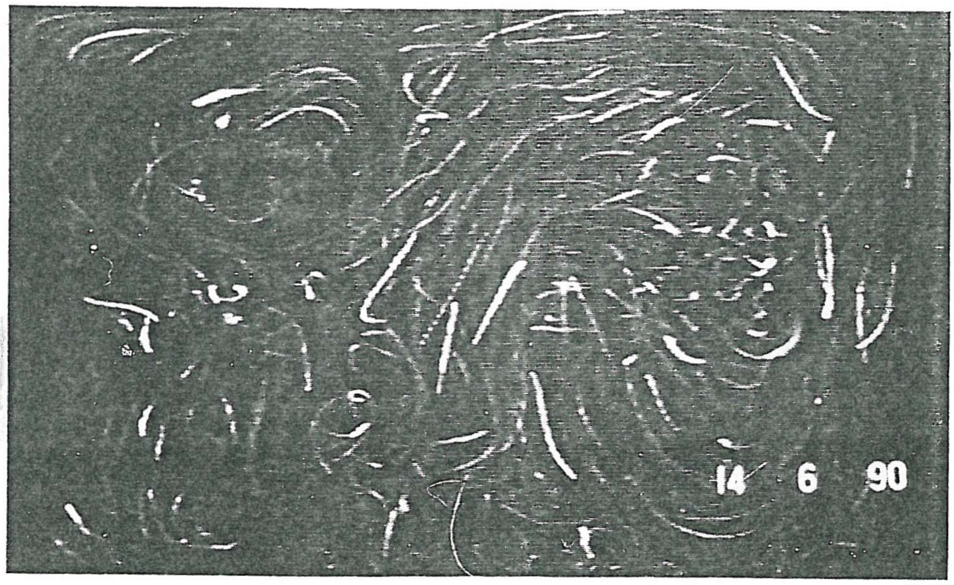

(j) t = 185 minutes

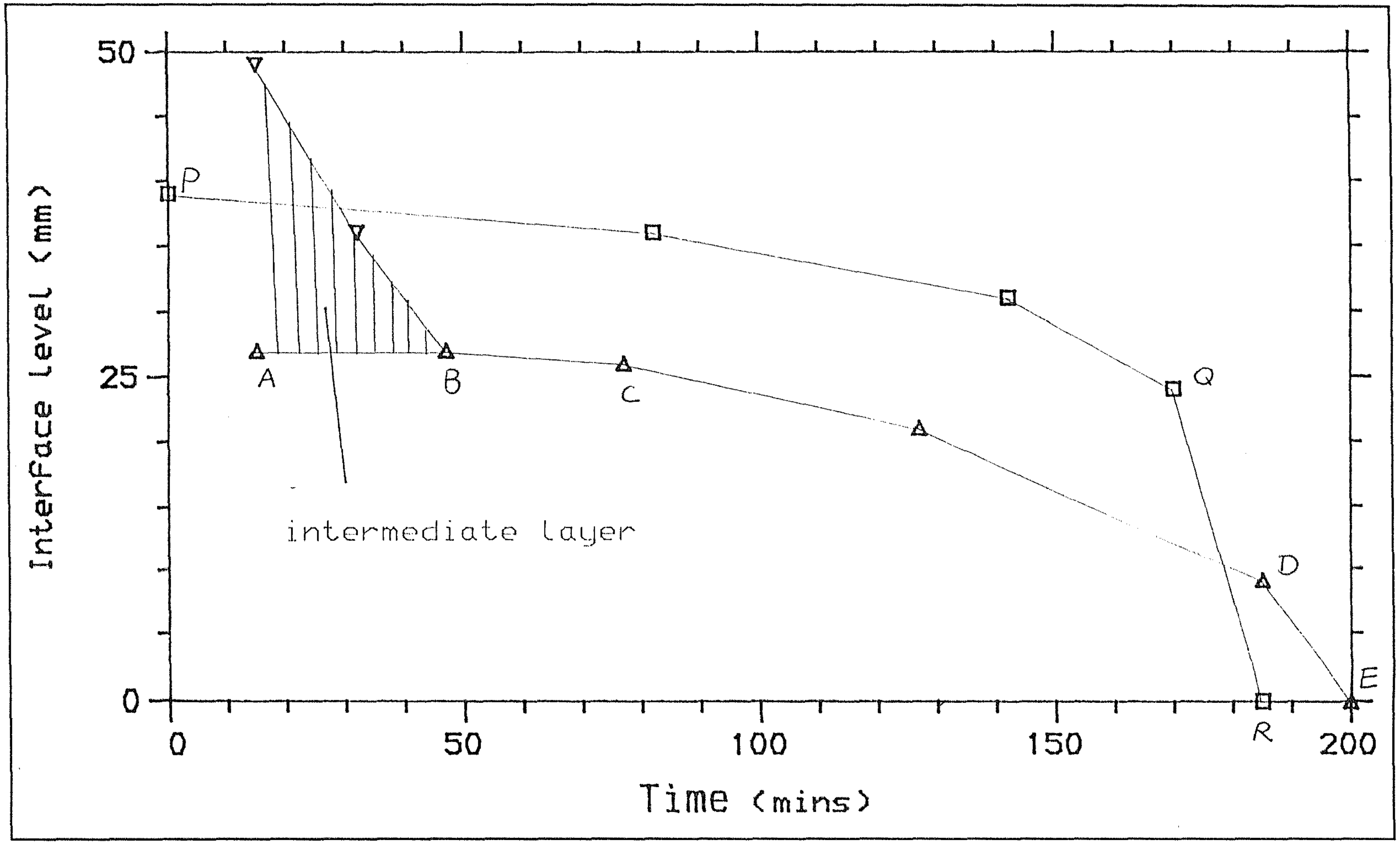

Fig. 6.4 Change of the interface level(s) with time. Δ,∇: side heating only; □: side & base heating.

Photographs b - e, t = 20 - 47 minutes

During this period the core flow of the top is seen to gradually penetrate into the intermediate layer, where the heavier liquid is entrained and mixed into the top layer. Eventually, the intermediate layer is completely mixed into the top layer.

Throughout this stage the interface between the intermediate layer and the bottom layer remains unmoved. This stage corresponds to line AB in Fig. 6.4.

Stage 2 47 - 185 minutes, (photographs e - g)

The migration of the interface

In the first half an hour of this stage(corresponding line BC in Fig. 6.4), the interface level is hardly changed, indicating the density difference between the two remaining layers is still considerable. In the same period, the movement of one particle in the bottom layer is caught. The trajectory of this particle is displayed in Fig. 6.5, from which a glimpse of the flow in the bottom layer may be obtained. Starting from the bottom end of the wall, it takes the particle 70 seconds(the exposure time) to complete the whole journey, of which 12 seconds is spent on the rising part along the wall. This rising speed is calculated to be at least two to three times smaller than that of the core flow of the top loop from photograph e. This ratio between the velocity of the core flow and that of the boundary flow in the lower layer is close to the prediction by the model (see Fig. 5.12).

Photographs f - g, t = 77 - 185 minutes

In this time period (corresponding to line CD in Fig. 6.4) the interface moves down at an increasing speed. Though no clear penetration of the core flow is observed, the impinging of the core flow on the interface is evident. Meanwhile, the interface is getting more and more unstable, indicating the density difference between the two layer is reducing with time.

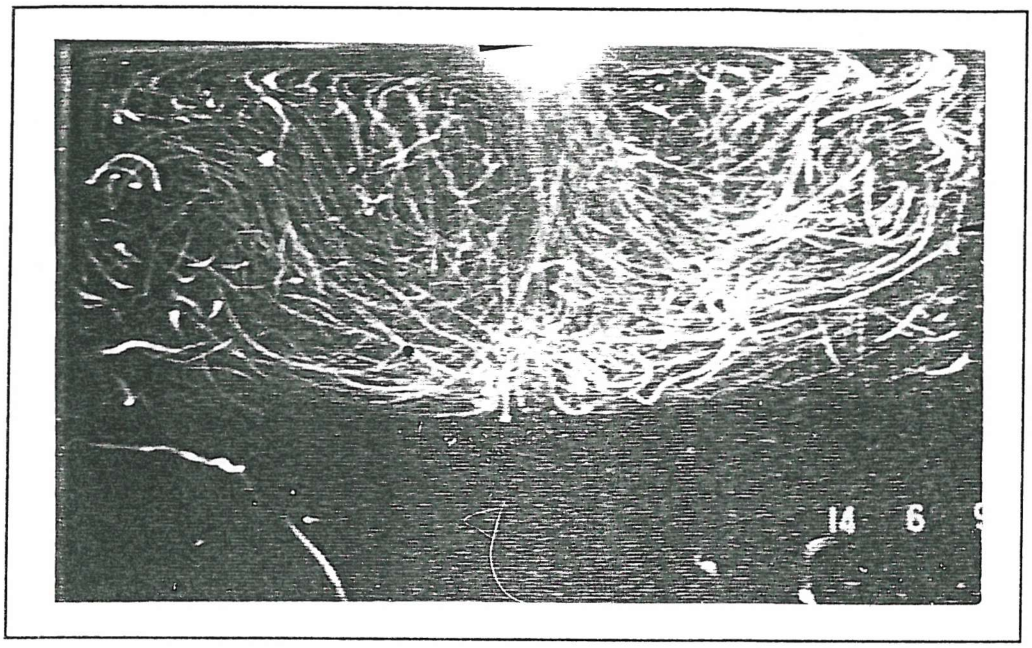

Fig. 6.5 Flow visualization photograph showing the trajectory of one particle in the bottom layer in a period of 70 seconds (side heating only).

Stage 3 185 - 200 minutes, (photographs g - l)
the rapid mixing of layers

The remaining bottom layer(9mm thick) is completely mixed into the top layer within 15 minutes(line DE in Fig. 6.4). The penetration by the core flow, which meanwhile becomes less and less well shaped, is clearly displayed in the photographs.

6.6.2 Side & base heating(Fig. 6.3)

The main flow features observed in this run is very similar to the one described above, notably, the gradual descending of the interface is eventually followed by the rapid mixing of layers. These can be clearly seen in Fig. 6.3 (photographs a - c illustrates the gradual descending of the interface, corresponding to P-Q in Fig. 6.4; photographs d - j shows the intense mixing of layers, corresponding to Q-R in

Fig. 6.4). The main difference lies in the intensity of the final mixing. It can be seen from Fig. 6.4 that the final rapid mixing in this run comes much more suddenly than the previous one in the sense that the bottom layer is still substantial(24mm thick compared to 9mm in the side heating only). Consequently the mixing is more intensified.

It is noticeable from Fig. 6.3 that an intermediate layer is not observed at the beginning. Clearly, mixing of two liquids is unavoidable during the filling of the lower layer, though the extent is closely related to the filling rate and position. It could well be the case, as discussed above, that this time the lower layer is stratified, which one could not see from the picture.

6.7 Discussion

6.7.1 Side Heating Only

It has been shown that the merging of two stratified layers is largely a gradual process characterised by first the gradual descent of the interface, and then the rapid mixing of layers. It is clear that the descent of the interface level is a result of the entrainment mixing at the interface facilitated by the core flow as it impinges on the interface. This observation generally agrees with the prediction by the model, despite the large difference in the Ra^*. When the density gradient at the interface is considerable, the interface is hardly depressed by the core flow, as observed in stage two of the flow development. On the other hand, when the density gradient is small, the core flow is able to penetrate into the layer below, as observed in stages 1 and 3 of the flow development. These features have also been observed by Bains[26] in his study on the entrainment mixing through the end of a forced plume (or jet) as it impinges on a density interface. The final mixing comes as the layer densities become nearly equalized; the core flow in the top layer penetrates into the lower layer while the interface becomes increasingly distorted. Eventually the two layers are completely mixed.

This mechanism of entrainment mixing at the interface is different from that of the boundary layer penetration identified by Morioka et al[10] in their rollover simulation experiments using fresh/salt water and also Nakand et al[11] using liquid freon. In a two-layer system subject to uniform sidewall heating only, the present study has shown that the boundary layer velocity of the lower layer is only a fraction of the velocity of the core flow of the upper layer. This why this boundary layer penetration has not been observed. In homogeneous flows, the existence of a strong core flow is largely due to the cooling effect of an isothermal surface. The absence of this strong core flow in [10] and [11] suggests that the free surface was not isothermal in these two experiments.

Fresh water/salt water stratification was used by Morioka et al in their rollover simulation experiments. Consequently very high heat fluxes(of order of 10^3 to 10^4 W/m^2) were used in order to generate convection of reasonable strength. Subject to such high heat fluxes, the surface temperature of the water is certain to rise from its initial value (ambient temperature). It might be anticipated that the interface would behave close to adiabatic, rather than isothermal. This has been confirmed by the temperature measurements provided in the paper, which is shown in Fig. 6.6. It is thus clear that the surface was not isothermal in Morioka's experiments[10]. It has been shown in chapter 6 that the use of freon 11/113 as flow media could also result in an quasi-adiabatic surface if the vapour dissipation is poor at the surface. In particular, if the tank is sealed at the top (except for venting). Since the test tank was indeed sealed(but with vent) in the experiments performed by Nakand et al, it could well be the case that the surface there was also quasi-adiabatic.

It has been shown that with a quasi-adiabatic surface, a strong core flow does not exist. It is thus not surprising to see that in such a two-layer system (without a strong core flow in the upper layer) mixing is controlled by an entirely different mechanism, such as boundary layer penetration. Clearly, this situation will not arise in cryogenic liquids, since then an isothermal surface is always maintained under atmospheric pressure. Sugawara et al[12] studied rollover in LNG and Agbabi[13] using

LIN/LOX, both report the entrainment mixing as the prime cause for the descent in the interface level.

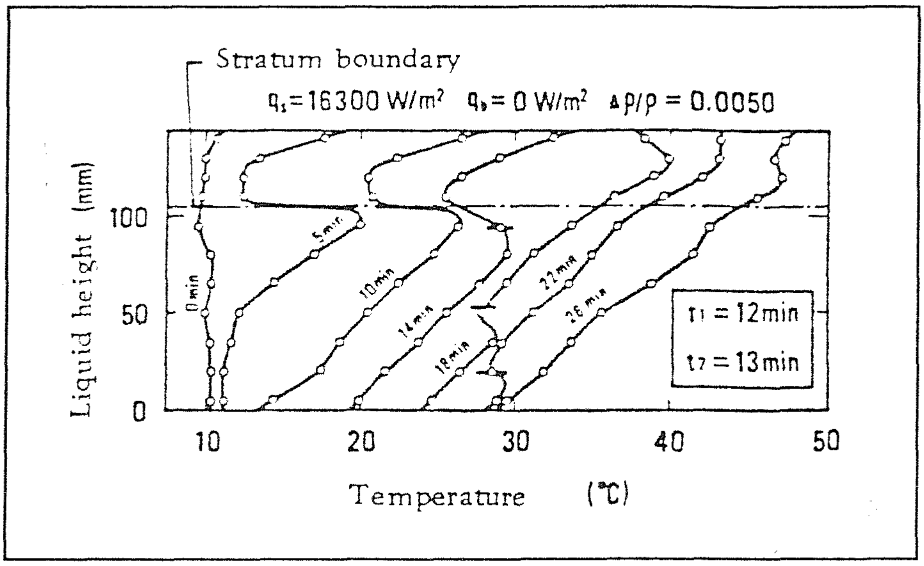

Fig. 6.6 Temperature profiles of water. From Morioka[10].

6.7.2 Side & Base Heating

The merging of two stratified layers under this heating condition is seen to be broadly similar to that of the side heating only, except that the final mixing is more intense and thus the fall in the interface level is sharper. Sugawara et al[12] carried out rollover simulation in a LNG system, where a heat flux of about 30 W/m^2 was supplied to the base as well as the side walls. In all the tests, the interface was observed to fall gradually initially, then descend rapidly before disappearing at the base.

The addition of base heating has two opposing effects on the interface movement: 1) convection generated by the base heat flux will help to maintain a uniform lower layer and a sharp interface; this tends to slow down the downward advancing of the interface. 2) the extra heat into the lower layer liquid would speed up the density equalization between layers (without substantial loss in the volume of the lower layer); this tends to increase the entrainment mixing at the interface. The change in the behaviour of the interface movement is essentially governed by these two factors. In general, the interface will move slower in the period up to the final mixing, but the final mixing will be intensified, resulting in a sharper fall in the interface level.

This effect due to base heating on the intensity of the (final) mixing thus depends on the base to side heat flux ratio. In general, the larger is this ratio, the more severe will be the final mixing. Consider an extreme case in which the heat flux into the base is sufficiently large that the entrainment at the interface by the convective current in the lower layer balances that by the core flow; the interface level would remain unchanged up to the final rapid mixing. This mode of rapid mixing has been reported in a number papers[11], [40] and [41] and is also assumed by most simulation models[4][5][6]. It turns out that for the case of La Spezia rollover, in which the base heat flux was about 3 times as large as the side one, the assumption of a fixed interface before mixing may well be applicable.

7.0 LIQUID-VAPOUR INTERFACE

The Numerical modelling and experimental studies described so far have been concerned with the mixing of stratified layers with the focus on the behaviour of the liquid-liquid interface movement. It has been shown that mixing is controlled by thermal-induced convective flows within separate layers. Now attention will be shifted to the liquid-vapour interface, where a different kind of convection, namely cellular surface convection, is present.

Liquid Surface Morphology

By conducting temperature measurements just below the surface of a column of evaporating LIN, Beduz et al[14] have established the following morphology of the surface layer region shown in Fig. 7.1,

1) The free surface at a temperature slightly above T_0, the temperature of the liquid when it is in thermodynamic equilibrium with its saturated pressure at a prescribed pressure p_0.

2) Immediately below the surface is a thermally conducting layer of a few hundred microns thick and with a steep temperature gradient(temperature increasing with depth).

3) An intermittent convection layer of about 4-5mm thick lies between the thermally conducting layer and a uniform superheated bulk. The cellular convection is believed to be driven by the sinking of cooled elements from the conducting layer due to instability of the colder surface layer.

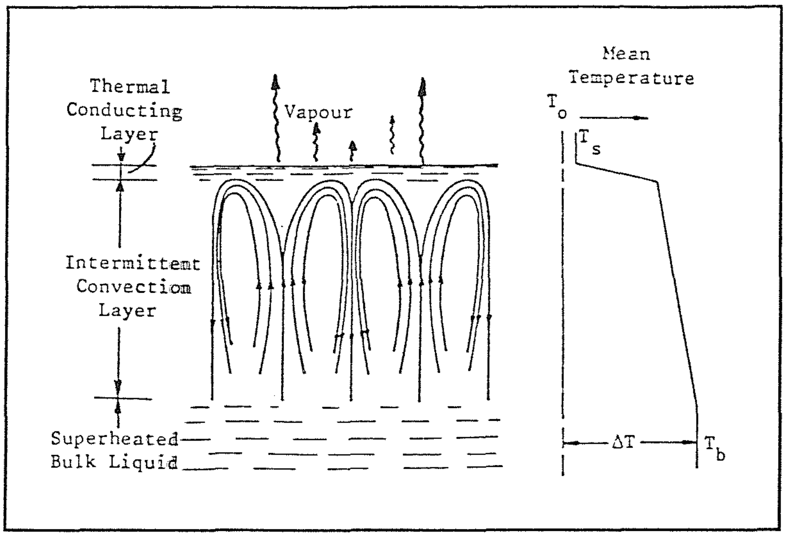

Fig. 7.1 Morphology of surface layers of liquid nitrogen. From Beduz[14].

7.1 Schlieren Flow Visualization

Schlieren flow visualization technique was employed to reveal surface convective patterns of a column of evaporating LIN under different evaporation rates.

7.1.1 Principles and System Assembly

The schlieren method is an optical visualization system which is designed to make refractive index gradient fields of a test medium(fluid) visible as light intensity variations on the image of the medium. Since the refractive index gradient at a point is closely related to the horizontal density (or temperature if no composition is involved) gradient, schlieren images(featuring patterns of bright and dark regions) actually represent the field of temperature gradient of the medium, and therefore can be used to follow the flow in a system where the temperature(or composition) varies with position.

The schlieren optical system used in this experiment is shown in Fig. 7.2, with the detail of the dewar given in Fig. 7.3. Parallel light rays entering the testing tube *e* are

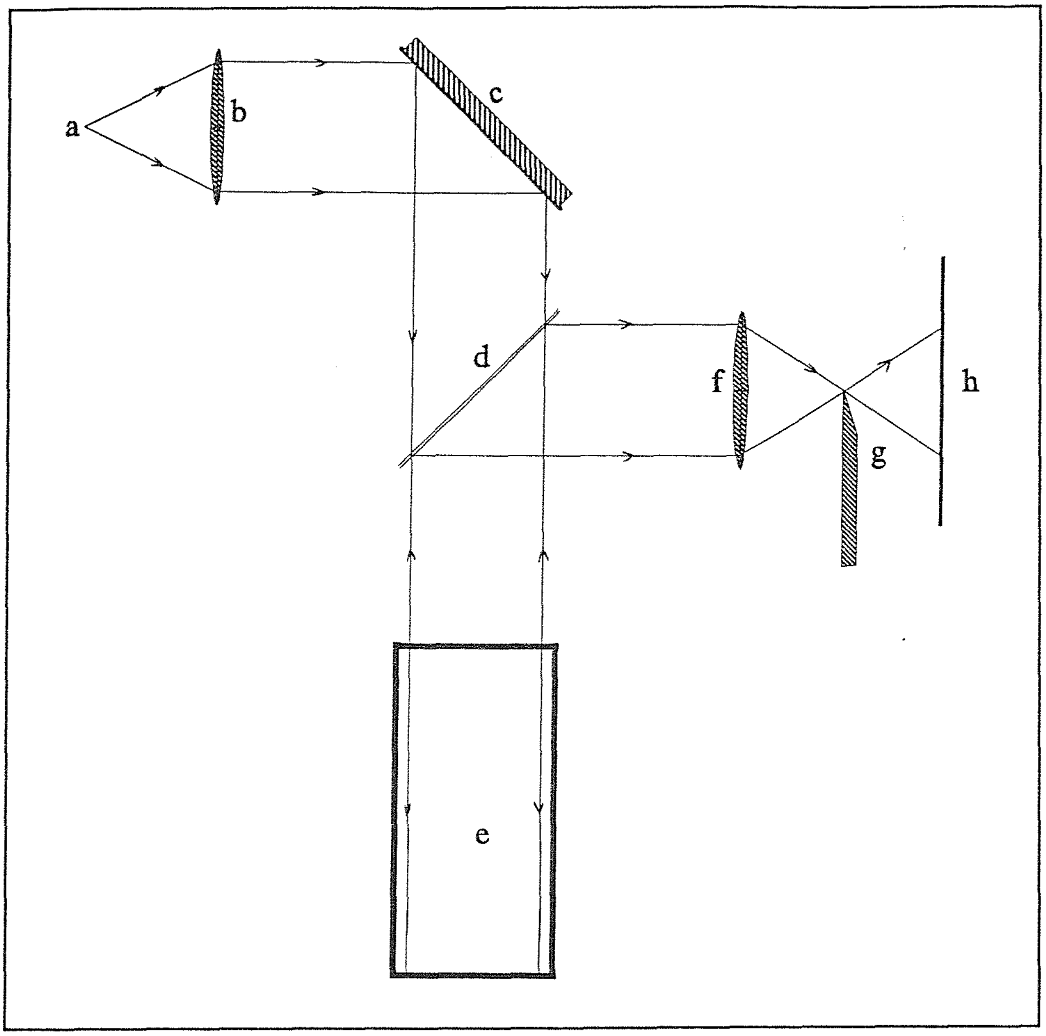

Fig. 7.2 Schlieren flow visualization system.

a: light source, b: lens, c: reflecting mirror,

d: semi-reflecting mirror, e: Schlieren dewar,

f: lens, g: knife edge, h: screen or camera.

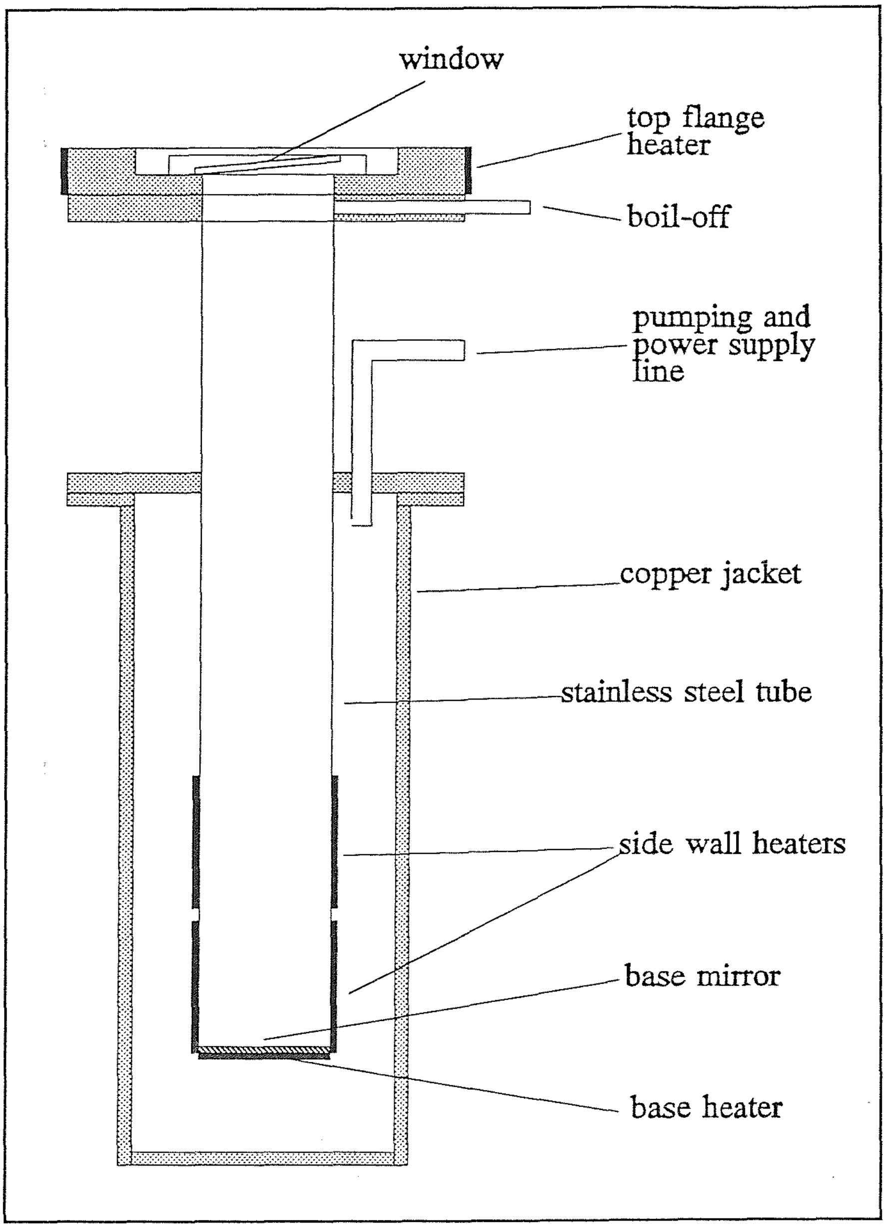

Fig. 7.3 Dewar for Schlieren flow vivualozation.

reflected back by the stainless steel mirror base before reaching the screen or camera *h*, on which an image of the medium is formed (note the medium is passed through twice). The key device is the adjustable knife-edge *g* situated at the focal plane of lens *f*. Cutting off part or all of the light source image produces an image corresponding to the inhomogeneities in local temperature distributions. It should be noted that, theoretically, what appears on the screen represents the integrated horizontal refractive index gradients over (twice) the entire depth of the liquid. The greatest temperature gradients however, occur at the liquid-vapour surface. Therefore time varying flow patterns at the free surface are actually observed.

Note that the top small glass plate for viewing was set slightly inclined to eliminate possible reflections from it. The top flange heater was installed to keep the viewing window free from any moisture generated during experiments. In order to reduce heat leak from the surroundings, the whole length of the outer copper casing was immersed into a LIN bath provided by another glass dewar.

7.1.2 Results and Discussion

Visualization studies were performed on a column of evaporating LIN. In all five Schlieren photographs (prints 1-5) are presented here. Prints 1 & 2 show surface flow patterns in the absence of sidewall heating. After the completion of filling, the liquid was pumped for a while to be sub-cooled. The whole body of liquid was then in equilibrium with its vapour pressure. At this stage, no motion could be observed. The equilibrium, however, was not stable due to heat leaking in from the surrounding; evaporation of vapour will increase the vapour pressure towards one atmosphere. Print 1 was taken when the liquid was still slightly sub-cooled. Prints 2 was taken some time later after the saturation was reached. Prints 3 to 5 were taken in a separate experimental run. They illustrate surface patterns at three steady states, corresponding to three different sidewall heat fluxes. The pool of liquid was about 2 to 3cm deep.

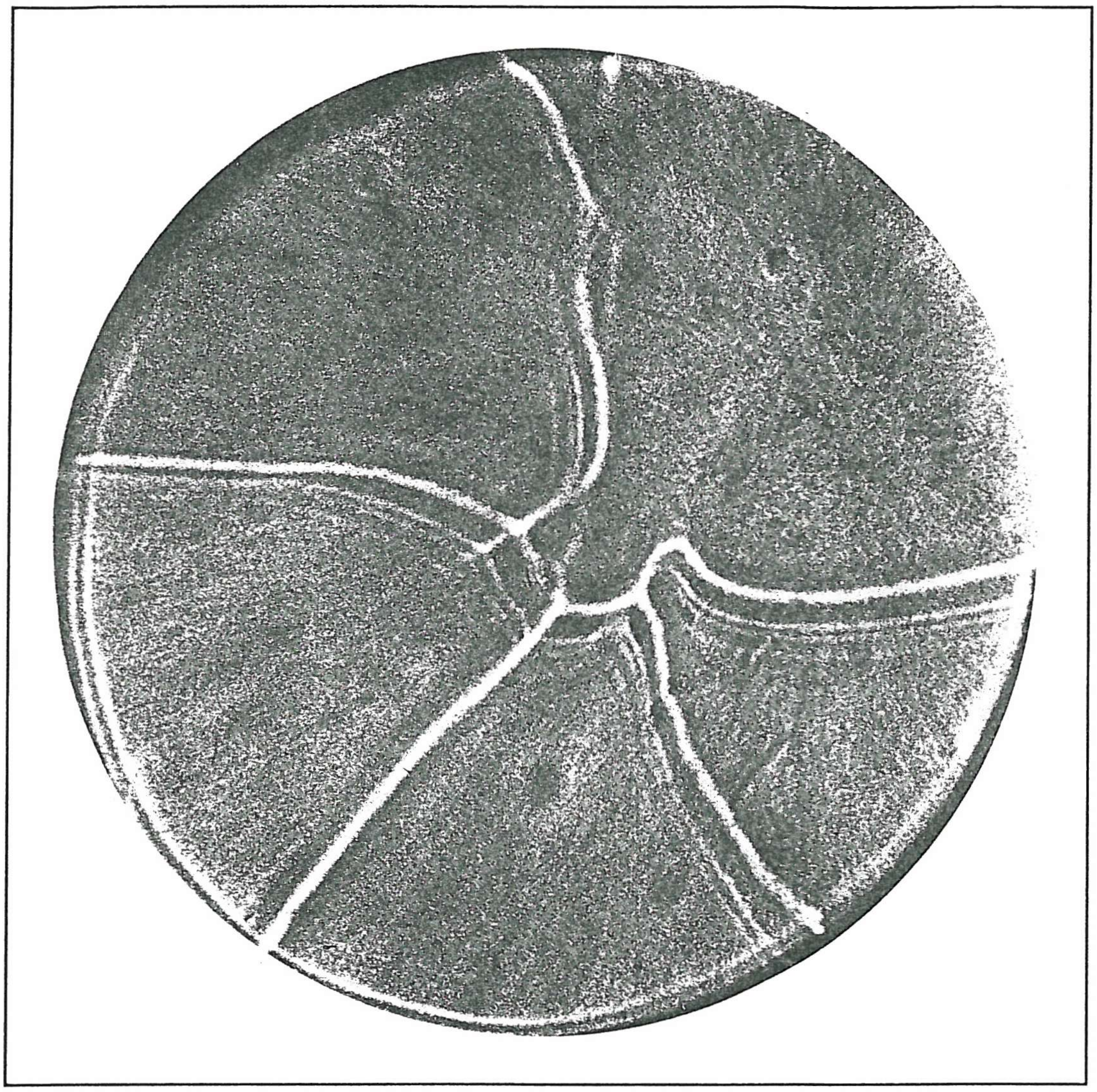

Print 1: Schlieren photograph showing randomly-moving streamers; no electrical heat was applied.

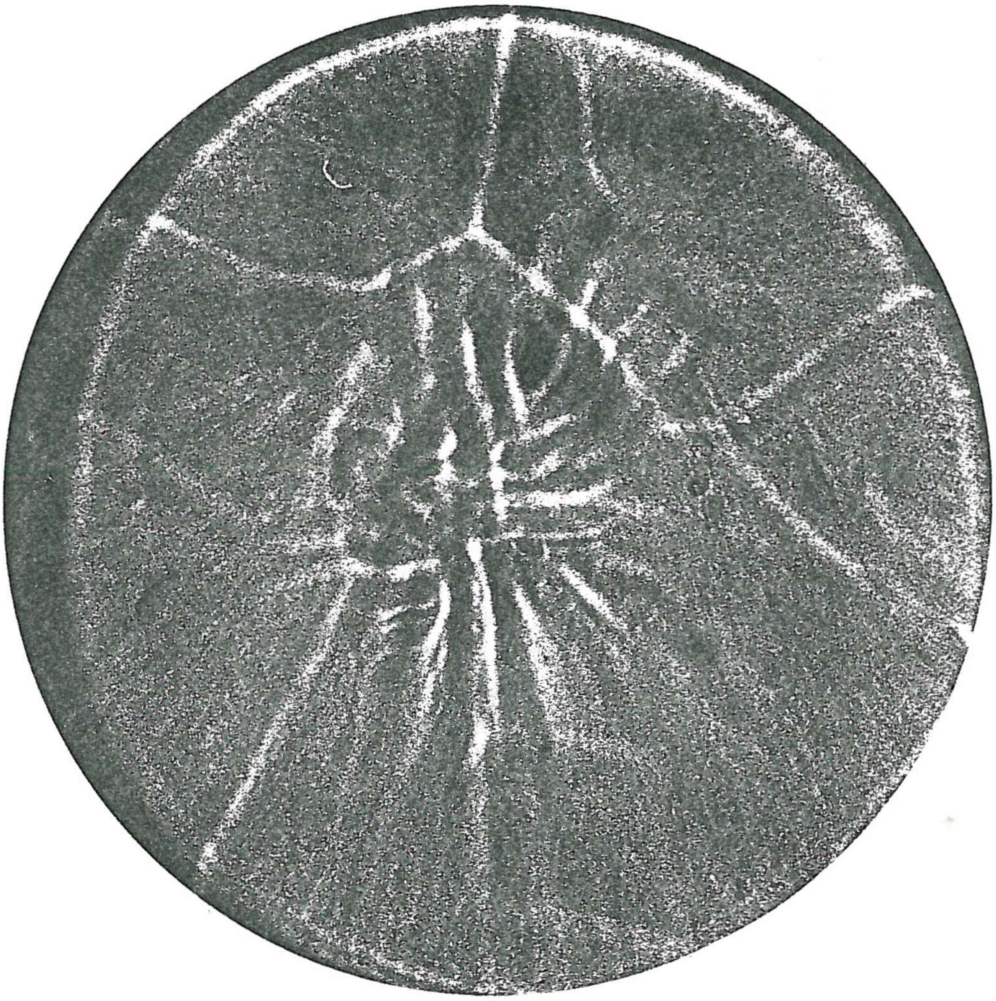

Print 2: Schlieren photograph showing a sudden break up of instability in the cold surface layer; no electrical heat was applied.

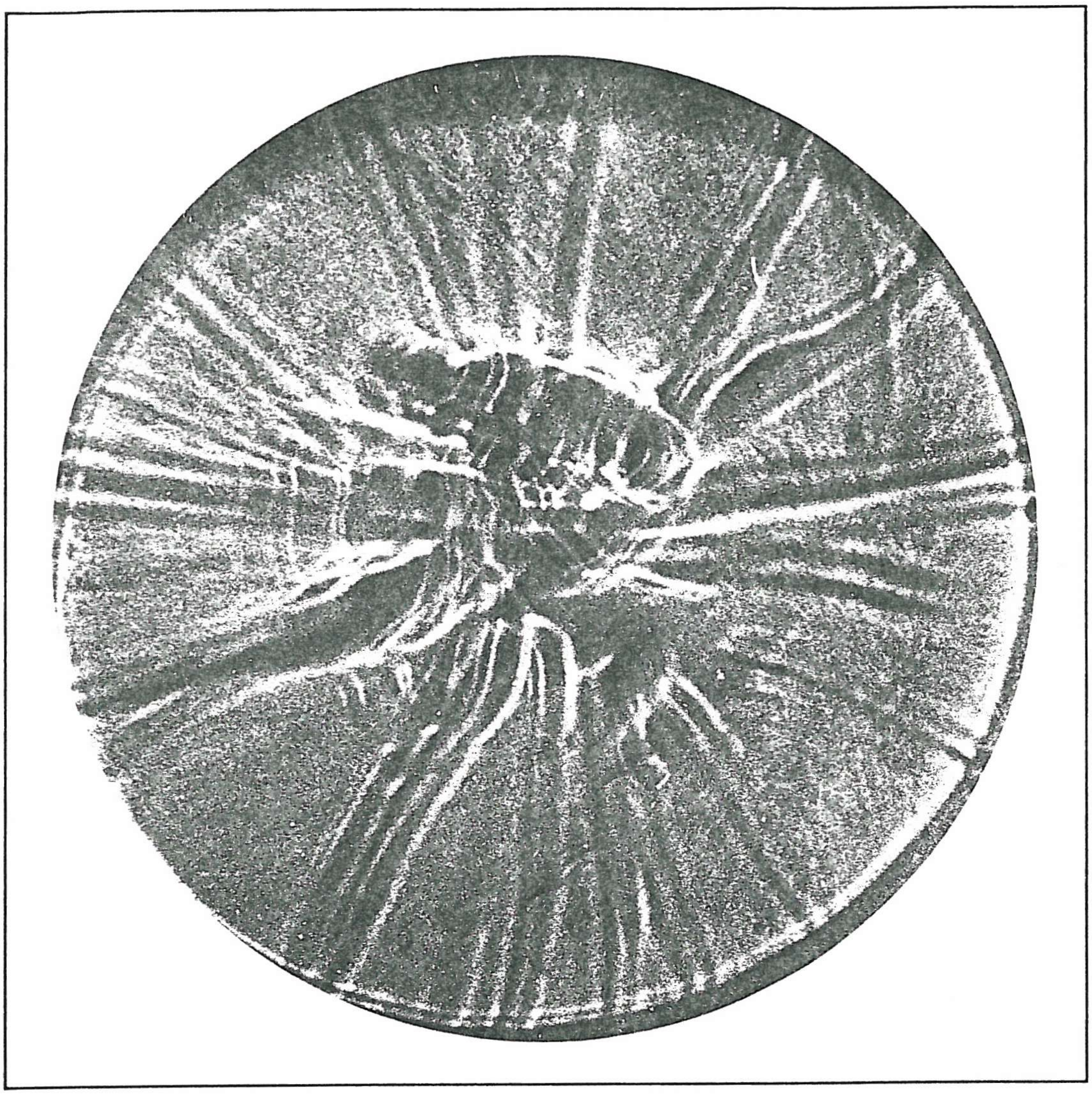

Print 3: Schlieren photograph showing radially aligned streamers; the liquid was 2-3cm deep and subject to a uniform wall heat flux of 19 W/m^2.

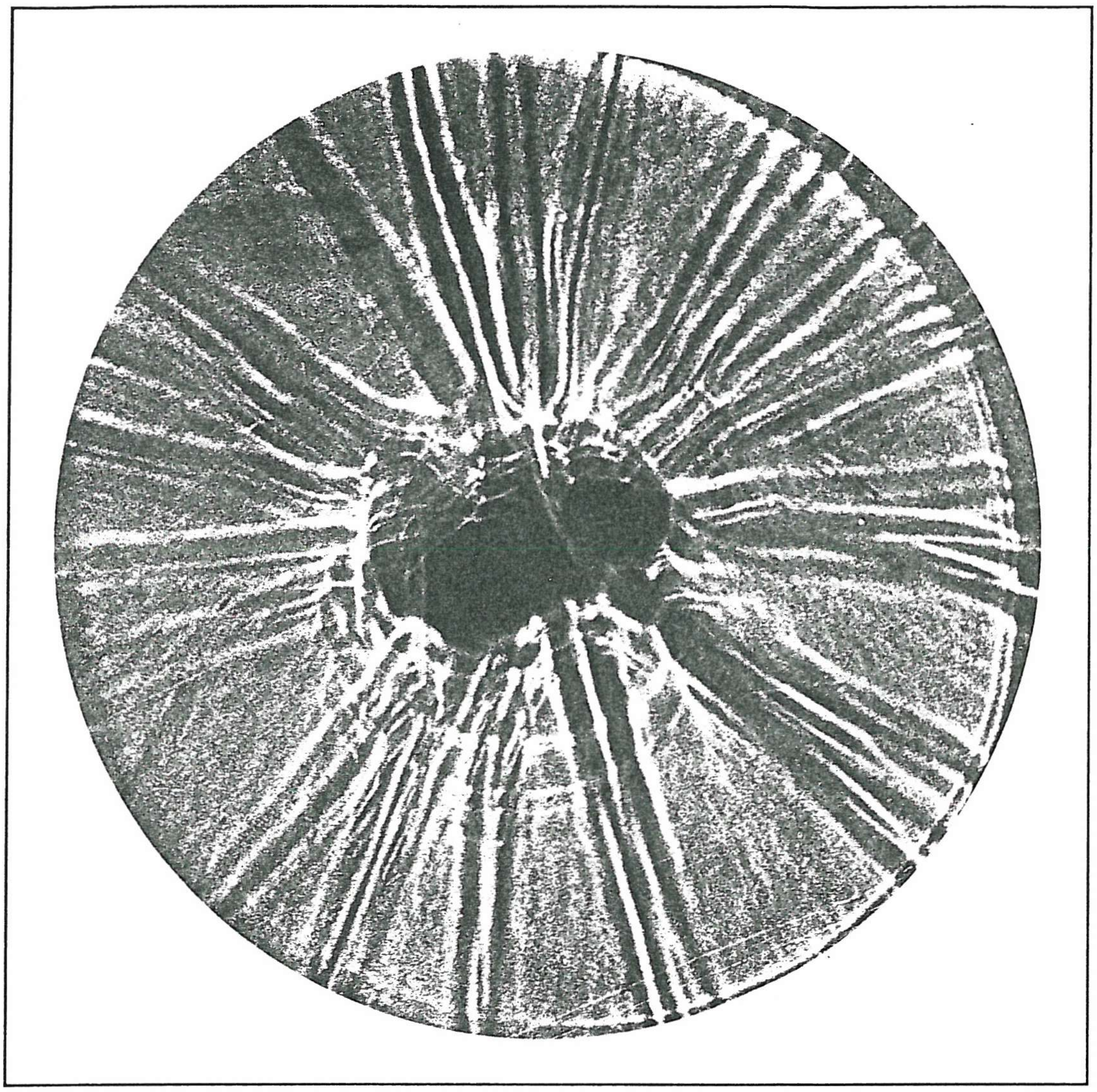

Print 4: Schlieren photograph showing radially aligned streamers; the liquid was 2-3cm deep and subject to a uniform wall heat flux of 34 W/m^2.

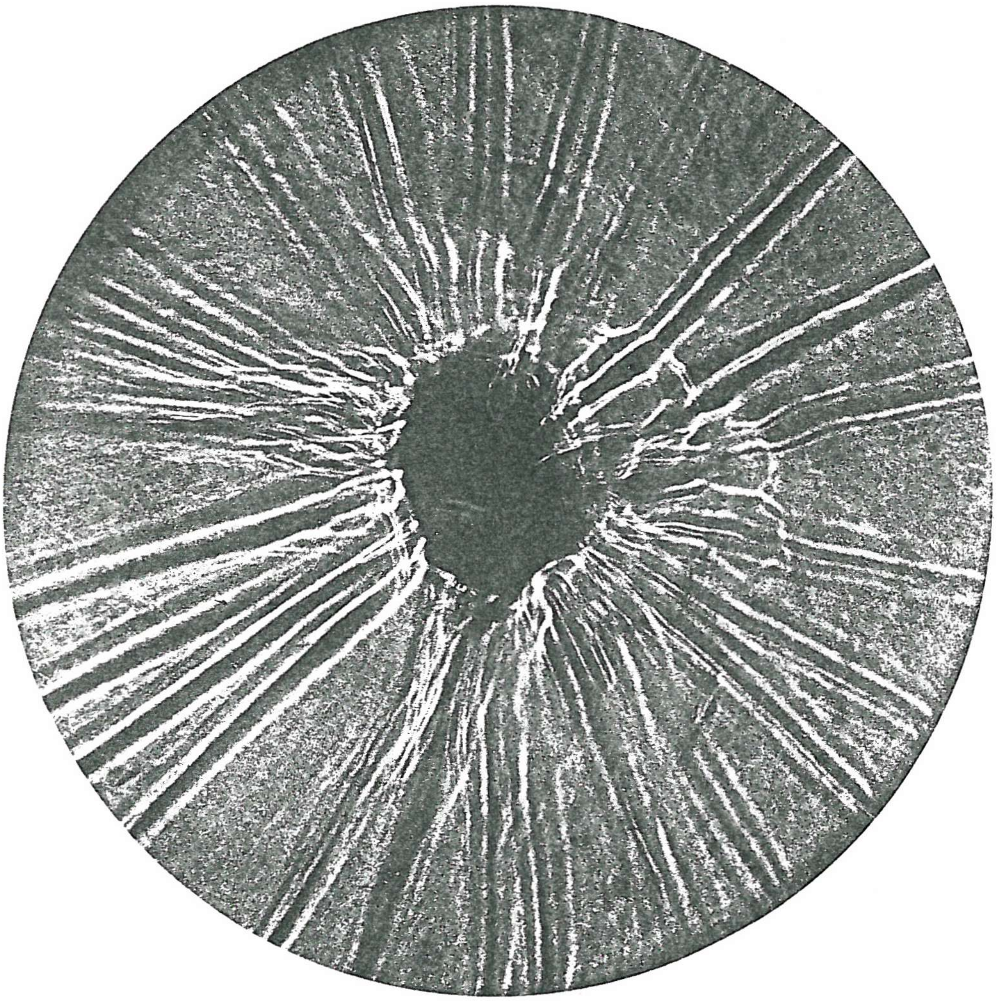

Print 5: Schlieren photograph showing radially aligned streamers; the liquid was 2-3cm deep and subject to a uniform wall heat flux of 76 W/m^2.

Before discussing these schlieren photographs, it might be helpful to summarise some previous results. Spangenberg & Rowland[37] studied convective circulation in water induced by evaporation cooling using the schlieren method. For liquid depth not less than 1cm, distinct bright lines, called streamers, were observed. These were thickened lines along which liquid would plunge into the bulk in sheets as a result of local instability of the cooled surface layer.

Berg[38] carried out a systematic study on evaporative convection patterns for a variety of pure liquids. Three convective patterns were identified for pure liquids.

a) Cellular convection similar to those observed by Benard[39], in which hot liquid rises in the centre of each cell then cools and descends along the cell periphery;

b) Streamers, along the length of which cooled liquid would plunge down in sheets, as illustrated in Fig. 7.4;

c) Ribs, consisting of intersecting streamers where the
cold liquid moves down and between which hot liquid rises to the surface.

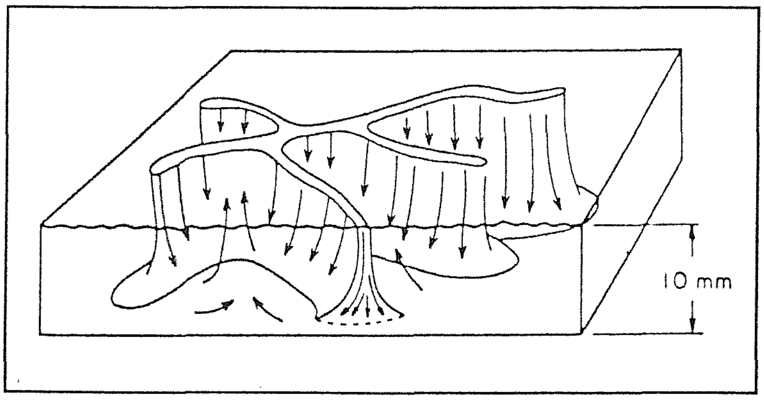

Fig. 7.4 Evaporative convection in cold streamers: cold fluid plunges along distinct lines in the surface and warm fluid rises slowly in the area between the streamers. From Berg[38].

Now the Schlieren photographs taken in the present study may be discussed. Print 1 shows streamers moving about at the surface. These streamers exist for only a few seconds before fading out. Print 2 shows a sudden break out of instability at the centre of the surface layer, resulting in the simultaneous plunge of sheets of cooled liquid.

In prints 3, 4 & 5 the streamers are seen aligned radially with the flow directions of the bulk convective loop at the surface. Sheets of cooled liquid plunge along the bright lines, between these warm liquid rise towards the surface. These patterns appear quasi-steady: some streamers fade while some emerge, but the overall pattern remains almost unchanged. The number density of streamers is seen to increase as the surface heat flux is increased. There appears to be a linear relationship between streamer density and surface heat flux, from which the streamers appear to have a evaporation mass flow per unit length associated with them.

A central dark region is observed in prints 4 and 5. This change in the light deflection from print 3 to print 4 suggests the (horizontal)temperature gradients in the central region underwent a dramatic change. A possible reason for this is that the central jet has entered the transient or turbulent region. The Ra^* associated with prints 3 and 4 is about of order 10^8, which is close to the prediction by the one-component model for buoyancy-induced convective flows in a square cavity.

7.2 Surface Heat Flux vs Bulk Superheat

Based on the thickness of the thermally conducting surface layer δ(and a temperature difference ΔT across it), a Rayleigh number $Rb = g\beta_T \Delta T \delta^3/\alpha\nu$ is defined by Atkinson et al[40] following Howard[41]. This Rayleigh number determines the condition for sustaining the cooled surface layer. (Note it is not the convectional one used to predict the onset of convection). δ may be expressed as

$$\delta = \left(\frac{\alpha\nu}{g\beta_T}\right)^{1/3} Rb^{1/3} \Delta T^{-1/3} \tag{7.1}$$

Assuming that the heat transfer across the thermally conducting surface layer is dominated by conduction, one obtains the correlation between the surface heat flux $\dot{q}$ and ΔT

$$\dot{q} = C_b \Delta T^{4/3} \tag{7.2}$$

where

$$C_b = kRb^{-1/3}\left(\frac{g\beta_T}{\alpha\nu}\right)^{-1/3} \tag{7.3}$$

This power law dependence of $\dot{q}$ on ΔT is identical with the Hashemi-Wesson formulation. Measurements performed on a range of cryogens by Rebiai[42] have generally confirmed this power law relationship. This dependence, however, was found to grossly underestimate the peak boil-off rate at La Spezia rollover. Otherwise, to match the 250 times increase in vapour flow rate recorded, a superheat of tens of degrees of kelvin is required, which is clearly not possible.

From the consideration of Ra^* number, wall boundary flows in Rebiai's experiments were in the laminar region. This means the radially inward surface flows were probably also laminar. Wall boundary flows associated with full scale LNG tanks and therefore the surface flows are, however, well into the turbulent region. From the nature of turbulence, it is reasonable to assume that the surface heat transfer will be enhanced in the latter case. The purpose of this experimental study was to see whether the 4/3 power, which has been confirmed for laminar surface flows, would alter if the flows become turbulent. An increase in the power might provide a clue to the huge peak evaporation rates observed in rollover events.

7.2.1 Experimental System

The experimental system is shown in Fig. 7.5. The double-walled glass dewar has up to 180cm high heated wall length(compared with 20-30cm in Rabiai's experiments). The diameter of the inner dewar is 6.5cm. Electrical heating is provided by thin constantan strips glued onto the inner wall in the vacuum space. Silicon rubber dissolved in toluene has been successfully used to bridge the considerable gap in thermal contraction between the glass wall and constantan heaters down to LIN temperature. The whole heated length is divided into three heaters: from bottom up, heater 1 (120cm), heater 2 (20cm) and heater 3 (40cm). From simple combinations, three different heating lengths are available, namely 120cm, 140cm and 180cm. In the experiments, a silicon diode thermometer was used for temperature measurements and a shell flow meter for the vapour flow rates. The sensor head is shielded by a copper case to prevent the sensor head, which is a potential source for nucleate boiling, from making contact with the working liquid to reduce the chance of nucleate boiling[43] in the superheated liquid.

7.2.2 Results and Discussion

Measurements of the bulk temperature T_b and surface vapour flow rate were carried out for three different layer depths of liquid (corresponding to the three heating lengths). The surface heat flux $\dot{q}$ is related to $\dot{m}$ by $\dot{q} = \dot{m}La$, where La is the latent heat of the testing liquid. For each liquid level, a range of heat fluxes was used to obtain a number of points. In each run, the heat flux was increased after the steady state was reached. This increase in the heat flux continued until the occurrence of nucleate boiling in the superheated liquid. At this point this particular run was abandoned. The measurements from all the three layer depths of liquid, together with Rebiai's data for LIN, are shown in Fig. 7.6 in log-log scale.

The data points with the 120cm and 140cm heating length are consistent and also in agreement with Rebiai's results. The straight line (AB) fitted to the data from these

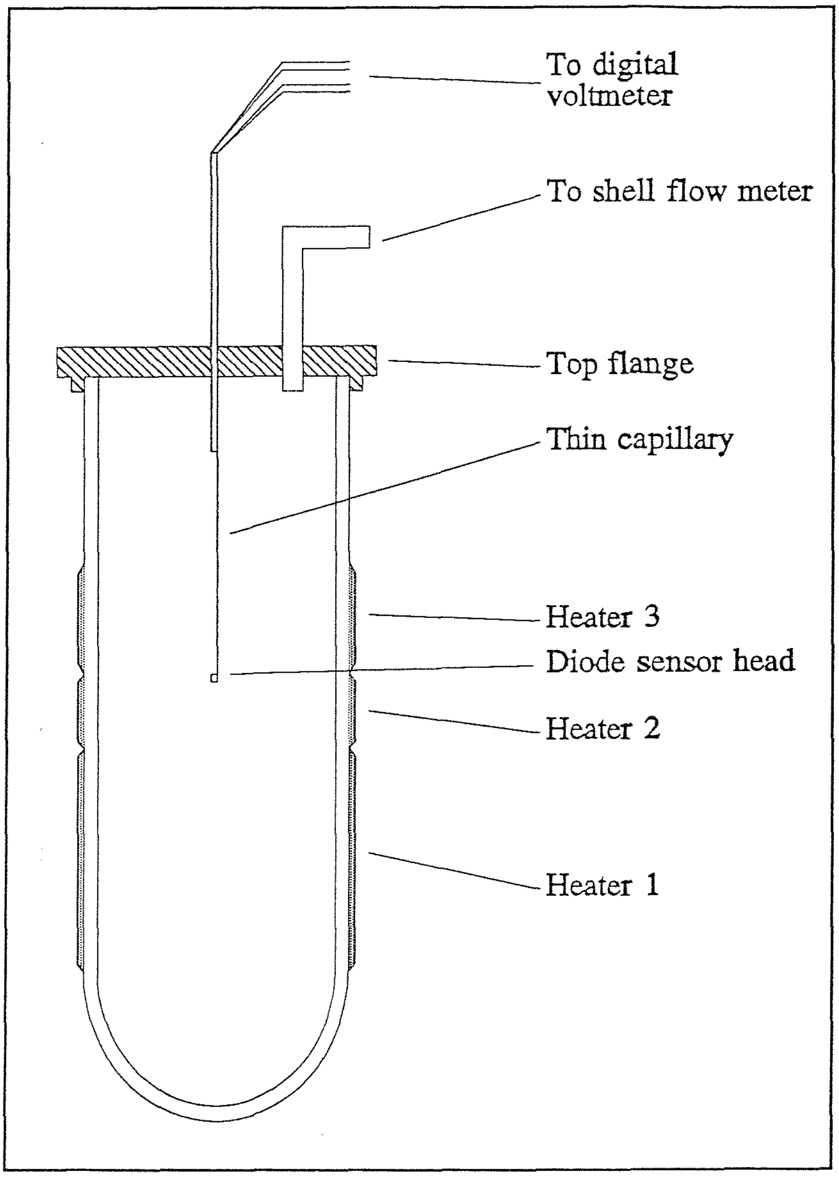

Fig. 7.5 Experimental system for simultaneous measurement of liquid temperature and surface evaporation rate.

two heating lengths may be expressed in the measurement range as

$$\dot{q} = 560\Delta T^{4/3} \qquad W/m^2 \tag{7.4}$$

The data points from the 180cm heating length, however, indicate a correlation (line CD) with a steeper slope(higher power law) but a smaller proportional constant than line AB. This deviation is not due to the difference in the modified Rayleigh number, since the range of Ra^* covered in all three heating lengths are about the same. A possible explanation comes from the consideration of the wall boundary layer thickness as the heated wall length is increased. Given the small inner diameter of the dewar used, the wall boundary layers could interfere with each other if the heated wall length is sufficient large, and therefore the temperature measurement might be distorted.

Estimations of the thickness of the wall boundary layers associated with the present experiments were made using Bayley's[44] analysis of turbulent free convection along a vertical wall. Calculations show that the thickness of the boundary layers are comparable with or even greater than the radius of the dewar for all the three heating lengths.

The modified Rayleigh numbers in the present measurements were all above 10^{14}. This means that, according to the measurements by Vliet et al[45], the boundary layer flows were in the fully turbulent region. The results of this experiment therefore have demonstrated that the 4/3 power law which controls the surface heat flux for a given bulk superheat holds for turbulent boundary flows as well as laminar flows.

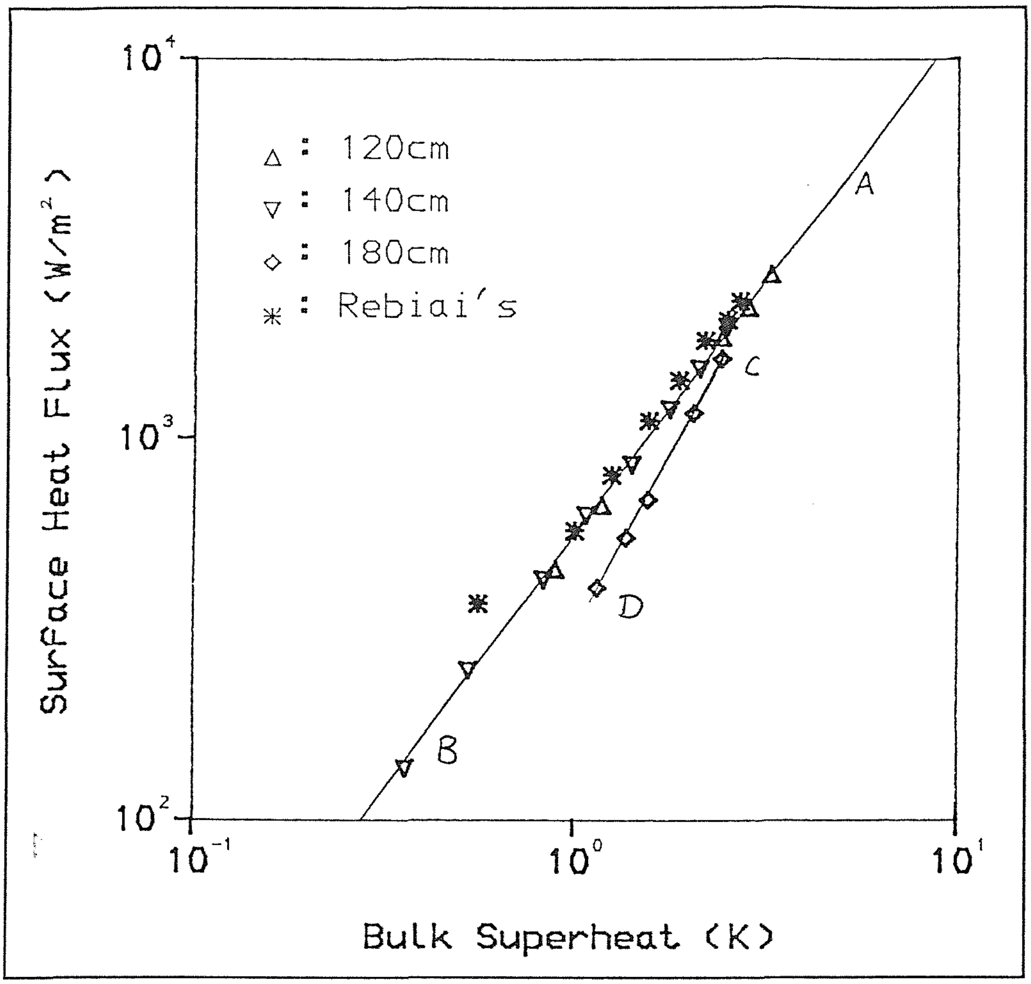

Fig. 7.6 The measured surface heat flux against bulk liquid superheat in liquid nitrogen; AB line is fitted to the data with 120 and 140cm heating length and CD line to 180cm heating length. The data by Rebiai[42] is also included.

CHAPTER 8 CONCLUSIONS

From this combined numerical and experimental study into LNG rollover, the following conclusions can be drawn.

1) In a two-layer system of cryogenic liquids (under atmospheric pressure), the free surface is almost isothermal, whereas the liquid-liquid interface is quasi-adiabatic. Consequently, buoyancy-induced convective flows in the two layers are distinctively different. Due to the cooling action of an isothermal surface, a strong core flow exists in the upper layer; in contrast, high fluid velocity is confine to the boundary layer in the lower layer.

2) Mixing of layers is primarily duo to entrainment of liquid at the interface through the core flow as it impinges on the interface; when the density difference across the interface is small, the core flow penetrates into the interface. The boundary layer penetration from the lower layer has not been predicted nor observed. This is because the boundary velocity of the lower is only a fraction of the core flow velocity. It has been shown that in Morioka's experiment, where the boundary layer penetration observation was first made, the surface was not isothermal but close to adiabatic, therefore a strong core flow did not exist in the upper layer. This situation corresponds a closed storage tank.

3) The ratio of base to side heat flux has a strong influence on the mixing pattern. The intensity of the final mixing between layers is closely linked to this ratio. Generally a higher flux ratio would lead to a more intensified final mixing.

4) The 4/3 power law correlation between the surface heat flux and bulk superheat is valid for both laminar and turbulent wall boundary layers.

5) Schlieren flow visualization studies show the formation of streamers as a result of local instability of the colder surface layer. For a pool of liquid nitrogen under uniform side heating, radially aligned streamers are observed. The number density of these streamers increases as the wall heat flux is increased.

RECOMMENDATIONS

1) A three dimensional turbulent model is required to simulate rollover at higher (modified) Rayleigh numbers.

2) Detailed measurements of entrainment mixing at the interface through the core flow as it impinges on the interface would be useful.

3) To study surface convection, local vapour flow rate measurements just above the surface, using say fast response hot-wires, may reveal the distribution of surface evaporation.

4) A turbulent boundary layer does not alter the 4/3 power dependence of the surface heat flux on the bulk superheat. An investigation into the effect of the destruction of the surface layer is highly desirable. The collapse of the surface layer may be achieved by upward plumes or thermals or rising bubbles initiated from point-sources within the bulk liquid.

ACKNOWLEDGEMENTS

I wish to thank Dr. C. Beduz for his supervising throughout this project.

I also wish to thank Dr. M. Burton for his valuable contribution to and advise on the numerical modelling side of the project.

I am grateful to Professor R. G. Scurlock for his encouragement and support given to me during the years.

I am also grateful to Dr. R. Webb for his many fruitful discussions.

My thanks go to I. Mears, M. Webb, and other staff of the institute who have helped me, and students past and present whose comments proved useful.

Finally, I wish to thank the British Council and the State Committee of Education, People's Republic of China for awarding me a scholarship to study in the United Kingdom.

REFERENCES

[1] Sarsten (1972), ' LNG Stratification and Rollover', Pipeline and Gas J. Vol. 199, p. 37.

[2] Bellus, Reveillard, Bonnawe & Chevalier (1977), ' Essais au terminal de fos sur le comportment du LNG dans les grands reservoirs' LNG Conference Papers 5.

[3] Chatterjee & Geist (1976), ' Spontaneous Stratification in LNG Tanks Containing Nitrogen', ASME Winter Annual Meeting, Paper 76-WA/P.10-6 .

[4] Chatterjee & Geist (1972), 'The Effects of Stratification on Boil-off Rates in LNG Tanks', Pipeline and Gas J. Vol. 199, p. 40.

[5] Germeles (1975), 'A Model for LNG Rollover', Advances in Cryogenics Engineering, Vol. 21 P. 330.

[6] Heestand, Shipman & Meader (1983), 'A Predictive Model For Rollover in Stratified LNG Tanks', AICHE Journal 29 No 2 P. 199-207.

[7] Turner (1965), 'The coupled Turbulent Transports of Salt and Heat Across a Sharp Density Interface', Int. J. Heat Trans. Vol. 8, p. 759.

[8] Huppert (1971), 'On the Stability of a Series of Double-diffusive Layers', Deep-Sea Res. Vol. 18, p. 1005.

[9] Heshemi & Wesson (1971), 'Cut LNG Storage Costs', Hydrocarbon Process, p. 117-120.

[10] Mikio Morioka & Shitaro Enya (1983), 'Natural Convection of Density-Stratified Layers in a Vessel I', Heat Transfer Japanese Research 12(4): 48.

[11] Nakand, Sugawara & Yamagata (1982), 'An Experimental Study on the Mixing of Stratified Using Liquefied Freon', Gastech.

[12] Sugawara, Kubota & Muraki (1983), 'Rollover Test in LNG Tank and Simulation Model', ACE(Colorado Springs) Vol. 29, p. 805-811.

[13] Agbabi (1985), Ph.D Thesis, Southampton University.

[14] Beduz, Rebiai & Scurlock (1984), 'Thermal Overfill, and the surface Vaporization of Cryogenic Liquids under Storage Conditions', Adv. Cryo. Eng. Vol. 29, P. 795.

[15] Maher & Gelder (1972), 'Rollover and Thermal Overfill in Flat Bottom LNG Tanks', Pipeline and Gas Journal, P. 46.

[16] Stommel et al (1965), ' An Oceanographical Curiosity: the Perpetual Salt Fountain', Deep-Sea Res. 3,152-3.[pp252].

[17] Stern (1960), 'the 'Salt Fountain' and Thermohaline Convection', Tellus.12,172-5.[pp252-258].

[18] Veronis (1965), 'On Finite Amplitude Instability in the Thermohaline Convection', J. Mar. Res. 23,1-17.[pp253-259].

[19] Bains and Gill, 'On Thermohaline Convection with Linea Gradients', J. Fluid Mech. 37,289-306. [pp253,256]

[20] Neild, 'the Thermohaline Rayleigh - Jeffreys Problem', J. Fluid Mech. 29,545-58. [pp.253,263]

[21] Turner (1979), 'Buoyancy Effects in Fluids', Cambridge University Press.

[22] Turner (1965) 'the Coupled Turbulent Transports of Salt and Heat Across a Sharp Interface', Int. J. Heat and mass Trans. 8, 759-67. [pp.274,276].

[23] Rouse and Dodu (1956), 'Turbulent Diffusion Across a Density Discontinuity', La Houille Blanche,10,530-2. [pp.289,295].

[24] Cromwell (1960), 'Pycnoclines Created by Mixing in an Aquariun Tank', J. Mar. Res. 18,73-82.[p.289].

[25] Turner (1968), ' The Influence of Molecular Diffusivity on Turbulent Entrainment Across a Density Interface', J. Fluid mech. 33, 639-56 [pp.290,296].

[26] Bains (1975), 'Entrainment by a Plume or Jet at a Density Interface', J. Fluid Mech. 68, 309-20. [pp.296,307].

[27] Patankar (1980), 'Numerical Heat Transfer and Fluid Flow', Hemisdhere Publishing Corproration.

[28] Gosman et al (1969), 'Heat and Mass Transfer in Recirculating Flows', Academic Press, London.

[29] Tritton (1977), 'Physical Fluid Dynamics', Van Nostrand Reinhold (UK) Co. Ltd.

[30] Davis (1983), Inter. J. for Numerical Methods in Fluids, Vol. 3, p. 249-264.

[31] Krichevsky (1936), et al, Phys. Chemie(A), 176, p. 338.

[32] Wilke & Changs (1955), AICHE J., Vol. 1, p. 264.

[33] Reddy & Doraiswamy (1967), Ind. Eng. Chem. Fundam, Vol. 6, p. 77.

[34] Wolfgang Merzkirch (1974), 'Flow Visualization', Academic Press.

[35] Kamiya et al (1985), Aut. Mtg. Am. Soc. Mech. Engrs., New York, USA.

[36] Morriso & Richardson (1990), 'An Experimental Study of the Instability of Stratified Layers and Rollover in LNG', Proceedings of Low Temp. Eng. And Cryogenics Conference, Southampton, UK.

[37] Spangenberg & Rowland (1964), Physics of Fluids, Vol. 18, p. 513.

[38] Berg (1964), Phd. thesis, University of California, Berkeley, California.

[39] Benard (1901), Ann. Chim. Phys., Vol. 23, p. 62.

[40] Atkinson et al (1984), 'Heat and Evaporation Mass Transfer Correlation at the Liquid-Vapour Interface of Cryogenic Liquids', International Cryogenic Engineering Conference, Helsinki.

[41] Howard, 'Convection at High Rayleigh Number', Proc. 11th Int. Cong. & App. Mech. Berlin, p. 1109-1115, 196.

[42] Rebiai (1985), Phd Thesis, University of Southampton.

[43] beduz, Rebiai & Scurlock (1982), 'Evaporation Instabilities in Cryogenic liquids, and the Solution of Water and Carbon Dioxide in Liquid Nitrogen', ICEC 9 papers, p. 802.

[44] Bayley (1955), 'An Analysis of Turbulent Free-Convection Heat Transfer', Proceedings of the Institute of Mechanical Engineers, Vol.109, No. 20.

[45] Vliet & Liu (1969), J. Heat Transfer, Trans ASME 91, p. 517.

APPENDIX I[1]

SUPPLEMENT TO THE DERIVATION OF THE GENERAL DISCRETIZATION EQUATION

The total flux(advection plus convection) of the general variable ϕ across an interface between two neighbouring grid points shown in Fig. 1 may be expressed as

$$J = u\phi - \Gamma\frac{d\phi}{dx} \tag{1}$$

where Γ is the diffusion coefficient specific to a particular meaning of ϕ. Introducing D and F as the diffusion conductance and mass flow rate respectively

$$D = \frac{\Gamma}{\delta}, \qquad F = u \tag{2}$$

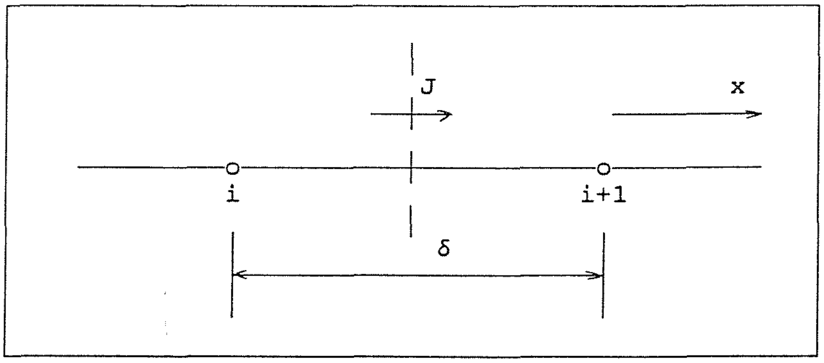

Fig. 1 Total flux across an interface between two grid points.

---

[1] To be consistent with the text, all the variables in the appendix are dimensionless.

we write

$$J^* = \frac{J}{D} = P\phi - \frac{d\phi}{d(x/\delta)} \tag{3}$$

where P is the Peclet number, defined as

$$P = \frac{F}{D} = \frac{u\delta}{\Gamma} \tag{4}$$

The value of ϕ at the interface will be some weighted average of ϕ_i and ϕ_{i+1}, while the gradient $d\phi/d(x/\delta)$ will be some multiple of $(\phi_i - \phi_{i+1})$. Thus one could write

$$J^* = P[a\phi_i + (1-a)\phi_{i+1}] - b(\phi_{i+1} - \phi_i) \tag{5}$$

where a and b are dimensionless multipliers that depend on P. Equation (5) may be rearranged into

$$J^* = B\phi_i - A\phi_{i+1} \tag{6}$$

where A and B are dimensionless coefficients that are functions of the Peclet number P.

There are two important properties that the functions A and B must hold.

Property 1:

$$B = A + P \tag{7}$$

This follows from setting $\phi_i = \phi_{i+1}$. In this case the diffusion flux must be zero, and J would then simply be the advection flux $\rho u\phi_i$.

Therefore

$$J^* = P\phi_i = P\phi_{i+1} \tag{8}$$

Combining equations (6) and (8) would lead to equation (7).

Property 2:

$$A(-P) = B(P) \tag{9a}$$

$$B(-P) = A(P) \tag{9b}$$

This property follows from considering reversing the coordinate axis, in which case P will become -P and the functions A and B will interchange their roles.

The implication of these properties is that if A(P) is known for $P > 0$ then A(P) and B(P) can be deduced for all P.

For $P < 0$,

$$\begin{aligned} A(P) &= B(P) - P && \text{from equation (7)} \\ &= A(-P) - P && \text{from equation (9a)} \\ &= A(|P|) - P && (10) \end{aligned}$$

Thus, for all values of P, positive and negative, one could write

$$A(P) = A(|P|) + \{-P, 0\} \tag{11a}$$

and

$$B(P) = A(|P|) + \{P, 0\} \tag{11b}$$

where the notation { } takes the maximum value of the elements within.

From equations (6) and (7), the following two relations can be obtained

$$J^{*} - P\phi_{i} = A(\phi_{i} - \phi_{i+1}) \tag{12a}$$

$$J^{*} - P\phi_{i+1} = B(\phi_{i} - \phi_{i+1}) \tag{12b}$$

or in terms of J (multiplied by D),

$$J - F\phi_{i} = DA(\phi_{i} - \phi_{i+1}) \tag{13a}$$

$$J - F\phi_{i+1} = DB(\phi_{i} - \phi_{i+1}) \tag{13b}$$

Applying equations (13a) and (13b) to the four interfaces of the central control volume in Fig. 3.3, one arrives at

$$\begin{aligned} &J_e - F_e\phi_P = A_E(\phi_P - \phi_E), \quad J_w - F_w\phi_P = -A_W(\phi_P - \phi_W) \\ &J_n - F_n\phi_P = A_N(\phi_P - \phi_N), \quad J_s - F_s\phi_P = -A_S(\phi_P - \phi_S) \end{aligned} \tag{3.17}$$

where

$$A_E = D_eA(P_e) = D_eA(|P_e|) + \{-F_e, 0\}$$

$$A_W = D_wA(P_w) = D_wA(|P_w|) + \{F_w, 0\}$$

$$A_N = D_nA(P_n) = D_nA(|P_n|) + \{-F_n, 0\}$$

$$A_S = D_sA(P_s) = D_sA(|P_s|) + \{F_s, 0\}$$

Now the function $A(|P|)$ will be discussed. We consider a steady one-dimensional situation in which only the convection and diffusion terms are present. The governing differential equation is

$$\frac{d}{dt}(u\phi) = \frac{d}{dx}(\Gamma\frac{d\phi}{dx}) \tag{14}$$

In the Boussinesq approximation Γ is assumed as a constant, and so is u as implied by the continuity equation. For a domain $0 \leq x \leq L$, with the boundary conditions

$$\phi = \phi_0 \quad \text{at } x = 0$$

and

$$\phi = \phi_L \quad \text{at } x = L$$

equation (14) may be solved as

$$\frac{\phi - \phi_0}{\phi_L - \phi_0} = \frac{\exp(Px/L) - 1}{\exp(P) - 1} \tag{15}$$

It should be noted that an exact solution cannot be found for two or three-dimensional problems. The exact solution (15) can be used as a profile between grid points i and i+1 in Fig. 1, with ϕ_i and ϕ_{i+1} replacing ϕ_0 and ϕ_L and the distance δ replacing L. The substitution of this profile into equation (1) yields

$$J = F(\phi_i + \frac{\phi_i - \phi_{i+1}}{\exp(P) - 1}) \tag{16}$$

Compare equations (13a) and (16), one obtains

$$A(P) = \frac{P}{\exp(P) - 1} \tag{17}$$

Combining equations (10) and (17) leads to

$$A(|(P)|) = \frac{|P|}{\exp(|P|) - 1} \tag{18}$$

Since exponential functions are usually expensive to compute, a power law approximation of equation (18) has been proposed by Patankar[27] which is

$$A(|P|) = \{0, (1 - |P|/10)^5\} \tag{19}$$

This power law approximation agrees with the exponential function well, as shown in Fig. 2, and is used in the model.

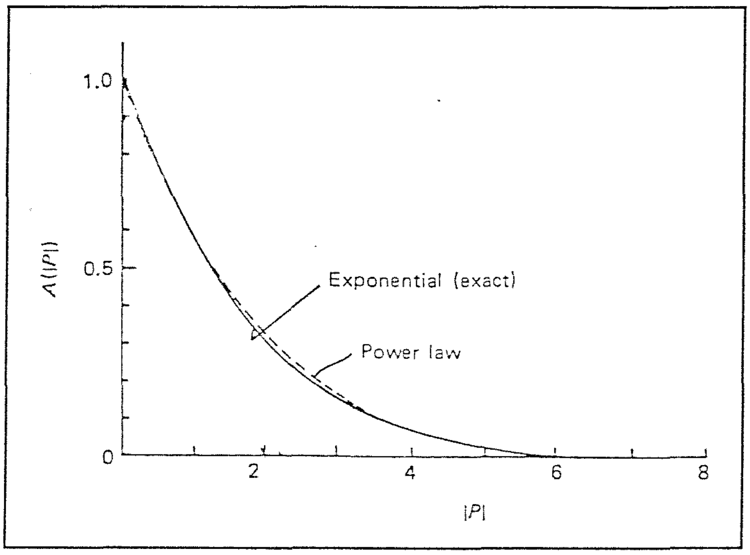

Fig. 2 Power law approximation of the exact solution

APPENDIX II

Paper 1:	presented at the 6th International Conference on Numerical Methods in Thermal Problems, Swansea UK (July 1989).
Paper 2:	presented at the Conference of Low Temperature Engineering and Cryogenics, Southampton UK (1990).

MODELLING CONVECTION AND ROLLOVER PHENOMENA IN CRYOGENIC LIQUIDS

J.Q. Shi, C. Beduz, M.J. Burton and R.G. Scurlock

Institute of Cryogenics, University of Southampton, England.

SUMMARY

A number of "Rollover" incidents have been reported in the large scale storage of liquid natural gas (LNG), some of which have resulted in a serious over pressurisation of the storage tank. As part of an overall research project, some numerical analysis has been applied to the double diffusion problem with the intention of providing a better understanding of the processes that control rollover. Experiments have been performed on two layers of liquid nitrogen, one of which was mixed with a small quantity of liquid oxygen to increase it's density. The numerical model has been used to simulate these experiments, in order that some validation of the results is possible.

1. INTRODUCTION

In the large scale storage of LNG, it is often the case that a cargo of liquified gas is pumped into a tank which is already partly filled with liquid of a slightly different composition (mainly methane) and density. Two separate stratified layers may result.

Heat leaking into the liquid from the surroundings is removed by evaporation at the free surface. A convection loop is established in which liquid in a boundary layer flows upwards over the vessels walls, absorbing heat from the surroundings, then across the free surface where the heat is removed by evaporation.

In the case of two stratified layers, the boundary layer in the lower layer is unable to reach the surface. The superheat in the bottom layer will build up because diffusion across the interface between the two layers is insufficient to match the heat leaking in from the vessel walls. This heating continues until the density in the lower layer falls to that of the upper layer, at which point the highly superheated liquid is suddenly allowed to reach the surface. This process, together with the sudden release of the superheat from the lower layer, is rather inaccurately known as "Rollover".

In a few instances, the sudden increase in the vaporisation rate has overwhelmed the vents on the storage vessel and caused a serious over-pressurisation of the system to occur. Fortunately, no rupture or leakage has resulted so far. An experimental research programme at Southampton, has been trying to identify the mechanisms and parameters which control rollover. The difficulty of observing the entire flow, temperature and density fields has prompted this application of some fairly simple numerical methods to the problem.

2. THE EXPERIMENTAL PROGRAMME

While this paper concerns the numerical approach to this problem, it is worthwhile to outline some of the experiments that have been used to validate the numerical results. Because of the difficulties and dangers of experimenting with even small quantities of LNG, the system has been simulated using two layers of liquid nitrogen (LIN), one of which is mixed with a small quantity of liquid oxygen (LOX) to increase the density.

Beresford (1) used laser doppler anemometry to measure the velocity profile 13mm below the surface of a single layer of liquid nitrogen in a 70mm diameter tube. This tube was surrounded by a glass vacuum dewar, partially filled with liquid nitrogen, in order to limit the heat flow to the inner tube.

Agbabi (2) observed the behaviour of two layers of liquid (pure LIN and a LIN/LOX mixture), when heated by two transparent electrical heaters (one for each layer). In order to reduce the heat leak from the surroundings, this dewar was suspended inside another larger one, the intervening space being filled with liquid nitrogen. Runs were carried out, with various combinations of heating to the top and bottom layers and with different initial density differences (dependent on the liquid oxygen concentration). Temperatures were measured down the central vertical axis of the dewar and concentration of liquid oxygen was measured on a vertical axis, offset from the centre. In addition, the evaporation rate was recorded.

Recent flow visualisation experiments with this rig have indicated that the flow is not very axi-symmetric, possibly due to inhomogeneity of the electrical heating and the large aspect ratio of the dewar (height to diameter). Further visualisation experiments have therefore been performed using a lower aspect ratio dewar. The natural heat leak from the surroundings drove the convection (an outer dewar supplied with cold nitrogen gas was used to limit this), rather than the electrical heaters.

3. THE NUMERICAL MODEL

The experimental programme outlined above enabled a broad insight to be gained of the rollover phenomenon. The aim of the numerical work was to investigate in some detail the way in which temperature and concentration gradients control the event. It was not desired to provide an accurate prediction of the occurrence of rollover, this has already been accomplished using far simpler (and more economical) models with considerable success (3), (4) and (5).

The decision was made to model the dewar as a 2-dimensional axi-symmetric problem. Since the flow is incompressible and the authors had some experience of the vorticity-stream function method, it was decided to use this rather than a primitive variables approach. Although the experiments were performed in dewars with hemi-spherical bottoms, it was decided that for the purposes of the model the bottom would be assumed flat.

A cartesian coordinate version of the code was validated against the bench mark solution of Markatos (6) up to Rayleigh numbers of 10^6 with very satisfactory results. This code was then converted to cylindrical polar coordinates. In common with the method presented by Gosman et al (7), ζ/r has been used as the dependent variable rather than simply the vorticity ζ.

Obtaining the velocity distribution (u and w) from the stream function (ψ) proved a little more troublesome than expected. In cylindrical polar coordinates :

$$u = \frac{1}{r}\frac{\partial\psi}{\partial z} \qquad \text{and} \quad w = \frac{1}{r}\frac{\partial\psi}{\partial r}$$

The u and w velocity components are required on the control volume faces to which they are normal. The most obvious way to approximate the partial differentials above was to use central difference equations between the values of the stream function at control volume corners. The corner values of stream function were obtained by linear interpolation between the values at the centres of the four adjacent volumes. While this procedure worked well in cartesian coordinates, the presence of the 1/r terms in the cylindrical polar form produced an unrealistic spike on the w velocity distribution at the centre line.

These spikes were removed by reversing the order of the above operations, ie. differentiate the stream function distribution and the interpolate to obtain velocities at the desired positions. Unfortunately it was found that interpolating the velocity distribution caused the mass continuity condition to be violated. Velocities calculated directly from stream function must by definition fulfil continuity; subsequent interpolation may destroy this property.

A better method of obtaining stream function at control volume corners was required so that normal velocities could be obtained directly. It is simple to show that where $\partial w/\partial r = 0$, as will be the case at and very close to the centre line, the stream function will be proportional to r^2. So a quadratic equation was fitted to each triplet of points in the radial direction and the corner values were calculated from these. This produced smooth velocity profiles while preserving mass continuity.

The vorticity boundary value for a centre line or free surface is zero. For the no-slip condition on the bottom and side walls, a first order vorticity boundary condition was used to promote maximum stability. A line of control volumes were located across the centre line; these thus appear as "half" volumes in the solution domain. The vorticity and stream function for these volumes were defined (zero), so no calculation was required, thus avoiding any singularity problems associated with 1/r terms. The other boundaries were located along control volume faces. Experiments previously performed at Southampton (2) indicated that the temperature boundary layer beneath the free surface, across which heat is conducted, is only of the order of 100's of microns thick. To allow surface heat fluxes in the model to equal those observed physically, the grid spacing in this region must be smaller than this. Accordingly the top layer of control volumes is very thin, with the thickness increasing downwards, initially in a roughly geometric progression. To simulate the evaporating surface, an isothermal boundary condition was used.

The solution procedure employed the ADI method within an iterative loop. The iteration was used to provide better estimates of the temperature and velocity distribution and the vorticity boundary conditions at the $n+\frac{1}{2}$ and $n+1$ time steps.

4. RESULTS

4.1 Single component model

In order to give some confidence that the two component model was producing realistic results, a one component version of the code was tested against the experimental velocity profile for convecting liquid nitrogen, mentioned in section 2. Unfortunately the heat flux into the dewar was unknown, so various heat fluxes were tried in the model until the velocity in the central jet matched the experimental value. A heat flux of 20 W/m^2 was found to give the best agreement, which is a very plausible value for heat transfer by radiation across the vacuum space of the glass dewar. From figure 1 it can be seen that the profile is predicted remarkably well with the exception of the maximum velocity in the outer boundary layer which is only about half the experimental value. However, since the numerical prediction fulfils mass continuity, it is clear that the experimental profile does not. It is possible that the laser doppler measurements near the curved glass walls were more susceptible to error. It is also possible that the flow was not truly axi-symmetric and that the central jet was displaced away from the side on which velocity was being measured.

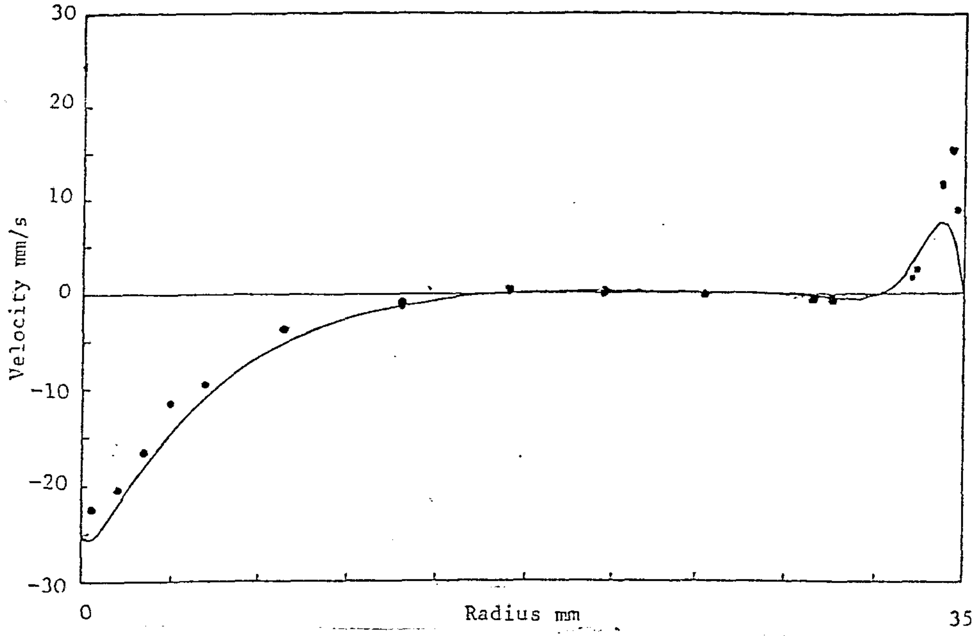

Figure 1 Comparison of experimental velocity profile in liquid nitrogen with numerical prediction

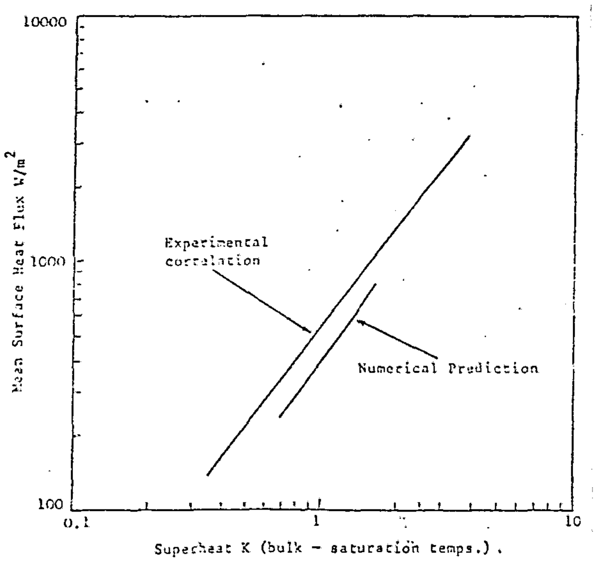

Figure 2 Comparison of experimental surface heat flux against superheat correlation with numerical prediction

Some earlier (unpublished) research had established an empirical relationship between the bulk superheat of the LIN at steady state and the heat flux away from the free surface (ie. the evaporation rate). Five tests were run to steady state, to see how well the model behaviour followed this empirical law. Figure 2 shows these results compared to the experimental results and correlation. The model correctly predicts a 4/3 power law relationship, but the constant of proportionality is a little lower. This may be accounted for by noting that in the experiments, cellular convection (similar to Bénard cells) was observed just below the surface which would tend to increase the heat flux across the surface layer. The model, being two dimensional, cannot represent this cellular convection.

4.2 Two component model

Two cases have been examined, both in a vessel of 140mm radius and 240mm height. The initial concentration conditions were identical in both cases; from the bottom to a height of 136mm, 97.9% LIN and 2.07% LOX (by mass) with a density of 815.5 kg/m^3, and from a height of 160mm to the top, pure LIN with a density of 807.3 kg/m^3. Between these two layers an intermediate layer with uniform concentration and density gradients. In the first case the side wall heat flux into the top and intermediate layers (initial positions) was 25W/m^2 and 31.5W/m^2 into the bottom layer with an adiabatic base. The second case was identical except that the heat flux into the bottom layer was 115W/m^2 from the base only, top and intermediate layers as above. In each case the heat flow into each layer is identical, but they represent the two extremes of bottom layer heating.

4.2(a) Case 1 - Side wall heating, adiabatic bottom

Three stages were observed leading to the complete mixing of the contents of the vessel after approximately 16 minutes.

(i) 0 - 12 minutes

In the upper and lower layers, primary temperature driven convection loops were set up as shown by the stream function plots in figure 3[1]. The intermediate layer was rather more confused with a number of small loops driven by gradients in both temperature and LOX concentration. The character of the two primary loops was quite different due to the action of the free surface on the upper layer. Liquid flow across the surface was strongly cooled and thus formed a central jet down the centre. This cooling effect was not present in the bottom layer and consequently no central jet was seen. The flow velocities in the bottom layer were generally lower than the top because of smaller temperature differentials.

The intermediate layer can be seen to have spread considerably between 2 and 6 minutes. The smaller loops in this region promoted mixing, which in turn enhanced diffusion and entrainment from the upper and lower layers. This spreading of the intermediate layer may be seen in figure 4.

---

[1] It should be noted that in cylindrical polar coordinates, it is not possible to directly infer the fluid velocity from the spacing of the stream function contours because of the 1/r terms in the definition of stream function. For a constant velocity, the stream lines will get farther apart as the centre line is approached.

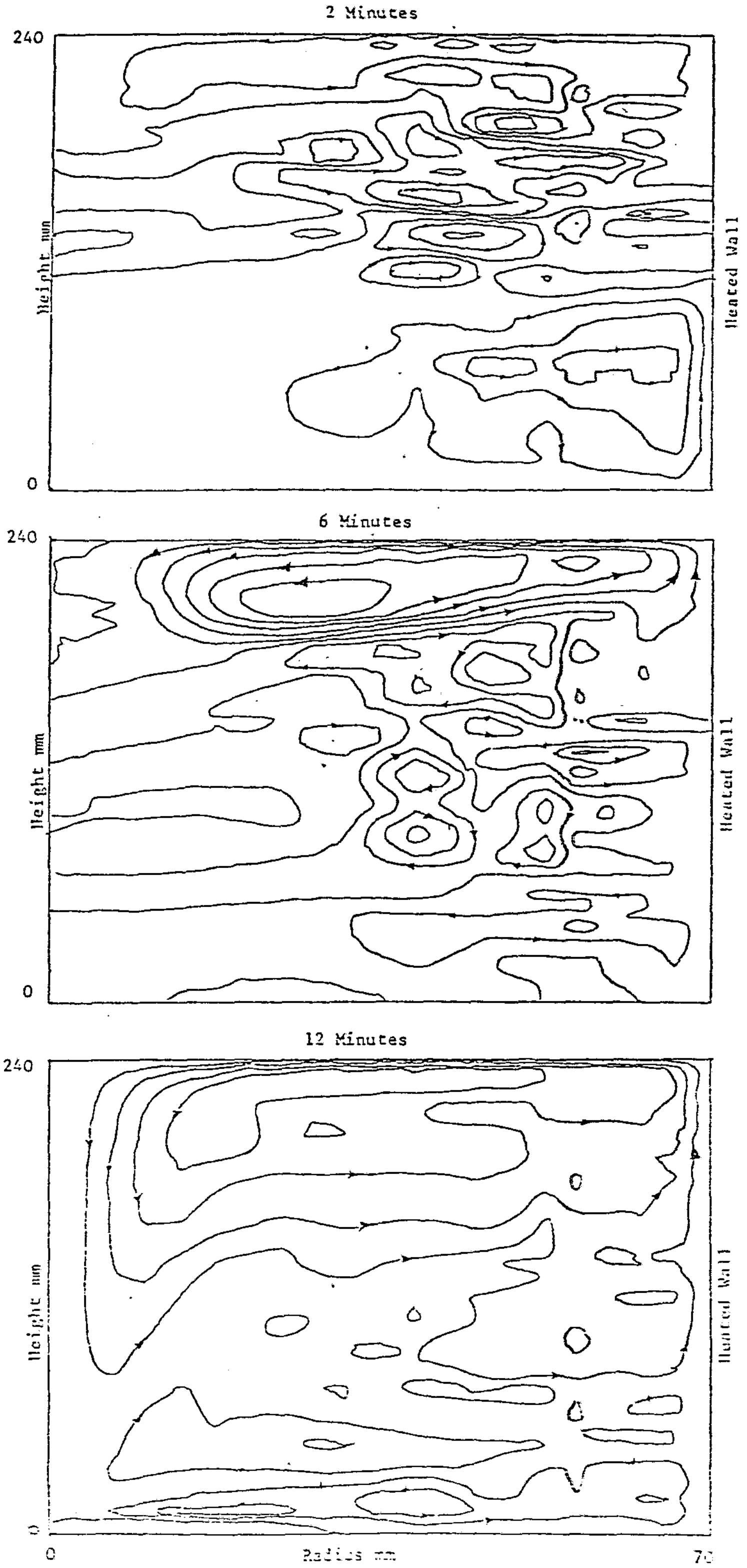

2 Minutes

6 Minutes

12 Minutes

Figure 3   Steam function contour plots at 2, 6 and 12 minutes

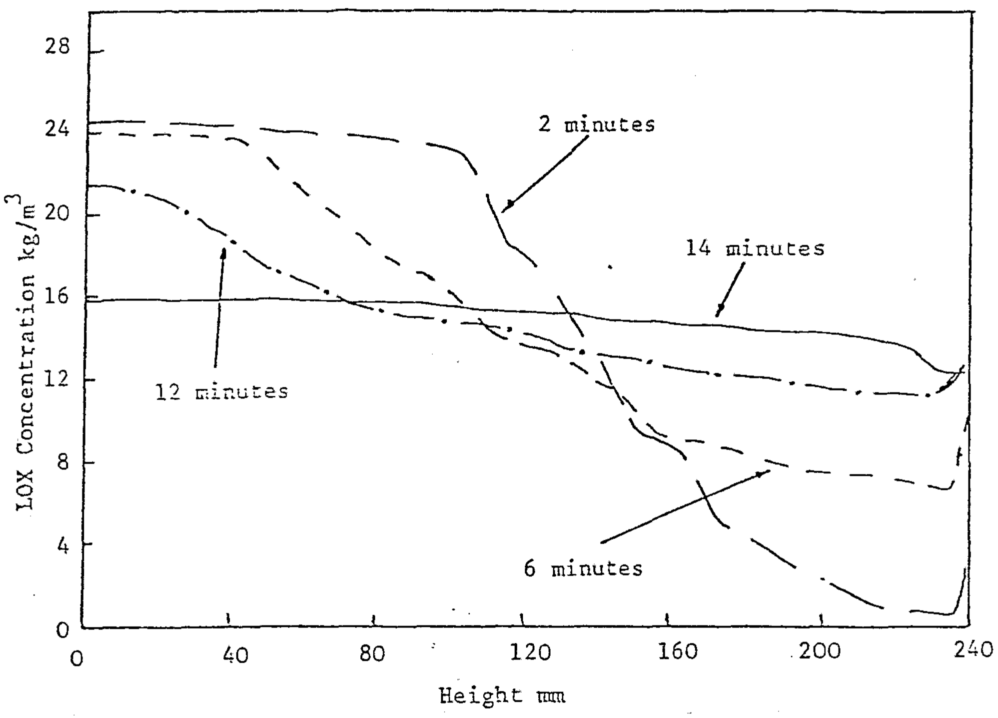

Figure 4 Vertical concentration profiles at mid-radius

Throughout this period, the central jet in the upper layer got generally stronger and penetrated deeper into the intermediate layer. There were two factors at work here; firstly the temperature differential was increasing due to the rising bulk temperature and secondly the concentration of LOX in the central region of the intermediate layer fell due to entrainment of nearly pure LIN from the central jet.

By 12 minutes the jet reached the bottom of the vessel. The intermediate layer had fallen and reduced in size. The lower primary loop was confined to the bottom 15% of the vessel and was still quite weak. This lowering of the intermediate layer was observed in the experiments of Agbabi (2) and the more recent flow visualisation experiments of the current authors.

(ii) 12 - 14 minutes

When the central jet reached the bottom of the vessel, a rapid flow was set up, radially outwards across the base. Some of the cool liquid from the central jet reached the bottom edge of the heated side wall and joined the thermal boundary layer here.

Two factors now contributed to a rapid acceleration of the lower convection loop, which from this point onwards totally dominated the flow. Firstly, the temperature differential was increased by the presence of cold liquid from the central jet. Secondly, flow across the base of the vessel enhanced the buoyancy driven flow by viscous drag. This strong convection loop was initially

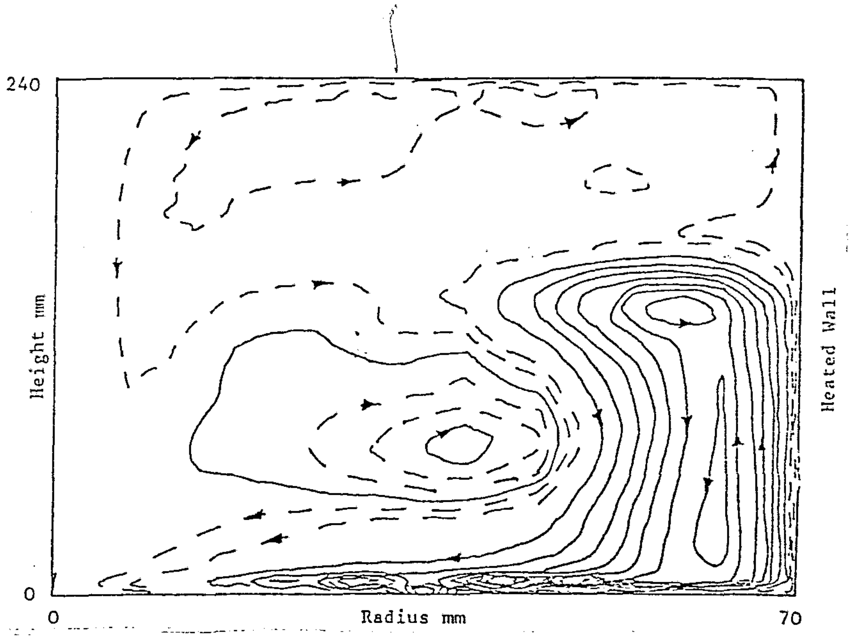

Figure 5 Stream function contours for 13 minutes and 20 seconds

unable to penetrate upwards into the top layer because of it's high LOX concentration. However, this was progressively reduced due to liquid from the upper layer being entrained, allowing the loop to penetrate further and further up the vessel. Figure 5[2] shows the stream function contours after a period of 13 minutes and 20 seconds, at which time the lower loop can be seen to have reached approximately 2/3 of the way up the vessel walls. After 14 minutes the loop reached all the way to the surface.

(iii) 14 - 16 minutes

From the concentration profile shown in figure 4, it can be seen that the mixing process was now nearly complete, only a small region of low LOX concentration remaining just under the surface. The main convection loop now began to spread across the free surface, turning near the centre line and flowing back towards the outer wall before flowing down to the bottom of the vessel. This raised the LOX concentration under surface, allowing the central flow to penetrate further down the vessel before being turned towards the outer wall. After 16 minutes, when all the concentration differences had been eradicated, the flow simply looped around the periphery and down the centre in the usual manner for a single component liquid.

Figure 6 shows the free surface heat flux (as a percentage of the heat input) throughout this run. This shows a steady rise

---

[2] It should be noted that, because of the strength of the convection, only every 6th contour has been drawn in figure 5 compared to figure 3, although some intermediate contours have been shown dotted to indicate the flow in the upper layer.

until 12 minutes at which time there is a small but sudden increase. This corresponds to the initiation of the strong convection loop in the bottom layer, which, by entrainment, promoted heat and mass exchange with the upper layer.

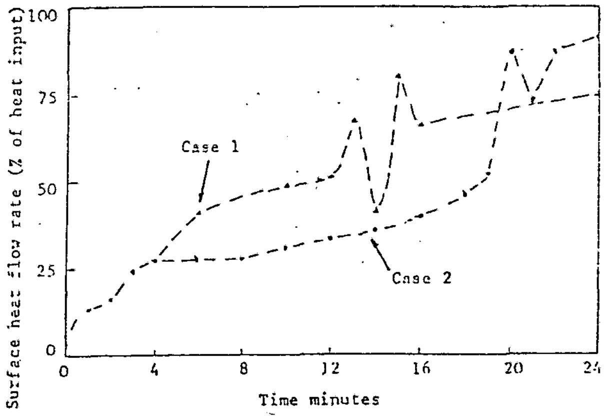

Figure 6 Surface heat flow rate

A sharp dip in the heat flow was observed at 14 minutes. At this stage the main convection loop had just reached the surface, the hot boundary layer was returning directly to the bottom of the vessel rather than flowing across the surface, hence very little heat could be lost. Once the main loop spread across the surface the heat flux peaked again until the mixing process was finally complete.

4.2(b) Case 2 - Side wall and bottom heating

This run has many features in common with Case 1, but there are some interesting differences. Relatively strong convection was set up in the bottom layer almost immediately, as a results of the heating on the bottom surface. The convection loops were quite transient; sometimes a single loop, sometimes a cellular pattern as shown in figure 7. The effect of this convection was to maintain a constant LOX concentration throughout the layer and thus to prevent the intermediate layer spreading and advancing downwards. This allowed more superheat to be stored in the bottom layer and therefore the rise in free surface heat flow rate after 4 minutes was slower (figure 6). In common with Case 1, the central jet in the upper layer gradually penetrated further and further into the lower layer until it reached the bottom surface after 18 minutes. From this point onwards the sequence of events was broadly similar to Case 1; a sudden acceleration of the bottom loop, which grew upwards to meet the surface over a period of about 2 minutes, accompanied by a sharp rise in the free surface heat flow rate.

5. Conclusions

The one-component version of the code has been shown to give good quantitative agreement with the experimental data available. The two-component code has allowed a detailed examination of roll-over behaviour for two different heating conditions. Some of the effects predicted, such as the lowering of the intermediate layer and the penetration of the central jet are in qualitative agreement with experimental observations.

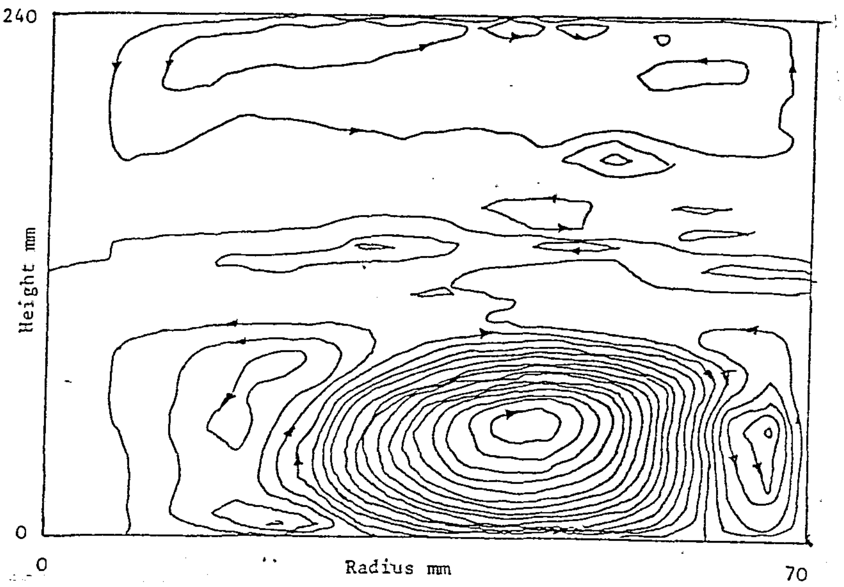

Figure 7 Stream function contours for Case 2 at 6 minutes

References

1. Beresford, G. - Laser Doppler Velocimetry Studies on Cryogenic Fluids, Ph.D. Thesis, University of Southampton, 1984.

2. Agbabi, T. - Rollover and Interfacial Studies in LNG Mixtures, Ph.D. Thesis, University of Southampton, 1987.

3. Chatterjee, N., and Geist, J.M., - The Effects of Stratification on Boil-Off Rates in LNG Tanks, Pipeline and Gas Journal, p.40, September 1982.

4. Germeles, A.E. - A Model for LNG tank rollover, Advances in Cryogenic Engineering, 21, p.326 (1975).

5. Heestand, J., Shipman, C.W. and Meader, J.W. - A Predictive Model for Rollover in Stratified LNG Tanks, AIChE Journal, 29, No.2, p.199 (1983).

6. Markatos, N.C. and Pericleous, K.A. - Laminar and Turbulent Natural Convection in an Enclosed Cavity, Int. Journal Heat and Mass Transfer, 27, No.5, pp.755-772 (1984).

7. Gosman, A.D. et al - Heat and Mass Transfer in Recirculating Flows, Academic Press, London, 1969.

Acknowledgements

The authors gratefully acknowledge the financial support provided for Mr. J.Q. Shi by the British Council and the State Committee of Education, Peoples Republic of China.

EVAPORATION STABILITY OF CRYOGENIC LIQUIDS UNDER STORAGE

T.Agbabi, C.Beduz,R.G.Scurlock, J.Shi

Institute of Cryogenics, University of Southampton, Southampton SO9 5NH, UK

The equilibrium boil-off process is via surface evaporation controlled by a steep temperature gradient and associated thermal conduction in a thin surface layer separating the interface from the bulk superheated liquid. A suggested mechanism for evaporative instability is when this surface layer is penetrated by the bulk superheated liquid, thereby lowering the evaporative impedance. Increases in boil-off by factors of 10-40 can then occur for short or longer periods of time. This mechanism is discussed in relation to vapour explosions and rollover. Experimental simulations of rollover are described with simultaneous measurement of layer density and temperature, together with video observation of the mixing process.

1. LIQUID CONVECTION IN A STORAGE TANK

For any reasonably well insulated tank, the major heat fluxes entering the liquid are through the wetted area of the inner containing wall and are typically less than 100 W/m^2. This level of heat flux is much too small for nucleate boiling to occur. For example, in liquid nitrogen a heat flux of 10,000 W/m^2 is required to initiate nucleate boiling, when there is a wall-liquid temperature difference of 2-4 K.

Heat entering the liquid is absorbed by convection currents which carry the heated liquid to the surface, at which surface evaporation takes place (Fig.1.) At the vertical walls, a high velocity boundary layer flow develops and carries heated liquid into the surface layers. Heated liquid in contact with the tank floor is swept across to join the vertical boundary flow at the walls. At the surface, the heated liquid moves radially inwards as evaporation takes place. At the centre, the liquid motion becomes focused into a strong downward jet. At no stage is there any boiling. The central jet carries excess heat, which is not released by surface evaporation, into the liquid core where secondary convective processes will produce mixing and superheating.

The largest fluid temperature is undoubtedly at the container-wall-liquid-vapour interface. Surface instabilities are likely to be induced near this region where the evaporation rate is larger than at the centre of the pool.

2. SURFACE EVAPORATION AND BULK SUPERHEAT

To study surface evaporation[1], we have carried out microthermometer studies on LIN, LOX, LA, LCH$_4$ and LNG[2,3] in an 80 mm inner diameter, double-walled vacuum insulated Dewar surrounded by a second liquid bath 120 mm inner diameter. The boil-off from the inner dewar could be varied via a uniform heat flux electrical heater mounted in the vacuum space around the inner wall. The micro-thermometer consisted of 25 μm copper/constantan thermocouple junctions mounted horizontally in differential or absolute configurations. For the differential configuration, the two junctions were separated vertically by a distance of approximately 100 mm, so that temperatures in the region of the surface could be measured relative to that of the bulk liquid. For the absolute configuration, the reference junction was the ice-point while a single calibration point was made again a Pt thermometer in rapidly boiling liquid nitrogen. The pool depth was kept between 200 and 250 mm.

The results are summarised as follows:

1. For each heater power level, the equilibrium bulk temperature T_b remained uniform to within ± 0.1 K throughout the liquid, apart from the boundary layer region at the wall, and the interface region within 5 mm of the surface.

2. The temperature difference $\Delta T = (T_b - T_o)$ i.e. the bulk superheat, was a sensitive function of heater power, and values of 3.0K in LIN and 4.0 K in LOX could be produced before any nucleation occurred.

3. Figure 1 presents a summary of experimental runs with a range of heater powers from which the following correlations were obtained.

$$\text{For LIN, } \dot{m} = 3.32\Delta T^{1.17} \times 10^{-3}\text{kg/(m}^2\text{s)} \qquad (1)$$

$$\text{For LOX, } \dot{m} = 2.84\Delta T^{1.26} \times 10^{-3}\text{kg/(m}^2\text{s)} \qquad (2)$$

$$\text{For LNG/LCH}_4\text{ } m = 1.30\ \Delta T^{1.33} \times 10^{-3}\text{ kg/(m}^2\text{s)} \qquad (3)$$

where $\dot{m}$ is the mass flux at the liquid vapour interface.

IMPEDANCES TO SURFACE EVAPORATION

The impedance mechanisms are revealed by the vertical temperature profiles within a few mm of the liquid-vapour interface. To produce the vertical temperature profiles, the liquid level was allowed to fall, as the LIN evaporated, and pass the rigidly fixed microthermometer system. An example of the vertical profiles in liquid nitrogen is shown in Figures 2 for a mass flux of $m = 510^{-3}$ kg/m^{2}s (= 1000 W/m^2).

At the interface, molecular evaporation takes place according to

$$\dot{m} = 90\ \alpha\ (T_s - T_o)\ \text{kg/m}_2\text{s} \qquad (4)$$

where T_s is the temperature of the liquid/vapour interface, T_o is the saturation temperature and α is the evaporation coefficient. The reciprocal of α can be regarded as an evaporation impedance factor which is related to the presence of impurities in the surface .

From our observations in LIN at $\dot{m} = 10^{-2}$ kg/(m^{2}s) where ΔT ($= T_b - T_o$) was 2.5 K, the estimated value of $T_s - T_o$ was 0.15 ± 0.10 K, close to the lower limit of sensitivity leading to an estimated value of the evaporation coefficient α of about 10^{-3} for liquid nitrogen, under the reproducible, equilibrium conditions in the cryostat. If impurities collect at the surface, α can be expected to fall to 10^{-5}.

Figure 2 indicates that the major temperature drop occurs across a liquid layer approximately 300 μm in thickness with a temperature gradient of 5000 K/m. Heat flow across this layer is by conduction and the heat flux for liquid nitrogen is

$$\dot{m}L = 460\ (T_c - T_s)\ \text{kg/m}^2\text{s} \qquad (5)$$

where T_c is the temperature at the bottom of the <u>thermally conducting surface layer.</u> Superimposed on the mean temperature profiles is an irregular time dependent variation, which can be observed with a fast response recorder.

The observed temperature variations are continuous and have a time constant of 0.3 s, and a mean amplitude of approximately 0.5 K within the temperature interval T_b to T_s

and depth interval 0.3 to 4.5 mm. For $d < 0.3$ mm, i.e. within the thermally conducting surface layer, the temperature amplitude decreases to zero as the surface is approached. For $d > 5$ mm, these rapid temperature variations appear to cease.

It is deduced that these temperature variations arise from turbulent convection cells with a vertical dimension of 4 - 5 mm which are driven by the cooling and sinking of elements of fluid from the thermally conducting surface layer in a much smaller temperature gradient of about 50 K/m.

This lower thick layer, which we call the intermediate layer, contains the mechanism whereby superheated liquid from the bulk convection loop is carried into the thermally conducting surface layer by a system of moving plumes.

From the microthermometer plot, the effective linear heat transfer equation for this layer is given by

$$\dot{m}L = 50,000\ (T_c - T_b)\ \mathrm{kg/m^2s} \qquad (6)$$

where T_b is the bulk temperature defined earlier.

Combining equations (4), (5) and (6), we obtain the overall impedance equation for surface evaporation with $L = 2 \times 10^5$ J/kg.

$$\Delta T = (T_b - T_o) = \dot{m}\ [\underbrace{\frac{1}{90\alpha}}_{I} + \underbrace{440}_{II} + \underbrace{4}_{III}] \qquad (7)$$

where the impedance terms represent contributions from

I Molecular evaporation including impurity effects

II The thermal conduction layer

III The intermediate layer

In the conventional sense, terms II and III together represent a convection process. It is clear that for $\alpha = 10^{-3}$, term II is dominant. Impurity effects will dominate if α is reduced to 10^{-5}.

Equation (7) is effective under equilibrium conditions and illustrates how the bulk superheated liquid is separated from the surface, where molecular evaporation is the only limiting mass flux process, by a thin (few mm) convective layer.

Any agitation of the surface will destroy the delicate impedance mechanism of the convection process and allow the bulk liquid to enter the molecular evaporation region with a drop in impedance and consequent rise in evaporation rate of 40-fold. This is a vapour explosion. If the surface agitation is maintained by, for example, nucleate boiling or mixing during rollover, then the high evaporation rate will be maintained until the thermal overfill energy is released.

SIMULATION OF ROLLOVER BETWEEN LIN AND LOX/LIN MIXTURES

To study rollover, the same 80 mm inner diameter, double walled dewar vessel surrounded by a second LIN/LOX bath 120 mm inner diameter was used. Two liquid layers of different density were placed in the inner dewar using different compositions of oxygen in nitrogen mixtures. Two uniform heat flux electrical heaters mounted in the vacuum space around the inner wall enabled different controlled heat fluxes to be injected into the two layers. At the same time, the temperature and oxygen composition of each layer could be measured, together with the boil-off rate over a period of time up to 400 minutes. During this observation period, mixing by rollover of the two layers could be studied on a reproducible basis.

Figures 3 and 4 show the experimental data for 2 rollover simulations. In Figure

3, the initial density difference was 19 kg/m^3 a heating rate of 67.1 W/m^2 was injected into the lower layer only and rollover occurred after 50 minutes, when the boil-off reached a peak of 1.6 x 10^{-3} kg/m^{2}s.

In Figure 4, the initial density difference was 8.7 kg/m^3 while much smaller heating rates of 4.2 and 3.6 W/m^2 were injected into the lower and upper layers respectively.

Rollover occurred after 360 minutes, when the boil-off reached a peak of 1.9 x 10^{-3} kg/m^{2}s, over 10 times the equilibrium value.

Conclusions to be drawn from these rollover simulations include:

(1) Peak values of boil-off mass flux during rollover in these laboratory simulations were considerably smaller than the boil-off recorded in the La Spezia incident.

(2) Mixing during rollover is by a process of penetrative convective oscillations of the interface between the 2 layers. The amplitude of these oscillations increase as the mixing proceeds, while the interface moves downwards.

(3) In most simulations the boil-off rate is controlled by the local liquid superheat near the liquid/vapour interface through the evaporative surface impedance described above. In one example however, shown in Figure 4, the peak boil-off was considerably in excess of the value corresponding to the liquid superheat and the evaporative surface impedance.

(4) There is no rollover of the 2 layers, by the lower layer displacing the upper. The term rollover is incorrect.

Finally, it should be emphasised that these conclusions are based on results obtained in small scale experiments and may be different for large scale storage tanks.

ACKNOWLEDGEMENTS

We wish to acknowledge the support of the following sponsors and students who contributed towards the development of the various experimental techniques and measurements: (SERC + British Gas), M.C.M.Atkinson and T.Agbabi,(CNAN, Algeria) R.Rebiai and (Chinese Government+ British Council) J.Shi.

REFERENCES

(1) Beduz C, Rebiai R and Scurlock R.G., Adv. Cryo. Eng. 29 (1985) 795.

(2) Agbabi T, Atkinson M.C.M., Beduz C and Scurlock R.G., Proc. ICEC 11 (1986) 627.

(3) Agbabi T, Ph.D. thesis, Southampton University (1989)

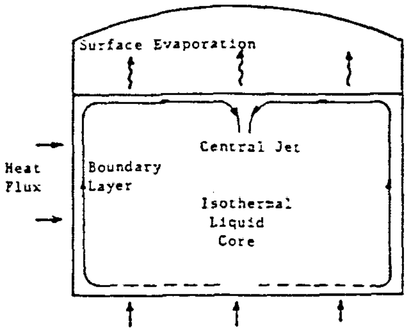

Fig.1. Primary liquid convection in storage tank

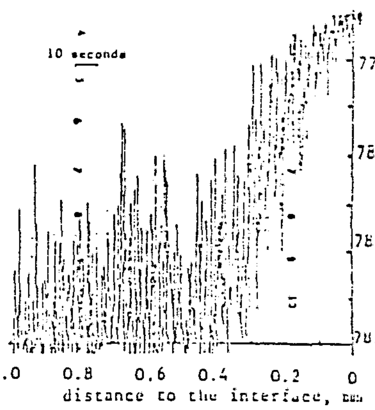

Fig. 2. Microthermometer plot showing temperature profile below surface with rapid variations superimposed. Mean bulk temperature T_b was 78.8 K.

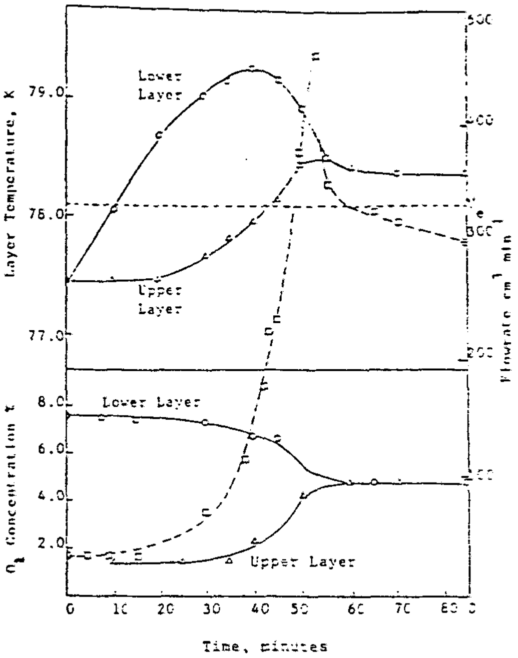

Fig.3 Variations of layer temperatures, oxygen concentrations and boil-off in rollover simulation. Initial density difference 19 kg/m^3.

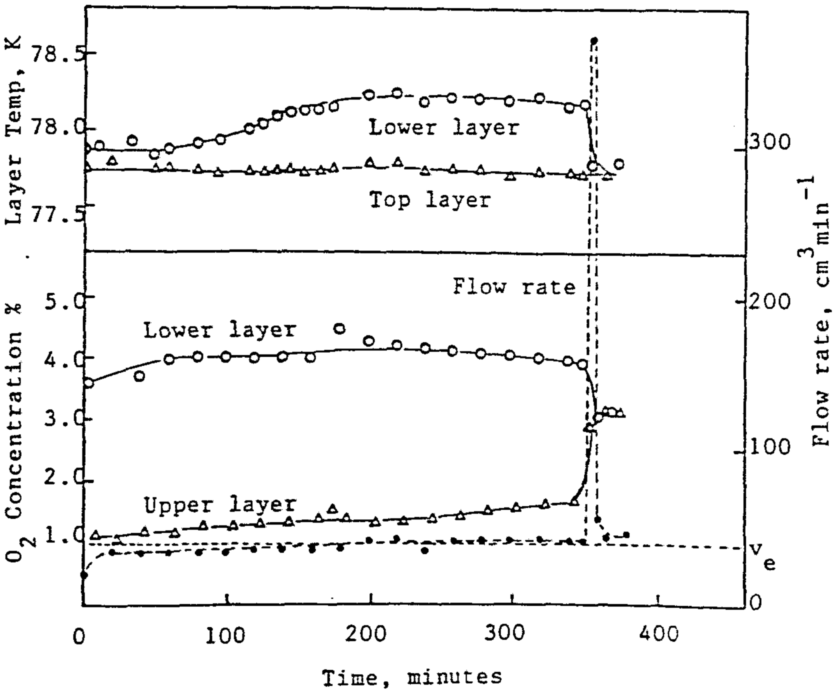

Fig. 4 Variation of layer temperatures, oxygen concentrations and boil-off in rollover simulation. Initial density difference 8.7 Kg/m^3.